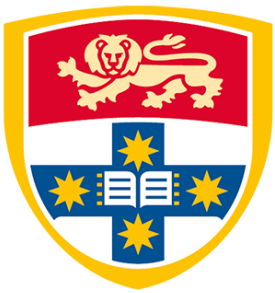

THE UNIVERSITY OF SYDNEY

Advanced Research in the development of green and sustainable processes for high-value chemical production from biomass

A thesis submitted to fulfil requirements for the degree of

Doctor of Philosophy

in

Faculty of Engineering and Information Technology

University of Sydney

by

Wenjie Yang

Accepted on the recommendation by

Supervisor: Prof. Jun Huang

2023

Statement of originality

I certify that the intellectual content of this thesis is the product of my own work and that all the assistance received in preparing this thesis and sources have been acknowledged.

I have not submitted this material for another degree at this or any other institution.

Wenjie Yang

February 2023

Authorship attribution statement

Part of *Chapter 1* of this thesis is published as

1) **Wenjie Yang**, Jun Haung. "Analysis of Local Structure, Acidic Property and Activity of Solid Acids by Solid-State Nuclear Magnetic Resonance Spectroscopy." *Chinese Journal of Magnetic Resonance* 38 (2021): 460-473.
2) **Wenjie Yang**, Zichun Wang, Jun Huang, Yijiao Jiang. "Qualitative and quantitative analysis of acid properties for solid acids by solid-state nuclear magnetic resonance spectroscopy." *The Journal of Physical Chemistry C* 125, no. 19 (2021): 10179-10197.

For which I wrote the drafts of the MS.

Part of *Chapter 2* and entire *Chapter 3* of this thesis is published as

1) **Wenjie Yang**, Kyung Duk Kim, Luke A. O'Dell, Lizhuo Wang, Haimei Xu, Mengtong Ruan, Wei Wang, Ryong Ryoo, Yijiao Jiang, Jun Huang. "Brønsted acid sites formation through penta-coordinated aluminum species on alumina-boria for phenylglyoxal conversion." *Journal of Catalysis* 416 (2022): 375-386.
2) **Wenjie Yang**, Weibin Liang, Luke A. O'Dell, Hamish D. Toop, Natasha Maddigan, Xingmo Zhang, Alena Kochubei, Christian J. Doonan, Yijiao Jiang, Jun Huang. "Insights into the Interaction between Immobilized Biocatalysts and Metal–Organic Frameworks: A Case Study of PCN-333." *JACS Au* 1, no. 12 (2021): 2172-2181.

I performed experiments, analysed the data, and wrote the drafts of the MS.

Chapter 5 of this thesis is published as

1) **Wenjie Yang**, Xiao Liu, Luke A. O'Dell, Xingxu Liu, Lizhuo Wang, Wenwen Zhang, Bin Shan, Yijiao Jiang, Jun Huang. " Atomic layer deposition of Lewis acidic aluminum species on mesoporous silica-alumina with Brønsted acidity for cascade catalysis" *JACS Au*

For which I performed experiments, analysed the data, and wrote the drafts of the MS.

In addition to the statements above, in cases where I am not the corresponding author of a published item, permission to include the published material has been granted by the corresponding author.

Wenjie Yang

February 2023

Abstract

Biomass conversion is of high value in the sustainable manufacturing of green chemicals, and it is well known as a viable way to turn waste into valuable products, which show high potential with both economic and environmental benefit in energy, chemical, pharmaceutical industries etc.

To achieve biomass conversion to aim product, catalyst is usually required to change the kinetics of chemical reaction without influencing the thermodynamics and thus improving the efficiency and selectivity. Alumina catalyst is a widely applied catalyst in the catalytic industry as both catalyst itself and catalyst support due to the favourable physiochemical properties, and the recently discovered functionality of penta-coordinated aluminium species attracted further attentions for designing solid acid catalysts with optimized surface acidity. Herein, the ***Chapter 1*** summarized the sustainable solid catalysts, reviewed the development of alumina containing solid acid, especially the recently developed Al^V catalysts, and the structure-acidity-activity of alumina containing acid catalysts.

This thesis presents the studies of controlling surface acidity of alumina-based catalysts for biomass conversion. Via the application of different synthesis approach, this thesis developed wet-chemistry method to establishes penta-coordinated aluminium specie based Brønsted acid site on varied mixed oxide and to precisely adjusts the spatial location of Brønsted acid site and Lewis acid site. In ***Chapter 3***, for the first time, the development of Al^V-BAS has been achieved on non-silica alumina material, and the principle of the research outcome can be applied to the Al^V-BAS formation within many other mixed oxide systems. Because that the current development of Al^V-BAS requires complex and expensive preparation method, which render the Al^V-BAS based acidic catalyst less optimal to its counterparts, in this scenario, in ***Chapter 4***, for the very first time, a simple and cheap wet-chemistry synthesis route has been reported in order to prepare silanol linked Al^V-BAS for acidic catalysis. This achievement presents promising opportunities for the large-scale industrial implementation of mesoporous silica-alumina with Al^V-BAS. Moreover, there are many acidic reactions requires both Brønsted acidity and Lewis acidity. Nevertheless, the currently applied bi-acidic catalysts has limitations, such as uncontrolled diffusion on acid sites and uncontrolled Brønsted-Lewis acid site synergy. With this in mind, we put efforts on preparing catalyst with cascade structure for active site separation. In ***Chapter 5***, a bi-acidic solid acid catalyst with cascade architectural structured BAS and LAS has been reported. Due to the spatial separation, the synergy between

BAS-LAS pair was limited, and which also showed the ability to direct the diffusion flow from BAS to LAS and contributed to enhanced cascade acid reaction performance. We reckon this work paves the way for designing bi-acidic catalyst with unique cascade architectural structure for efficient cascade reactions.

Therefore, this thesis gives comprehensive understanding on precisely control the surface acidity features including the population of acid sites, Brønsted acid site /Lewis acid site ratio, acid site distribution/location etc for enhanced catalytic performance for varied biomass conversion.

Additionally, for this research, solid-state nuclear magnetic resonance spectroscopy has been applied as the core characterization method to understand the formation, structure, and acidity of amorphous solid acids. With the help of solid-state nuclear magnetic resonance spectroscopy, this thesis provides detailed understanding on the structure-acidity-catalytic activity relationship of alumina-based catalyst.

Acknowledgment

On a cloudy afternoon, I found myself seated at my cluttered desk, reflecting on my three and a half years of PhD experience. It seemed like just yesterday that I started, with bright and hopeful aspirations, and now it was all over in a flash. As Michael Jackson's song played on a loop in my head, I realized how time flies by so quickly during a PhD. I reminisced on the multitude of memories, including moments of joy, sadness, disappointment, excitement, and much more. Looking back, there were numerous individuals who played a significant role in my academic journey, and without their support, I doubt I would have been able to complete my PhD as seamlessly as I did.

Above all, I want to express my profound appreciation for Professor. Jun Huang, my supervisor, whose guidance, support, and encouragement were indispensable in helping me navigate the complexities of the research process. Your unwavering faith in me, as well as your invaluable insights, have inspired me to pursue excellence at every turn. Your patience, sense of responsibility, and attention to detail are the qualities that I will always remember and cherish as some of the most valuable lessons from my PhD experience. During my first year as a Ph.D candidate, you instilled in me the importance of remaining calm, patient, and learning from the basics. You emphasized the significance of laying a solid foundation to prepare for future brilliance. In my second year, you provided me with the opportunity to learn the most advanced techniques in solid-state Nuclear Magnetic Resonance Spectroscopy. Despite making several significant mistakes that resulted in losses, you did not chastise me but instead encouraged me to do better, pay more attention, and be more careful. This motivated me and gave me the confidence to strive for improvement. In my third year, you offered enhanced training on leadership, teaching, and writing skills, which have equipped me with a more comprehensive and unique skill set that will prove valuable for future works. Professor Jun, thank you for giving me the chance to become a 'better me'.

I would also like to express my sincere gratitude to my co-supervisors and collaborators, particularly (in alphabetical order) A/Prof. Luke O'Dell, Prof. Xiaozhou Liao, A/Prof. Yijiao Jiang, Prof. Zichun Wang, and others, who have dedicated their time and expertise to help me develop my research and writing skills. Your critical and creative thinking skills have helped me to refine my ideas and produce more rigorous contributions to the field. Your guidance and support have been invaluable, and I am grateful for the opportunity to work alongside such exceptional mentors.

I wish to extend my gratitude to my colleagues and fellow graduate students, particularly (in alphabetical order) Dr. Aleksei Marianov, Dr. Kyung Duk Kim, Dr. Lizhuo Wang, Dr. Sarah Kelloway, Dr. Shufang Zhao, Dr. Weibin Liang, Ms Xingxu Liu, Dr. Yutong Zhao, and many others, for creating a supportive and intellectually stimulating academic environment. Your camaraderie, discussions, and debates have enriched my learning experience and inspired me to explore new avenues of research. I appreciate the sense of community that we have fostered together, and I am thankful for the friendships that I have developed during my time as a Ph.D. candidate.

I would like to express my appreciation to the funding agencies and my alma mater, the University of Sydney, where I resided for eight years. Their generous financial support has made it possible for me to undertake this research project, and for that, I am grateful. Their investment in my education and research has not only benefited me but also contributed to the advancement of knowledge in my field.

I would also like to express my gratitude to my family and friends, whose unwavering love, encouragement, and understanding have sustained me during the ups and downs of the PhD journey. Your unwavering support and encouragement have made it all possible.

My parents have instilled in me the values of hard work, perseverance, and determination, which have been crucial in helping me to achieve my goals. Your constant belief in me, even during times of doubt, has been a driving force behind my success. I am forever grateful for you, and I will always cherish the memories of your love, support, and guidance. 谢谢爸爸妈妈对我这么多年的培养，您们辛苦了!

Lastly, to my future family, my beloved Tiantian Ma, I want to acknowledge that this journey has not been easy for me, but also for those closest to me. I am deeply grateful for the unwavering support, encouragement, and inspiration provided by my girlfriend throughout my Ph.D. period. Her patient understanding, continuous motivation, and invaluable guidance have been pivotal in helping me to overcome obstacles and achieve my goals. She has been a constant source of strength, and I owe much of my success to her presence in my life. Her unwavering belief in me has kept me going during difficult times and has been a driving force behind my academic achievements. I cannot express enough how much I appreciate your presence in my life and your unwavering support during this journey. With that in mind, I would be honoured if you would do me the great privilege of becoming my spouse. So, Tiantian, will you marry me?

To everyone who has contributed to my PhD journey, thank you from the bottom of my heart.

Wenjie Yang

Feb 2023

List of Research Activities

Publications

1) **Wenjie Yang**, Xiao Liu, Luke A. O'Dell, Xingxu Liu, Lizhuo Wang, Wenwen Zhang, Bin Shan, Yijiao Jiang, Jun Huang. " Atomic layer deposition of Lewis acidic aluminum species on mesoporous silica-alumina with Brønsted acidity for cascade catalysis" *JACS Au*
2) **Wenjie Yang**, Kyung Duk Kim, Luke A. O'Dell, Lizhuo Wang, Haimei Xu, Mengtong Ruan, Wei Wang, Ryong Ryoo, Yijiao Jiang, Jun Huang. "Brønsted acid sites formation through penta-coordinated aluminum species on alumina-boria for phenylglyoxal conversion." *Journal of Catalysis* 416 (2022): 375-386.
3) **Wenjie Yang**, Weibin Liang, Luke A. O'Dell, Hamish D. Toop, Natasha Maddigan, Xingmo Zhang, Alena Kochubei, Christian J. Doonan, Yijiao Jiang, Jun Huang. "Insights into the Interaction between Immobilized Biocatalysts and Metal–Organic Frameworks: A Case Study of PCN-333." *JACS Au* 1, no. 12 (2021): 2172-2181.
4) **Wenjie Yang**, Zichun Wang, Jun Huang, Yijiao Jiang. "Qualitative and quantitative analysis of acid properties for solid acids by solid-state nuclear magnetic resonance spectroscopy." *The Journal of Physical Chemistry C* 125, no. 19 (2021): 10179-10197.
5) **Wenjie Yang**, Binbin Xia, Lizhuo Wang, Suonghua Ma, Huazheng Liang, David Wang, Jun Huang. "Shape effects of gold nanoparticles in photothermal cancer therapy." *Materials Today Sustainability* 13 (2021): 100078.
6) **Wenjie Yang**, Jun Haung. "Analysis of Local Structure, Acidic Property and Activity of Solid Acids by Solid-State Nuclear Magnetic Resonance Spectroscopy." *Chinese Journal of Magnetic Resonance* 38 (2021): 460-473.
7) **Wenjie Yang**, Jinhui Zhao, Hao Tian, Lizhuo Wang, Xinyao Wang, Sheng Ye, Jian Liu, Jun Huang. "Solar - driven carbon nanoreactor coupling gold and platinum nanocatalysts for alcohol oxidations." *Small* 16, no. 30 (2020): 2002236.
8) **Wenjie Yang**, Huazheng Liang, Songhua Ma, Devin Wang, and Jun Huang. "Gold nanoparticle based photothermal therapy: Development and application for effective cancer treatment." *Sustainable Materials and Technologies* 22 (2019): e00109.
9) Shufang Zhao*, **Wenjie Yang***, Kyung Duk Kim, Lizhuo Wang, Zichun Wang, Ryong Ryoo, Jun Huang. "Synergy of Extraframework Al3+ Cations and Brønsted Acid Sites on Hierarchical ZSM-5 Zeolites for Butanol-to-Olefin Conversion." *The Journal of Physical Chemistry C* 125, no. 21 (2021): 11665-11676.
10) **Wenjie Yang**, Xiao Liu, Luke A. O'Dell, Xingxu Liu, Lizhuo Wang, Wenwen Zhang, Bin Shan, Yijiao Jiang, Jun Huang. " Atomic layer deposition of Lewis acidic aluminum species on mesoporous silica-alumina with Brønsted acidity for cascade catalysis" *Angewandte Chemie* (Submitted)
11) Weibin Liang, Xuelong Wang, **Wenjie Yang**, Shufang Zhao, Dianne Wiley, Brian S Haynes, Yijiao Jiang, Ping Liu, Jun Huang. "Tailoring and Identifying Brønsted Acid Sites on Metal Oxo-Clusters of Metal–Organic Frameworks for Catalytic Transformation" *ACS Central Science* 9 (2023) 27–35
12) Haoyue Sun, Rui Tang, Xingmo Zhang, Shuzhen Zhang, **Wenjie Yang**, Lizhuo Wang, Weibin Liang, Fengwang Li, Rongkun Zheng, Jun Huang " Interfacial energy band

engineered CsPbBr3/NiFe-LDH heterostructure catalyst with tunable visible light driven photocatalytic CO2 reduction capability" 13 (2023) 1154-1163

13) Sophie R Thomas, **Wenjie Yang**, David J. Morgan, Thomas E. Davies, Jiao Jiao Li, Roland A. Fischer, Jun Huang, Nikolaos Dimitratos, Angela Casini. "Bottom - up Synthesis of Water - Soluble Gold Nanoparticles Stabilized by N - Heterocyclic Carbenes: From Structural Characterization to Applications." *Chemistry–A European Journal* 28, no. 56 (2022): e202201575.
14) Rui Tang, Haoyue Sun, Lizhuo Wang, **Wenjie Yang**, Alena Kochubei, Yijiao Jiang, Rongkun Zheng, Jun Huang. "Perovskite-Nanoparticle-Incorporated NH2-MIL-125 (Ti) Nanoreactors with an Optimal Conduction Band Offset for Visible-Light-Driven CO2 Reduction." *ACS Sustainable Chemistry & Engineering* 10, no. 36 (2022): 11939-11947.
15) Zichun Wang, Yijiao Jiang, **Wenjie Yang**, Ang Li, Michael Hunger, Alfons Baiker, Jun Huang. "Tailoring single site VO4 on flame-made V/Al2O3 catalysts for selective oxidation of n-butane." *Journal of Catalysis* 413 (2022): 93-105.
16) Yaolin Wang, **Wenjie Yang**, Shanshan Xu, Shufang Zhao, Guoxing Chen, Anke Weidenkaff, Christopher Hardacre, Xiaolei Fan, Jun Huang, Xin Tu. "Shielding protection by mesoporous catalysts for improving plasma-catalytic ambient ammonia synthesis." *Journal of the American Chemical Society* 144, no. 27 (2022): 12020-12031.
17) Binbin Xia, **Wenjie Yang**, Huazheng Liang, Sonia Liu, Devin Wang, Jun Huang. "Cancer Prevention Effects of Foods, Food Groups, Nutrients, and Their Underlying Mechanisms." *ACS Food Science & Technology* 2, no. 3 (2022): 437-454.
18) Rui Tang, Haoyue Sun, Zhenyu Zhang, Lu Liu, Fanning Meng, Xingmo Zhang, **Wenjie Yang**, Zhoutong Li, Zifeng Zhao, Rongkun Zheng, Jun Huang. "Incorporating plasmonic Au-nanoparticles into three-dimensionally ordered macroporous perovskite frameworks for efficient photocatalytic CO2 reduction." *Chemical Engineering Journal* 429 (2022): 132137.
19) Zichun Wang, Kuizhi Chen, Yijiao Jiang, Julien Trebosc, **Wenjie Yang**, Jean-Paul Amoureux, Ivan Hung, Zhehong Gan, Alfons Baiker, Olivier Lafon, Jun Huang. "Revealing Brønsted acidic bridging SiOHAl groups on amorphous silica–alumina by ultrahigh field solid-state NMR." *The Journal of Physical Chemistry Letters* 12, no. 47 (2021): 11563-11572.
20) Rui Tang, Lizhuo Wang, Zhenyu Zhang, **Wenjie Yang**, Haimei Xu, Amanj Kheradmand, Yijiao Jiang, Rongkun Zheng, Jun Huang. "Fabrication of MOFs' derivatives assisted perovskite nanocrystal on TiO2 photoanode for photoelectrochemical glycerol oxidation with simultaneous hydrogen production." *Applied Catalysis B: Environmental* 296 (2021): 120382.
21) Meihui Ying, Rui Tang, Shenlong Zhao, **Wenjie Yang**, Weibin Liang, Xingmo Zhang, Guizeng Yang, Rongkun Zheng, Haibo Pan, Xiaozhou Liao, Jun Huang. "Correlation and Improvement of Bimetallic Electronegativity on Metal–Organic Frameworks for Electrocatalytic Water Oxidation." *Advanced Energy and Sustainability Research* 2, no. 10 (2021): 2100055.
22) Haoyue Sun, Shangjun Chen, **Wenjie Yang**, Lizhuo Wang, Rui Tang, Xingmo Zhang, Rongkun Zheng, Shengshen Gu, Yijiao Jiang, Weibin Liang, Jun Huang. "Plasmon-enhanced alcohol oxidations over porous carbon nanosphere-supported palladium and gold bimetallic nanocatalyst." *Applied Catalysis B: Environmental* 292 (2021): 120151.

23) Yutong Zhao, Zichun Wang, **Wenjie Yang**, Shengshen Gu, Xiaoxia Yang, Amanj Kheradmand, Xingmo Zhang, Yongming Luo, Jun Huang, Yijiao Jiang. "Promotional Effect of Ni− Sn Interaction over Ni Supported on Sn-incorporated MCM-41 Catalysts for CO2 Reforming of CH4." *ChemNanoMat* 7, no. 8 (2021): 927-934.
24) Lizhuo Wang, Rui Tang, Amanj Kheradmand, Yijiao Jiang, Hao Wang, **Wenjie Yang**, Zibin Chen, Xia Zhong, Simon P Ringer, Xiaozhou Liao, Weibin Liang, Jun Huang. "Enhanced solar-driven benzaldehyde oxidation with simultaneous hydrogen production on Pt single-atom catalyst." *Applied Catalysis B: Environmental* 284 (2021): 119759.
25) Rui Tang, Lizhuo Wang, Meihui Ying, **Wenjie Yang**, Amanj Kheradmand, Yijiao Jiang, Zhiyun Li, Yi Cui, Rongkun Zheng, Jun Huang. "Multigraded Heterojunction Hole Extraction Layer of ZIF-CoxZn1− x on Co3O4/TiO2 Skeleton for a New Photoanode Architecture in Water Oxidation." *Small Science* 1, no. 4 (2021): 2000033.
26) Yutong Zhao, Lizhuo Wang, Alena Kochubei, **Wenjie Yang**, Haimei Xu, Yongming Luo, Alfons Baiker, Jun Huang, Zichun Wang, Yijiao Jiang. "Formation and Location of Pt Single Sites Induced by Pentacoordinated Al Species on Amorphous Silica–Alumina." *The Journal of Physical Chemistry Letters* 12, no. 10 (2021): 2536-2546.
27) Meihui Ying, Rui Tang, **Wenjie Yang**, Weibin Liang, Guizeng Yang, Haibo Pan, Xiaozhou Liao, and Jun Huang. "Tailoring Electronegativity of Bimetallic Ni/Fe Metal–Organic Framework Nanosheets for Electrocatalytic Water Oxidation." *ACS Applied Nano Materials* 4, no. 2 (2021): 1967-1975.

Conferences

Oral Presentation

1) The 3rd Australian Circular Economy conference and 1st Net Zero Initiative Conference, 2022
2) The 9th Tokyo Conference on Advanced Catalytic Science and Technology, 2022
3) The Australian and New Zealand Society for Magnetic Resonance Virtual Seminar Series, 2021
4) X-ray absorption fine structure 2021 Virtual Conference, 2021

Session Chair

1) The 10th Australian Council for Undergraduate Research Conference, 2022

Patent

1) Particulate catalyst for dry reforming of methane (PCT/AU2022/050697). Jun Huang and **Wenjie Yang**

Contents

List of Figures

List of Tables

List of Schemes

1. Introduction

1.1 Sustainable Heterogenous Catalysis

Global energy demand is expected to keep growing in foreseeable future with fossil fuels as the dominant sources. The unsustainable consumption of fossil fuels will undoubtedly cause inevitable environmental problems and energy crises. Therefore, producing fuel and chemical or developing unsustainable energy and consumable alternatives in a more efficient manner are critical for a more sustainable society. Catalysis has long been widely applied in the chemical and fuel industry.[1] Suitable catalysts can help to improve the yield and selectivity of desired products with minimizing the by-product waste, which ultimately achieves sustainability.

Heterogenous catalysis, refers to catalytic reaction happens at the interface of two different phases. Heterogeneous catalysts refer to functional materials with surface active sites that can react with reactants under certain conditions to change the reaction rate without affecting the thermodynamic equilibrium.[2] Currently, Langmuir-Hinshelwood model (Equation 1.1) explains the most surface reaction by chain propagation on heterogeneous catalyst.[3]

$$A + B \rightarrow C \qquad \text{Equation 1.1}$$

1) The reactant molecules A and B absorb to the surface-active sites of heterogeneous catalyst; 2) On the surface active sites, molecule A and B approaches, combines, and reacts, which forms product molecule C; 3) The product molecule C desorb from the active sites of heterogeneous catalyst, and leaves unchanged surface active site for the next cycle of catalytic reaction.

Currently, majority of the utilized catalysts in industry are solid heterogenous catalysts. Compared to liquid homogeneous catalysts, it owns some unique advantages. The solid heterogenous catalyst can be easily separated from the reaction system at the end of reaction, which gives the heterogenous catalyst a recycle capability. However, there are still some challenges of heterogenous catalyst need to overcome. For example, heterogenous catalyst maintains relatively lower catalytic efficiency, as not all catalytic active sites can be utilized. Besides, the steps of catalytic reaction occurred on the surface of heterogenous catalysts usually are more complex compared to homogenous catalytic reaction and need to go through the extra process of adsorption and desorption of reactants, therefore, heterogenous catalytic kinetics is generally more complex than homogeneous catalytic kinetics. This gives difficulty in understanding the reaction mechanism and optimizing the design of the heterogenous catalysts.

Thus, in current pursuit of green and sustainable development, the optimization of heterogenous catalysts that can realize high catalytic efficiency, high selectivity, high recycle ability have huge application value, and the high-performance catalysts show potentials to create substantial economic benefits since more than 35% of the global gross domestic product are affected by catalysis[4].

1.2 Sustainable Solid Acid Catalyst

Solid acid catalyst, as one type of typical heterogenous catalyst, is extensively utilized in producing petrochemicals, pharmaceuticals, fine chemicals and renewable fuels and chemicals,[5-7] particularly, accounting for ca. 85 % of the world's energy consumption.[8] Solid acids are of great interest in replacing corrosive and hazard liquid acids since they are eco-friendly, safety to handle, and simple to separate and regenerate.[9, 10] Two types of acid sites are identified on solid acids as Brønsted acid sites (BAS) and Lewis acid sites (LAS). The Brønsted acid theory was proposed in 1923 by Johannes Nicolaus Brønsted and Thomas Martin Lowry. Based on the definition, BAS works as a proton donor, while a base molecule is a proton acceptor (Equation 1.2).[11]

$$AH + B^- \rightarrow A^- + BH \qquad \text{Equation 1.2}$$

In industry, BAS can protonate hydrocarbon molecules to form carbocations, and thus, to drive various important industrial reactions, such as (hydro-)cracking, isomerization, alkylation and methanol-to-olefins.[12-15]

Lewis acid theory was developed by Gilbert N. Lewis. For which, a base molecule provides a pair of electrons, and the LAS accepts the electrons and form a chemical bond in between (Equation 1.3).

$$A{+}{:}B \rightarrow A{:}B \qquad Equation\ 1.3$$

In another word, LAS can abstract electron-pair from the reactant to initialize reactions, such as alcohol dehydration and sugar conversion reactions.[16-19]

Comparing to BAS or LAS solely, BAS and LAS could have cooperativity. The cooperativity can promote catalytic reactions via enhancing acid strength, tuning and integrating multiple acid-catalyzed reaction steps.[20-27] In the reactions of large molecules, the catalytic performance of solid acids strongly depends on the accessibility of acid sites to reactant(s),[28, 29] for instance, about 20 times higher turnover frequency (TOF) was obtained with surface acid sites on amorphous silica-aluminas than those on microporous dealuminated HY zeolite in the

onversion of phenylglyoxal. As excellent supports, the density and strength of acids sites on solid acids are key to stabilize and tune the catalytic properties of and/or cooperate with metal active sites for selective hydrogenation and oxidation reactions.[30-34] Due to the variation in the element compositions, physical global/local structure, and the chemical properties of surface acid sites, solid acids can be divided into different groups. Typical examples of solid acid catalysts are summarized in **Table 1-1**.

Table 1-1 Summary of typical solid acid catalysts

Class	Examples
Zeolite	ZSM-5, X-/Y-zeolites, Erionite, Analcime, Gemelinite, etc
Metal Oxide	Al_2O_3, TiO_2, Nb_2O_5, WO_3, etc
Mixed Metal Oxide	SiO_2-Al_2O_3, TiO_2-Al_2O_3, WO_3-ZrO_2, SiO_2-ZrO_2, etc
Metal Salt	$AlPO_4$, $NaHCO_3$, NaH_2PO_4, $FeCl_3$, $AlCl_3$, etc
Heteropoly	$H_3PMo_{12}O_{40}$, $H_6P_2Mo_{18}O_{62}$, $H_4SiMo_{12}O_{40}$, etc
Metal Organic Framework	PCN-333(Al), Zr_6-MOF-808, UIO-66(Zr), etc

1.3 Penta-Coordinated Aluminum Species Based Catalysts

Among solid acids, aluminium-containing materials have long been considered an important catalyst with broad industrial catalytic applications. Due to the advantages of high surface area, tunable porous structures, mechanical and thermal stability, aluminium-containing materials such as alumina, zeolites, amorphous silica alumina, and alumina based mixed oxides show extremely high application value in petroleum refining and processing, petrochemical, coal chemical, biorefining, and fine chemical industries. In aluminium-containing catalysts, researchers have focused on the contribution of unsaturated four-coordinated aluminium to catalytic performances and have conducted extensive studies on how to obtain abundant surface-accessible catalytically active Al^{IV} species by structure adjustment and how to collaborate this species with other surface active sites. Recently, researchers have found that in addition to tetra-coordinated aluminium, the value of unsaturated penta-coordinated aluminium for catalytic reactions in aluminium-containing materials cannot be ignored. It has been approved that with an oxygen vacancy as defect site, the surface distributed Al^{V} species show capability to act as Lewis acid site[35], Brønsted acid site[36], and anchor site for single atom catalysts[37] (**Figure 1-1**). Therefore, the development of surface Al^{V} for catalytic applications allows the addition of extra active sites aside the Al^{IV} species, which helps to improve the efficiency of catalytic reactions.

Herein, this section efforts the enrichment of Al^V species on the development of solid acid catalysts and multifunctional catalysts. In this section, various promising synthetic methods for enriching Al^V species will be discussed with the purpose of producing surface Al^V species in different systems. The roles of Al^V species in the development of solid acid catalysts and single atom catalysts will be highlighted and the challenges and outlook regarding the establishment of Al^V enriched catalyst will be elucidated.

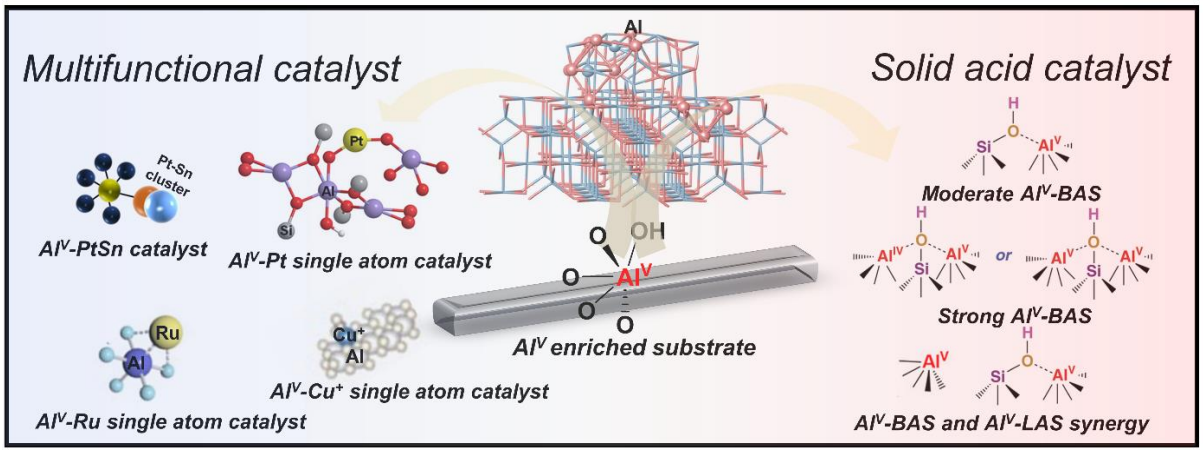

Figure 1-1 Summary of Al^V species functionality for the construction of solid acid catalysts and multifunctional catalysts.

1.3.1 Preparation of Al^V species on catalysts

In general, on common aluminium-containing crystalline oxides prepared under mild conditions, such as those prepared by conventional wet chemistry and post-treatment modification techniques, saturated six-coordinated aluminium and unsaturated four-coordinated aluminium present within the platform as the dominant aluminum species. The synthesis of high content metastable penta-coordinated aluminum species usually requires more complex synthetic scheme within the oxide framework.

To construct mixed oxide platforms dominated by unsaturated penta-coordinated aluminium species, flame spray pyrolysis (FSP) has shown its unique capability[38]. In the FSP process, uniform aluminium containing nanoparticles are produced by combustion and following thermophoresis of the atomized fuel with aluminium precursor solution. The precursors combust, thermophoresis and react rapidly under the gas phase and high temperature harsh FSP conditions. The ensuring nucleation and growth of crystalline structure of the aluminum containing nanomaterial is limited. Thus, amorphous nanoparticles with metastable phases of penta-coordinated aluminium and polymorphs are purposefully generated. Currently, based on the FSP method, our group has successfully prepared amorphous silica alumina with up to 55.5%

of the dominant penta-coordinated aluminium species[38]. Additionally, with dual channels, the double-flame FSP can mix separately generated atomized fuels. This advanced method can be applied to control the generation of mixed oxide with Al^{V} enriched alumina nanodomain and a uniform distribution of intermixed components at the interface[39].

Atomic layer deposition (ALD), an important method for fabricating semiconductors and modifying the surface of nanomaterials, can also play a role in establishing substrate with enriched penta-coordinated aluminium species[40]. Amorphous alumina thin films can be slowly deposited on the outer surface of the nanomaterials by repeated exposure to aluminum precursors, such as trimethylaluminum and aluminium tri-isopropoxide. Importantly, not only the deposited amorphous structure of alumina overlayer provides the preconditions to reach 44.9% of unsaturated penta-coordinated aluminum[41], but also these penta-coordinated aluminum species are distributed as surface sites on the outermost surface due to the nanoscale surface deposition.

Evaporation induced self-assembly (EISA), a commonly used simple and effective synthetic method for preparing mesoporous nanomaterial, can also be applied to enrich unsaturated penta-coordinated aluminium species on alumina frameworks. Via the rapid evaporation of solvent and formation of hybrid mesosphere containing structure agent and aluminium precursor, hybrid amorphous alumina framework could be envisioned[42]. The alumina-based network with distorted local structure can then be further hardened slowly by condensation. On such an alumina framework, it is not only possible to produce unsaturated penta-coordinated aluminum species, but it also integrates the advantages of large surface area and diffusion control due to the presence of mesopores.

Amorphous alumina nanosheets also have their place in the construction of aluminium-containing materials with abundant penta-coordinated aluminium species. Unlike bulk materials, the two-dimensional ultra-thin structure of nanosheets is advantageous for the construction of materials with enriched surface accessible penta-coordinated aluminium. This provides up to 49% surface active penta-coordinated aluminium sites for further modification or catalytic reactions[43]. Not only that, from a kinetic point of view, the ultra-thin nanosheet structure is also ideal for improving mass transfer and diffusion kinetics[44].

Different preparation methods show their unique characteristics in integrating enrichment of penta-coordinated aluminium species and other advantages. On the platforms prepared by these

methods, mixed oxides containing enriched penta-coordinated aluminum species can be further constructed by simple one-pot or post-synthetic addition of other metal precursors.

1.3.2 Formation of strong acidic Al^V-Brønsted acid site for solid acid catalysts

Similar to unsaturated three- and four-coordinated aluminium species, the surface exposed five coordinated aluminium species are considered as the Lewis acid site and have been shown to play important roles in alcohol dehydrations[45]. However, Busca et al[26] emphasized that while penta-coordinated Al ions may exist, their catalytic activity may not be as significant as previously thought. The conventional assumption that these ions are the primary source of acidity in silica-alumina materials is challenged by alternative theories, such as the presence of Brønsted acid sites, which could play a more dominant role in catalysis. Therefore, it becomes imperative to critically assess the evidence supporting the importance of penta-coordinated Al ions in specific catalytic processes and consider alternative explanations.

To prove the catalytic activity of penta-coordinated Al, in 2016, our group demonstrated experimentally for the first time the presence of Al^V based Brønsted acid site in amorphous silica alumina (ASA) by solid-state nuclear magnetic resonance (ssNMR) characterization[2]. This new discovery undoubtedly points to a viable research direction for five-coordination aluminum catalysts and has also aroused researchers to ponder their value on industrial chemistry processes. Using dynamic nuclear polarization (DNP) enhanced ssNMR techniques, the researchers confirmed that BAS was generated in ASA due to the presence of pseudo-bridging silanol (PBS)[46]. Compared with zeolitic bridging silanol with short Al-O distance (1.88−2.0 Å), BAS resulting from Al^{IV}- and Al^V- PBS with long Al-O distance (2.94−4.43 Å) is relatively weaker in acidity. The weaker acidity enables these Al^{IV}- and Al^V- PBS based BAS on ASA to demonstrate their unique superiority in biomass conversion because the activation energy required to activate C-O and OH bonds in biomass conversion is much lower than the energy required to break C-C and C-H bonds in strong acid-catalysed catalytic cracking. The weaker acidity also helps prevent side reactions such as over-oxidation, thus improving the selectivity of the target product. In addition, it was found that Al^V-BAS has similar acidic properties as Al^{IV}-BAS in ASA[47]. This suggests that the establishment of Al^V-BAS not only helps to increase the amount of BAS, but also has a limited influence on the acidity distribution on the catalyst surface. This facilitates the increase of the reaction rate without affecting the selectivity of weak/moderate acid-catalysed catalytic reaction.

For Al^V enriched mesoporous ASAs with fewer diffusion limitations than microporous zeolites, the viable applications of Al^V-BAS would be greatly increased if it could provide strong BAS

acidity similar to that of acid sites on zeolites, since most industrial chemical processes are currently dominated by microporous zeolites with strong acid sites. As mentioned above, in general, Al^{IV}- and Al^{V}-BAS have similar local structure and moderate acid strengths in amorphous aluminum-containing materials. Nevertheless, this is based on the premises that 1) the Al content in the material is low, 2) there is no spatial influence no spatial influence between Al species, and 3) each surface pseudo-bridging silanol site has and at most one adjacent $Al^{IV/V}$ species. When the Al content increases, penta-coordinated aluminum species tend to aggregate and form Al^{V} domains[43]. Thus, within Al^{V} enriched material at high Al content, the uniformly introduced heteroatom could be surrounded by multiple adjacent Al^{V} species, and the caused stronger polarization on the hydroxyl oxygen results in the generation of PBS with strong acidity and the stronger polarization induced on the hydroxyl oxygen leads to the production of pseudo-bridging groups with strong acidity. The formation of Al^{V}-BAS with strong acidity has been confirmed in FSP-ASA[47]. Utilize H/D exchange with d_6-benzene as the test reaction, the strong BAS established from spatially correlated multiple Al^{V} species and silanol exhibits an even stronger acidity than bridging silanol on H-ZSM5 zeolite ($k=0.0078\ min^{-1}$ and $k=0.0072\ min^{-1}$, respectively)[47]. This suggests that the Al^{V} contributed strong acid sites on ASA could be of great significance to the key step of industrial hydrocarbon conversion, and the application can be extended to cracking, isomerization, dehydration reactions, etc.

In addition to the construction of novel Al^{V}-BAS to increase the amount or strength of surface BAS, the construction of Al^{V}-enriched solid acid materials as bi-acidic catalysts is of industrial importance. On conventional commercial zeolites, Lewis acids are usually built up by post-treatment with dealumination or aluminum exchange. In long or repeated cascade reactions or multi-step acid reactions, LAS may be detached from the surface, resulting in rapid catalyst deactivation. Compared to the extra-framework Al species with Lewis acidity on zeolite, the Al^{V} species enriched on the material surface and the BAS and LAS constructed from them show strong thermal stability[39]. Such properties make Al^{V} enriched material with bi-acidity become very potential for cascade acid reactions or multi-step acid reactions.

1.3.3 Formation of Al^{V}-metal atom anchor site for multifunctional catalysts

The construction of highly dispersed metal nanoclusters or even single-atom catalysts on alumina is challenge. Recently, researchers found that the coordinatively unsaturated Al^{V} exhibited excellent metal-anchor ability as a coordination defect[37]. Through weak oxygen bridging and corresponding coordination saturation, unsaturated penta-coordinated aluminum species can bond to the metal atoms. The formation of Al^{V}-O-Metal can lead to high dispersion

of metal sites, which shows great potential for the construction of single-atom catalysts, single site catalysts, or 2D raft catalysts. In 2009, Kwak et al. successfully anchored platinum atoms on penta-coordinated aluminum species of γ-Al_2O_3. By adjusting the amount of Pt, they successfully prepared Pt single atom catalyst and Pt two-dimensional raft catalyst[37]. Except anchoring single metal species, metal alloy or bimetallic site could also be stably anchored on Al^V site. For example, the bimetallic Pt-Sn clusters anchored by penta-coordinated aluminium species on Al^V-enriched γ- Al_2O_3 nanosheets showed excellent thermal stability and anti-coke ability[44]. The catalyst exhibited >99% propylene selectivity on prolonged propane dehydration reactions. In addition, even at high metal loading, uniformly surface-distributed Al^V species can be used as anchor sites for the construction of single-atom catalysts. This is of great industrial significance because single atom catalyst is considered as a bridge between homogeneous and heterogeneous catalysts[48]. The construction of single-atom catalysts with high metal loading has greatly facilitated the application of heterogeneous catalysts to conventional homogeneous catalytic reactions. For instance, over Al^V-enriched Al_2O_3 support, with up to 8.7% Cu loading, Cu atoms were atomically dispersed and anchored on the Al^V sites, and which showed comparable catalytic activity and stability to homogenous catalysts for selective synthesis of homoallylboronates[49].

In addition to providing metal atom anchor sites, in Al^V-enriched mixed oxides, such as on FSP-ASA, some of the surface Al^V species in proximity to heteroatom site, can also exist as BAS sites (Si-OH---Al^V) as mentioned above. Thus, synergetic effects of these BAS and metal single atom sites could be expected. In the hydrogenation of alcohols and ketones, in addition to the size, geometry, dispersion, and electronic properties of the metal active site, the acidity of the support also affects the yield and selectivity. Thus, multifunctional catalysts constructed using Al^V-enriched mixed oxide carriers show great potential for selective hydrogenation reactions due to their metal site anchoring and BAS formation capabilities. For example, in selective hydrogenation reactions, researchers found that the synergetic effect of BAS and active metal site can facilitate the diffusion of reactant molecules to the surface of dispersed metal sites[50]. The surface BAS also serves as an additional hydrogen spill-over site to facilitate chemo-selective hydrogenation reactions. On Al^V-BAS enriched ASA materials, via anchoring Pt or Pd atoms on Al^V species, excellent chemo-selectivity to hydrogenation of C═O groups have been observed[50].

1.3.4 Current challenge and outlook for Al^V enriched catalyst

Alumina, as a prominent solid acid/support, shows great industrial value in catalytic applications. In addition to high surface area and thermostability, the surface properties of different alumina polymorphs link to the distribution of active sites and corresponding catalytic performance. However, in the most widely used alumina polymorphs such as γ-Al_2O_3 and α-Al_2O_3, the concentration of surface active Al^V species is much lower compared to the dominant Al^{IV} or Al^{VI} species. From a synthetic point of view, it is more difficult to construct alumina containing materials with abundant surface active Al^V sites under mild condition than to construct Al^{IV} species with surface activity. This is because that Al^V species usually has a largely distorted local structure, the Al^{IV} and Al^{VI} species with a more symmetrical local structure have a higher probability of occurring in alumina with crystallinity. Therefore, the enrichment of Al^V species in Al-containing crystalline systems remains a challenge, which is important for the construction of active Al^V in different systems and the extension of its catalytic applications. The characterization of the geometric and electronic structure of Al^V enriched system is also a challenge. Widely used analytical techniques such as X-ray diffraction (XRD) and transmission electron microscopy (TEM) are not suitable for characterizing the surface of Al^V enriched systems due to their poor crystallinity. Another popular advanced electronic and geometric structure characterization technique, X-ray absorption (XAS), is also not the optimal method for characterizing Al^V enriched systems due to insensitivity to light elements with only a few electrons. The most promising technique for local structure characterization, solid-state nuclear magnetic resonance spectroscopy (ssNMR), is not available in all existing laboratories due to its high cost, large size, and high maintenance costs. In summary, these aforementioned issues lead to a significant difficulty in the routine characterization of Al^V enriched materials.

Furthermore, in the absence of existing general models for Al^V-rich amorphous materials, density functional theory (DFT) studies provide conflicting information and are to some extent inconsistent with experimental results. For example, DFT transition state calculations performed by Larmier et al. showed that Al^V was the active Lewis acid site for isopropanol dehydration[1], while others computational study with multiple models showed that the Al^V is the least acidic site on γ-Al_2O_3[51, 52]. Therefore, further development is still needed to propose a plausible generic DFT model for Al^V enrich systems, and to use the DFT model to gain insight into the contribution of Al^V species regarding varied catalytic reactions.

Since surface distributed Al^{V} species is proposed to show similar properties as surface exposed Al^{IV} species, establishing Al^{V}-BAS in micro or mesoporous zeolite materials to provide extra active sites could be a next step on enhancing catalytic efficiency for versatile zeolitic applications. Besides, due to the demonstrated ability to anchor single atoms, the development of Al^{V} enriched support with high surface area and structural stability is of practical interest for single-atom catalysts in industrial-scale applications such as reforming, water-gas shift reaction, CO oxidation, etc. With a better understanding of Al^{V} species for the construction of Lewis acid sites, Brønsted acid sites and the anchor of single atom structures, the development of simple, inexpensive, and scalable preparation methods for Al^{V} enriched systems (e.g., conventional wet chemical preparation) is of practical importance for industrial and chemical economy.

In conclusion, pentacoordinated aluminum species present several advantages in catalysis, including high acidity, selectivity, and stability. They offer the potential for enhancing catalytic activity, reducing side reactions, and supporting various reaction types based on previously mentioned examples. Moreover, their tunable properties and potentials to be incorporated into different supports make them relatively versatile in heterogeneous catalysis and environmentally friendly processes. However, it is critical to acknowledge the challenges associated with characterizing and controlling these species. The debate surrounding their significance in catalysis and the existence of alternative mechanisms, like Brønsted acidity and corresponding performance, underscores the need for a nuanced understanding and careful consideration of their role in specific applications. Overall, while Al^{V} species hold promise, their practical implementation requires a balanced assessment of their advantages and limitations compared to its counterparts such as Al^{IV}-based solid catalysts.

1.4 Green Solid Acid Catalyst Characterization

Surface acid sites of solid acid catalyst plays a vital role in controlling the catalytic reaction. Characterization of acid sites, including their types, densities, strength, accessibility, location, and the nature of acid sites, are essential to understand their functions and behaviors for rational design of solid acids with optimized surface acidity and their supported metal catalysts, the so called structure-acidity relationship. Besides, it also helps the catalyst optimization for target reactions, the so called acidity-catalytic activity relationship.

Several techniques are employed to study the acidity of solid acids, such as titration of acidity in aprotic solvents, infrared spectroscopy (IR), temperature-programmed desorption (TPD) and solid-state nuclear magnetic resonance (SSNMR) spectroscopy with and without probe

molecules, as well as probe reactions.[53-58] Titration with bases (e.g. *n*-butylamine) mainly provide overall density and strength of surface acid sites without distinguish the type of acid sites.[5, 6] TPD of bases, typically NH_3, is a more frequently used to study the density and strength of specific acid sites without distinguishing their types, but is questioned as a standard approach recently.[56] In TPD experiments, the density and strength of acid sites are obtained from the area under desorption curve at each temperature. However, the desorption of bases not only depends on the desorption temperature, but also strongly influences by the presence of co-catalysts, adsorption geometry, surface coverage, and diffusion of bases, leading to TPD method is unreliable. In comparison, IR and SSNMR spectroscopy are comparable in determining the types, density and strength of acid sites using probe molecules.[55, 59] Moreover, ssNMR spectroscopy is powerful in characterizing the local structure of acid sites compared to other techniques,[53, 54] thereby SSNMR can provide a comprehensive understanding of surface sites on solid acids.

Started from the last several decades, the qualitative and quantitative analysis of surface acid sites using SSNMR spectroscopy developed rapidly.[53, 54, 60] The type, density and strength of acid sites can be well characterized using SSNMR spectroscopy directly or indirectly with probe molecules, through evaluating the chemical shifts and intensities of the resulting peaks. The adsorption of probe molecules of different size on acid sites can provide their accessibility by SSNMR spectroscopy. Moreover, the local structure of acid sites can be characterized by SSNMR spectroscopic approaches utilizing dipole–dipole interactions, quadrupole interactions, and indirect spin–spin (*j*) coupling.[61-63] Besides, the reactivity of acid sites in acid-catalyzed reactions can also be characterized by H/D exchange experiments and *in situ* SSNMR techniques. The fundamental understanding of the key elements of ssNMR in acid catalyst characterization have been drawn in **Figure 1-2**. Among acidity investigations, silica-alumina catalysts, including crystalline zeolites and amorphous silica-alumina (ASA), stand in the center because of they are the most popular solid acids applied in chemical and fuel industries. This section summarized the recent progress of ssNMR in solid acid catalyst characterization, introduced the study of ssNMR in revealing the surface absorbate and plausible reaction mechanisms in the field of heterogeneous catalysis. The information disclosed by ssNMR is of significance in the rational design of high-performance catalysts and their application for sustainability.

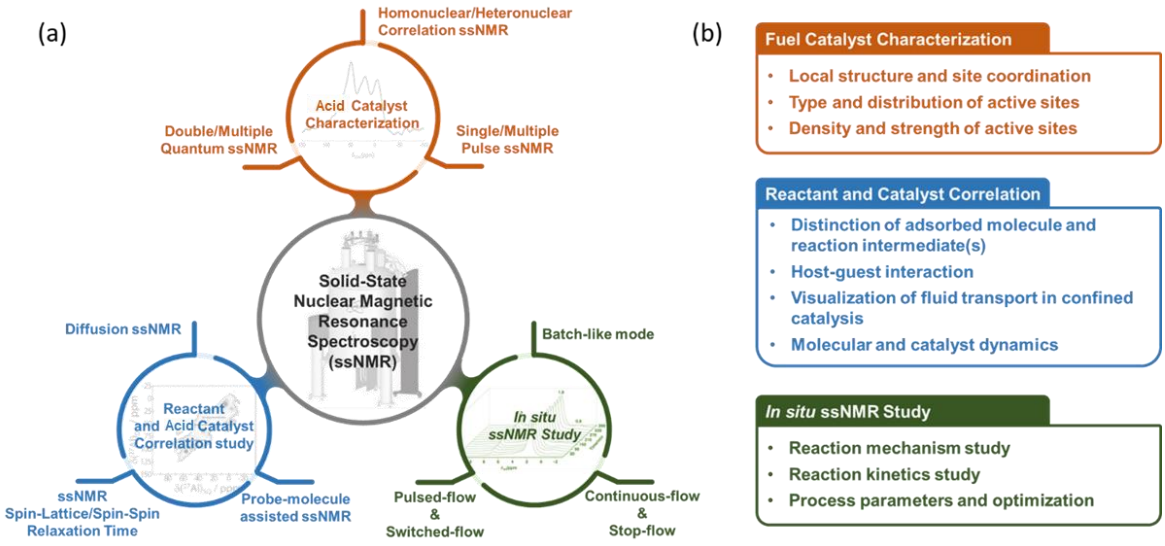

Figure 1-2 ssNMR characterization for green solid acid catalyst (a) The scheme of different ssNMR technologies. (b) Summarized essential characterization information can be obtained via ssNMR.

1.4.1 Experimental Approach of ssNMR characterization

Scheme 1-1 shows a general workflow for the characterization of solid acids using SSNMR spectroscopy. Practically, solid acids are often utilized after activation. Prior to SSNMR characterization, activated solid acids are often prepared through complete dehydration (e.g. at 473-723 K) under vacuum. The dehydrated samples were sealed or utilized for *in-situ* loading with probe molecules on a vacuum line, followed by heating or at room temperature to evacuate physisorbed molecules. Then the obtained samples are sealed in glass ampoule or transferred directly into a gas-tight MAS NMR rotor in a glovebox purged with a dry and inert gas (e.g. N_2). Liquid N_2 is often applied to assist the contact and diffusion of probe molecules with catalytic samples and to resist reactions of probe molecules, which can be achieved by a simultaneous cooling of the catalytic samples at the bottom of the glass ampoule. Controlled loading and heating/desorption temperature of probe molecules should be carefully optimized for the purpose of study, for instance, loading deuterated benzene molecule at BAS with a ratio of 1:1 is essential in the H/D exchange experiments to compare the activity and acid strength of BAS of zeolites and ASAs by *in situ* ^{1}H MAS NMR spectroscopy.

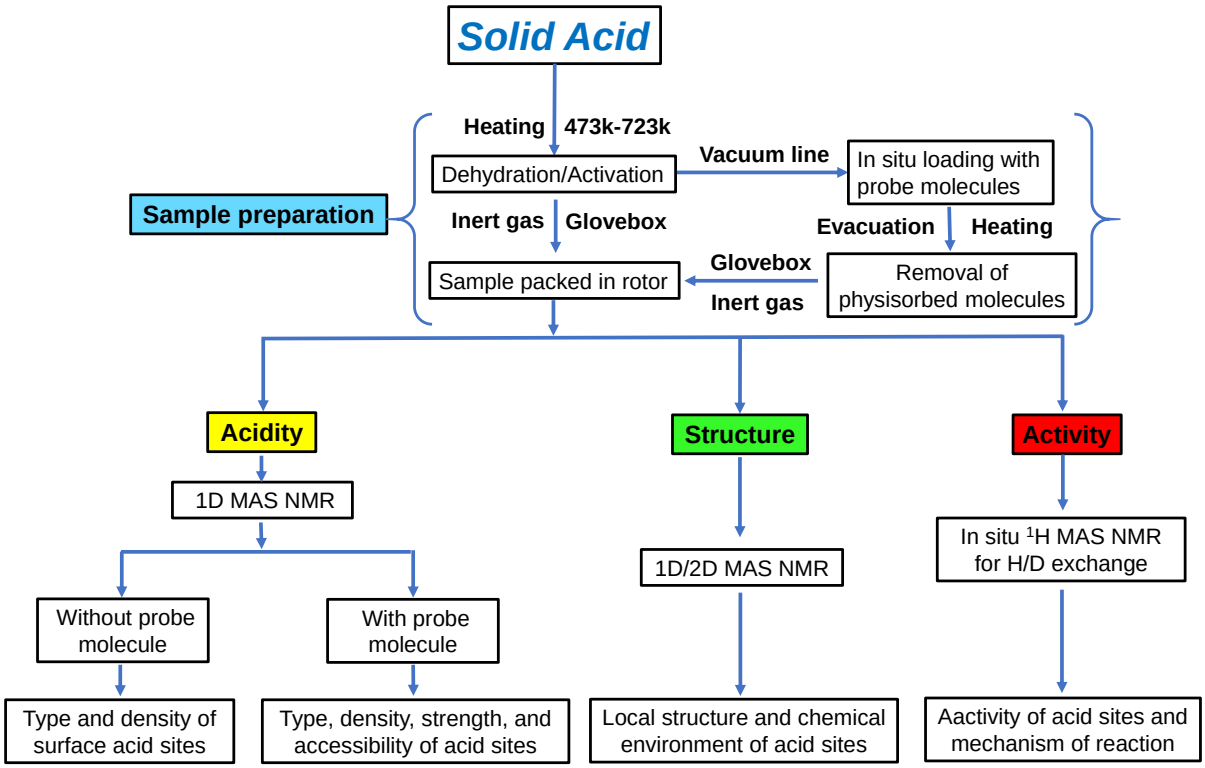

Scheme 1-1 A standard workflow for characterizing solid acids by SSNMR spectroscopy

The type, density, strength, and accessibility of surface acid sites are often determined by one-Dimensional (1D) MAS NMR spectroscopy with/without probe molecules. Hydroxyl protons acting as BAS can be directly studied using ^{1}H NMR spectroscopy with distinct ^{1}H chemical shift, such as Si(OH)Al groups in crystalline zeolites. However, in ASAs and metal-doped mesoporous catalysts (e.g. silicious MCM-41), BAS is hardly to be distinguished from the main peak of SiOH groups. And the direct identification of LAS and evaluation of their density and strength is difficult by SSNMR solely. Adsorption of basic probe molecules on surface acid sites can result in adsorbate-induced chemical shifts of corresponding NMR peaks depending on the type and strength of the acid sites. These spectral parameter changes of probe molecules and surface hydroxyl protons can be detected by ^{1}H, ^{13}C, ^{15}N, and ^{31}P ssNMR spectroscopy based on the probe molecules applied. An important advantage of using these spin I = 1/2 systems is the concentration of surface sites can be determined from the intensities of peaks with an internal or external intensity standard due to their nature of isotropic chemical shift. Moreover, the accessibility of surface acid sites is often evaluated by their interaction with probe molecules of distinct size, such as those located at external surface, in sodalite cages and super cages of zeolites.

A limitation of using ssNMR spectroscopy is the low spectral resolution. A routine technique to improve the sensitivity on ssNMR spectroscopy is to spin the sample around a rotation axis

in the angle (θ = 54.7°) to the direction of the external magnetic field, called magic-angle spinning (MAS).[64, 65] MASNMR spectroscopy can improve the spectral resolution of abundant nuclei with $I = 1/2$ (e.g. ^{1}H and ^{31}P) with significant line narrowing. In the case of non-abundant nuclei, such as ^{13}C and ^{15}N isotopes, the sensitivity of non-abundant nuclei *S* can be remarkably enhanced in cross polarization (CP) experiments, in which the polarization is transferred from the abundant spin *I* to spin *S*. The sensitivity enhancement in CP experiments largely depends on a higher gyromagnetic ratio or a higher concentration of spin *I* than the spin *S* and the dipolar coupling between spins *I* and *S* is not averaged by thermal mobility.[66] For the nuclei with $I > 1/2$, such as ^{27}Al ($I = 5/2$), they are often involved in quadrupolar interactions due to their electric quadrupole moment (eQ), leading to low sensitivity caused by significant line broadening. The application of ultra-high magnetic fields (up to $B_0 = 35.2$ T)[67, 68] and ultra-fast spinning rate (e.g. 111 kHz for 0.7 nm MAS rotor)[69, 70] is effective to enhance the sensitivity by strong line narrowing, which is improtant to determine the structural parameters of quadrupolar nuclei involved in local chemical environments. Recently, the SENS-DNP technique (surface-enhanced NMR spectroscopy using dynamic nuclear polarization) has been extensively utilized in the characterization of solid acids at high megnatic fields[71-77]. By introducing paramagnetic radical agents selectively interacting with surface sites, SENS-DNP could significantly enhance sensitivity of SSNMR spectroscopy up to 1-2 orders of magnitude.[73, 76]

The formation and local structure of surface acid sites can be discovered by various 1D and 2D SSNMR. The coordination information and chemical environment parameters, such as the isotropic chemical shift (δ_{iso}), quadrupole coupling constant (C_{QCC}) and the asymmetry parameter (η), of the selective nucleus can be determined from multiple quantum MAS (MQMAS) ssNMR experiments[67, 78-80]. In silica-aluminas, the essential coordination and structural parameters of Al species are offered by analyzing ^{27}Al MQMAS spectra,[78, 81, 82] through which, the relative population of the Al species can be achieved by simulating the corresponding 1D ^{27}Al MASNMR spectrum.[81, 83] Acid sites formation in zeolites and ASAs depends on Al distribution,[53, 62, 84] for instance, homogeneous distribution of Al into silica framework/network promotes BAS formation and the Al clusters or alumina phase formation from aggregation of Al atoms results in LAS, which can be mapped by the correlation between Al species. The ^{27}Al double-quantum single-quantum (DQ-SQ) through-space homonuclear correlation (HOMCOR) NMR experiments are extensively used in the study of Al correlations.[26, 75, 85-87] ^{27}Al DQ-SQ experiments allow us to probe ^{27}Al-^{27}Al proximities by

applying recoupling sequences that restore the dipolar interaction between neighboring ^{27}Al spins. The connectivity of Al sites with neigiboring heteronucleus (other than Al) can be selectively probed by TRAPDOR (transfer of population in double resonance) experiment, in which, the intensity of ^{1}H spin-echo MAS NMR peaks decreases by suppressing the dipolar dephasing of ^{1}H-^{27}Al pairs with continuous ^{27}Al irradiation.[88-90] In a ^{1}H/^{27}Al TRAPDOR experiment, the interaction between Al sites and neighboring protons can be characterized by the ^{1}H MAS NMR difference spectrum recorded without and with ^{27}Al irradiation. However, ^{1}H/^{27}Al TRAPDOR experiment is unable to identify which Al species interacting with surface protons. To further clarify the local structure of acid sites, such as bridging OH groups (SiOHAl) in zeolites, heteronuclear multiple quantum correlation (HMQC) NMR 2D experiments provides direct and detailed correlation information on heteronucleus, such as ^{29}Si-^{27}Al, ^{1}H-^{27}Al, and ^{1}H-^{17}O.[24, 67, 68, 72, 91-93] By dipolar-mediated enhanced HMQC (D-HMQC), a new type of BAS has been discovered in ASA based on the correlation between penta-coordinated Al (Al^{V}) species and SiOH groups.[91] On the other hand, HMQC and other heteronuclear correlation spectra are also utilized in the study on the synergy of acid sites with metal active sites nearby for activity enhancement.[94] Moreover, the acid strength of BAS is proposed to depend on the distance of Al-OH or O-H,[53, 94, 95] which can be determined by REDOR (rotational echo double resonance) experiment.[66] Through 3D ^{17}O{^{1}H, ^{27}Al} saturation-pulse REDOR-TRAPDOR experiments, the Al-O distance for BAS in zeolites (0.188 to 0.2 nm) and ASAs (0.294 to 0.4 nm) are determined, respectively.[71]

In situ ssNMR can provide direct experimental evidence to identify surface absorbate on catalysts, reveal host-guest interaction, and elucidate the chemical conversion mechanisms; thus, guiding the design of catalytic processes and robust catalysts. Currently, the development of continuous flow (CF) *in situ* ssNMR allows the direct study of the surface intermediates on catalysts (**Figure 1-3**).[96] This rendered the *in situ* ^{13}C MAS NMR a suitable technique for mechanism study in a real-time fashion with minimizing the interference caused by reactants and products accumulation in the ampule.

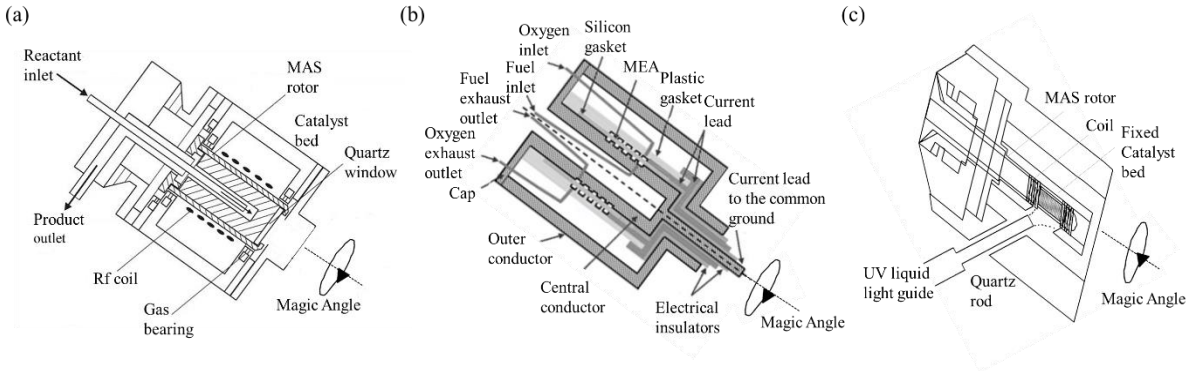

Figure 1-3 Typical schematic diagrams of in situ MAS NMR probe head used for *in situ* characterization of (a) heterogeneous catalysis, (b) electrocatalysis, and (c) photocatalysis. Modified from Ref.[96-98]

1.4.2 Local Structure of Acid Sites Characterization Using ssNMR

1.4.2.1 Nature of BAS and LAS in zeolites

Brønsted acidic zeolites are the most popular heterogeneous catalysts utilized in oil refining and petrochemical industries. In pure silica zeolites, the framework consists of mainly tetrahedrally coordinated silicon atoms shared by four neighboring oxygens (SiO_4), offering very weak acidity.[99] Introducing of framework heteroatoms (e.g. B, Al, Ga, Fe) to replace Si^{4+} requires extra-framework alkaline cations to neutralize the negative charges of framework heteroatoms. The exchange of extra-framework alkaline cations by ammonium ions and calcination results in framework protons that are connected with the oxygens shared by SiO_4 and MeO_4 (Me = e.g. B, Al, Ga, Fe) tetrahedra, well-known as bridging OH groups (e.g. Si-OH-Al).[20, 23, 24, 27]

Various NMR techniques are applied to characterize the local structure of BAS in zeolites in the past decades. Recently, more visible evidence is achieved from HETCOR 2D NMR experiments. Detection of BAS by ^{17}O-MAS-NMR and ^{1}H-^{17}O HETCOR NMR experiments (**Figure 1-4A**) shows that the replacement of Si atoms by Al^{IV} atoms results in a remarkably distortion on the local oxygen in the framework.[79, 100] The distortion can strongly polarize the hydroxyl proton with a significant ^{1}H shift to higher frequency (4.0-4.8 ppm) compared to SiOH groups (1.2-2.3 ppm), hinting an enhanced Brønsted acid strength. $^{27}Al^{59}$ 2D correlation NMR experiments at 35.2 T magnetic field (**Figure 1-4B**) revealed that the formation of bridging OH groups corelates to at least two kinds of tetrahedral Al (Al^{IV}) sites,[68] denoted as framework Al^{IV} and partially bonded Al^{IV} species at framework defects. Combined these results with theoretical calculation studies, the structure of bridging OH groups in zeolites can be well established.

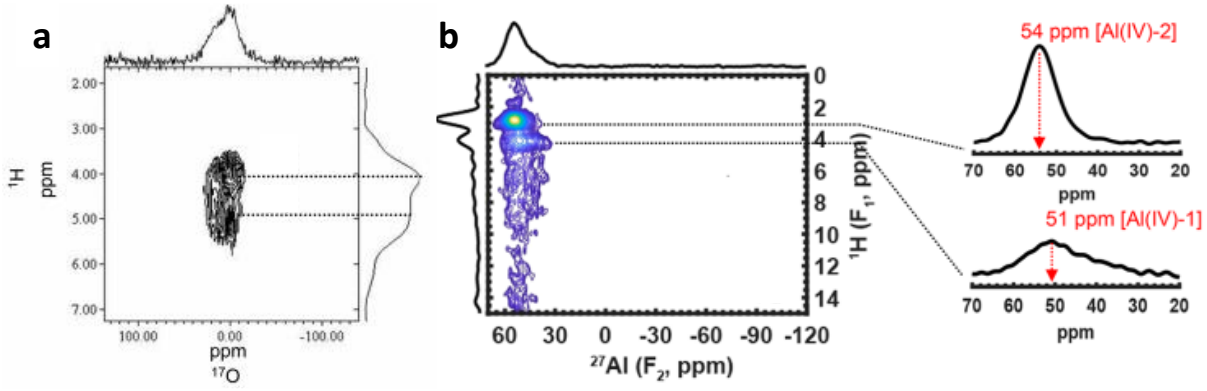

Figure 1-4 SSNMR investigation of surface acid sites dehydrated zeolites. (a) ^{1}H-^{17}O HETCOR NMR at 17.6 T of dry H-MOR with contact time of 100 µs. Reproduced with permission from ref [79]. Copyright 2012 American Chemical Society. (b) ^{27}Al{^{1}H} D-HMQC MAS NMR spectrum recorded at 35.2 T. Reproduced from ref [68].

Bridging OH groups in zeolites can be also generated by ion-exchange of extra-framework alkaline cations on as-synthesized zeolites with multivalent metal cations (e.g. Al^{3+}, Mg^{2+}, Ca^{2+}, Zn^{2+}, La^{3+}, Ga^{3+}, Ce^{3+}, *etc.*) followed by calcination (473-550 K).[20, 27, 94, 101] The thermal dehydration above 473 K drives the dissociation of water molecules in the strong electrostatic fields of the multivalent extra-framework cations inside the zeolite pores and cages, forming metal hydroxyl groups and releasing protons bounded to negative framework oxygen atoms (bridging OH groups).[102] Moreover, Lewis acidic metal cations introduced in proximity to bridging OH groups can results in a Brønsted/Lewis acid synergy to increases the acid strength of BAS, which is similar to those widely reported in dealuminated zeolites.[23, 85, 103-105]

Besides the Brønsted/Lewis acid synergy, introducing extra-framework metal cations can increase the Lewis acidity of zeolites. For instance, EFAl species generated by dealumination and Al-exchange process, such as $Al(OH)_3$, AlOOH, AlO^+, $Al(OH)^{2+}$, $AlOH^{2+}$ and Al^{3+} species, are characterized by ^{1}H DQ-SQ and ^{27}Al DQ-SQ NMR experiments.[85, 103, 106] Increasing the EFAl species often correlates to the increase of LAS along with the decrease of BAS in dealuminated zeolites.[21, 24, 107] On the other hand, pure Lewis acidic zeolite are synthesized by the substitution of Si atoms by Sn or Ti atoms in the zeolite framework. Sn-Beta zeolite is promising Lewis acidic catalysts for versatile biomass conversions.[108, 109] Recent studies on the behavior of Sn under dehydration and rehydration treatment reveals the incorporation of Sn into the zeolite framework by 2D ^{1}H-^{119}Sn and ^{1}H-^{29}Si D-HMQC NMR experiments.[110]

1.4.2.2 Nature of BAS and LAS in Amorphous Silica Alumina

ASAs are mixed oxides of silica and alumina. Adding Al into non-acidic pure silica give rise to the Brønsted acidity in ASAs. ^{29}Si MAS NMR can show systematic changes with increasing Al addition to demonstrates Al incorporate into the silica network.[111-113] A connectivity between Si and Al nuclei on ASA surfaces has been directly probed in ASAs by using 2D ^{29}Si-

^{27}Al DNP SENS NMR spectroscopy.[72] ^{1}H/^{27}Al TRAPDOR MAS NMR experiments shows that Al sites mainly interact with hydroxyl protons of SiOH groups (e.g. δ_{1H} = ca. 1.8 ppm), and sometimes, along with a small amount of AlOH groups (e.g. δ_{1H} = ca. 2.6 ppm) from Al_2O_3 phases due to the heterogeneity of preparation methods.[88, 89, 111, 113] Therefore, the formation of BAS has been widely accepted by SiOH groups interacting with unsaturated Al sites as a part of the silica network or of an interface region between silica and alumina.[62, 84, 95]

So far, several models are proposed for the formation of BAS in ASAs (**Figure 1-5**). Zeolite-like bridging OH group model has been proposed for ASA (**Figure 1-5A**),[114, 115] but strongly under debate due to the much weaker acidity of ASAs than that of zeolites.[5] Theoretical calculation studies suggested an much longer average Al-O distance of PBS in ASAs (2.939-4.435 Å) for the latter than bridging OH groups in crystalline zeolite (1.8-2.2 Å).[116, 117] This has been supported experimentally by measuring the Al-OH distance using ^{17}O{^{27}Al} TRAPDOR dephasing curves of hydroxyl oxygen, obtained from ^{17}O{^{1}H, ^{27}Al} RESPDOR-TRAPDOR experiments.[71] The longer Al-OH distance is often considered to response for the weaker BAS strength in ASA than in zeolites, and thus, the presence of bridging OH groups in ASAs is less favored.

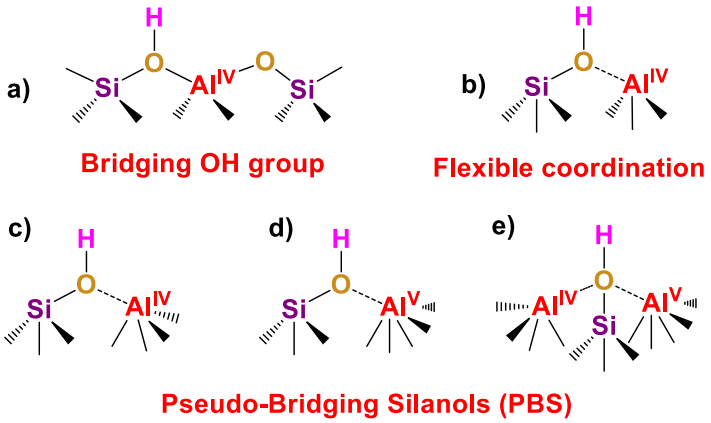

Figure 1-5 Proposed models for Brønsted acid sites (BAS) in silica-alumina catalysts. (a) bridging OH groups in zeolites.[54] (b) BAS formed by Al^{IV} flexible coordinated to neighboring SiOH.[118] (c, d) BAS formed via a pseudo-bridging silanol (PBS) interacting with Al^{IV} or Al^{V} site.[91, 117] e) BAS consisting of the synergy of tetra- and penta-coordinated Al (Al^{IV} and Al^{V}) sites with the same SiOH.[26] In (b)-(e), the dotted line does not denote a covalent bond but only the close proximity between O and Al atoms.

A widely shared opinion is an Al atom flexibly coordinated to a neighboring silanol oxygen atom[9, 88, 119] (**Figure 1-5B**) or forming pseudo-bridging silanols (PBS, **Figure 1-5** and **Figure 1-5D).**[26, 71, 117] The correlation between SiOH groups with Al^{IV} or Al^{V} sites has been directly evidenced recently by using 2D ^{27}Al-{^{1}H} D-HMQC NMR experiments.[91] These sites are able to protonate ammonia, and thus, are BAS in nature. In the low-Al-content ASAs ($Al_2O_3 \leq 25$ wt.%, Al/Si $\leq$ 0.4), quantitative analysis of the ^{1}H NMR decays shows the absence of decay

component of AlOH groups (T_2 ~20 μs) of Al_2O_3 phases but it strongly increased at higher Al_2O_3 contents.[120] ^{27}Al DQ-SQ NMR experiments demonstrates nearly no ^{27}Al-^{27}Al spin pairs can be detected in ASAs (Al/Si ≤ 0.4), in line with EDX atom mapping analysis and the reconstruction of the 3D structure by atom probe tomography (APT).[26, 78] These observations suggest that Al species can be well-dispersed into the silica network. The formation of BAS via single Al sites interacting with per SiOH is preferred in these ASAs, such as via PBS model, offering mainly moderate BAS strength as often reported.

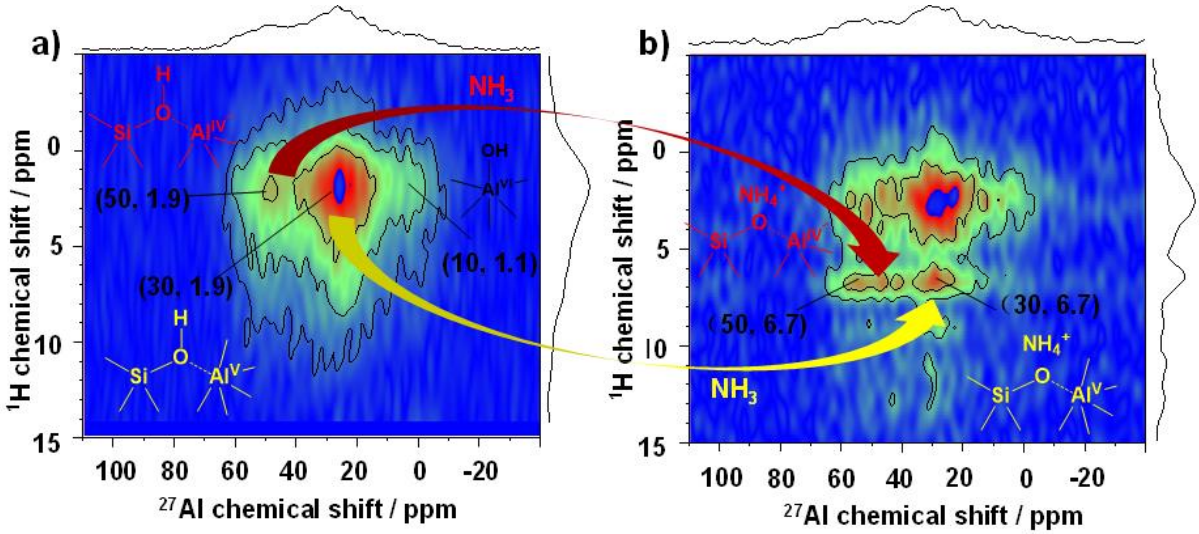

Figure 1-6 ^{27}Al-{^{1}H} D-HMQC 2D spectrum of SA/50. (a) SA/50 dehydrated at 723 K for 12 h under vacuum, and (b) after ammonia loading and evacuated at 373 K for 1 h. The spectra were recorded at 18.8 T with a MAS frequency of ν_R = 20 kHz and τ_{rec} = 1.0 ms for dehydrated and τ_{rec} = 900 μs for ammonia-loaded sample, respectively. Reproduced from ref[91].

The formation of strong BAS with zeolitic strength have been reported for ASAs prepared by various techniques.[121-123] Alumina-rich ASAs synthesized by flame-spray pyrolysis technique (Al/Si ≥ 1) provides a homogeneous distribution of silicon throughout an alumina-rich matrix, and a significant amount of strong BAS can be generated.[113] Comparing with low-Al-content ASAs, the reconstruction of the 3D structure by APT shows that two or more Al sites could exist in the proximity to the same Si atom.[26] In the same work, strong peaks of ^{27}Al-^{27}Al spin pairs, such as Al^{IV}-Al^{V} and Al^{V}-Al^{V}, are detected in ^{27}Al DQ-SQ NMR experiments, which is unable to be observed in low-Al-content ASAs. Since no alumina phase is detected in alumina-rich ASAs, there is a high probability that these Al spin pairs could exist in the local structure of the same silanols. At high Al/Si, increasing the local ionicity promote the interaction between Al spin pairs and local silanol via a pseudo "oxygen tri- or tetra-cluster" model as shown in **Figure 1-5E**, which is reported in aluminosilicate glasses and ASAs prepared by SiO_2 grafted on Al_2O_3 supports.[72, 124] Compare to those proposed in low-Al-content ASA, an extra

Al center pseudo-bound to the same silanol could result in Brønsted/Lewis acid synergy to increases the BAS strength from weak to strong, similar to those reported for dealuminated zeolites.[23] In ASAs prepared by co-gelation and Al-grafting silica, a small amount of strong BAS is probed with similar reactivity to zeolite counterpart in the test reactions.[121-123, 125] Zeolite-like bridging OH groups is suggested responsible for the formation of those strong BAS. However, the existing of bridging OH groups lack direct experimental evidence, such as ^{1}H shift at 3.3-4.4 ppm. On the other hand, the comparison of ASAs and crystalline zeolites with distinct structure could be affected by various factors other than their acid strength, such as surface diffusion of molecules, relative concentration of reactant per active sites, confinement effects in zeolites, intermediate formation and decomposition, and synergy of BAS with other functional groups (e.g. LAS).[29, 126-129] A distribution of Si at the alumina-rich local environment is observed in those ASAs due to their intrinsic inhomogeneity.[123, 125, 130] Like in alumina-rich ASAs, the model proposed in **Figure 1-5E** is thus highly possible for strong BAS in those ASAs, as an alternative explanation besides bridging OH groups.

The formation of LAS in ASAs depends on their intrinsic inhomogeneity or presence of specific sites. For instance, at high Al/Si ratio (i.e. Al/Si $\geq$ 0.4), a significant Al_2O_3 phase is formed.[120] Al_2O_3 is often used as Lewis acid catalyst, resulting in strong Al^{VI} peaks in the ^{27}Al MAS SSNMR spectra.[75] Surface defects on Al_2O_3, such as Al^{V} identified as Al^{VI} with an oxygen vacancy,[131] are LAS to promote versatile reactions (e.g. alcohol dehydration).[17, 18] This has been confirmed by ^{27}Al-{^{1}H} D-HMQC 2D NMR experiments recorded with ASAs before and after ammonia loading (**Figure 1-6**), showing ammonia adsorbed at unsaturated Al^{IV} and Al^{V} sites,[91] denoted as surface LAS. As observed with extra-framework Al cations, surface defects and unsaturated Al species are often involved in strong line broadening, leads to difficulties in the direct detection and quantification of these sites.[24, 27, 78, 107]

1.4.3 The Acidity and Structure of BAS Characterization Using ssNMR

1.4.3.1 Direct detection of BAS by 1H MAS NMR spectroscopy

^{1}H MAS NMR spectroscopy is a powerful technique in the study of surface protons, including BAS. The ^{1}H NMR chemical shifts correlates to the local structures or environments of surface protons. The typical ^{1}H NMR chemical shifts of surface OH groups on solid acids are summarized in **Table 1-2**. The ^{1}H chemical shifts (δ_{1H}) of hydroxyl groups in dehydrated solid acids often cover the range of δ_{1H} = -0.5-16 ppm. Hydroxyl groups in silica and alumina are of none to very weak acid strength. As demonstrated earlier, the acid strength of silanols

increase in the order of geminal < isolated < vicinal.[132-135] When involved in strong hydrogen bonding in small cages, the peak of SiOH in zeolites could be shifted up to δ_{1H} = 10-16 ppm.

Table 1-2 Typical ^{1}H MAS NMR chemical shifts (δ_{1H}) of various hydroxyl group in various solid acid catalysts

Solid Acid	Hydroxyl Group	δ_{1H}/ppm	Assignment	References
Silica	SiOH	1.8	Isolated silanols.	[136]
	$Si(OH)_2$	2.2	Geminal silanols.	
	(SiO)H···(Si)OH	2.6	Vicinal silanols, (poly-)hydrogen-bonded silanols.	
alumina	AlOH	-1.0-0.7	Terminal AlOH groups.	[67]
	Al(OH)Al	1.0-3.0	Doubly bridging AlOH groups.	
	$Al_3(OH)$	3.0-5.0	Triply bridging AlOH groups.	
	MeOH	3.3-6.7	MeOH (Me = Mo, V and Ti) groups of pure metal oxides and bridging M(OH)Al groups on Al_2O_3 supports	[137-139]
Silica-aluminas	MeOH	-0.5-1.8	Terminal MeOH (Me = Al, Ca, Zr, Zn and Mg) groups in large cages or on the external particle surface	[101, 105, 140-142]
	SiOH	1.2-2.3	Silanol groups on the external surface or at lattice defects.	[9, 22, 91, 113, 143-156]
	AlOH	1.0-3.6	Extra framework AlOH groups in narrow channels or small cages involved in hydrogen bonding, and Al species at framework defects.	[27, 68, 85, 86, 148, 151, 156-164]

	MeOH	2.8-6.2	MeOH (Me = Al, Ca, Mg and La) groups involved in hydroxyl proton bounded to or electrostatic interaction with neighboring oxygen atoms in sodalite cages of FAU-type zeolites or channels of ZSM-5	101, 113, 142, 144, 145, 164-169
	Si(OH)Al	3.3-4.4	Bridging hydroxyl groups in large cages and channels.	10, 20, 23, 27, 68, 143, 145, 156, 168, 170
	Si(OH)Al	4.6-8.0	Bridging hydroxyl groups in sodalite cage/small channel with hydrogen bonding or disturbed by framework via electrostatic interaction.	10, 20, 27, 54, 59, 171
	Si(OH)Si	10-16	Dual Silanol groups after probe molecule absorption or hydrogen-bonded internal silanol groups.	172-174
Mixed oxides	ZrOH	3.8-4.8	Hydrogen-bonded ZrOH groups or ZrOH groups with LAS in their vicinity (e.g. Zr^{4+}) on the surface	140, 141
	MeOH···H_2O	9.5-10.3	Bridged metal hydroxyl groups interact with water molecules, or the rigid water correlates with	86, 175

			framework and extra-framework Al species.	
Metal-organic framework	Al(OH)Al	1.7-2.7	Bridging hydroxyl groups at metal-organic frameworks, such as MIL-53(Al) and MIL-118(Al).	[145, 176-179]
Heteropoly acid	Keggin units H^+	6.7-9.3	Acidic hydroxyl group in the Keggin structure, e.g. Mo(OH)Mo and W(OH)W in $H_3PMo_{12}O_{40}$ and $H_2PW_{12}O_{40}$, and various ion exchanged forms.	[142, 180-183]

Bridging OH groups in zeolites often exhibit δ_{1H} at 3.3-4.4 ppm, well-distinguished from typical SiOH and AlOH groups (δ_{1H} = -0.5-2.3 ppm). Bridging OH groups located in small cages or channels could interact with neighboring oxygen atoms via hydrogen bonding or electrostatic interaction, which shifts the δ_{1H} of these disturbed bridging OH groups to a higher frequency (4.6-8.0 ppm). Even with obvious different δ_{1H}, the two kinds of bridging OH are characterized with the similar acid strength.[151, 184, 185]

Taking advantage of the linear correlation between the peak intensity and spin concentration for ^1H nuclei, the concentration of hydroxyl groups in solid catalysts could be quantified using a suitable external/internal standard.[53, 99] The total number of hydroxyl groups could be calculated by equation

$$c_{OH} = c_{st} m_{st} A_{OH} / (m A_{st})$$

where c_{st}, m_{st} and A_{st} are the concentration of hydroxyl groups, weight and total integral intensity with standard sample, while m and A_{OH} are the weight and total integral intensity of the sample measured. However, the signals of different types of hydroxyl groups are often observed with strong overlap, thus, suitable simulation methods should be applied to determine the concentration of each type of OH groups.

1.4.3.2 Detection of surface acid sites through host-guest interaction with probe molecules

Unlike zeolites, the ^{1}H MAS NMR spectra of the dehydrated ASA is often dominated by the silanol groups at δ_{1H} = 1.2-2.2 ppm, and no peaks at 3.3-4.4 ppm for bridging OH groups can be detected, leading to the detection of BAS in ASA via ^{1}H MAS NMR spectroscopy is impossible. On the other hand, the ^{1}H chemical shift of protons could be significantly influenced by the local environment, such as shifted from 3.3-4.4 ppm to 4.6-8.0 ppm for bridging OH groups involved in strong hydrogen bonding (see **Table 1-1**). Therefore, evaluating the BAS strength by ^{1}H SSNMR directly is less accurate. Due to the large quadrupole coupling constants (C_{QCC}),[186] the detection and the quantification of LAS, often Al cations and surface Al defects on γ-alumina, ASAs, and zeolites, is quite challenge by 1D and 2D ^{27}Al and/or ^{1}H MAS SSNMR directly, which mainly provide information on the chemical environment of Al species.

These acidic properties can be achieved by using basic probe molecules combined with SSNMR spectroscopy. Basic probe molecules interacting with surface acid sites results in adsorbate-induced chemical shifts of corresponding NMR peaks, depending on the type and strength of the acid sites. Frequently used probe molecules and their functions in the characterization of solid acids are summarized in **Table 1-3**. Strong basic molecules (e.g. NH_3 and pyridine) could interact with acid sites from weak to strong. With external or internal standard, the total number of acid sites can be determined from the peak intensity in corresponding SSNMR spectrum of probe molecules. Using weak basis molecules (e.g. $(CH_3)_2{}^{13}CO$ and CD_3CN), the adsorbate-induced chemical shifts correlate to the various strength of acid sites, and thus they are utilized to assess the acidic strength. Additionally, by applying probe molecules of various sizes (e.g. TMP and TMPO), the accessibility of acid sites can be evaluated, which will be explained in detail in later section.

Table 1-3 Probe molecules for solid acid acidity characterization[a]

Probe molecule	nucleus	Type		Strength		Density		Accessibility
		B	L	B	L	B	L	
Trimethylphosphine (TMP)	^{31}P	☺	☺	☺	-	☺	☺	☺
Acetone-2-^{13}C $(CH_3)_2{}^{13}CO$)	^{13}C	☺	☺	☺	😐	-	-	😐
Ammonia (NH_3)	^{1}H	☺	☺	-	-	☺	😐	😐
Pyridine-d_5 (C_5D_5N)	^{1}H	☺	-	☺	-	😐	-	☺

^{15}N-pyridine	^{15}N	☺	☺	☺	☺	☺	☺	☺
Trialkylphosphine oxides (R_3PO)	^{31}P	☺	☺	☺	😐	☺	☺	☺
Acetonitrile-d_3 (CD_3CN)	^{1}H	☺	-	☺	-	☺	-	😐
Perfluorotributylamine	^{1}H	☺	-	-	-	😐	-	☺

[a]B represents Brønsted acid; L represents Lewis acid; ☺, excellent; 😐, acceptable; -, poor

Ammonia, as a strong base, can be adsorbed at both BAS and LAS from weak to strong, thereby it can be utilized to identify BAS and LAS in a quantitative manner. At BAS, the protonation of ammonia shows a peak of ammonium ions (NH_4^+) at δ_{1H} = 6.5-7 ppm in ^{1}H MAS SSNMR (Table 3). This peak is well distinguished from the peaks of SiOH groups (δ_{1H} = 1.2-2.3 ppm), and thus, often used to identify the presence of BAS in ASAs from other overlapped hydroxyl groups.[113, 187] Recently, ammonia adsorbed at LAS on γ-Al_2O_3, TiO_2/anatase, and lithium-exchanged zeolite Na-Y is characterized with δ_{1H} = -0.5-3.0 ppm.[188] In comparison with the peak of NH_4^+, the strong adsorption of ammonia at LAS results in a broad peak with strong sidebands in ^{1}H MAS SSNMR experiments.[188, 189] In zeolites, ammonia adsorbed at extra-framework Al cations shows peaks at δ_{1H} = 2.6-4.6 ppm.[149, 190] Ammonia molecules coordinated at Lewis acidic Al sites (e.g. Al^V) on ASAs (δ_{1H} = 2.2-3.0 ppm) is observed in ^{27}Al-{^{1}H} D-HMQC 2D NMR experiments,[91] which is further evidenced by various ^{1}H MAS NMR experiments on ammonia-loaded ASAs desorbed at different temperatures, allowing the distinction from ammonium ions (δ_{1H} = 6.7 ppm) formed at BAS.[189] As an example, ^{1}H/^{27}Al TRAPDOR spectra of dehydrated ASA (Fig. 4a bottom) shows that part of SiOH groups (δ_{1H} = 1.8 ppm) overlapped by the other groups having proximity with Al centers.[111] These SiOH groups are able to protonate ammonia with a peak at δ_{1H} = 6.7 ppm (**Fig. 1-7A** bottom), while an additional peak at δ_{1H} = 3.0 ppm is observed. The peak at δ_{1H} = 3.0 ppm is featured with broad sidebands and relative strong intensity at elevating desorption temperature, hinting a strong adsorption of ammonia compared to those at BAS (**Figure 1-7B** bottom and **Figure 1-7C**), which are attributed to ammonia adsorbed at Lewis acidic Al sites.[189] In general, the incorporation of Al into silica network/framework or Si atoms throughout the Al matrix promote the formation of BAS, and high Al content results in more Al defects as LAS, leading to the increasing peak intensities at δ_{1H} = 6.7 and 3.0 ppm with boosting the Al/Si up to 7/3

(**Figure 1-7D**). Since each ammonia molecule can protonate or adsorbed at only one BAS or LAS, the intensity of corresponding peak in the ^{1}H MAS SSNMR spectrum can be utilized to evaluate the concentration of acid sites existing in solid acids.[191, 192]

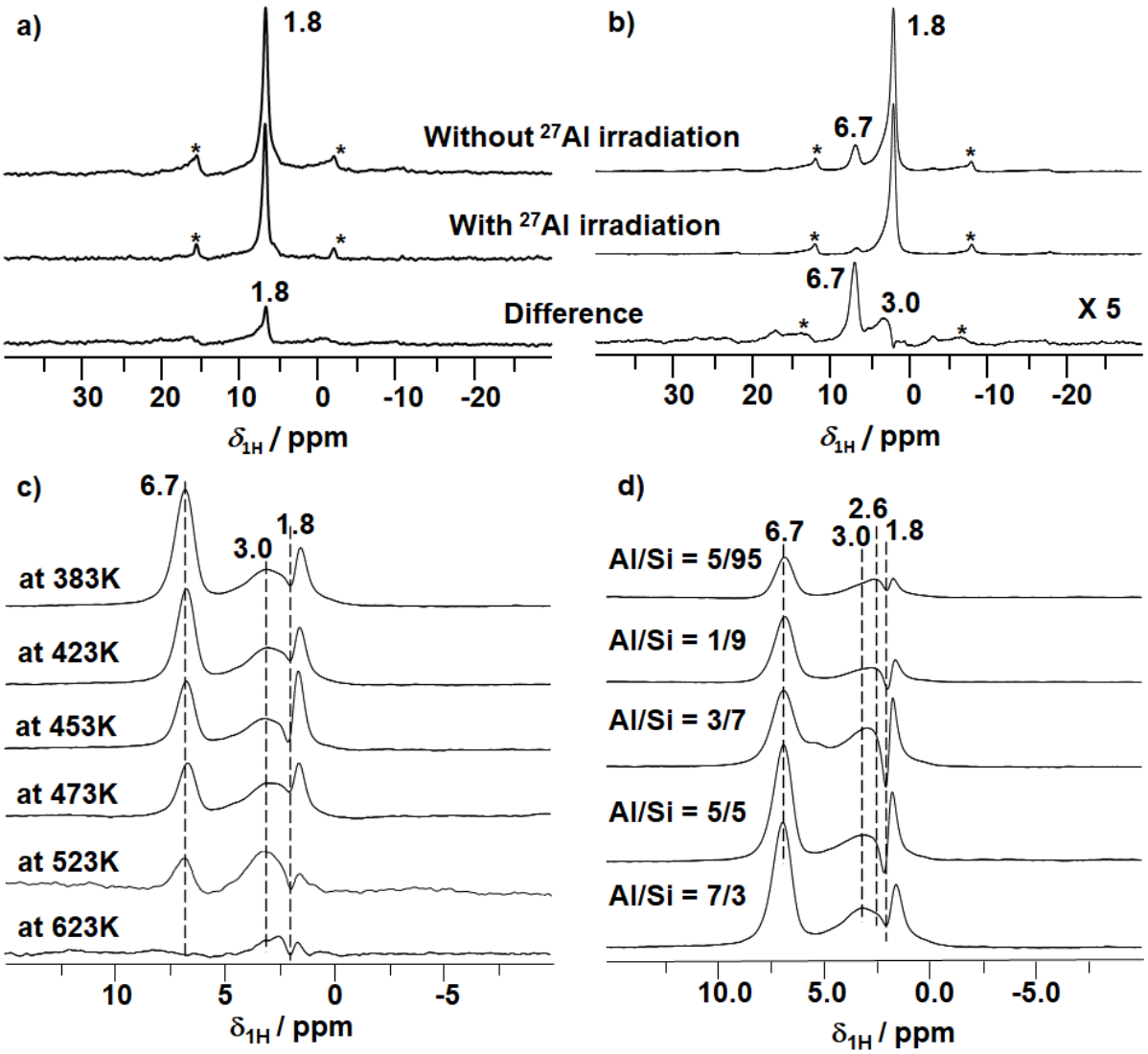

Figure 1-7 ^{1}H/^{27}Al TRAPDOR spectra of ASA (Al/Si = 7/3). (a) dehydrated for 12 h at 723 K and at a pressure of less than 10^{-2} bar (Reproduced from ref [111]. Copyright 2019 Elsevier), and (b) dehydrated sample after loading with NH_3 and subsequent evacuation at 383 K for 1 h. ^{1}H MAS NMR difference spectra recorded before and after ammonia loading on dehydrated ASAs: (c) desorption at elevating temperature (Al/Si = 7/3) and (d) with different Al content. Reproduced with permission from ref [189]. Copyright 2020 Wiley.

Table 1-4 Probe molecules for surface acid sites strength characterization

Probe and Resonance	Acidity characterization	Reference
Ammonia (NH_3)	**BAS**: 6.5-7.0 ppm for ammonium ions	9, 22, 30, 31, 91, 111,
^{1}H (δ_{1H})	**LAS**: -0.5-4.6 ppm for adsorbed ammonia molecules	112, 149, 155, 188-194
Pyridine-d_5 (C_5D_5N)	Hydrogen-bonded pyridine at SiOH: ca. 10 ppm	168, 195-200

^{1}H (δ_{1H})	**BAS**: 12-20 ppm for pyridium ions	
^{15}N-pyridine	Hydrogen-bonded pyridine at SiOH: 290-295 ppm	201-207
^{15}N (δ_{15N})	**BAS**: 212-288 ppm for pyridium ions;	
	LAS: 233-285 ppm	
Acetonitrile-d_3	Hydrogen-bonded CD_3CN at AlOH: $\Delta\delta_{1H} \approx 1.2$ ppm	10, 28, 113, 136, 145,
(CD_3CN)	Hydrogen-bonded CD_3CN at SiOH: $\Delta\delta_{1H} \approx 3.0$ ppm	168, 178, 199, 208
^{1}H ($\Delta\delta_{1H}$)	**BAS**: $\Delta\delta_{1H}$ = 3.6 ppm → 9.6ppm (Weak → Strong)	
Acetone-2-^{13}C	Hydrogen-bonded $(CH_3)_2{}^{13}CO$ at SiOH: 210-213	9, 20, 22, 23, 30, 31, 53,
$(CH_3)_2{}^{13}CO$	ppm	89, 103, 111-113, 140,
^{13}C (δ_{13C})	**BAS**: 213 ppm → 235 ppm (Weak → Strong)	155, 183, 188, 194, 209-
	LAS: 233 ppm → 250 ppm (Weak → Strong)	214
Trimethylphosphine	**BAS**: -2 ~ -5 ppm for protonated TMP	88, 140, 213, 215-229
(TMP) ^{31}P (δ_{31P})	**LAS**: -20 ~ -67 ppm	
Trimethylphosphine	Physisorbed TMPO at δ_{31P} = 41-46 ppm	24, 27, 230-243
oxide (TMPO)	**BAS**: δ_{31P} = 45-88 ppm	
^{31}P (δ_{31P})	**LAS**: δ_{31P} = 32-65 ppm	

[a] Super Acid represents those solid acid with an H_0 value below -11.93 (100% sulfuric acid), - represent no distinguishable signal.

Pyridine is another commonly used strong basic probe molecule in acidity characterization by various techniques, including SSNMR. Adsorption of fully deuterated pyridine (pyridine-d_5) leads to a complete proton transfer from BAS to pyridine-d_5. The resulting pyridinium ions ($PyrH^+$) can be detected with ^{1}H MAS NMR peaks at δ_{1H} = 12-20 ppm, while the peaks for hydrogen-bonded pyridine-d_5 at ca. δ_{1H} = 10 ppm (Table 3). For instance, protonation of C_5D_5N at Si(OH)Al groups in supercages of lanthanum-exchanged zeolites Y displays a peak at δ_{1H} = 14 ppm, while Si(OH)Al groups in sodalite cages stay the same (δ_{1H} = 4.8 ppm).[199] The latter is attributed to restriction of pyridine in these small cages. Thus, pyridine can be used to assess the accessibility of acid sites. Compared to ^{1}H MAS NMR experiments, BAS and LAS can be distinguished by ^{15}N MAS NMR experiments using ^{15}N-pyridine (**Table 1-4**). The δ_{15N} correlates well with the electronegativity of the metal center.[204] Moreover, the lower induced

$\Delta\delta_{15N}$ indicates a higher acid strength for both BAS and LAS. However, the utilization of ^{15}N-pyridine for acidity characterization is strongly hampered by the high costs and the dependence of δ_{15N} on the thermal mobility.

Weak bases, such as acetone-2-^{13}C, acetonitrile-d_3, perchloroethylene and trimethylhosphine oxide, are extensively applied in the discrimination of BAS with various strength. Instead of full protonation of strong bases at all BAS, weak bases adsorbed at BAS via hydrogen bonding, resulting in an adsorbate-induced $\Delta\delta$ that correlates to the strength of BAS. For instance, hydrogen bonds (O–H···N) are generated between hydroxyl groups and CD_3CN upon adsorption, shifting the corresponding ^{1}H MAS NMR peak to a higher frequency. Adsorption of CD_3CN on terminal SiOH groups is observed with a $\Delta\delta_{1H} \approx 3.0$ for both silica and zeolites.[10, 113] With enhanced strength, CD_3CN hydrogen-bounded to bridging OH groups in zeolites lead to a larger $\Delta\delta_{1H}$. The increase in $\Delta\delta_{1H}$ is in line with the acid strength of bridging OH groups in zeolites, such as 5.1, 7.1 and 7.9 ppm for zeolites HY, H-Beta and H-ZSM-5.[10, 28, 145, 199] On the other hand, $\Delta\delta_{1H}$ raises at a higher framework Si/Al ratio of zeolite H-Beta,[10, 28] corresponding to a higher acid strength since the increase of electronegativity of the framework.[244, 245]

Another commonly used probe molecule for evaluating the strength of both BAS and LAS is Acetone-2-^{13}C. Acetone complexes on acids (both liquid and solid acids) is formed via the electron-rich carbonyl oxygen atom of acetone. The length of C=O bond depends on the strength of acid sites involved.[246] Therefore, the adsorbate-induced higher-frequency shift of the ^{13}C MAS NMR peak (δ_{13C} or $\Delta\delta_{13C}$) of C=O group is widely utilized to evaluated the strength of acid sites. Typically, a larger $\Delta\delta_{13C}$ or δ_{13C} shifted to a high-frequency of acetone-2-^{13}C reflects a higher acid strength of acid sites and *vice versa*. As shown in **Figure 1-8**, acetone-2-^{13}C adsorbed on SiOH groups in silicious [Si]MCM-41 shows a peak at 210 ppm. Al addition into the silica network results in moderate BAS, leading to a peak at higher frequency (δ_{13C} = 213 ppm). In comparison, the formation of strong BAS, such as bridging OH groups as in zeolite H-ZSM-5, raise a peak at δ_{13C} = 223 ppm. Further increasing the acid strength of H-ZSM-5 by Al exchange leads to a peak at δ_{13C} = 228 ppm, while Lewis acidic EFAl gives a peak at δ_{13C} = 235 ppm. Moreover, the δ_{13C} of various solid acids are determined and compared with the δ_{13C} of acetone-2-^{13}C dissolved in aqueous sulfuric acid with different concentration, which has been utilized as a scale to measure the strength of acid sites.[209] It should be careful to perform these measurements under controlled low loading and at low

temperature to avoid the fast intermolecular condensation of acetone-2-^{13}C at strong acid sites.[23, 194, 211, 213]

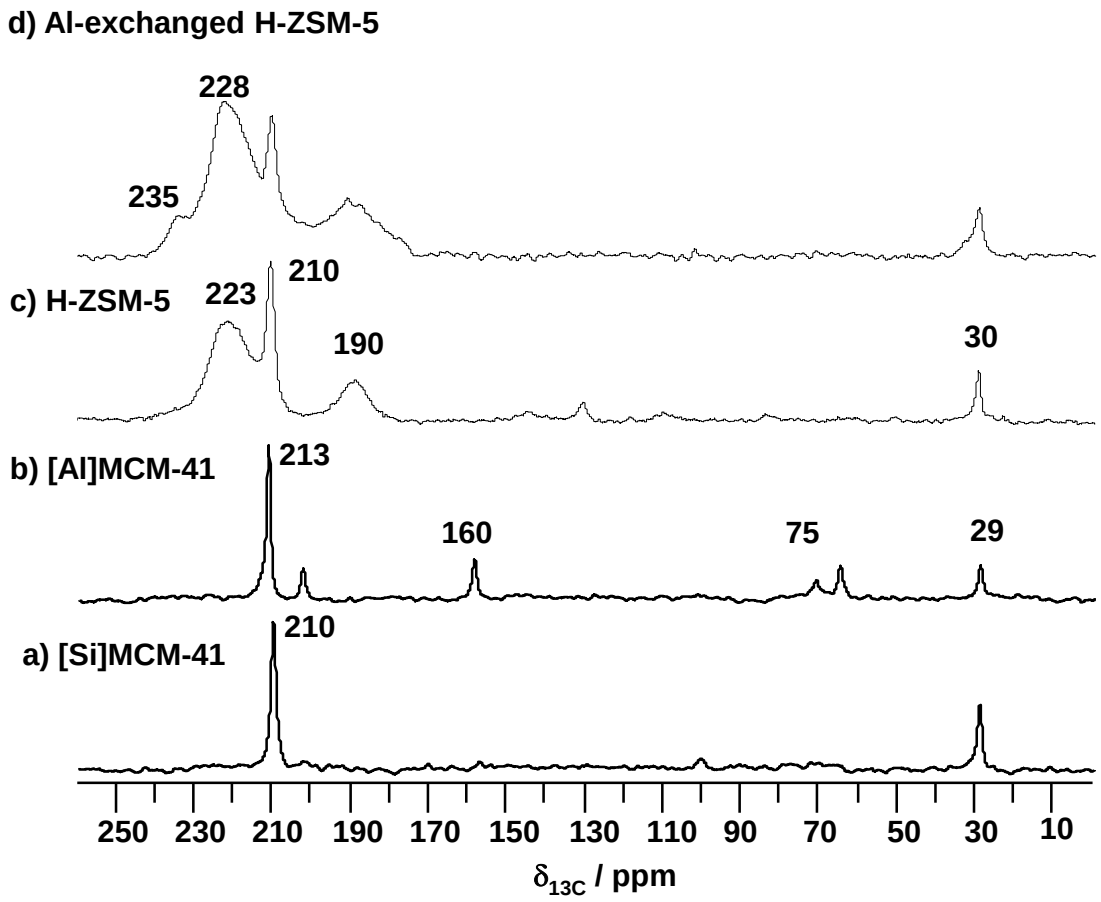

Figure 1-8 ^{13}C CP/MAS NMR spectra of (a) [Si]MCM-41 and (b) [Al]MCM-41 (Si/Al = 50) (Reproduced with permission from ref [112]. Copyright 2013 Wiley) and of (c) H-ZSM-5 (Si/Al = 16) and (d) Al-exchanged H-ZSM-5. Reproduced from ref [20].

Acidity characterization by ^{31}P MAS NMR using trimethylphosphine (TMP) and trialkylphosphine oxide (R_3PO; R = C_nH_{2n+1}, n = 1, 2, 4, and 8) as probe molecules is recently reviewed by Deng and co-workers.[60, 61] TMP can be protonated at BAS to form $[(CH_3)_3PH]^+$ complexes, and be coordinated to LAS via the electron pair of the phosphorus atom. Typically, δ_{31P} = -2 to -5 ppm represents TMP protonated at BAS, while the TMP chemisorbed on LAS shows a broader peak from -20 to -67 ppm. Theoretical calculation study demonstrates that the higher acid strength corresponds to the lower deprotonation energy of a BAS, reflected by the increase of δ_{31P}.[215] TMP are effective in evaluating the acid strength of LAS with the broad detection range of δ_{31P}, but less effective for BAS. Besides, TMP is a toxic and pyrophoric molecule. Compared to TMP, R_3PO molecules are much safer in characterizing the strength of acid sites. Recent studies on Al-exchanged H-ZSM-5 zeolites loaded with trimethylphosphine oxide (TMPO) demonstrate that versatile BAS with enhance strength are generated after Al

exchange with δ_{31P} = 44-77 ppm (**Figure 1-9A**),[27] in line with those observed in ^{13}C NMR spectra using acetone-2-^{13}C as probe molecule.[20] The peaks at 38 and 32 ppm in Al-exchanged H-ZSM-5 zeolite (**Figure 1-9B**) are disappeared after rehydration, indicating a weak adsorption of TMPO on LAS according to Zheng et al.[247] Since TMPO are weakly adsorbed at LAS and tend to form weak BAS upon water adsorption, TMPO area effective in evaluating the strength of BAS over LAS from stable $TMPOH^+$ complexes at BAS. The adsorption of TMPO on zeolites H,Na-Y, H-Beta, H-ZSM-5 shows δ_{31P} at 65, 78 and 86 ppm, which is well in line with the increasing BAS strength in these zeolites. The correlation between δ_{31P} and the BAS strength has been clarified by theoretical calculation study through the distance between oxygen of P=O and the proton of bridging OH groups on model MFI zeolite.[248]

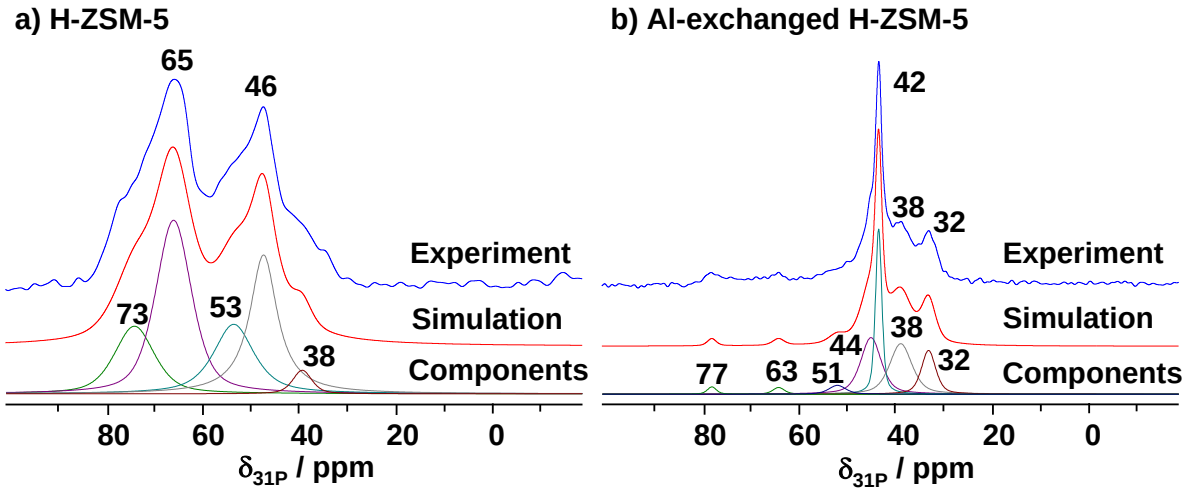

Figure 1-9 ^{31}P SPE-MAS NMR spectra of dehydrated (500 °C) H-ZSM-5 (a) and Al-exchanged H-ZSM-5 (b) zeolites loaded with TMPO. Reproduced from ref [27].

The accessibility of acid sites at the internal and external surface, or inside sodalite cages and super cages, can be clarified by using probe molecules with various sizes.[145, 215, 242, 249, 250] One typical example is using TMPO and tributylphosphine oxide (TBPO) to determine the accessibility of reactants into zeolite pores (diameter ca. 0.60 nm),[215, 242] which is of great industrial interest. The acidic sites on the outer surface and inside the pores can both be accessed by TMPO (diameter ca. 0.55 nm), but only external acid sites of the zeolite are accessible for TBPO (diameter ca. 0.82 nm). Another example is Si(OH)Al groups in super and sodalite cages in zeolite H,Na-Y show two peaks at δ_{1H} = 3.9 and 4.7 ppm.[145] CD_3CN adsorption shifts the former to a higher frequency by $\Delta\delta_{1H}$ = 5.1 ppm, however, it exerts no effect on the latter, demonstrating a sterical hindrance of Si(OH)Al groups in the sodalite cages.

1.4.3.3 H/D exchange studies for activity test and acidity characterization

The activation of C-H bond is of great importance in various hydrocarbon conversion reactions.[5, 6] The activity of solid acids in the activation of C-H bond often depends on the strength of BAS. Hydrogen-deuterium exchange (H/D exchange) with deuterated hydrocarbon is extensively utilized in the study of C-H bond activation and reaction mechanism over aluminosilicates,[145, 152, 251-257] in which a proton on BAS is exchanged with a deuterium of a deuterated reactant molecule or a deuterium on a deuterated BAS exchanged with a proton of reactant molecule. By in situ ^{1}H MAS NMR experiments, the kinetic parameters (e.g. reaction rate k and activation energy E_a) of a H/D exchange reaction can be achieved to compare the activity and strength of BAS on various solid acids (**Table 1-5**).[162,237,24126]

The H/D exchange of various deuterated aromatic with BAS in different zeolites is performed exclusively between BAS and deuterons bound to the aromatic rings.[145] The obtained E_a values are summarized in Table 4. For the same deuterated aromatic, the E_a value decreased in the order of H-Y ≥ La,NaY > H-ZSM-5 in all cases. Reducing the E_a values is in accordance with the increase in the BAS strength of zeolites, scaled by the larger $\Delta\delta_{1H}$ values using CD_3CN as probe molecule.

Table 1-5 Activation energies E_a of the H/D exchange of BAS in dehydrated zeolites H-Y, La,Na-Y, and H-ZSM-5 with deuterated benzene, ethylbenzene, toluene, and *p*-xylene[145].

Zeolite	Activation energies of H/D exchange in kJ/mol				$\Delta\delta_{1H}$ in ppm[a]
	Benzene	Ethylbenzene	Toluene	*p*-Xylene	
H-Y	76 ± 3	41 ± 2	32 ± 2	27 ± 2	5.1 ± 0.1
La,Na-Y	67 ± 4	39 ± 3	29 ± 1	26 ± 2	5.7 ± 0.1
H-ZSM-5	46 ± 2	29 ± 3	25 ± 2	20 ± 2	7.9 ± 0.1

[a]the high-frequency shifts $\Delta\delta_{1H}$ of the ^{1}H MAS NMR signals of accessible BAS upon adsorption of CD_3CN are given.

Evaluating the BAS strength by E_a values is effective for solid acids having similar structures, since E_a values are strongly influenced by hydrocarbon loading, internal mass transfer and synergy of BAS with other functional groups.[126-129, 258] Recent studies on the H/D exchange of C_6D_6 shows that ASA provide only half of E_a (~ 30 kJ/mol) than that of H-ZSM-5 (~ 60 kJ/mol),[78] which is often characterized with distinct structure and much weaker BAS strength compared to those of zeolite H-ZSM-5. To avoid the effect of reactant concentration and mass transfer within different structures, a deuterated reactant to BAS loading ratio of 1:1 was

applied, and the diffusion of reactant to BAS was controlled at low temperature to minimize their reaction.

The H/D exchange between deuterated benzene (C_6D_6) and ASA is studied by in situ ^{1}H MAS NMR experiments at 313K with a C_6D_6 to BAS ratio of 1:1.[26] The stack plot (**Figure 1-10A**) shows that the peak intensity at 7.3 ppm for H bounded to aromatic ring is increasing with the consumption of BAS at 1.8 ppm during the H/D exchange reaction. The reaction rate *k* is obtained via fitting the curve of experimental results and shown in **Figure 1-10B** with an exponential relationship:[145] The obtained *k* values follow the sequence: ASA (Al/Si = 50/50, *k* = 0.0078 min^{-1}) ≈ H-ZSM-5 (0.0072 min^{-1}) > SA/10 (Al/Si = 10/90, 0.0045 min^{-1}). The increasing *k* values correlates well with the enhanced BAS strength, characterized by ^{13}C MAS NMR spectroscopy using acetone-2-^{13}C as a probe.[113] The formation of strong BAS in Al-rich ASA (Al/Si ≥ 50/50) has been proposed by the Bronsted/Lewis acid synergy in ASAs, caused by more than one unsaturated Al site with proximity to one SiOH group for acidity enhancement.[26]

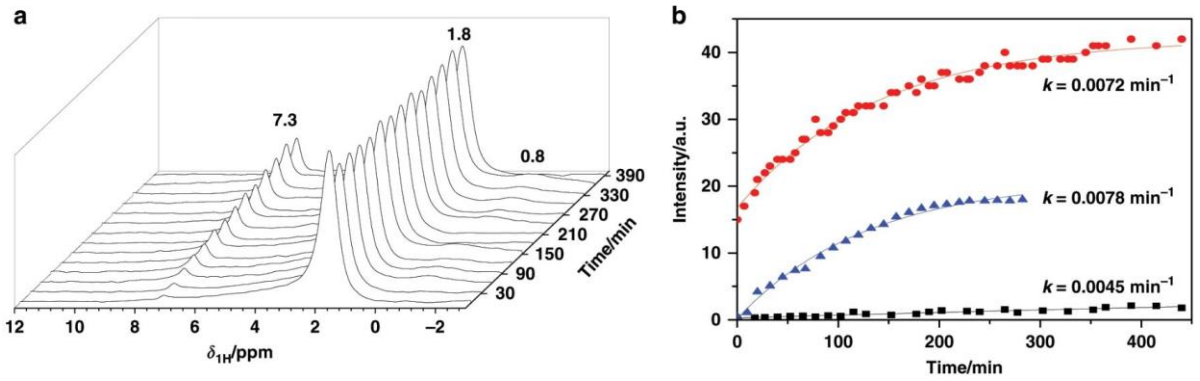

Figure 1-10 ^{1}H H/D exchange MAS NMR of ASA. (a) Stack plot of ^{1}H MAS NMR spectra, acquired from in situ ^{1}H MAS NMR at 313K on ASA (Al/Si = 50/50) during H/D exchange with C_6D_6. (b) Kinetics study of the H/D exchange rate between the C_6D_6 and the acid sites at 313K in H-ZSM-5 (red), ASAs with Al/Si ratio of 50/50 (blue) and 10/90 (Black). Adapted from reference. Reproduced from ref [26].

1.4.4 Summary and outlook of ssNMR characterization ‘

Qualitative and quantitative analysis of the acidic properties and the local structure of surface sites on solid acids is crucial to understand their catalytic behavior and activity. Solid-state NMR spectroscopy represents a state-of-art technology in discovering the local environment of resonating nuclei in solids. This chapter focused on recent progresses on the comprehensive characterization of solid acid, including the type, density, strength, accessibility and structure-activity of acid sites using SSNMR spectroscopy.

With or without probe molecules, various BAS and LAS can be directly identified via the application of SSNMR. In detail, the utilization of bases such as ammonia, deuterated or ^{15}N-

enrihed pyridine, acetonitrile-d_3, acetone-2-^{13}C, trimethylphosphine (TMP) and trimethylphosphine oxide (TMPO) as probe molecules in the acidity characterization are demonstrated. Typically, strong bases (ammonia, pyridine and TMP) are often utilized in the identification of the type and quantifying the number of acid sites, while weak bases (acetonitrile-d_3, acetone-2-^{13}C and TMPO) are effective in scaling the acid strength of surface site. The accessibility of surface acid sites located at external surface, in sodalite cages and super cages in zeolites can be distinguished by applying probe molecules with various sizes. For nuclei with spin I = 1/2, the ^{1}H, ^{13}C, ^{15}N, and ^{31}P SSNMR spectroscopy can be applied for detecting the changes of probe molecules and surface hydroxyl protons can be performed in a quantitative manner by using internal or external intensity standard. Moreover, the reaction rate and activation energy of H/D exchange determined by in situ ^{1}H SSNMR spectroscopy correlates well to the strength of acid sites. This renders H/D exchange a widely utilized manner to evaluate the activity of acid sites in the activation of C-H bond in hydrocarbon conversions.

The local structure of surface acid sites can be characterized by various 2D ssNMR experiments. In the case of silica-aluminas, the characterization of Al species involved in strong quadrupole interactions is the key to reveal the local structure of acid sites. The coordination and structural parameters can be determined from ^{27}Al MQMAS NMR experiments. The connectivity between Al species and with other atoms in their local structure can be studied by homonuclear or heteronuclear correlation 2D NMR experiments. The comprehensive investigation with combination of these 2D SSNMR techniques reveals the structure of various acid sites in zeolites and ASAs.

So far, the characterization of LAS is still challenging. LAS can be investigated by using probe molecules. As in silica-aluminas, Al sites are often involved in strong quadrupolar interactions, lowering their sensitivity to even invisible under the investigation of ^{27}Al ssNMR spectroscopy. In many cases, various Lewis acidic Al sites exist together in silica-aluminas. Distinguishing their functions is currently difficult even with using probe molecules by 1D SSNMR spectroscopy. The application of 2D ssNMR spectroscopy to identify their guest-host interaction in the local structure requires the combination of various techniques, which could significantly increase the complexity of the experiment and should be carefully studied.

In summary, solid-state NMR spectroscopy is a powerful technique in both qualitive and quantitative studies of solid acids. The application of approaches described in this chapter can

be applied for the characterization of the acidic properties and local structure of a broader variety of solid adsorbents and catalysts beyond silica-aluminas, which should shed light on the fundamental understanding of the structure–activity relationship in heterogeneous catalytic systems.

1.5 High-Value Chemical Production from Biomass

With the increasing severity of fossil fuel energy crisis, it is imperative to develop green renewable energy. Biomass, as an important renewable resource with wide distribution and abundant reserves, has received wide attention as an important source of organic chemicals, fuels, and materials. In 2021, biomass provided nearly 5 quadrillion British thermal units (Btu) and about 5% of total primary energy use in the United States.[259] However, due to its high oxygen content, biomass cannot directly replace fossil fuels as the energy resource and hardly be utilized directly as valuable chemicals.

In the chemical industry, dehydration is recognized as one of the effective methods to obtain high value-added chemicals and the solid acid catalyst have shown its potential in promoting such reaction. One typical example is the dehydration of alpha hydroxy acid (AHA) to obtain value-added fine chemicals. AHA is a class of chemical compounds that consist of a carboxylic acid substituted with a hydroxyl group on the adjacent carbon. Different types of AHA may be naturally occurring. However, only small amount of AHAs and derivatives can be separated naturally, which gives the reason of high price of AHA. The AHA are mainly used in the synthesize of pharmaceutical and fine chemicals, it has been largely utilized especially in skin care products, which has a dramatically increasing demand in recent ten years. Thus, if AHA can be synthesized from renewable biomass in a large scale, not only just the price of AHA will be lower, but also it would be a great long-term sustainable process. Among the AHA and its derivatives, mandelate is important raw materials used in food, skin care, healthcare formulations, and biodegradable polymer productions.[260] The demand of that is expected to reach 3 million tons in this year.[261] Currently, most of industrial AHA and derivative production is based on large scale liquid base-catalysed isomerization, which requires a costive separation process to isolate products, requires large amount of energy to achieve high reaction temperature, and can only produce products with moderate yield. However, AHA derivatives can also be produced by solid acids like alumina, based on Cannizzaro reaction. Compared with liquid base catalysation, it showed many advantages such as easy separation and lower reaction temperature, and it has the potential to achieve a greener process. Recently, the direct production of α-hydroxy carboxylic acids and their derivatives from α-keto aldehydes via

catalytic dehydration has received interest. For example, the selective conversion of phenylglyoxal (PG) to ethyl lactate (EM) have been intensively studied within five years. Utilizing the solid acid catalyst of mesoporous zirconium oxophosphate Haimei et al. found that the catalyst with LAS/BAS ratio of 2.1 gave the optimized performance i.e., 82% of PG conversion and 92% of EM selectivity.[262] And they proposed that the PG could directly convert into EM on the LAS, Zr cation site, while the BAS formed by OH-P-O-Zr lead to the formation of the intermediate hemiacetal. Differently, with different solid acid catalyst, such as alumina and silica-zirconia, different reaction pathways have been proposed, where BAS instead of LAS drives the reaction. Therefore, there is still a gap between the understanding of reaction mechanism and preparation of the optimized catalysts. And this should be further studied with detail in order to increase the yield of α-hydroxy carboxylic acids and their derivatives.[263]

Cascade reaction have been considered as another useful method to produce fine chemicals from biomass. One typical example is the conversion of glucose into valuable platform chemical, 5-hydroxymethylfurfural (HMF)[264]. Liquid catalysts have been commercially applied for the conversion of biomass, glucose into varied fine chemicals. However, compared to solid catalyst, the separation of the liquid catalyst and product cost a lot of money. In this sense, solid acid with bi-acidity have received many interests in order to conduct glucose conversion. For cascade glucose conversion on solid acid, it is widely accepted that the LAS promotes the isomerization of glucose to fructose, while BAS is responsible for the secondary dehydration steps. Besides, the selectivity of which is largely determined by the acidic properties of catalyst present[265]. Thus, many efforts have been applied to optimize the acidity of the solid acid in order to increase the yield of 5-HMF under mild reaction condition. However, conflict results have been reported and there is no common agreement on the best catalysts. For example, on modified Al-beta-zeolite catalysts with bi-acidity, Hyejin An et al.[266] observed increase conversion of glucose to approx. 80% with an increase in LAS/(BAS+LAS) ratio till reaching 0.89, and recorded that the best HMF selectivity (~20% yield) can be achieved when the ratio is about 0.76. Conflictingly, in another dealuminated beta-zeolite case with both surface LAS and BAS, optimized catalytic performance over three hours reaction have been identified on catalysts with LAS/(BAS+LAS) ratio of only 0.51[267]. With further increase in LAS ratio, little variation has been observed on glucose conversion and HMF selectivity. Therefore, there is a need for deeper research on the influence of acidity and related properties on the catalytic performance of biomass conversion such as cascade glucose conversion.

2.Experimental and methodology

2.1 Introduction

In this work, aluminium containing solid acid catalyst such as alumina-boria material and alumina-silica material have been prepared based on different methods for catalytic conversion of biomass. After preparing the catalysts, the physical properties of the materials have been characterized by the techniques of X-ray diffraction (XRD), N_2-adsorption/desorption, Transmission electron microscopy (TEM), Energy Electron Loss Spectroscopy (EELS), X-ray photoelectron spectroscopy (XPS), and Fourier Transform Infrared Spectroscopy (FTIR). The chemical properties such as acid site identity, location, local structure, and acidity have been measured by means of NH_3 temperature-programmed desorption (NH_3-TPD), and solid-state Nuclear Magnetic Resonance Spectroscopy (ssNMR). After optimizing the physical and chemical properties of the prepared catalysts, the catalytic performance on biomass conversion have been tested in the catalytic conversion of bio-phenylglyoxal to ethyl mandelate, cascade glucose conversion to 5-hydroxymethylfurfural (5-HMF), and biomass 1,2-Propanediol dehydration to propanal, respectively. The product yield and selectivity have been analysed by Gas chromatography (GC) or High Pressure Liquid Chromatography (HPLC). The reaction mechanisms have been studied by *in situ* means of solution state nuclear magnetic resonance spectroscopy (NMR) or Diffuse reflectance infrared Fourier transform spectroscopy (DRIFTS).

2.2 Catalyst synthesis

2.2.1 Preparation of B/m-Al_2O_3 catalyst

To construct alumina involved mixed oxide with high concentration Al^V species, evaporation-induced self-assembly (EISA) has been applied to synthesis mesostructured amorphous Al_2O_3 with boron incorporation[42]. 1 g of $EO_{20}PO_{70}EO_{20}$ (P123, Poly(ethylene glycol)-block-poly(propylene glycol)-block-poly(ethylene glycol), MW = 5800) was added into 20 mL of pure ethanol with ultrasonication for 10 min till the solution become clear. Under 2200 rpm magnetic stirring, 0.617 g of aluminum isopropoxide (AIP, >98%) was added into the clear solution. Keep stirring the solution for 1 h in a closed system under room temperature, 0.267 g of anhydrous aluminium chloride (99.99%) was added under same condition and stirring the solution for further 4 h. To construct alumina based mixed oxide, lastly, when the solution turns to translucent white colour, stoichiometric amount of boric acid (99.5%) was added into the solution, and then the solution was left for magnetic stirring at 2200 rpm for 24 h in the closed system. Based on the loading ratio of boron to aluminium, the synthesized catalysts are named as xB/m-Al_2O_3, where x = n(B)/n(Al). The resulting solution was self-evaporated at 40 ^oC for

3 days and then dried at 80 ºC for another 2 days in an oven. With the solvent ethanol evaporates during the process of EISA, the concentration of homogenous aluminum species, boron species, and surfactant P123 have been enriched. Upon the exceed concentration of critical micelle have been approached during the evaporation, B/m-Al_2O_3 with mesopores can be established[268]. Then the final catalyst was obtained by calcining the dried gel at 400 ºC for 6 h on air with temperature increase of 1 ºC/min. The catalysts are highly reproducible in up to five times scaled-up synthesis.

2.2.2 Preparation of Al_{ALD}@high silica substrate catalyst

The construction of the mesostructured amorphous silica subtract was reported previously by our group via a one-step room-temperature preparation[269]. Utilized chemicals were purchased from Sigma-Aldrich and listed here: ammonium hydroxide solution (28 % NH_3 in H_2O, 0.9 g/mL), tetraethylorthosilicate (TEOS, >98 %), hexadecyltrimethylammonium chloride solution (CTAC, 25wt % in H_2O), and aluminum (III) nitrate nonahydrate ($Al(NO_3)_3 \cdot 9H_2O$, >98 %). Briefly, without aluminum precursor loading, the pure silica were synthesized as follows: in 200 mL deionized water with 5 mL CTAC and 5mL NH_4OH solution, 5 mL TEOS were added under vigorous stirring at a temperature of 298 K. After the formation of white colour gel, the formed gel has experienced a 20 mins ultrasonication, followed by another one-hour vigorous stirring. The solid content of the prepared gel was then collected via vacuum filtration and washed by deionized water and ethanol for three times. After drying the obtained solid overnight under 80ºC, the collected solid have experienced a calcination process at 550ºC for six hours with a temperature increase rate of 1ºC/min from room temperature under the presence of air. The prepared substrate is named m-S (Mesostructured amorphous Silica). Compared to the preparation for pure m-S, for alumina doped m-S, the only difference in the preparation method is that the addition of $Al(NO_3)_3 \cdot 9H_2O$ after the formation of white gel. With the molar ratio of n(Si)/n(Al) = 40, the prepared catalyst is named m-SA (Mesostructured amorphous Silica Alumina).

Al_2O_{3ALD} on prepared substrate (Al_{ALD}@high silica substrate) was performed by a custom-made rotary fluidized ALD reactor (AngstromBlock Scale-R01 ALD system) as reported in a previous study[270]. The temperature of the reactor was set at 200 ºC and the rotation speed of powder cartridge was set to 100 rpm. The Al precursor was trimethylaluminum (TMA) and oxygen source was deionized H_2O. The pulse time and purge time for both TMA and H_2O were 60 s and 120 s, respectively. 20 cycles of Al_2O_3 ALD were carried out on samples in this work

and after 500°C calcination for 6 hours, the catalysts were named as Al_{ALD}@m-S and Al_{ALD}@m-SA.

2.2.3 Preparation of n-SiO_2@am-Al_2O_3

The parent penta-coordinated aluminium species enriched Al_2O_3 have been prepared based on the modification of previously published evaporation-induced self-assembly (EISA) method[271]. In brief, in 40 ml of pure ethanol, 2 g of P123 was added and well dissolved. Under mild magnetic stirring, AIP was added into the closed solution system for 1 h. Under room temperature, anhydrous aluminium nitride was then added and leave for overnight. Then, the solution was poured into a dish in oven for self-evaporation. It was kept at 40°C for 3 days before dried at 80°C for 2 days. Then the obtained solid was calcinated at 400°C for the preparation of Al^V-enriched amorphous Al_2O_3 substrate.

The preparation of SiO_2@am-Al_2O_3 was modified from previously published base-catalyzed deposition method[272]. In 10 ml ethanol, 1 g of Al^V-enriched am-Al_2O_3 was dispersed. Then the solution PH was adjusted by the addition of 2ml NH_4OH (33 wt%, aqueous solution). After 30 mins sonication, Tetraethyl orthosilicate (TEOS, 99%) was added (n(Si)/n(Al)=100) and the mixture was shaken for 1 h. The above procedure constitutes the 1st cycle of SiO_2 overcoating. The following cycles of SiO_2 deposition involves identical procedures. All materials were washed with pure ethanol before drying. After drying overnight, the materials have been calcinated at 400 °C at 1°C/min and held for 4 h under static air. Based on the cycles of SiO_2 deposition, the materials have been named as 1SiO_2@am-Al_2O_3, 2SiO_2@amAl_2O_3, 5SiO_2@amAl_2O_3, respectively.

2.3 Physical properties Characterization Techniques

2.3.1 X-ray diffraction

X-ray diffraction is a technique to study the atom arrangement in crystals. When a incoming X-ray contact with the observing crystal with a known certain angle θ, the X-ray will be reflected from the atomic planes of the crystal at a distance *d* with identical angle θ. Thus, with an understanding on Bragg law that

$$n\lambda=2d\sin\theta \qquad \textbf{(Equation 2-1)}$$

where n mush be a whole number of wavelength λ, the atom arrangement of the observing crystal can be deduced by understanding the interference pattern via Bragg law[273] (**Figure 2-1**).

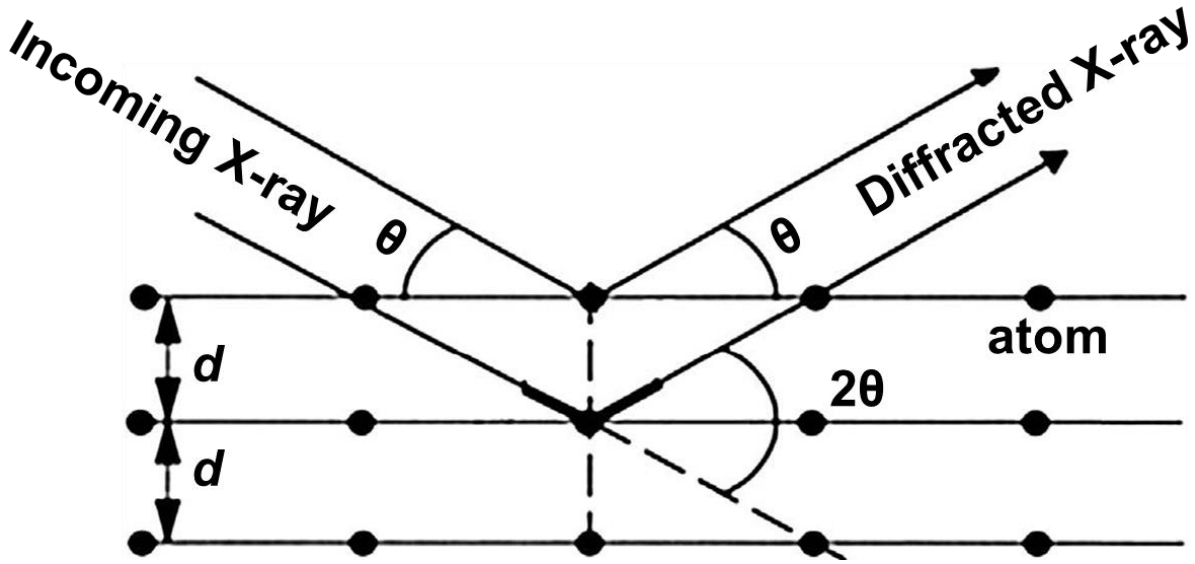

Figure 2-1 Geometrical schematic diagram for x-ray diffraction from lattice planes of crystal, modified from[7]

To be specific, for the XRD characterization for the aluminium containing solid acid material, the grinding fine powder samples were utilized to perform XRD experiment. The XRD pattern was recorded by a PANalytical XPert Pro powder diffractometer in the Bragg-Brentano geometry with CoKa radiation (k = 0.1789 nm, 40 kV, 40 mA). The wide-angle XRD patterns were collected in the range of 2θ = 10 to 70^{o}. The small-angle XRD patterns were collected in the range of 2θ = 1 to 5^{o}. The obtained XRD pattern for samples were compared to Joint Committee on Powder Diffraction Standards (JCPDS) on software of Jade 5.0.

2.3.2 N_2-adsorption/desorption

N_2-adsorption/desorption stands as a method to measuring the amount of N_2 gas absorbs on the surface of material. In our cases, the nitrogen adsorption/desorption isotherm curves for solid acid were obtained on a Autosorb iQ3 automated gas sorption analyzer. Chemisorption of N_2 gas was avoided by liquid nitrogen cooling (-196 ^{0}C).

To be specific, for the test of N_2-adsorption/desorption, the solid acid samples were firstly dehydrated and outgassed. Then the isotherm curve data was displayed in a plot of the amount of adsorbed nitrogen as a function of the relative pressure (P/P_0).

The Brunauer-Emmett-Teller (BET) method and the Barrett Joyner Halenda (BJT) method was applied to measure and evaluate the surface area, pore volume and pore size distribution of solid acid samples.

2.3.3 Transmission Electron Microscopy

Transmission electron microscopy (**Figure 2-2**) is an advanced technique to image solid acid samples in the micro-level. On a very thin and flat solid acid sample, the accelerated and concentrated electron beam can be focused. Then, the electrons within the incoming beam will collide with the exist atoms in the thin sample, and the direction of the beam will be changed after the collision. Therefore, the nonzero solid angle scattering will appear.

Because the brightness and darkness of the image is dependent on the scattering angle, which is correspondent to the density and thickness of the specific sample, the observed image with different grayscale represent the micro-level structure of the sample.

To be specific, to obtain the solid acid catalyst TEM image, the JEOL 2100 TEM was utilized. It was operated at a voltage of 100 kV to obtain the detailed micro-level structure of the samples. To obtain electron energy loss spectroscopy mapping information, Themis Z equipped with double spherical aberration corrector and monochromator have been utilized on a JEOL-2200FS TEM system. The high tension of the instrument was 300 kV. Gatan® electromagnetic prims was applied to generate the EELS spectra. Additionally, for elemental mapping of the solid acid materials, high angle annular dark-field (HAADF) scanning transmission electron microscopy (STEM) images were acquired. The distribution of different elements was understanded by a FEI Themis Z TEM equipped with double spherical aberration correctors which worked at 300 kV[274].

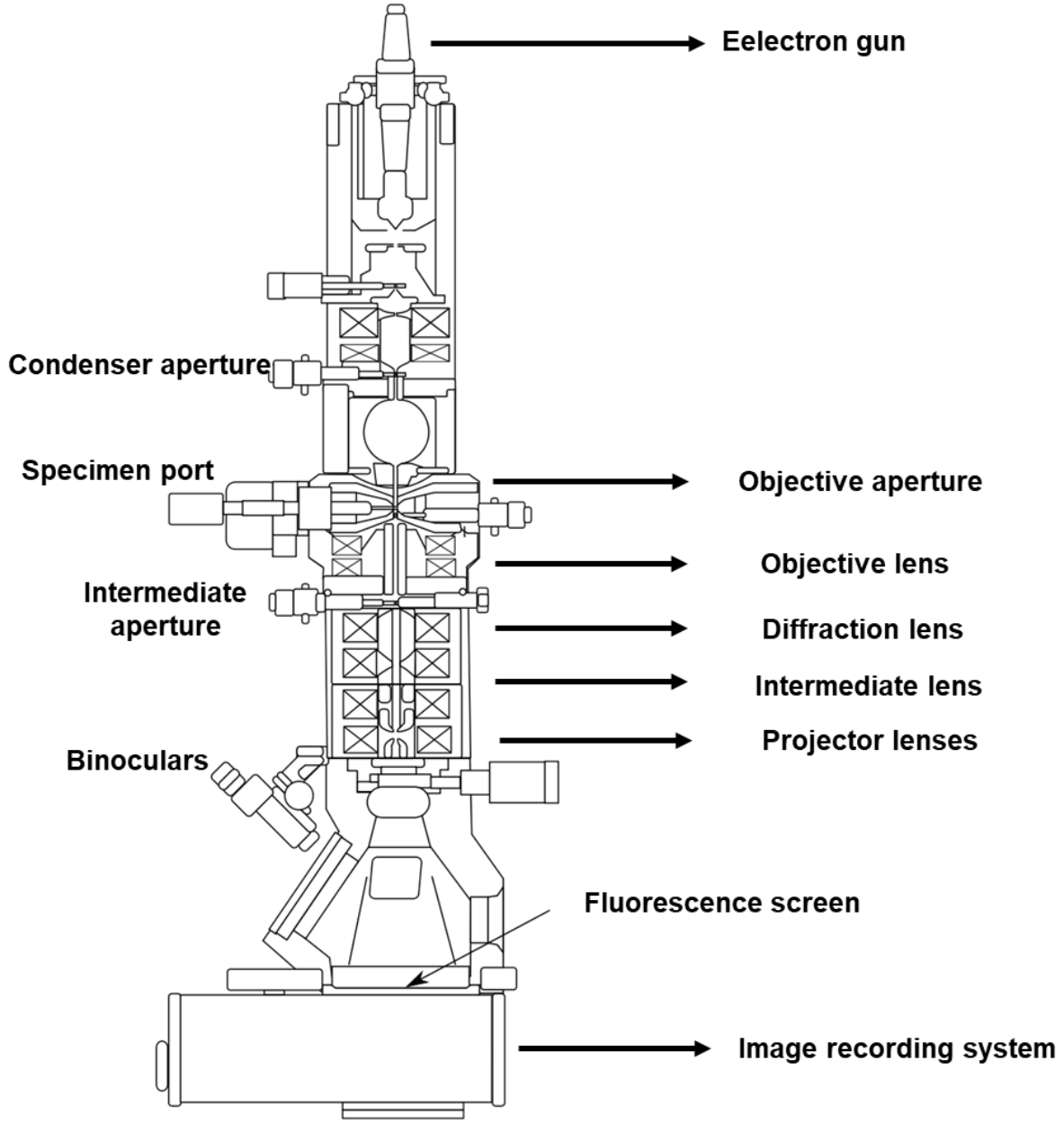

Figure 2-2 The schematic diagram of basic optical components of a Transmission Electron Microscopy, modified from[275]

2.4 Chemical properties characterizations

2.4.1 X-ray photoelectron spectroscopy

X-ray photoelectron spectroscopy is a well-known technique for understanding the surface chemistry of material in micro-level. It can not only be utilized for elemental composition analysis, but also a good method to understand the chemical and electronic state of the elements.

In brief, the basic physics for XPS is based on the understanding of photoelectric effect equation

$$E_{binding} = E_{photon} - (E_{kinetic} + \Phi) \quad \textbf{(Equation 2-2)}$$

where $E_{binding}$ represents the specific binding energy corresponding to the chemical potential of electron on the surface of measured solid sample, E_{photon} represents the applied X-ray photon energy, and $E_{kinetic}$ and Φ are measured electron energy by instrument and work function term, respectively. Thus, based on the known applied X-ray photon energy (E_{photon}) and recorded electron energy of a specific surface ($E_{kinetic}$), the intensity information relative to binding energy can be obtained. And **Figure 2-3** demonstrated the basic components of a XPS system.

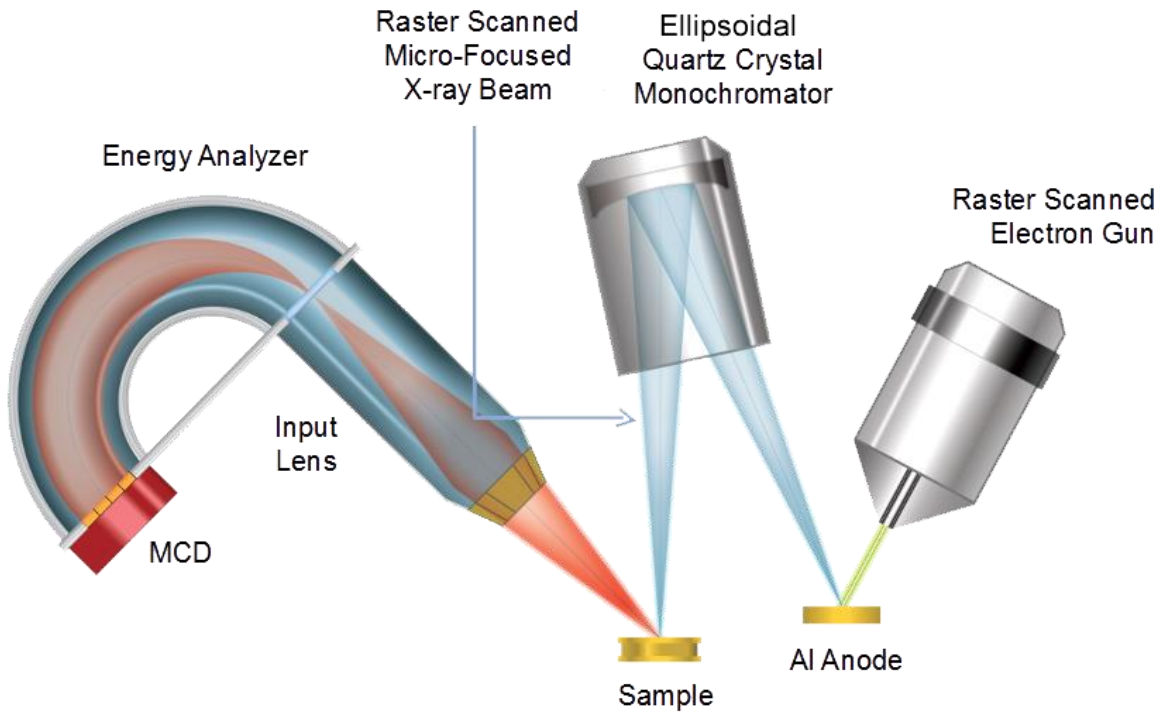

Figure 2-3 Basic components of a XPS system[276]

To be specific, to obtaining the surface information of solid acid materials have utilized in this thesis, the XPS measurements were conducted on a Thermo Fisher ESCALAB 250Xi spectrometer, and the focus source for XPS was monochromatic Al Kα-rays (1486.6 eV).

2.4.2 Diffuse reflectance infrared Fourier transform spectroscopy

Diffuse reflectance infrared Fourier transform spectroscopy (DRIFTS) was used to understand the surface local structure of solid acid samples and the in situ DRIFTS was applied to understand reaction mechanisms of 1,2 PDO conversion to propanal.

The DRIFTS measures the reflection and following diffusely scattering of the incident light from the rough surface of solid. To be specific, to measure the rough surface of solid acid samples, the experiments were conduct on room temperature (297 K). The utilized instrument was EQUINOX 55 spectrometer (Bruker Optics) equipped with a HgCdTe detector which

requires a liquid nitrogen cooling system. Before conducting the characterizations, the catalysts were dehydrated at 300 ^{o}C in a plug-flow DRIFTS cell under the flow of N_2 (20 ml/min). The DRIFTS spectra were collected by obtaining 256 scans for each sample, and the *in situ* DRIFTS spectra were collected by averaging 64 scans at 4 cm^{-1} resolution.

2.4.3 Solution state Nuclear Magnetic Resonance Spectroscopy

Solution state NMR studies the molecular information by recording the resonance between the observing nuclei of molecules and the introduced radiofrequency electromagnetic radiations. In this thesis, the *in situ* solution state NMR was utilized to understand the reaction mechanism of bio-phenylglyoxal to ethyl mandelate. To be specific, the in-situ solution-state NMR experiments were conducted on a Bruker Avance III 500WB spectrometer. In NMR tube, 0.6 mL of d4-Methanol (anhydrous, >99.5 atom% D, Sigma-Alrich), 6 mg of PG was dissolved and then 2 mg dehydrated solid acid catalyst sample was added. A slow temperature ramping process of 5 K per 15 min, from 273 K to 323 K have been applied for the recording of the in-situ NMR signal. At each temperature, ^{1}H NMR spectra were collected by obtaining 128 scans with p/2 pulse.

2.5 Solid state Nuclear Magnetic Resonance Spectroscopy

In recent years, the development of ssNMR methodology is fast. Much published research have shown the power of ssNMR on determining the local structure, dynamics, and surface interactions of materials[277]. Compared to well-developed methods such as XRD and TEM which could only be applied for the investigation on materials with long-term order crystalline structure, the ssNMR is advantageous on studying the structure of amorphous materials. In this thesis, we mainly applied ssNMR for understanding the surface active centres of amorphous aluminium containing solid acid.

2.5.1 One-dimensional single pulse magic angle spinning NMR spectroscopy without probe molecule

All magic angle spinning magnetic resonance spectroscopy (MASNMR) investigation were conducted on a Bruker Avance III 400WB or 500WB spectrometer. For dehydrated sample characterization, all sample were dehydrated at 300^{o}C overnight under a pressure of less than 10^{-2} mbar. After dehydration, the sample were transferred into the MASNMR rotor inside a N_2 glovebox.

By giving a strong excitation single pulse, the MASNMR spectra can be obtained by recording the Free induction decay (FID) information (**Figure 2-4**). Herein, the MASNMR measurements for ^{1}H, ^{27}Al, and ^{29}Si on 500WB spectrometer were carried out at a resonance

frequency of 500.1 MHz, 130.3 MHz, and 99.4 MHz respectively. For one-dimensional ^{1}H and ^{27}Al MASNMR measurements, spinning rate of 12 kHz was applied with 4 mm MAS rotor. For one-dimensional ^{29}Si MASNMR measurements, spinning rate of 25 kHz was applied with 2.5 mm MAS rotor. Spectra were recorded after single pulse p/2, p/6, and p/2 excitation with repetition times of 20, 0.5, 20 s for investigation of ^{1}H, ^{27}Al, and ^{29}Si nuclei, respectively.

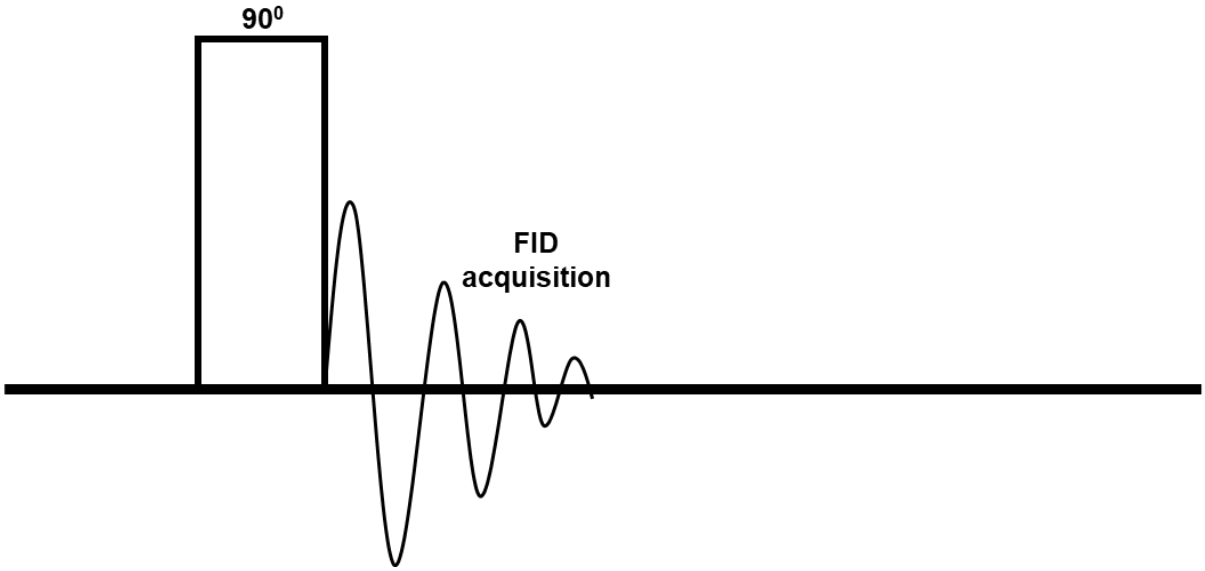

Figure 2-4 Typical p/2 single pulse MASNMR sequence

The ^{1}H, ^{11}B and ^{27}Al single pulse MASNMR measurements on 400WB spectrometer were carried out at a resonance frequency of 400.1 MHz, 104.3 MHz, and 128.4 MHz with spinning rate of 12 kHz and 4 mm MAS rotor. Spectra were recorded after single pulse p/2, p/6, and p/2 excitation with repetition times of 20, 0.5, and 3 s.

2.5.2 One-dimensional single pulse magic angle spinning NMR spectroscopy with Probe molecule

To evaluate the acidity of the material, probe molecule is usually required to identify the surface acid site. In this case, low concentration of trimethylphosphine oxide (TMPO) (5% w/w) probe molecule or NH_3 gas were added/absorbed to the dehydrated sample. Before addition of probe molecule, all sample were dehydrated at 300^{o}C overnight under a pressure of less than 10^{-2} mbar.

For TMPO probe molecule loading, the sealed mixture was heated to 160 ^{o}C to eliminate the physical absorbed TMPO molecule. After weighting the samples, they are transferred into MASNMR 4 mm rotor inside the N_2 glovebox. The ^{31}P MASNMR measurements for TMPO loaded solid acid material were conducted on 500WB spectrometer, where a resonance

frequency of 202.5 MHz has been utilized. With spinning rate of 12 kHz, repetition time of 5 s and scan number of 4000, ^{31}P MASNMR spectra can be obtained.

For NH_3 probe molecule loading, the solid acid material was put into a sample tube system. After eliminating the air in the tube system by N_2 gas, the ammonia should be introduced into the tube system. During the NH_3 adsorption, the mixture was warmed up by hair dryer/hand for 10 mins. Then, the vacuum pump will be opened in order to remove gases in the tube system. To fully eliminate the physically absorbed ammonia, a 2 h heating at 150 ^{o}C was performed. Finally, the mixture in the vacuumed tube system was transferred into a 4 mm NMR rotor in the N_2 glovebox.

2.5.3 One-dimensional TRAnsfer of Population in DOuble Resonance NMR spectroscopy

The TRAnsfer of Population in DOuble Resonance (TRAPDOR) pulse sequences have been applied to understand the spatial interaction between half-integer quadrupole spin of nuclei X and spin of ^{1}H. As shown in **Figure 2-5**, without REDOR pulse, all proton signals can be observed in the ^{1}H spectra; while after the application of ^{27}Al dephasing pulse of P_1 with irradiation period of t_1, the adjacent ^{1}H-^{27}Al pair dephasing, which suppress the peak intensity of the specific proton. Thus, via the subtraction of the ^{27}Al dephasing pulse ^{1}H spectrum from ^{1}H spectrum obtained without REDOR pulse, the information regarding the ^{1}H and ^{27}Al with proximity can be obtained (difference spectra = S_0-S)[278].

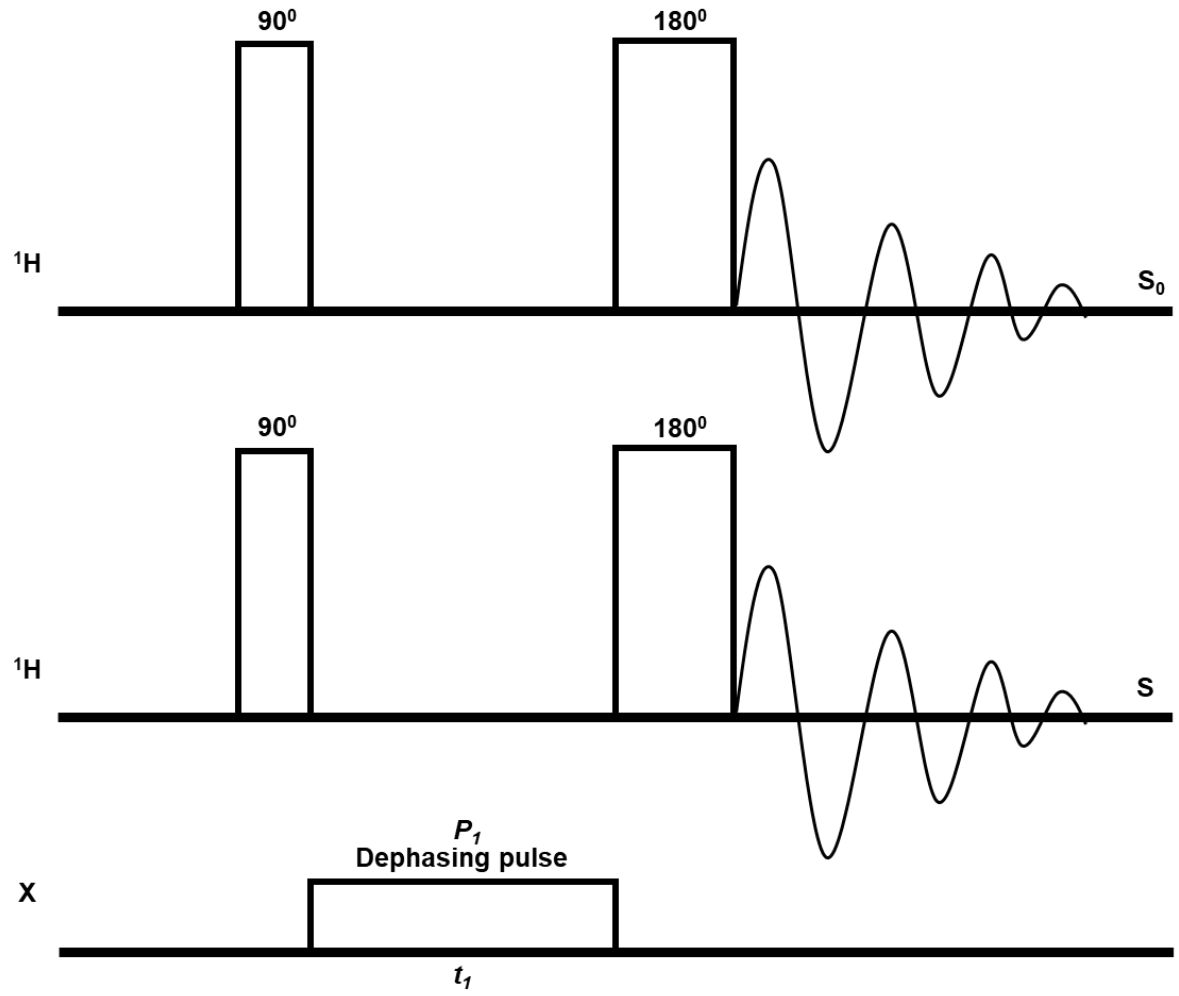

Figure 2-5 TRAnsfer of Population in DOuble Resonance pulse sequences

Here, the 1H/27Al TRAPDOR NMR spectroscopy was measured to understand the spatial relationship between hydroxyl proton and Al species. As an NMR technique, the TRAPDOR sequence can be utilized to ascertain spatial information such as proximity, connectivity, and interaction via facilitating the recoupling of the heteronuclear dipole coupling between ^{27}Al quadrupole and ^{1}H nuclei. The dephasing pulse utilized was 50W ^{27}Al dephasing pulse with 160 μs irradiation period.

2.5.4 Two-dimensional multiple quantum magic angle spinning NMR spectroscopy

The two-dimensional ^{11}B and ^{27}Al multiple quantum MASNMR spectra (MQ MASNMR) was utilized to distinguish the different species in the solid acid samples. The typical MQ MASNMR sequence is shown in **Figure 2-6**. With MAS and echo sequence, both first order and second order quadrupolar interaction can be supressed and the residual signal width of the central transition of quadrupolar nuclei such as ^{11}B and ^{27}Al can be eliminated. In **Figure 2-6**, the excitation pulse should be a strong pulse, and the t_1 represents the multiple quantum

evolution time, after a weak pulse, the so-called conversion pulse, the multiple quantum transition can be transferred into single quantum transition, and the t_2 is the signal recording time[279].

In this work, MQ MASNMR spectra were recorded at the same spectrometer using a three-pulse z-filter pulse sequency with pulse lengths of 3.0, 1.25, and 12 s, and 3.8, 1.4, and 25 s, respectively. The repetition time for the experiment was 200 ms and the sample spinning rate was 15 kHz.

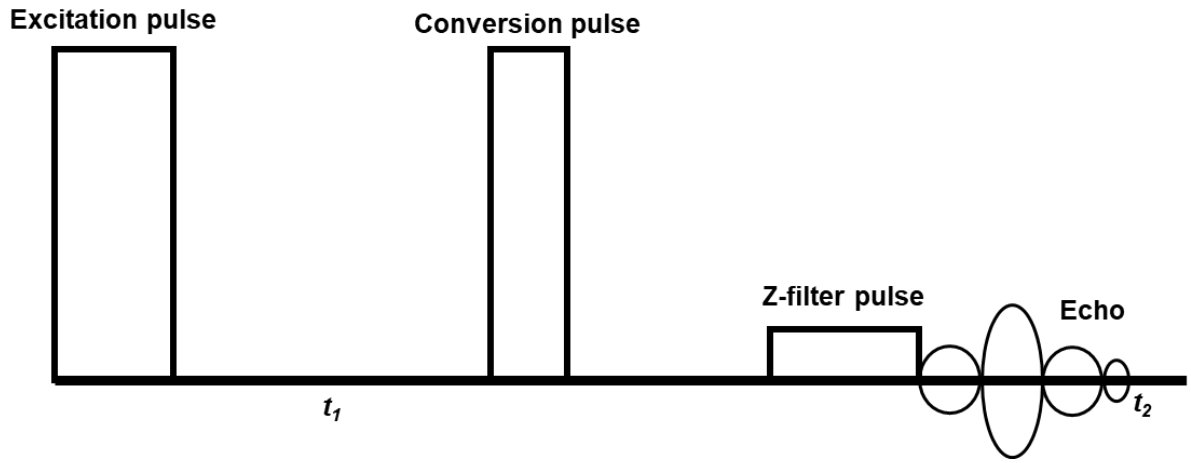

Figure 2-6 Typical multiple quantum MASNMR sequence

The obtained single pulse 11B and 27Al MAS NMR spectra were decomposed by the tool of Dmfit[280]. For dehydrated sample, with largely distorted local structure, quadrupolar MAS model (Q MAS) has been applied for the best fit. While for fully hydrated samples, due to the presence of large amount of hydrogen bonds from hydration, a large increase in the structure symmetry is envisioned. Thus, Gaussian/Lorentzian model (Gaus/Lor) has been applied for simulation. Parameters for decomposition of dehydrated sample spectra were obtained based on the 2D MQMAS NMR spectra. Parameters were calculated as following[281]:

$$SOQE^2 = \frac{\delta_{iso} - \delta_{F_2}}{k} \quad \textbf{(Equation 2-3)}$$

$$\delta_{iso} = \frac{17}{27}\delta_{F_1} + \frac{10}{27}\delta_{F_2} \quad \textbf{(Equation 2-4)}$$

$$k = \frac{3}{10}\frac{4I(I+1)-3}{[4I(2I-1)\nu_o]^2} \times 10^6 \quad \textbf{(Equation 2-5)}$$

$$SOQE = C_{QCC}\sqrt{1 + (\eta^2/3)} \quad \textbf{(Equation 2-6)}$$

In which, δ_{iso} represent the isotropic chemical shift, SOQE stand as the second order quadrupolar effect parameter, δ_{F1} and δ_{F2} are the centres of gravity of the MQMAS signal in

the F1 and F2 dimension. CQCC is the quadrupolar coupling constant, g is the asymmetry parameter, and B represent the magnetic field. Specifically, in this work, the I and Vo, the spin and Larmor frequency, was 5/2 and 104.3 MHz for ^{27}Al MQMAS NMR, and 3/2 and 128.4 MHz for ^{11}B MQMAS NMR, respectively.

2.5.5 Two dimensional Dipolar Heteronuclear Correlation NMR spectroscopy

Heteronuclear correlation MASNMR using cross-polarization sequence (2D CP/MAS HETCOR) can be applied to reveal spatial relationship between multiple species. The **Figure 2-7** showed the typical heteronuclear correlation sequence for MASNMR. After the first strong p/2 pulse on ^{1}H nuclei for evolution, the t_1 represent the ^{1}H nuclei and X nuclei contact time. After mixing the excitation, another strong p/2 pulse should be applied to X nuclei on the observation channel. During the heteronuclear decoupling process, the FID acquisition should be conducted in order to obtain readable spectra information. In the spectra, the strong contour of (δ_1, δ_2) observed in the HETCOR NMR spectra indicates the spatial proximity between species 1 of nuclei A along *F1* direction and species 2 of nuclei B along *F2* direction.

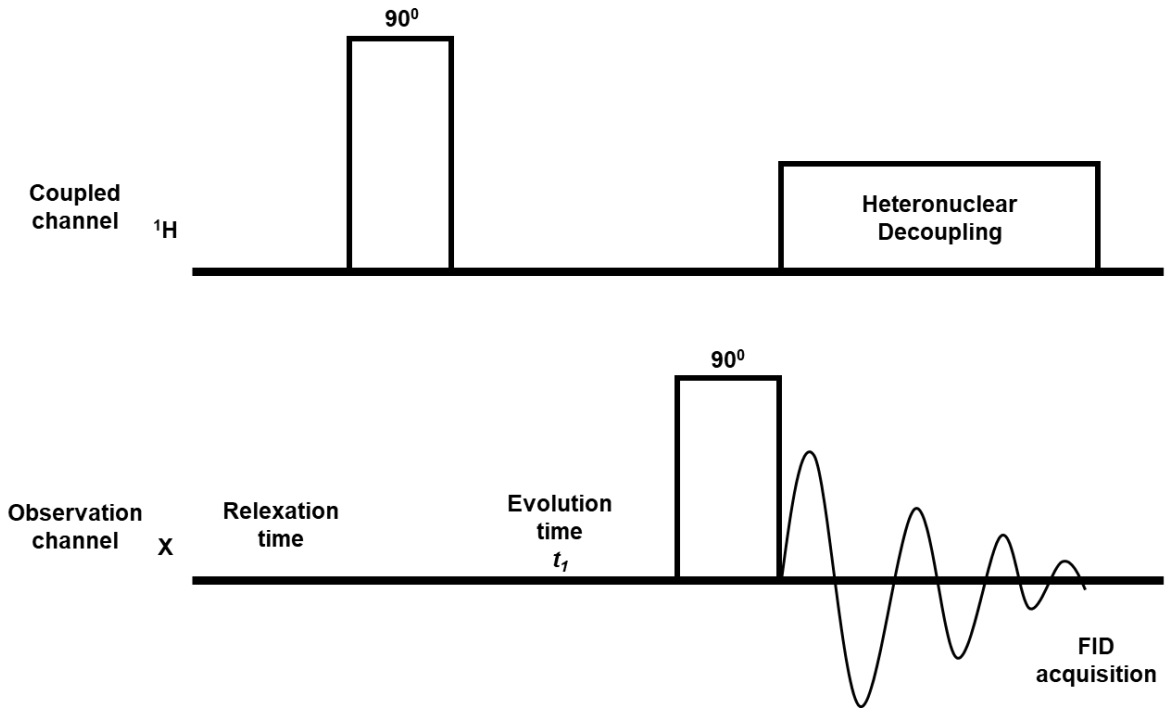

Figure 2-7 Typical heteronuclear correlation NMR sequence

In this thesis, the HETCOR NMR experiments all conducted on a 500WB spectrometer. The spatial correlation between ^{1}H and ^{27}Al have been characterized with a heteronuclear correlation (HETCOR) sequence, where sample were sealed in a 2.5 mm MASNMR rotor and 0.5 ms and 1 ms contact time with spin rate of 25 kHz has been used. Each slice in both 2D

spectra resulted from the accumulation of 2500 scans with recycle delays of 1 s, and in total 16 slices have been applied for the establishment of 2D HETCOR NMR spectra.

2.6 Catalytic biomass conversions

2.6.1 Catalytic conversion of bio-phenylglyoxal to ethyl mandelate

Catalytic studies of bio-phenylglyoxal to ethyl mandelate conversion were applied as a model reaction to test the catalytic performance of the B/m-Al2O3 catalysts mentioned in Chapter 3. Prior the reaction, 50 mg catalyst should be dehydrated and activated at 300 °C overnight under a N_2 flow. After the catalyst cooled in N_2, 1.25 mL of alcohol solution containing 0.4 M PG was added to a glass vial with preactivated catalyst. The reaction was carried out in tightly closed glass vials with oil bath at 90 °C at moderate stirring for 4 h. The products were collected at a regular time interval under ice bath and dissolved in ethanol for further GC evaluation. The reaction mixture was analyzed using a Shimadzu GCMS-QP2010 Ultra with an Rtx- 5MS column (30 m x 0.25 mm x 0.25 m) and quantified by a Shimadzu GC-FID equipped with a 25QC3/BP1 column (25 m x 0.32 mm x 5 m). The selectivity S to EM was calculated as SEM (%) = 100 x (EM)/[(PG)inital – (PG)final], all the abbreviation corresponds to the molar concentration of EM and PG, respectively. The catalysts were recycled by collecting the catalysts after experiment via centrifugation. The collected catalysts were washed three times by ethanol, followed by dehydration at 300 °C overnight under N_2 flow. With the recycled catalysts, the catalyst recycling PG conversion experiment were conduction at same conditions as above mentioned.

2.6.2 Catalytic cascade conversion of glucose to 5-hydroxymethylfurfural

Catalytic studies of cascade conversion of glucose to 5-hydroxymethylfurfural were applied as a model reaction to test the cascade catalytic performance of the Al_{ALD}@high silica substrate catalysts mentioned in Chapter 4. In a 25 mL glass pressure reactor, a biphasic system with volume ratio of V(deionized water)/V(dimethyl sulfoxide, DMSO, ⩾ 99.5%, Sigma-Aldrich) = 3/7 has been prepared as the solvent. Reactant 60 mg glucose (⩾ 99.5%, Sigma-Aldrich) or D-(−)-Fructose (⩾ 99%, Sigma-Aldrich) was then dissolved in the solvent and ready for further catalytic test. Prior to the reaction, the catalysts should be pretreated and activated at 673 K under nitrogen environment and then 20 mg catalyst has been transferred into the reactor for each run. At an oil both with temperature of 433 K, the reaction was conducted with vigorous magnetic stirring. To measure the catalytic performance of catalysts, samples of reaction mixture have been collected every 30 mins till reach 180 min (for glucose conversion) or every 15 mins till reach 90 mins (for fructose conversion). The collected samples were

diluted into deionized water and filtered by 0.22 μm syringe filter for further High-Performance Liquid Chromatography (HPLC) analysis. With mobile phase of filtered 0.005 M H_2SO_4 aqueous solution, the reactant and product were analyzed by an Agilent 1260 system equipped with a Biorad Aminex HPX-87H column (300 × 7.8 mm, 9 μm) and via a refractive index detector and a multiwavelength detector, respectively.

2.6.3 Catalytic conversion of biomass 1,2-Propanediol dehydration to propanal

Catalytic reaction of 1,2 propanediol conversion to propanal was applied to test the Brønsted acid site performance of the SiO_2@am-Al_2O_3 mentioned in Chapter 5. Prior the reaction, 50 mg catalyst shall be activated at 300 °C for 2 h under a N_2 flow. Then the temperature shall be decrease to 180^{o}C and the reactant shall be added after the stabilization of the temperature. The catalytic reaction was conducted with pure 1,2 propanediol or with 1,2 propanediol containing 10 or 20 wt% cofed steam, with carrier gas of H_2. The flow rate of the reactant was 0.6 mL/h, and a ice bath was set in order to collect liquid product. The reaction mixture was analysed using a Shimadzu GCMS-QP2010 Ultra with a SH-Rtx-Wax Capillary column. The selectivity of propanal to 1,2 PDO was calculated as S (%) = 100 X (propanal)/[$(1,2\ PDO)_{inital}$ − $(1,2\ PDO)_{final}$]. The recycled catalysts were washed by deionized water before reactivated at 300^{o}C. Identical reaction condition has been applied for the recycling 1,2 PDO conversion experiment.

3.Brønsted acid sites formation through penta-coordinated aluminum species on alumina-boria

3.1 Introduction

Solid acid catalysts, well known by its wide application in the transformation of hydrocarbons and bio-refining of biomass as well as the supports for nanocatalysts[282-286], have made contributions to industrial processes. On the surface of solid acids, Brønsted acid sites (BAS) and Lewis acid sites (LAS) can exist alone or co-exist for various reactions[287]. BAS is generally required for most of acid catalysis process involving hydrocarbon cations and hydrogen transformation[288-290]. The mixed oxides are one kind of popular solid acids, and their BAS is formed due to the varied electronegativity of framework heteroatoms[291]. The hydroxyl group links the host atom (X_1) and the isomorphously substitute atom (X_2), which lead to the formation of Brønsted acidic OH group with catalytic activity (X_1-OH-X_2)[292]. For instance, on zeolites or amorphous silica-alumina (ASA), surface Al can replace four-coordinated Si, the formed four-coordinated Al in crystal or amorphous SiO_2 framework can generate surface Brønsted acid sites by the establishment of bridging hydroxyl groups (Si-OH-Al^{IV}) on zeolites or the pseudo-bridging/flexible hydroxyl groups (Si-(OH) $\cdots Al^{IV}$) on ASA.

Unlike SiO_2, which contains only neutral silanol in the absence of a doped second oxide, alumina such as γ-Al_2O_3 itself contains electron deficient surface with unsaturated aluminium centers from either incomplete or terminal tetrahedral site (Al^{III} and Al^{IV}), contributing to the intrinsic Lewis acidity[293, 294]. As a solid acid contains mainly LAS, Al_2O_3 has been applied to drive many catalytic reactions including dehydration, ethanol etherification[295], and dehydrofluorination[296]. Additionally, similar to SiO_2, Al_2O_3 is an alternative platform for the development of BAS via doping a second oxide. With varied electronegativity between the hetero-species, BAS type hydroxyl groups between tetrahedral aluminium species (Al^{IV}) and unsaturated sites of doped species on interface can be formed. Examples can be found on this type of acids such as Al_2O_3-TiO_2[297], Al_2O_3- B_2O_3[298, 299], and Al_2O_3- ZrO_2[300].

It should be noted from the discussion above that framework Al^{IV} species is dominant in BAS formation on both SiO_2 based and Al_2O_3 based solid acids. While extra-framework incomplete tetrahedral or octahedral aluminium species on zeolites work as a strong LAS for the reactions or enhance the acidity of the nearby BAS via polarization[301, 302]. Beside above popular Al species, the penta-coordinated aluminium species (Al^V) was rarely observed. And it was

considered as the trace intermediate or transition state of saturated six-coordinated Al species during the phase transromation[303]. Recently, we applied flame spray pyrolysis (FSP) process to prepare Al^V dominant (over 48%) ASAs via precursor combustion, ultra-fast nucleation and quenching[304]. Since studies have shown that Al^V species on the surface could act not only as strong LAS to stabilize single-atom catalysts[305-307], but also form strong BAS that contribute to improved catalytic performance in many reactions[308-309]. It could be concluded that Al^V species aids for tailoring acid catalysts.

However, whether the generation of Al^V-BAS is a general principle for various synthesis methods and hetero-atoms as that for Al^{IV}-BAS is still an open question. It was reported that amorphous Al_2O_3 (m-Al_2O_3) prepared via wet-chemical synthesis contains high density of Al^V species[310], which is an ideal parent platform for Al^V-BAS generation with other atoms through available methods other than FSP-ASA. Herein, we incorporate boron (B) into Al^V species enriched mesoporous amorphous Al_2O_3 as the first example. Due to the lack of the crystallinity, the surface structure at an atomic level of such mixed oxide can hardly be characterized by the widely utilized approaches such as X-ray diffraction spectroscopy (XRD) and high-resolution transmission electron microscopy (HRTEM). In contrast, due to the ability to characterize local structure without long range order, solid-state nuclear magnetic resonance spectroscopy (ssNMR) has been used as a powerful and sensitive characterization tool to study the formation, structure, and acidity of amorphous solid acids[311-313] through various NMR pulse programs such as one-dimensional (1D) single pulse NMR[314-315], two-dimensional (2D) multiple-quantum magic-angle spinning NMR (2D MQMAS NMR) and heteronuclear correlation (HETCOR) MASNMR[316-318]. In particular, here, with the 2D ^{1}H-^{27}Al CP/MAS HETCOR NMR, the local structure of BAS has been probed, the formation and predominance of Al^V-BAS on alumina-boria has been revealed, which is the first experimental evidence to the best of our knowledge[314, 319, 320]. Furthermore, our *in-situ* NMR investigation and the test reaction confirmed the high activity of the Al^V-BAS on the surface and drove the bio-phenylglyoxal conversion with enhanced performance. This research is focused on Al^V-BAS with boria, but the principle of the research outcome can be applied to BAS formation within many other mixed oxide systems.

3.2 Results and Discussion

3.2.1 The Morphology of Catalyst

The morphology of the obtained catalysts has been characterized first. As shown in **Figure 3-1A**, the existence of ordered mesoporous structure has been observed for 0.05B/m-Al_2O_3 and

0.10B/m-Al_2O_3 by the low-angle XRD patterns. An intense peak at 0.82° and 0.80° can be identified and corresponding to 10.76 nm and 11.03 nm d-spacing, respectively. For 0.05B/m-Al_2O_3, another diffraction peak can also be observed at 1.42°, hinting a 2D hexagonal structure[321]. For 0.20B/m-Al_2O_3 catalysts, only one relatively poor-resolved peak can be observed at about 0.80° in the low-angle XRD pattern, indicating that the sample have low ordered mesopores. It suggests that the loading of boron content disturbs the long-range order of the Al_2O_3 mesopores. As demonstrated by wide-angle XRD patterns (**Figure 3-1B**), no observable crystalline boria or alumina phases could be detected, while only weak and board peaks can be seen for all samples, hinting the amorphous bulk structures for the prepared B/m-Al_2O_3 samples. The parent m-Al_2O_3 has no crystalline peak in XRD pattern (**Figure 3-2**). This confirmed the successfully preparation of amorphous structure of substrate via EISA method[322]. Thus, after addition of boron content, all observed board peaks should be assigned to boron related phases. The intensity of both two weak peaks range of about 22-28° and 40-45° enhances with the increase in boron concentration. Thus, the board peak at 22-28° and 40-45° can be assigned to the boria containing phases such as AlBO (PDF#45-0207) and A_2B ($2Al_2O_3•B_2O_3$) phase, respectively[321].

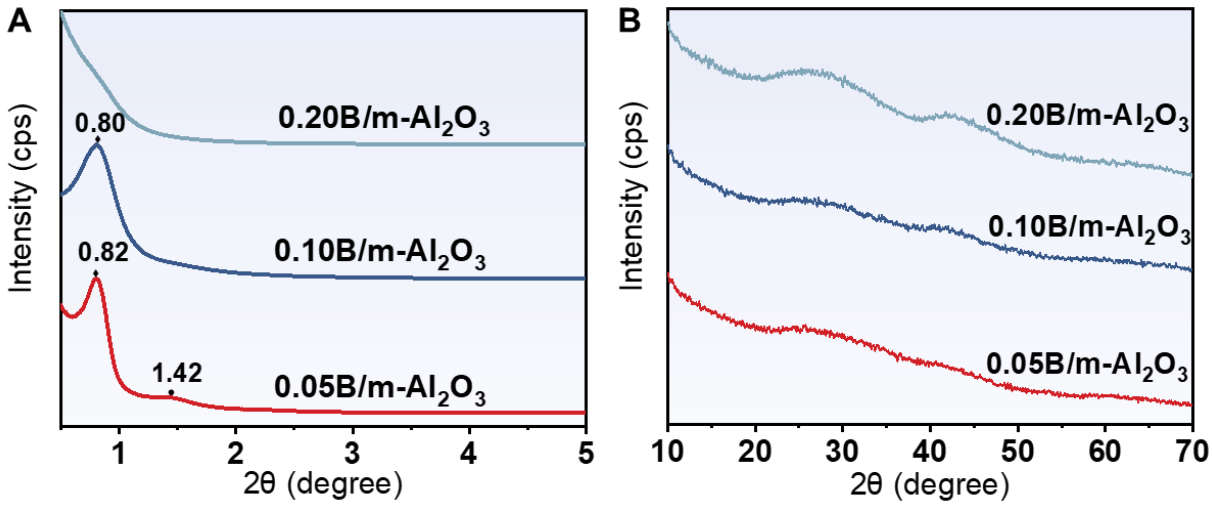

Figure 3-1 (A) Small-angle XRD patterns and (B) wide-angle XRD patterns of 0.05B/m-Al_2O_3, 0.10B/m-Al_2O_3, and 0.20B/m-Al_2O_3 samples.

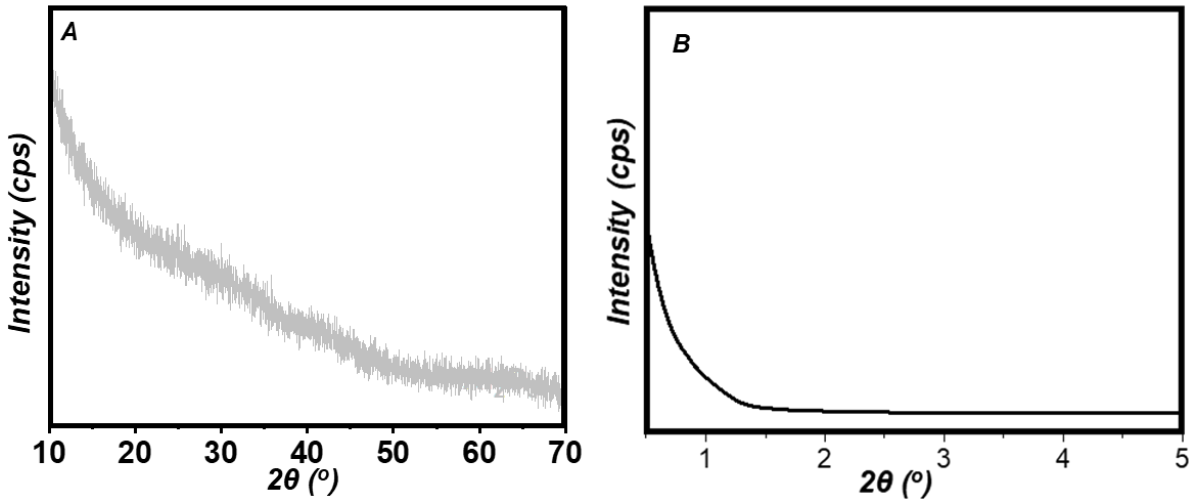

Figure 3-2 (A)wide-angle XRD patterns and (B) small-angle XRD patterns of parent m-Al_2O_3

Consistent with results obtained from small-angle XRD (**Figure 3-1** and **Figure 3-2**), the typical type IV isotherms in **Figure 3-3A** confirm the presence of mesoporous structure. 0.05B/m-Al_2O_3 shows a H2 type hysteresis loops, implies the presence of relatively uniform channel-like pores. While the H1 and H4 type hysteresis loops of 0.10B/m-Al_2O_3 and 0.20B/m-Al_2O_3 catalysts implies that they have cylindrical pore geometry and internal voids of irregular shape, respectively. Thus, in a good agreement with the low-angle XRD results, the change in the isotherms suggested that by varying the boron loading content, the textural properties can be disturbed. Additional, compared with parent m-Al_2O_3, with the addition of boron, a mesoporous structure has been established with pore size of ca. 9 nm (**Figure 3-3B**). Information regarding specific surface area, average pore diameter, and total pore volume are listed in **Table 3-1**. All B/m-Al_2O_3 samples showed much larger specific surface areas and pore volumes than that of amorphous Al_2O_3 prepared by the similar method. This could originate from the increase in the volume of mesopores constructed via boron addition (**Figure S1**).

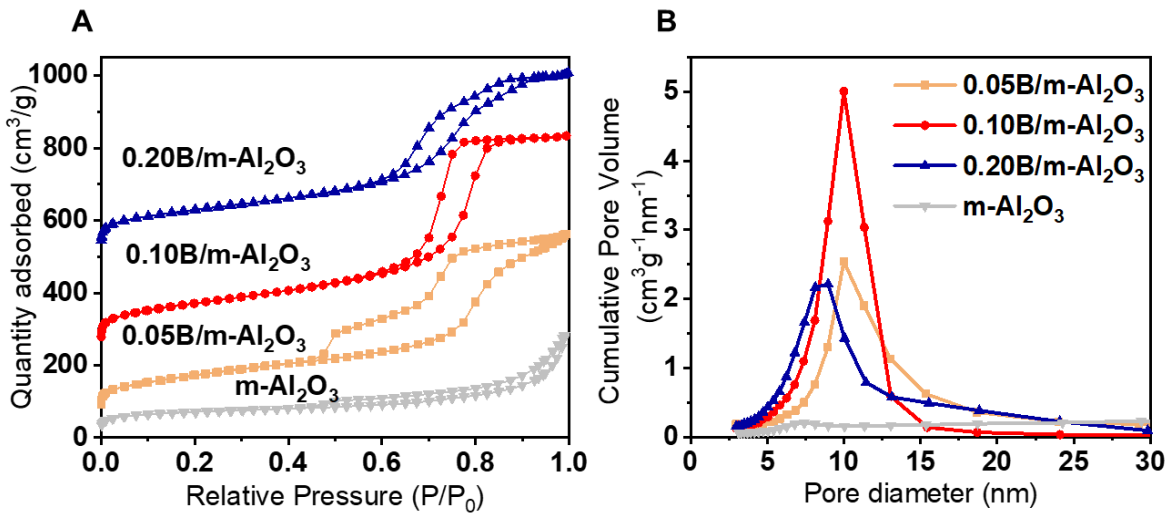

Figure 3-3 (A) N_2 adsorption/desorption isotherms, and (B) BJH pore size distribution calculation of B/m-Al_2O_3 catalyst with various boria loading, the pore size was determined from the adsorption branch.

Transmission electron microscope (TEM) is applied to further confirm the morphology of the B/m-Al_2O_3 catalysts (**Figures 3-5**). Agreed well with the XRD patterns (**Figure 3-1**), no crystalline phase can be identified for all catalysts. The TEM image of the 0.05B/m-Al_2O_3 catalyst shows a regular structural ordering with uniform channel-like pores. Increasing boron loading amount, the amorphous nature with higher disorder could be observed in 0.20B/m-Al_2O_3. Agreed well with the small angle XRD patterns and BJH pore size distributions (**Figure 3-1** to **3-3**), the TEM images also showed that the addition of boron contribute to the mesoporous structure of B/m-Al_2O_3 (**Figure 3-4** and **Figure 3-5**). Calculated from the TEM images, the pore-center correlation distances of the ordered mesopores were 10.4 nm for B/m-Al_2O_3 solid acids. This is in line with the average pore size determined by BJH method and the calculated d-spacing based on the small-angle XRD results (**Table 3-1**). In addition, the EDS-Mapping images indicate that the boron species were well distributed through the m-Al_2O_3 network with no obvious aggregation of aluminum or boron species.

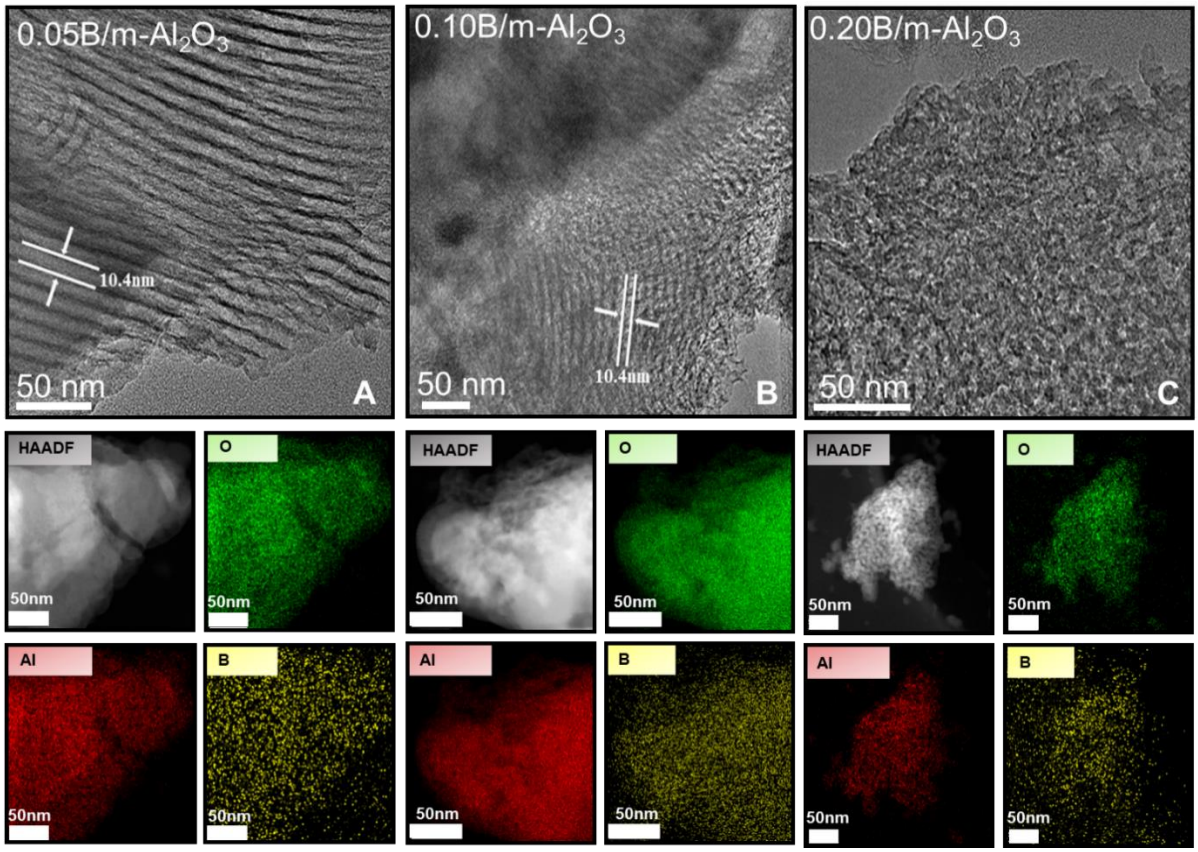

Figure 3-4 TEM image and SEM-EDS elemental mapping images of (A) 0.05B/m-Al_2O_3, (B) 0.10B/m-Al_2O_3, and (C) 0.20B/m-Al_2O_3

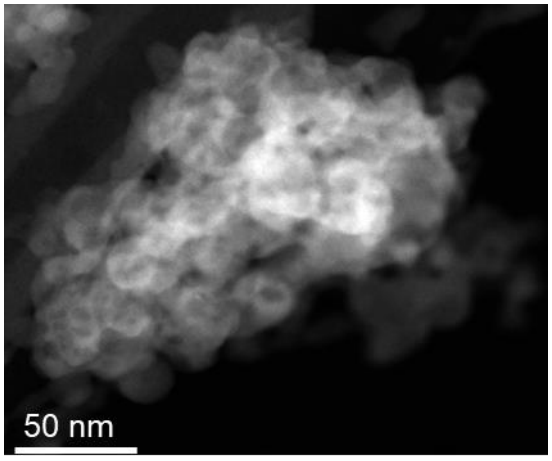

Figure 3-5 TEM image of parent m-Al_2O_3

Table 3-1 Summary of surface area, average pore size, distribution of Brønsted acid sites and Lewis acid sites, and catalytic data of PG conversion to EM over the Alumina-boria catalysts. [a]

Catalysts	Boron[b] (%)	SA[c] (m^2/g)	V_{pore}[c] (cm^3/g)	d_{BJH}[c] (nm)	BAS[d] (μmol/g)	LAS[d] (μmol/g)	LAS /BAS	C_{PG}[e] (%)	S_{EM}[f] (%)	TOF[g] (h^{-1})
m-Al_2O_3	-	233.1	0.44	-	-	26.7	-	52.9 (33.3)	65.7 (65.1)	1.88
0.05B/m-Al_2O_3	5.7	408.2	0.78	10.0	21.7	21.1	0.97	96.6 (77.8)	98.9 (98.5)	8.97
0.10B/m-Al_2O_3	10.0	435.0	0.90	10.0	25.5	29.9	1.17	99.4 (94.8)	99.6 (99.6)	11.36
0.20B/m-Al_2O_3	19.2	451.0	0.79	9.0	25.8	35.5	1.45	98.3 (87.1)	99.4 (99.4)	10.07
deAl-HY[43]	-	671.0	0.39	1.1	Total 1750		0.49	90.0	90.0	0.56

[a]Conversion of PG (0.4M) in ethanol (1.25 mL) using 50 mg catalyst at 90°C for 4 h in a sealed batch reactor. [b]The composition ratio was calculated based on the result of inductively coupled plasma - optical emission spectrometry (ICP-OES). [c]The specific surface area (SA), volume of pores (V_{pore}), and pore diameter (d_{BJH}) of alumina-boria were determined from the adsorption of the N_2 isotherms and corresponding BJH calculation. [d]Total density of acid sites were calculated based on the results of NH_3-TPD, the density of Brønsted acid sites (BAS), and density of Lewis acid sites (LAS) were determined based on the NH_3-TPD and simulation of ^{31}P MAS NMR spectra. [e]C_{PG}= conversion of PG. [f]S_{EM}= selectivity of EM. (the catalytic performances after 2 h reaction are given in parentheses). [g] Turnover frequency (TOF) calculated based on the PG conversion at 60°C with conversion of less than 10%.

3.2.2 Local Structure and Formation of Brønsted Acid Sites

As a powerful tool to investigate the detailed local structure, ssNMR is applied to identify various Al and B species and their coordination behavior for the formation of BAS on B/m-Al_2O_3. As shown in **Figure 3-6**, the ^{27}Al MASNMR spectra of fully hydrated B/m-Al_2O_3 catalysts consist of three well-resolved peaks. The main peaks appeared at around δ_{27Al} = 2 ~ 3 ppm is assigned to the octahedral aluminum spices (Al^{VI}). While the peaks at around δ_{27Al} ~ 33 ppm and δ_{27Al} ~ 64 ppm is assigned to penta-coordinated Al (Al^{V}) and tetra-coordinated Al (Al^{IV}), respectively[314-315]. In one-dimensional ^{11}B ssNMR (**Figure 3-7**), two different boron species are identified for all samples. They are assigned to trigonal boron species (B^{III}, δ_{11B} = ca. 17 ppm) and tetrahedral boron species (B^{IV}, δ_{11B} = ca. 0 ppm), respectively. With more boron atoms incorporated into the alumina network, the main peak of Al^{VI} species shift from 2.0 ppm (for m-Al_2O_3) to lower field with the increase in loading of boron species (2.4, 2.8, 2.9 ppm for 0.05B/m-Al_2O_3, 0.10B/m-Al_2O_3, and 0.20B/m-Al_2O_3, respectively). Attributed to the greater electronegativity of boron species, electron cloud density aluminum species with proximity have been attracted toward boron center, thereby giving a de-shield effect to aluminum species and result in a downfield chemical shift. This observation indicates the Al_2O_3 network penetration ability of boron species.

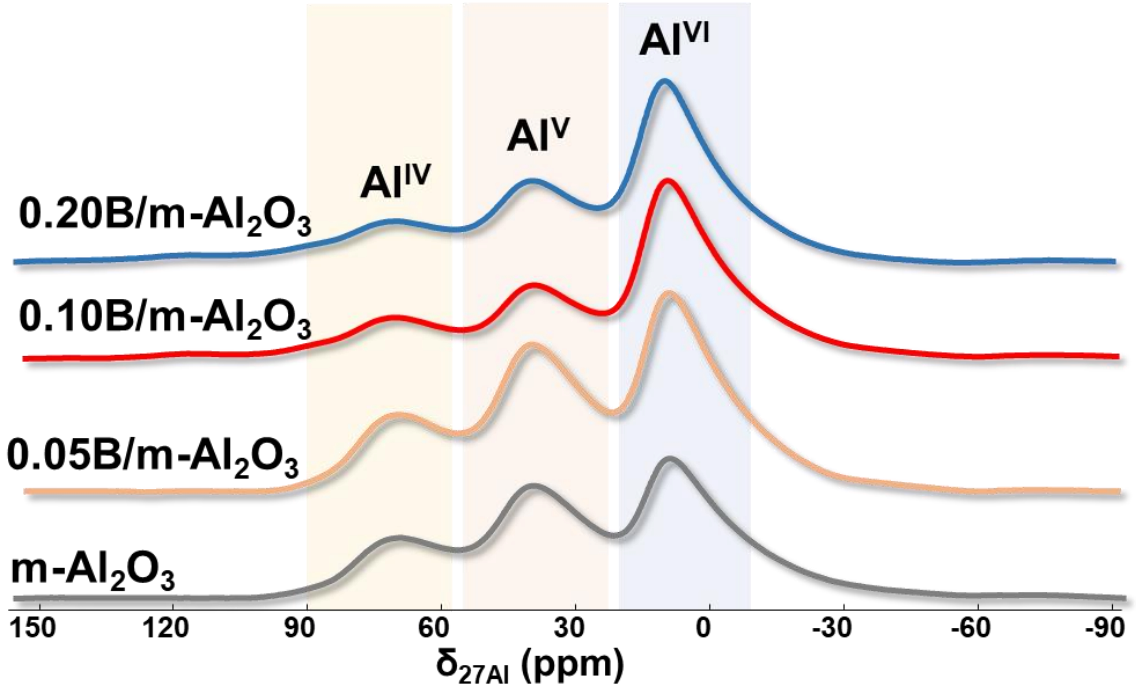

Figure 3-6 Local structural characterization of fully hydrated alumina-boria samples via ^{27}Al ssNMR spectra

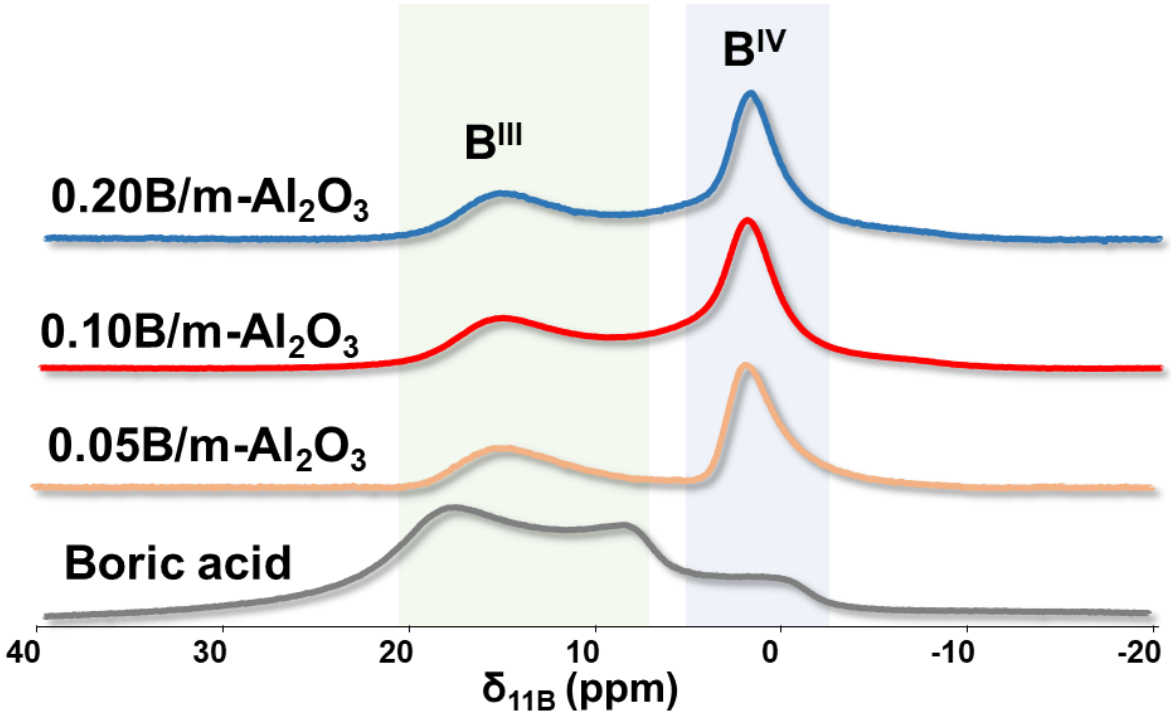

Figure 3-7 Local structural characterization of fully hydrated alumina-boria samples via ^{11}B ssNMR spectra

Table 3-2 The chemical shift of main peak, Al^{VI}, of hydrated B/m-Al_2O_3 catalysts.

	Al^{VI} (ppm)
m-Al_2O_3	2.0
0.05B/m-Al_2O_3	2.4
0.10B/m-Al_2O_3	2.8
0.20B/m-Al_2O_3	2.9

Table 3-3 Summary of deconvolution results and DMFit calculated aluminum and boron species ratio of the fully hydrated catalysts.

	Al^{IV} (%)	Al^{V} (%)	Al^{VI} (%)	B^{III} (%)	B^{IV} (%)
m-Al_2O_3	20.6	31.6	47.9	-	-
0.05B/m-Al_2O_3	17.0	44.7	38.4	43.1	56.9
0.10B/m-Al_2O_3	17.4	20.5	62.1	38.7	61.3
0.20B/m-Al_2O_3	17.3	16.1	66.6	35.6	64.4

To obtain detailed species information and to better understand the formation of surface acid sites, the MQMAS NMR has been applied, which avoids the second-order quadrupolar

broadening of Al and B species in spectrum and achieves acceptable ssNMR resolution[325]. Since only accessible surface sites are considered to be catalytically functional, the hydration process of samples has been applied to identify surface Al and B species by observing their transformation from surface unsaturated Al and B species to the saturated ones. Therefore, by comparing the hydrated (hy-) ^{27}Al and ^{11}B MASNMR spectra with the dehydrated ones (de-) (**Figures 3-6** to **3-9** and **Table 3-3** and **Table 3-5)**, the large number of transferred unsaturated Al and B species to saturated Al^{VI} and B^{IV} on B/m-Al_2O_3 after hydration suggests the presence of large quantity of unsaturated species on the surface[322] (de-Al^{VI}/hy-Al^{VI} = 16.2%/38.4%, 24.5%/62.1%, 33.6%/66.6% and de-B^{IV}/hy-B^{IV} = 31.3%/56.9%, 36.7%/61.3%, 39.2%/64.4% for 0.05B/m-Al_2O_3, 0.10B/m-Al_2O_3, and 0.20B/m-Al_2O_3, respectively). Especially, among the unsaturated species, the large decrease in the Al^V species of hydrated sample suggests that there is a large amount of Al^V species are located on surface and accessible to guest molecules. From ^{27}Al MQMAS NMR spectra (**Figure 3-8A-C**), Al contour regions for tetrahedral (Al^{IV}), pentahedral (Al^V), and octahedral (Al^{VI}) can be observed for all samples. The five different Al species can be identified via the identification of contour centers on the dehydrated B/m-Al_2O_3. Due to the presence of second order quadrupolar interaction[326, 327]. These species have been assigned to tetrahedral Al^{IV}a (δ_{iso}= *ca.* 77 ppm) and Al^{IV}b (δ_{iso} = *ca.* 67 ppm), pentahedral Al^Va (δ_{iso} = *ca.* 41 ppm) and Al^Vb (δ_{iso} = *ca.* 33 ppm), and octahedral Al^{IV} (δ_{iso} = *ca.* 9 ppm) (**Figure 3-8**). Quadrupolar parameters such as quadrupole coupling constant (C_{QCC}) and asymmetry parameters (η) have been summarized in **Table 3-4**, and which have been utilized for the decomposition of corresponding 1D ssNMR spectra with quadrupolar MAS model in DMFit (**Figure 3-8D-F**). The dominance of strong contours of Al^V species aids and abets the prerequisite for the formation potential five-coordinated aluminum-based BAS. The rapid reduce in Al^{IV} contours intensity and the large increase in the contours intensity of saturated Al^{VI} on the 0.20B/m-Al_2O_3 sample compared to other two samples can be explained by the decreases in the final PH of synthesis due to the addition of extra boron source, boric acid[328], which give rise to the presence of extra $Al(H_2O)_6^{3+}$ [48]. This is in agreement with reported studies by Skibsted et al[329], in ^{27}Al 2D MQMAS NMR spectra, the Al^{IV} resonance observed on alumina-boria is much weaker compared to pure alumina synthesized by the same method without the addition of an acidic boron source.

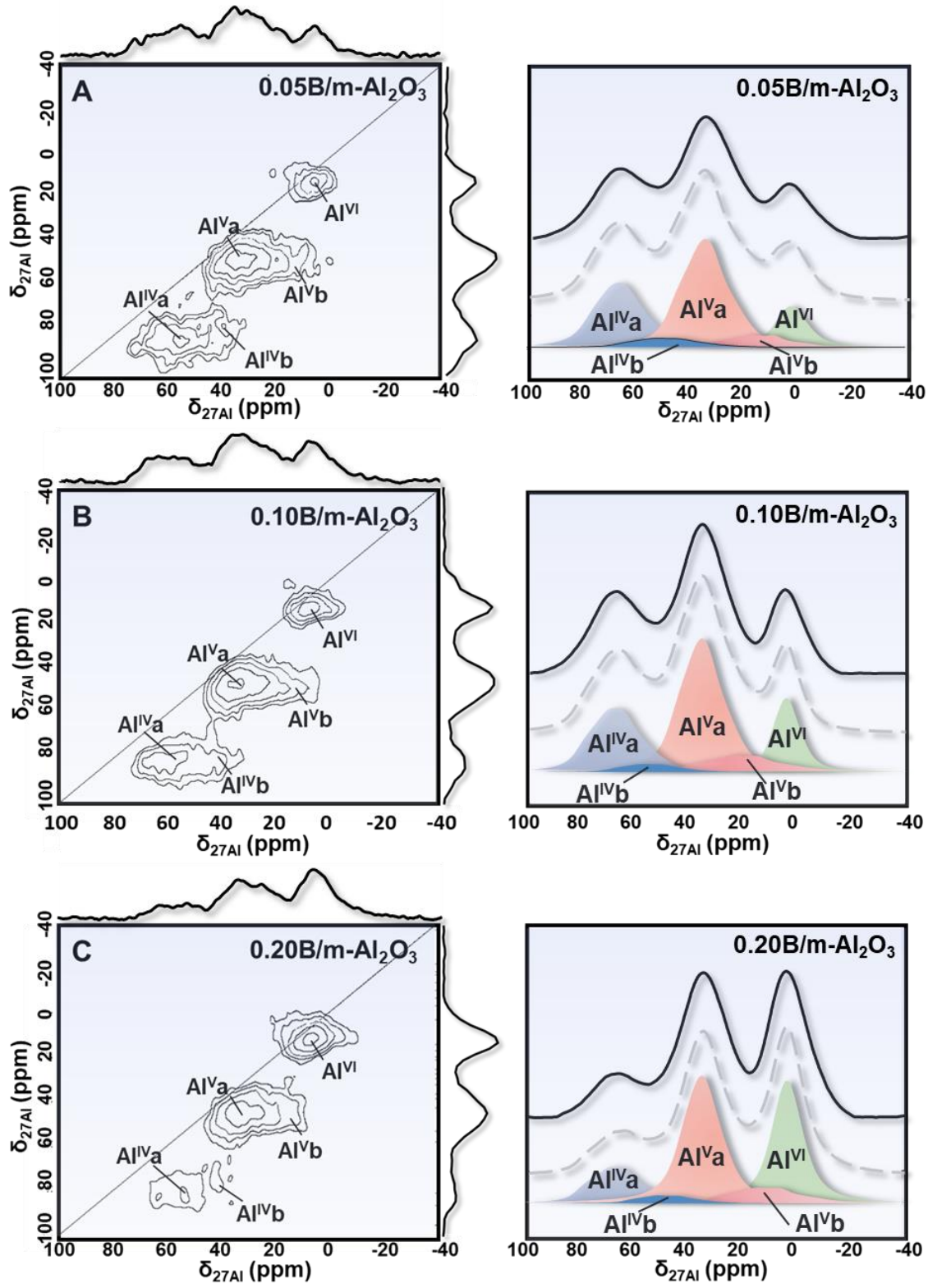

Figure 3-8 Local structure characterization of dehydrated B/m-Al_2O_3 catalysts. 2D ^{27}Al MQMAS NMR spectra of (A) 0.05B/m-Al_2O_3 (B) 0.10B/m-Al_2O_3, (C) 0.20B/m-Al_2O_3 and the corresponding 1D ^{27}Al MASNMR spectra and DMFit deconvoluted spectra simulated by using quadrupole line shapes are plotted on D-F (black: spectra; grey: simulation; colour block: components). Spectra obtained under Bruker Avance III 400WB spectrometer with spin rate of 15 kHz.

With a relatively higher local structure symmetry (i.e. smaller C_{QCC} compared to the counterparts), the Al^{IV}a and Al^{V}a, are assigned to the network Al species without the affection/substitution of heteroatoms. These Al^{IV}a and Al^{V}a species together with Al^{VI} species, coordinate mesoporous Al_2O_3 network[330]. Al^{IV}b and Al^{V}b species with larger local asymmetry (C_{QCC} = *ca.* 6.6 and *ca.* 5.9 MHz, respectively, **Table 3-4**) can be attributed to the disturbance on local electric field gradient along these Al sites by neighbouring heteroatoms[48]. In this sense, they could be assigned to network $Al^{IV/V}$-O···B and/or surface $Al^{IV/V}$-OH···B. The interaction between $Al^{IV/V}$b species and B species is also confirmed by the absence of the second Al^{IV} and Al^{V} species in m-Al_2O_3 (**Figure 3-10**), where only network Al^{IV}, Al^{V}, and Al^{VI} species can be identified. Via the interaction between the Al^{IV}b/Al^{V}b species and neighbouring B center, the formed $Al^{IV/V}$-OH···B hydroxyl groups could be functional as potential Brønsted acid sites.

The ^{11}B 2D MQMAS NMR spectra further supports the above assignments. In **Figures 3-9A-C**, two types of trigonal boron species (B^{III}) are identified (B^{III}a, δ_{iso}= 18ppm and B^{III}b, δ_{iso}= 15 ppm) and assigned by analogy to network B^{III}a (C_{QCC} = *ca.* 2.3 MHz) and AlOH interacted B^{III}b species (C_{QCC} = *ca.* 3.0 MHz). This is supported by the variation in the fractions of species, with the same increase trend as Al^{IV}b and Al^{V}b species, B^{III}b increases with boron concentration (**Table 3-5**). In addition, based on the ^{11}B ssNMR spectra of hydrated samples and the corresponding simulations (**Figure 3-7** and T**able 3-3**), the increase in the ratio of bulk B^{IV} species after hydration are very close to the fraction of B^{III}b species on dehydrated samples. This observation suggests that the majority of the B^{III}b species are surface accessible species. These above-mentioned fraction variations aid the assignment of the local structure of $Al^{IV/V}$-OH···B^{III}. The observed formation of only one B^{IV} species (δ_{iso}= 0 ppm) with high structure symmetry (C_{QCC} = *ca.* 1.2 MHz) can be explained by the existence of small BO_x domains. This is supported by the reported characterization on alumina-boria materials, where minor fraction of B^{IV} can incorporate in the alumina bulk[330].

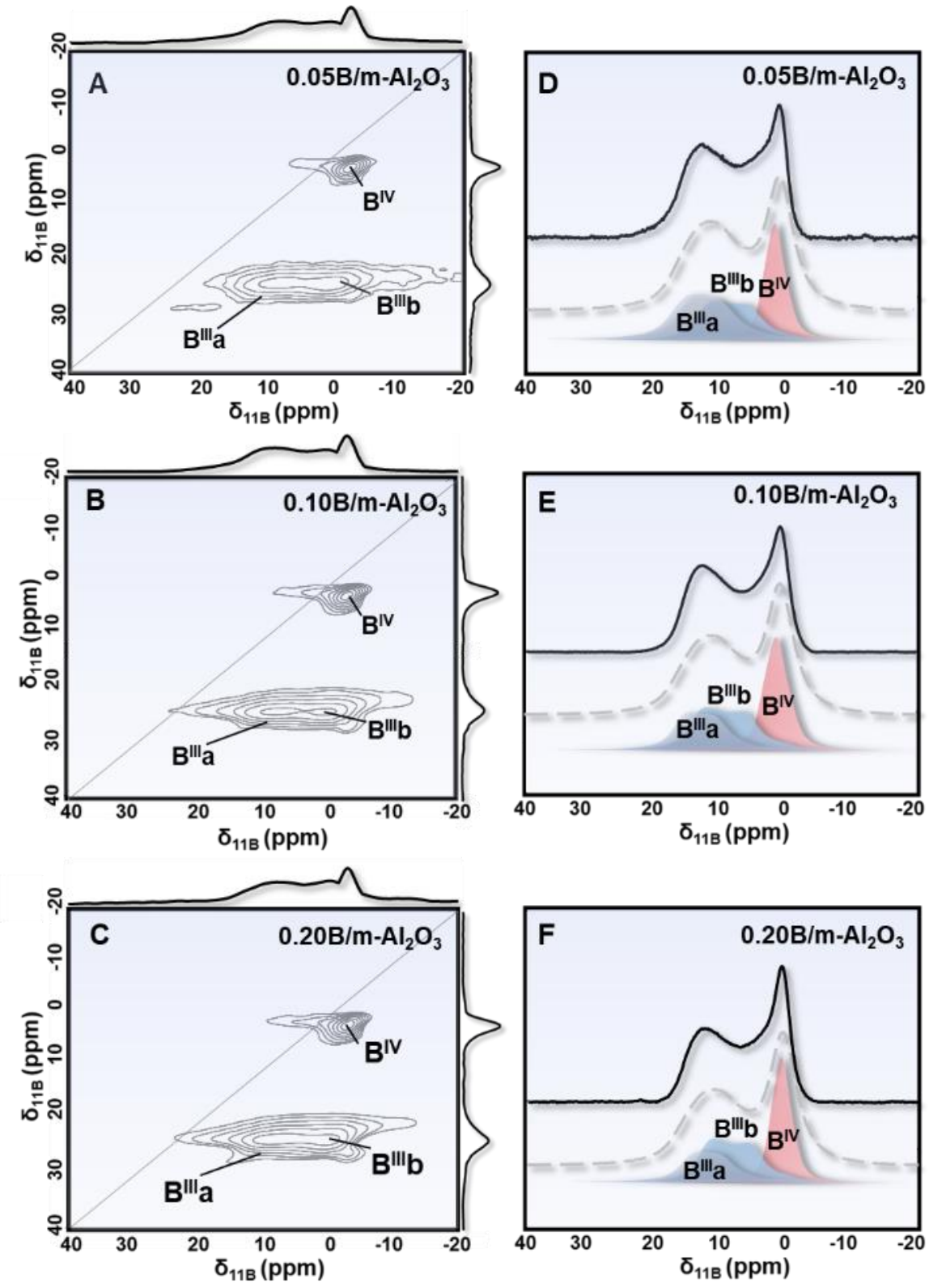

Figure 3-9 Local structure characterization of dehydrated B/m-Al_2O_3 catalysts. 2D ^{11}B MQMAS NMR spectra of (A) 0.05B/m-Al_2O_3 (B) 0.10B/m-Al_2O_3, (C) 0.20B/m-Al_2O_3 and the corresponding 1D ^{11}B MASNMR spectra and DMFit deconvoluted spectra simulated by using quadrupole line shapes are plotted on D-F. (black: spectra; grey: simulation; colour block: components). Spectra obtained under Bruker Avance III 400WB spectrometer with spin rate of 15 kHz.

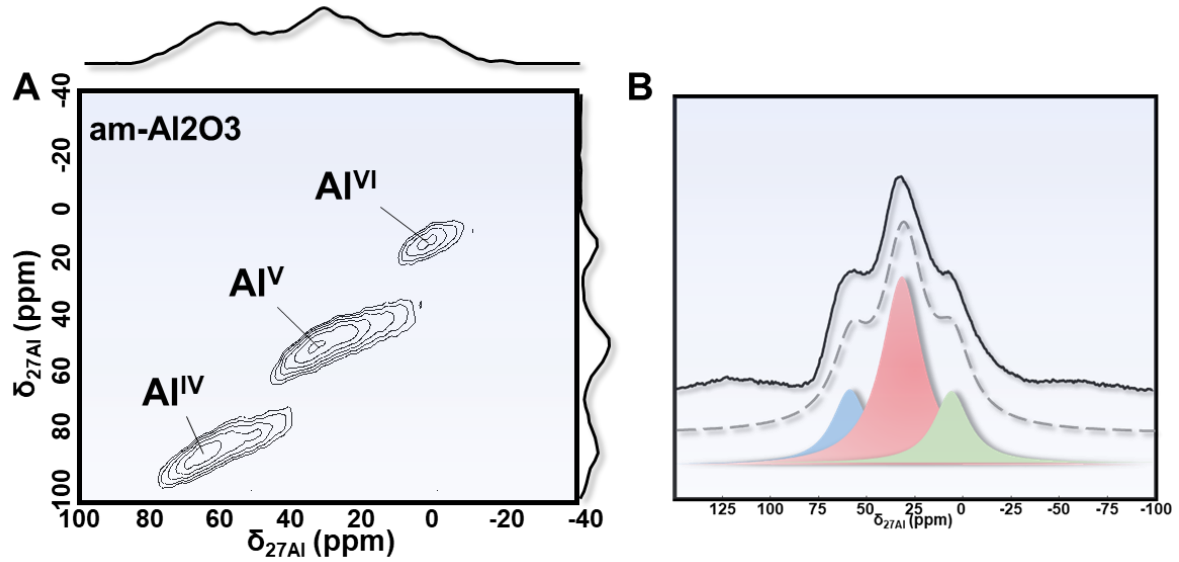

Figure 3-10 Local structure characterization of dehydrated m-Al_2O_3 catalysts. 2D ^{27}Al MQMAS NMR spectra of Al_2O_3 and the corresponding 1D ^{27}Al MASNMR spectra and DMFit deconvoluted spectra simulated by using quadrupole line shapes. Spectra obtained under Bruker Avance III 400WB spectrometer with spin rate of 15 kHz.

Table 3-4 Summary of 2D MQMAS NMR parameters and deconvolution results[a]

	0.05B/m-Al_2O_3			**0.10B/m-Al_2O_3**			**0.20B/m-Al_2O_3**		
	δiso (ppm)	C_{QCC} (MHz)	η	δiso (ppm)	C_{QCC} (MHz)	η	δiso (ppm)	C_{QCC} (MHz)	η
Al^{IV}a	77	4.5	0.6	75	4.7	0.6	76	4.4	0.6
Al^{IV}b	68	6.7	0.5	67	6.7	0.5	68	6.6	0.5
Al^{V}a	43	3.6	0.6	43	3.5	0.6	41	3.5	0.6
Al^{V}b	33	6.1	0.5	34	6.2	0.5	33	5.9	0.5
Al^{IV}	9	2.2	0.7	11	2.1	0.7	10	2.2	0.7
$B^{[3]}$a	18	2.4	0.2	18	2.4	0.2	18	2.3	0.2
$B^{[3]}$b	15	3.1	0.2	15	3.0	0.2	15	3.1	0.2
$B^{[4]}$	0	1.3	0.6	0	1.2	0.6	0	1.3	0.6

[a] Isotropic chemical shifts (δ_{iso}), quadrupole coupling constant (C_{QCC}) and asymmetry parameters (η) of each aluminum species and boron species were determined by the MQMAS NMR spectra and corresponding calculation of dehydrated AlBOx samples.

Table 3-5 Summary of deconvolution results of aluminium and boron species ratio of the dehydrated B/m-Al_2O_3.

	Al^{IV}a (%)	Al^{IV}b (%)	Al^{V}a (%)	Al^{V}b (%)	Al^{VI} (%)	$B^{[3]}$a (%)	$B^{[3]}$b (%)	$B^{[4]}$ (%)
0.05B/m-Al_2O_3	29.9	3.0	43.8	7.1	16.2	37.3	31.4	31.3
0.10B/m-Al_2O_3	22.8	3.4	40.9	8.4	24.5	28.4	34.9	36.7
0.20B/m-Al_2O_3	14.5	3.5	39.6	8.8	33.6	23.7	37.1	39.2

In the case of using probe molecule such as NH_3, ^1H MASNMR can be used to identify the BAS. As shown in **Figure 3-11** and **3-12**, after NH_3 loading, a large decrease in the signal intensity of peak at δ_{1H} = 1.9 ppm can be observed on B/m-Al_2O_3 accompanied with the signal intensity increases at δ_{1H}= ca. 7 ppm. The signal intensity increases at δ_{1H}= ca. 7 ppm indicates the ammonium ions occurrence due to the protonation of NH_3 by surface BAS at 1.9 ppm in ^1H MASNMR spectra[332].

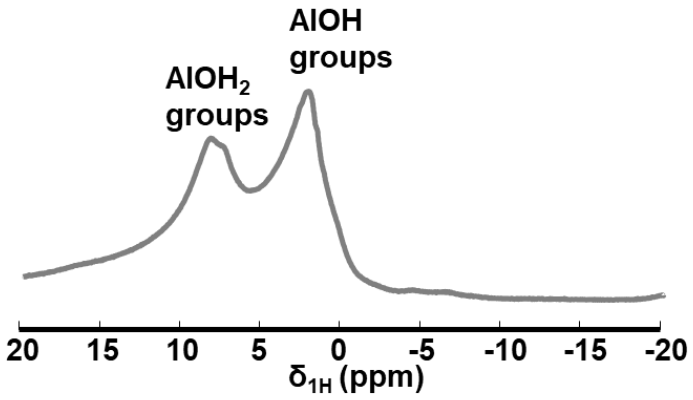

Figure 3-11 ^1H MAS ssNMR spectra of dehydrated m-Al_2O_3

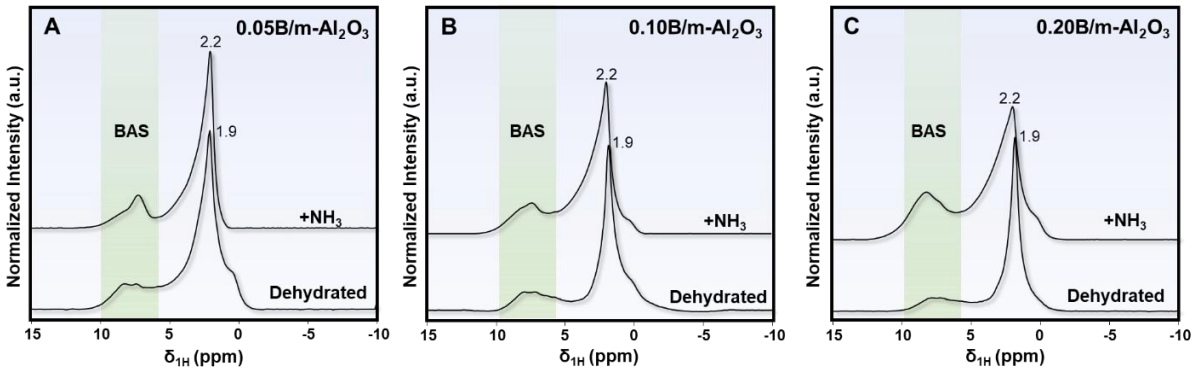

Figure 3-12 ^1H MAS ssNMR spectra of dehydrated and NH_3 absorbed (A) 0.05B/m-Al_2O_3, (B) 0.10B/m-Al_2O_3, (C) 0.20B/m-Al_2O_3

The local structure of Brønsted acidic hydroxyl group at 1.9 ppm is verified by the 2D ^1H-^{27}Al CP/MAS HETCOR spectra (**Figure 3-13**). Strong contours regarding BAS hydroxyl groups can be identified at (δ_{1H} = 1.9 ppm, δ_{27Al} = 67.1 ppm) and (δ_{1H} = 1.9 ppm, δ_{27Al} = 34.3 ppm). These contours show correlations between BAS hydroxyl and Al^{IV} species and Al^{V} species, respectively (**Figure 3-13A**), to form $Al^{IV/V}$-OH$\cdots B^{III}$. The interaction between nearby boron cation and AlOH induce negatively charged oxygens with higher electrical dipole moment[333]. To reach local charge neutrality, the oxygen of the terminal AlO_x form covalent bond with

positively charged protons, thereby generating Brønsted OH groups ($Al^{IV/V}$-OH···B^{III})[334, 335]. More interestingly, regarding the corresponding slice of ^{1}H-^{27}Al CP/MAS HETCOR spectra (δ_{1H} = 1.9 ppm, **Figure 3-13B**), the more potent Al^{V} peak compared to Al^{IV} suggests that majority of the BAS are provided by Al^{V} species. The strong contour intensity hints the predominance of Al^{V} based BAS (Al^{V}- OH ···B^{III}) in the samples.

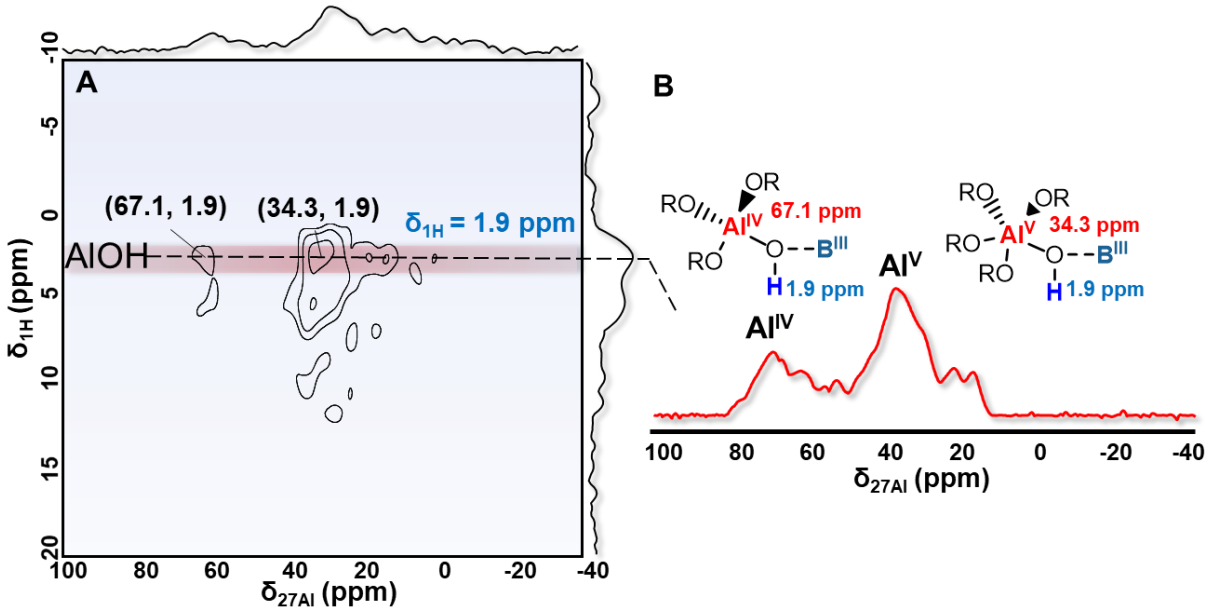

Figure 3-13 (A) 2D ^{1}H-^{27}Al CP/MAS HETCOR spectrum of representative 0.10B/m-Al_2O_3 catalyst, (B) The ^{27}Al slices at the F_1 chemical shift of δ_{1H} = 1.9 ppm extracted from the 2D spectrum. Spectra obtained under Bruker Avance III 500WB spectrometer with spin rate of 25 kHz.

Figure 3-14 shows the NH_3 -TPD results for B/m-Al_2O_3 and parent m-Al_2O_3. It is utilized to qualitatively measure the acidic properties of alumina-boria catalysts. The area of the NH_3 desorption peak regions represents the quantity of the total surface acid sites on the oxide mixtures, and the quantities of acid sites have been listed in **Table 3-1**. According to **Figure 3-14**, all B/m-Al_2O_3 catalysts shows board peaks with similar positions, which implied that they have acidic sites with unvaried strength. And the m-Al_2O_3 substrate only contains LAS.

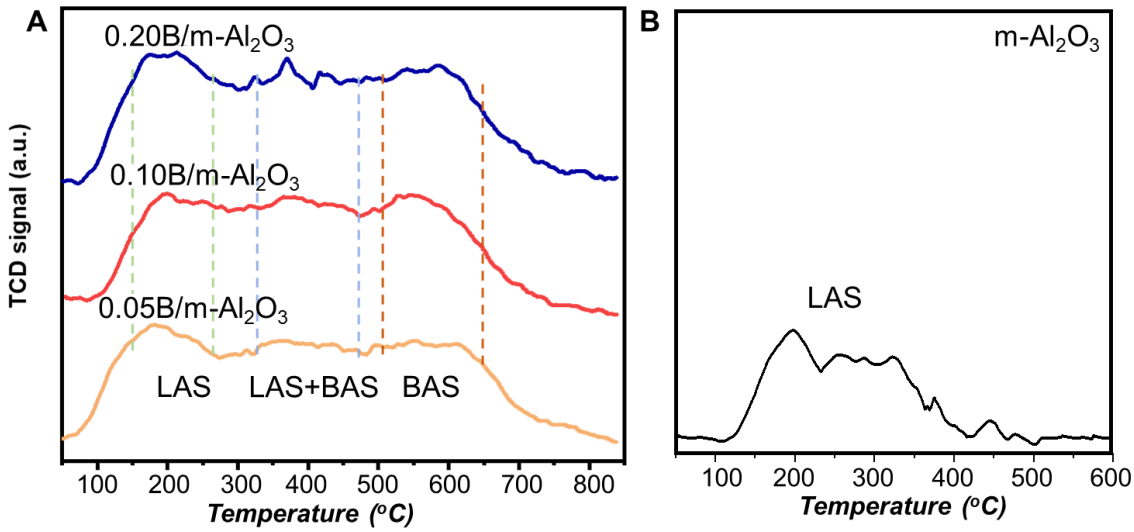

Figure 3-14 NH_3-TPD profiles of the (A) B/m-Al_2O_3 catalysts and (B) parent m-Al_2O_3

With the help of probe molecule trimethylphosphine oxide (TMPO), ^{31}P MASNMR spectroscopy have been further applied to quantitatively verify the surface acid sites[336-338]. In ^{31}P spectra, two peaks can be observed for all samples (**Figure 3-15**). In line with the NH_3-TPD results which show similar peaks for different B/m-Al_2O_3 mixed oxides (**See Figure 3-14**), the unvaried chemical shift positions of peak in different B/m-Al_2O_3 implies that the catalyst composition (n(Al)/n(B) ratio) only affect the ratio and quantities of surface acid site instead of generating new acid sites with varied acidity. The peak at δ_{31P} = 62 ppm is assigned to $TMPOH^+$ ions to probe BAS. This is consistent with the proposed Al^V-OH···B^{III} structure, the moderate Brønsted acidity could be explained by the flexible interaction between B and O and a long B-O spatial distance. The signal appeared at δ_{31P} = 48 ppm was attributed to the adsorbed TMPO on LAS like surface incomplete tetrahedral or octahedral sites[339-342]. Typically, without the effect of heteroatoms on aluminium site local structure, with little BAS but a high concentration of LAS, only observable LAS peak at δ_{31P} < 48 ppm can be identified on ^{31}P MAS NMR spectra of TMPO absorbed m-Al_2O_3 (**Figure 3-16**)[343]. The existence of large quantity of BAS on B/m-Al_2O_3 suggests that the majority of BAS are constructed after the addition of boron and support the proposed BAS structure of Al-OH···B. The corresponding quantity of LAS, BAS, and total acid sites of B/m-Al_2O_3 are calculated and listed in **Table 3-1**. According to that, boron addition increases the total number of acid site, and ratio of LAS to BAS increases from 0.97 to 1.45. This is in agreement with the acid sites increasement in alumina-boria mixed oxide reported by Sato et al. and Chen et al.[344, 345]. Additionally, the correlation between the increase trend in the concentration of BAS and B^{III}b and the total ratio

of $Al^{IV}b$ and $Al^{V}b$ further supports the assignment for these species and the existence of $Al^{IV/V}$-$OH\cdots B^{III}$ based on these species (**Figure 3-17, Table 3-1, Table 3-5**). Thus, the ssNMR results in this work discovered that Al^{V}-BAS can be also generated on non-silica aluminate materials, like amorphous alumina-boria.

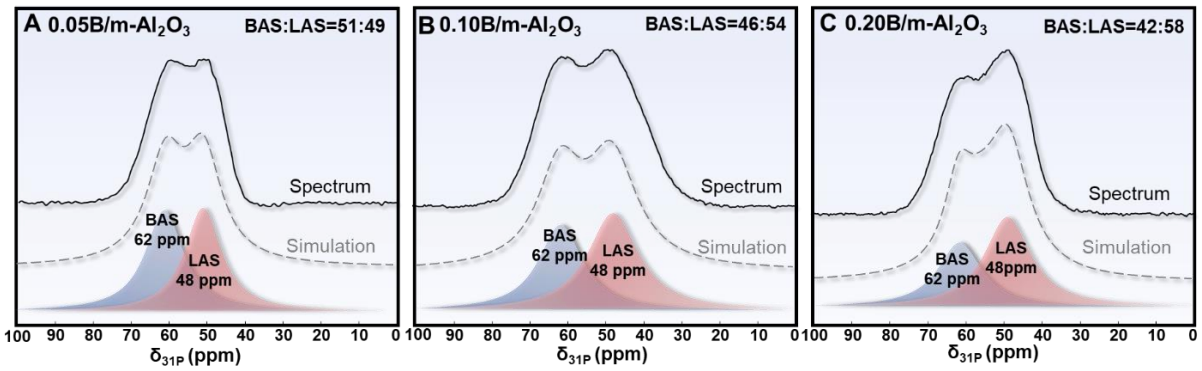

Figure 3-15 ^{31}P MAS NMR spectra of TMPO adsorbed on (A) 0.05B/m-Al_2O_3, (B) 0.10B/m-Al_2O_3, and (C) 0.20B/m-Al_2O_3 samples. Spectra obtained under Bruker Avance III 400WB spectrometer with spin rate of 12 kHz; (D) Scheme for different acid sites interact with TMPO molecule.

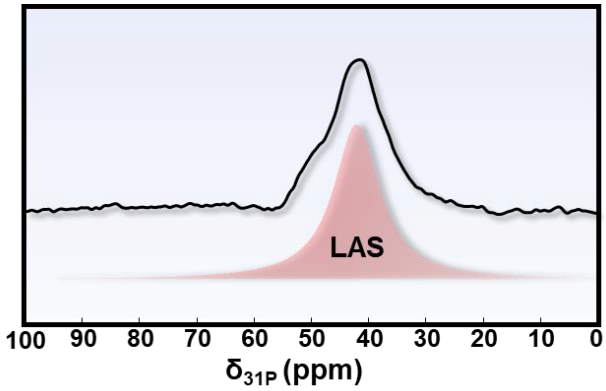

Figure 3-16 ^{31}P MAS NMR spectra of TMPO adsorbed on m-Al_2O_3

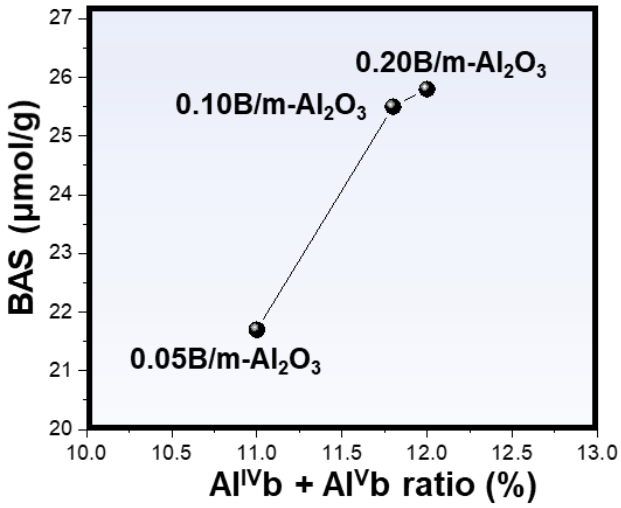

Figure 3-17 The curved relationship between the surface BAS concentration and the total ratio of $Al^{IV}c$ and $Al^{V}c$ species

3.2.3 Catalytic Performance of AlV-BAS in phenylglyoxal conversion

The catalytic performance of Al^{V}-BAS enriched B/m-Al_2O_3 catalysts has been tested by phenylglyoxal (PG) conversion. m-Al_2O_3 containing only LAS has been used as a reference catalyst in the reaction.

Compared to the LAS only m-Al_2O_3, which shows only 52.9% conversion of PG after 4 h reaction under 90^{o}C, the 0.05B/m-Al_2O_3 with Al^{V}-BAS, showed a much-accelerated PG conversion rate (96.6%) with improved EM selectivity (>98%) after 4 hours reaction (**Figure 3-18A, Table 3-1**). The observed enhancement in catalytic activity of B/m-Al_2O_3 catalysts can be explained by the introduction of Al^{V}-BAS on surface, suggesting that BAS is the better active site for PG conversion compared to surface LAS. Besides, the higher EM selectivity on all B/m-Al_2O_3 catalysts compared to parent m-Al_2O_3 hint that the LAS leads to side reactions, and the high EM selectivity on B/m-Al_2O_3 also suggest the importance of the unvaried acid distribution on inhibiting side reactions. Among B/m-Al_2O_3 catalysts, the 0.10B/m-Al_2O_3 catalysts showed the best catalytic performance on converting PG into EM based on the calculation of turnover frequency (TOF), As demonstrated by **Table 3-1**. However, notably, although 0.20B/m-Al_2O_3 have the highest concentration of BAS, but it also contains a much larger quantities of LAS. Thus, the relatively worse catalytic performance of 0.20B/m-Al_2O_3 catalysts than that of 0.10B/m-Al_2O_3 catalyst may be explained by the better flexibility and accessibility of BAS and worse desorption ability of strong LAS. With higher LAS concentration, more PG molecules could be absorbed on LAS, which delays the conversion of PG into EM. This suggests the dominant role of BAS in PG conversion to EM. Furthermore, compare to microporous zeolites deAl-HY, which possessed much larger quantity of strong acid sites, alumina-boria oxide catalysts showed a better performance in PG conversion. This is not only consisting with previous research that the total amount of the acid sites has no correlation with the yield of EM, but also demonstrated the importance of the mesoporous and amorphous structure for the conversion of large molecules such as PG molecules.

Furthermore, the stability of Al^{V}-BAS on the prepared catalysts is tested with the most promising 0.10B/m-Al_2O_3 catalyst. After five cycles of reactions under identical condition, an unvaried catalytic performance had been identified (**Figure 3-18B**). Additionally, no boron content could be detected on the 5th reaction solution (Not shown). Combining with the stable reaction performance and undetectable boron content leaching, the leaching resistance of active Al^{V}- OH $\cdots B^{III}$ has been demonstrated, confirmed that the Al^{V}-BAS on the alumina-boria catalysts act as stable active sites.

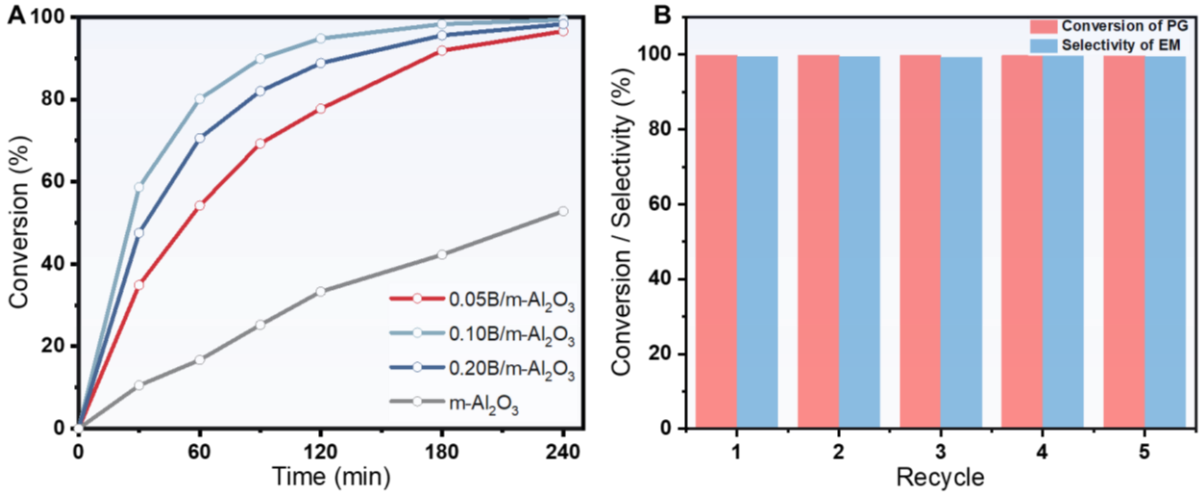

Figure 3-18 Reaction performance of alumina-boria catalysts. (a) PG conversion as a function of reaction time over various catalysts. (b) Recycling experiments for PG conversion, which repeated five times. Reaction conditions: 50 mg of the alumina-boria catalysts, 1.25 mL ethanol solution containing 0.4 M PG at 90 °C after a reaction time of 4 h under continuous stirring.

To show how the Al^V-BAS promotes PG conversion, *in-situ* ^1H NMR was applied to monitor the reaction process in a real time fashion in methanol-d_4 solvent. Compared to the PG conversion on ethanol solvent, which was too fast to observe detailed changes from reactants to products, the PG conversion on methanol was slower under the identical conditions. With minimized solvent influence on mechanism due to the identical functional group, the slower reaction rate facilitates our ability to observe and identify changes and intermediates by *in-situ* NMR and thus predict the mechanism of PG conversion more accurately. **Figure 3-19A** gives the plots of ^1H NMR spectra during the conversion of PG within solvent methanol-d_4 on representative 0.10B/m-Al_2O_3 catalyst with enriched Al^V-BAS at 363K. Since phenylglyoxal is not stable and can easily react with water molecule, no signal for aldehyde group of PG molecule but the proton H_a (δ_{1H} = 5.53 ppm) of -CH of hydrated PG can be observed at the start of recording, while the hydroxyl proton H_b overlapped with the hydroxyl signal of methanol and water signal at δ_{1H} = 4.59 ppm. Demonstrated by **Figure 3-19A**, the intensities of protons from aim product methyl mandelate **(**δ_{1H} = *ca.* 7.42, 7.30, and 7.35 ppm for aromatic protons H_h, H_i, and H_j, respectively and δ_{1H} = 5.18 ppm for the -CH proton, H_g) increase while the intensities of protons from reactant (δ_{1H} = *ca.* 8.06, 7.62, and 7.50 ppm for aromatic protons H_c, H_d, and H_e, respectively and δ_{1H} = 5.53 ppm for the -CH signal of H_a) decrease as a function of reaction time. The absence of methyl protons was attributed to the deuteration (-CD_3) in the methanol-d_4 solution which largely inhibited the -CH signal. While the un-observable hydroxyl proton signal of product (H_f) can be explained by the existence of hydroxyl proton H_b and

hydroxyl proton residual of d_4-methanol hydroxyl which have possible similar ^1H chemical shift positions at *ca.* $\delta_{1H} = 4.59$ ppm (**Figure 3-19A**).

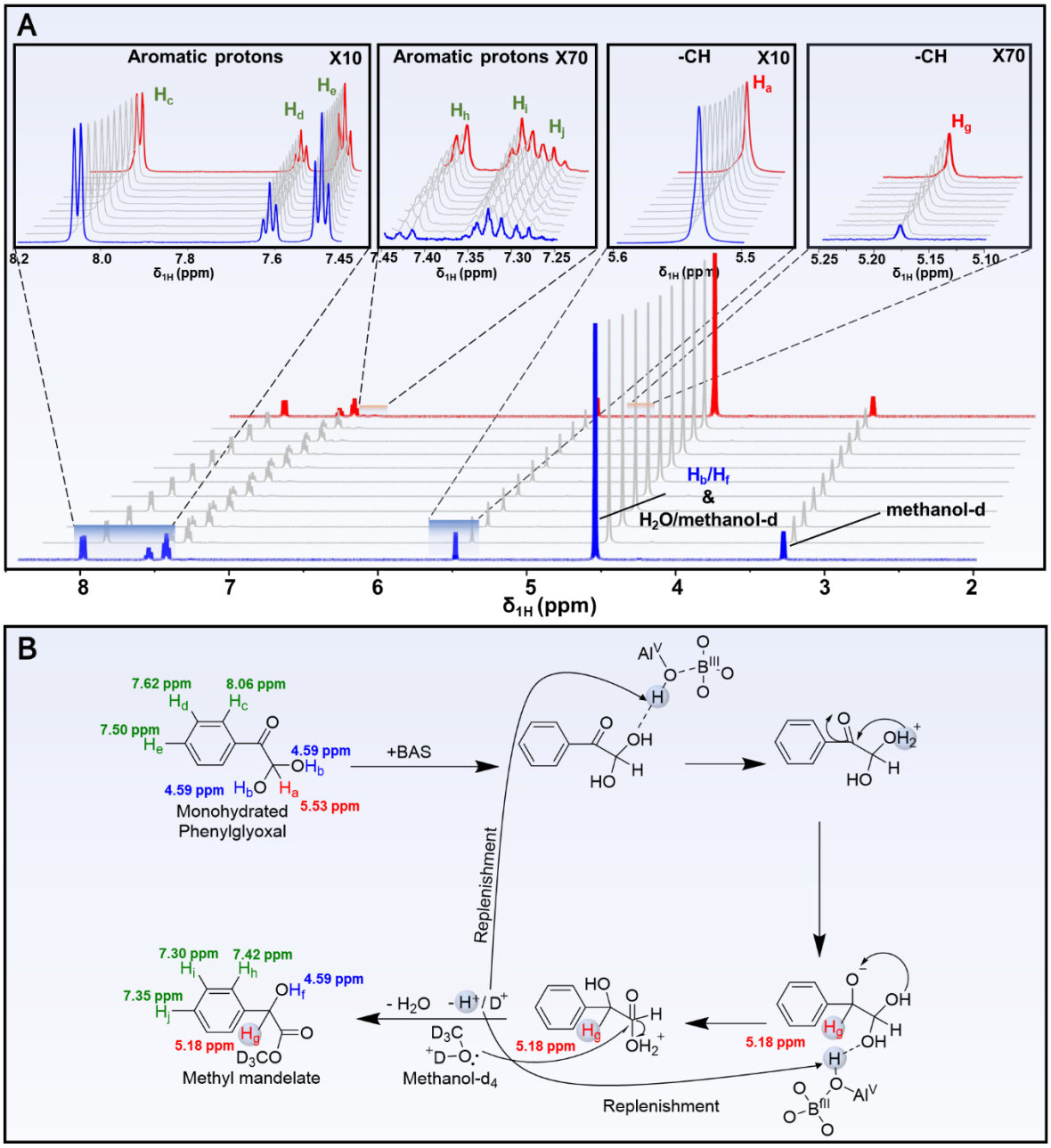

Figure 3-19 Stack plots of (9) ^{1}H liquid-state NMR spectra of PG conversion recorded in the solvent of methanol-d_4 at 363K during 2 h reaction time (10 mins (blue), 120 mins (red)), the Stack plots of the *in situ* ^{1}H NMR spectra in highlighted region have been zoomed for the identification of reactant and product signals. (B) Corresponding scheme of plausible reaction pathway of PG conversion to α-hydroxy carboxylate on the Al^{V}-BAS enriched B/m-Al_2O_3 catalysts in alcoholic solvent.

The corresponding plausible reaction pathway has been drawn in **Figure 3-19B**. Initially, the hydration process converts the aldehyde group of the unstable anhydrous phenylglyoxal into two hydroxyl groups due to the presence of moisture[346]. After the introduction of catalysts, the initial reaction step involves the activation of the hydroxyl groups on hydrated PG by the protons of Al^{V}-BAS, while the carbonyl group remain intact. The following disproportionate

reaction, intramolecular Cannizzaro reaction, inferred by the large increase in the intensity of H_g (δ_{1H} = 5.18 ppm) during the in-situ NMR observation (**Figure 3-19A**), then happen rapidly on this unstable structure and considered as the key step. It causes the simultaneous reduction of OH_2^+ and the oxidation of C=O groups via intramolecular hydride shift[347, 348]. Because no intermediate was identified during the *in-situ* NMR observation, instead of reacting with solvent alcohol and yielding the intermediate hemiacetal, similar to regular Cannizzaro reaction, proton transfer happens between the hydroxyl group and the O^- oxidized from the carbonyl group. With the identical activation of hydroxyl by another Al^V-BAS, the unstable species is then rapidly bound to the alcoholic oxygen and followed by alcoholysis with deuterated alcoholic solvent (CD_3OD in this case), which lead to the decrease signal intensity of H_a (δ_{1H} = 5.53 ppm) and continuously generate the corresponding aim α-hydroxy carboxylate product and free deuterons for the replenishment of proton species of Al^V-BAS. The observation on *in-situ* ^1H NMR spectra confirms that the reaction was driven by BAS instead of LAS, especially the surface dominant Al^V-BAS. This is in line with the experimental results that the poor PG conversion performance was observed on m-Al_2O_3 containing only LAS, while B/m-Al_2O_3 containing Al^V-BAS gave improved performance in PG conversion.

3.3 Conclusions

In conclusion, this work demonstrates the design of a series of Al^V enriched and mesostructured amorphous alumina-boria catalysts with various n(B)/n(Al) ratio. Assisted by the MQMAS NMR spectra, the highly disordered local structure of the B/m-Al_2O_3 have been characterized with the identification of interacting species of Al^{IV}, Al^V, and B^{III}. Via the application of the 2D ^1H-^{27}Al HETCOR MASNMR, for the first time, in non-silica aluminate materials, the partial of Al^V centers have been evidenced and assigned to the formation of dominant BAS via Al^V-OH···B^{III}. Aided by the ^{31}P ssNMR characterization with TMPO probe molecules, the observed Al^V-BAS have similar acidic properties as the Al^{IV}-BAS with similar Al-OH···B structure. These ssNMR characterizations confirm that the amorphous alumina substrate can be applied to construct Al^V enriched mixed oxide with highly active and stable Al^V-BAS for catalytic reactions. The reaction mechanism of the novel Al^V-BAS in the test PG conversion has been studied by the *in-situ* NMR investigation. Thus, the present study shed light that the Al^V-BAS can exists with promising acidic properties in non-silica aluminate materials, such as amorphous alumina-boria. And the establishment of catalytically active Al^V based BAS can be applied as a new frontier to improve the performance of acid reaction.

4. Coordinating silanol with single Al^V site for Brønsted acidity on mesoporous amorphous Al_2O_3

4.1 Introduction

Acid catalysis plays a critical role in over 50% of industrially important catalytic applications since the last century, such as petrol oil cracking, pharmaceuticals synthesis, and biomass transformation[349]. The most commonly used acid catalysts are liquid Brønsted acids, such as HCl, H_2SO_4, and H_3PO_4, despite their corrosive and environmentally harmful nature[350]. To promote cleaner and more sustainable processes, solid Brønsted acids like ZSM-5 zeolite[351], heteropolyacids[352], Amberlyst-15[353, 354], and Montmorillonite clay[355] have been developed and are now widely used in the chemical industry as alternatives to liquid catalysts.

Zeolite and amorphous silica-alumina are among the most commonly used solid acids in the chemical industry. The predominant Brønsted acidity (BAS) in these materials is generated through the incorporation of aluminum species into the SiO_2 framework of crystal zeolites or into the SiO_2 network of amorphous silica-alumina. The tetrahedrally coordinated silicon species in the SiO_2 framework are substituted by the tetra-coordinated aluminium species (Al^{IV}) to produce Si-OH-Al groups and and the Al^{IV} species can thereby stay stable with relatively high population on both amorphous and crystal silica-alumina. Due to the electronegativity of the silica-alumina framework, the generated Si-OH-Al^{IV} groups act as Brønsted acid sites and can donate H^+ during reactions. Therefore, the tetra-coordinated aluminum species (Al^{IV}) and its bridging or pseudo-bridging Si-OH-Al^{IV} structures are considered necessary factors for generating BAS on silica-alumina based catalysts.

Alternatively, Al^V has recently been discovered to form the Brønsted acid site with silanol on silica-alumina (Si-OH-Al^{IV}) by flame spray pyrolysis (FSP)[356,357]. The density, strength, and activity of BAS on Al^V based ASAs have been largely enhanced[358, 359]. However, FSP is mainly producing nanoparticle type of acid catalysts[360]. Due to the particle-like geometry resulted limited specific surface area, the availability of surface exposed active Al^V site is restricted. Also, from a kinetic point of view, the non-porous structure is less optimal for improving mass transfer and diffusion kinetics[357]. Therefore, creating nano-porous structures with Al^V based BASs can provide multiple benefits for enhancing catalytic reaction efficiency. However, to

the best of our knowledge, there have been no publications on the development of Al^V based Brønsted acid site (Al^V-BAS) with a nano-porous structure till now.

It has been reported that the mesoporous alumina has high density of Al^V species on surface, which has been applied for stabilizing metal sites on many highly efficient catalysts[361, 362]. For example, as a coordination defect with metal-anchor ability, Al^V on a mesoporous alumina led to the formation of Al^V-O-Cu^+, contributing to the high dispersion of Cu metal sites and hindered the reduction of Cu^+ to Cu^0 [363]. The mesoporous structure allows for a significant increase in specific surface area, resulting in a higher concentration of exposed Al^V sites on the surface. Thus, we develop a new strategy to introduce Si precursor for a surface reaction with single Al^V sites to form the Al^V based Brønsted acid site. By combining the advantages of the nano-porous structure and the Al^V coordination defects, there was a large improvement in the catalytic activity.

Herein, in this research, we report the preparation of Al^V-BAS with mesoporous geometry via cheap and simple wet-chemistry synthesis strategy, it combines the advantages of active Al^V site, mesoporous structure, and cheap synthesis route. By base-catalyzed condensation, we coordinate the introduced silanol on surface exposed Al^V site, to form Al^V-BAS on the surface SiO_2-Al_2O_3 nanolayer. We applied the Electron Energy Loss Spectroscopy (EELS) and X-Ray Photoelectron Spectroscopy (XPS) to verify the formation of silanol linked surface silica-alumina nanolayer. And the Multinuclear Solid-State Nuclear Magnetic Resonance Spectroscopy (ssNMR) has been applied to prove the formation of Al^V-based Brønsted acid site at the nanolayer of the SiO_2-Al_2O_3 network, and to characterize the identity, structure, strength, quantity and location of the formed BAS. And the catalytic activity of the penta-coordinated aluminium species-based BAS has been proven to be efficient for the 1,2 propanediol conversion to propanal as a test reaction. To our best knowledge, this is the very first report on the simple and inexpensive wet-chemistry method for the preparation of Al^V-BAS on nano-porous alumina-silica material. It opens up possibilities for large-scale industrial applications of mesoporous silica-alumina with Al^V-BAS.

4.2 Results and Discussion

4.2.1 Establishing silanol linkage on Al^V enriched alumina

On the mesoporous Al^V enriched alumina support prepared based on previously reported EISA method[364], stepwise addition of tetraethyl orthosilicate have been cycled in order to coordinate surface silanol linkage on the surface of alumina. When in a basic environment, the surface-

accessible protons of AlOH group can be substituted with Si atoms, resulting in the creation of a silanol linkage (**Figure 4-1A**). **Figure 4-1B** showed the Electron Energy Loss Spectroscopy (EELS) mappings for 1-SiO_2@am-Al_2O_3. The observed relatively uniform silica enriched domain on the outermost surface confirmed that the addition of Si species led to the formation of a relatively homogenous surface SiO_2-Al_2O_3 nanolayer by creating coordinated silanol linkage. As the cycles increases, the interlayer accessible AlOH protons instead of the surface SiOH will prefer continues to be replaced by Si atoms, creating additional silanol linkages and thicker SiO_2-Al_2O_3 overlayer (from *ca.* 1.4 to 2.2 and 5.7 nm for 1-SiO_2@am-Al_2O_3 to 2-SiO_2@am-Al_2O_3 and 5-SiO_2@am-Al_2O_3, respectively, **Figures 4-1C-D**) instead of pure SiO_2 overcoat. The formation of SiO_2-Al_2O_3 nanolayer rather than SiO_2 overcoat had also been confirmed by the ^{29}Si ssNMR spectrum (**Figure S4-1**). The Si species distribution on 5SiO_2@am-Al_2O_3 was close to the homogeneous random distribution of Si species calculated by McMillan et al[365], suggesting the absence of separated large Si domain. The absence of six-coordinated silica species in the ^{29}Si MASNMR spectra confirmed that the addition of silica did not incorporated with the alumina framework but led to the silanol linked SiO_2-Al_2O_3 nanolayer[366]. Additionally, the observation of thicker SiO_2-Al_2O_3 overlayer suggested the presence of surface accessible silanol linkage with larger quantity, demonstrated that the silanol linkage density can be regulated by the stepwise addition cycles of Si species. It provided the prerequisite for the formation of surface silanol based surface site with Brønsted acidity.

The geometry of crystalline and porous structure the silanol linked Al^V enriched mesoporous alumina have been further studied. In **Figure 4-1E**, no well-resolved crystalline peak can be identified for SiO_2@am-Al_2O_3 materials, demonstrating that the Si addition was independent with the crystalline geometry of alumina matrix at the inner bulk. Also, the absence of silica-related peaks implies that either the formed SiO_2-Al_2O_3 had an amorphous geometry or the formed crystalline phase was too small to be detected[367]. Based on the **Figure 4-1F-G**, in addition to the global amorphous geometry, the silanol linked Al^V alumina maintained the nanopores after the addition of Si species. **Table 4-1** summarized the physical properties of the SiO_2@am-Al_2O_3 materials. The similar pore diameters for different SiO_2@am-Al_2O_3 and the Al^V enriched substrate suggests that the addition of Si species was also independent of the geometry of the nanopore.

Thus, based on the abovementioned characterizations, we confirmed that, on the mesostructured Al^V enriched alumina support, the stepwise deposition of Si species produces SiO_2-Al_2O_3 mixed oxide nanolayer on the outermost surface with varied thickness. The

increase in the cycles of the stepwise addition contributes to no effect to the global mesoporous geometry but only the thickness of the mixed oxide-oxide layer thickness (**Figure 4-1H**). The silanol linked silica-alumina nanolayer lead to the formation of oxide-oxide interfaces on the Al^{V} enriched mesoporous alumina, which provides the prerequisite for Al^{V} environment-based Brønsted acid site formation.

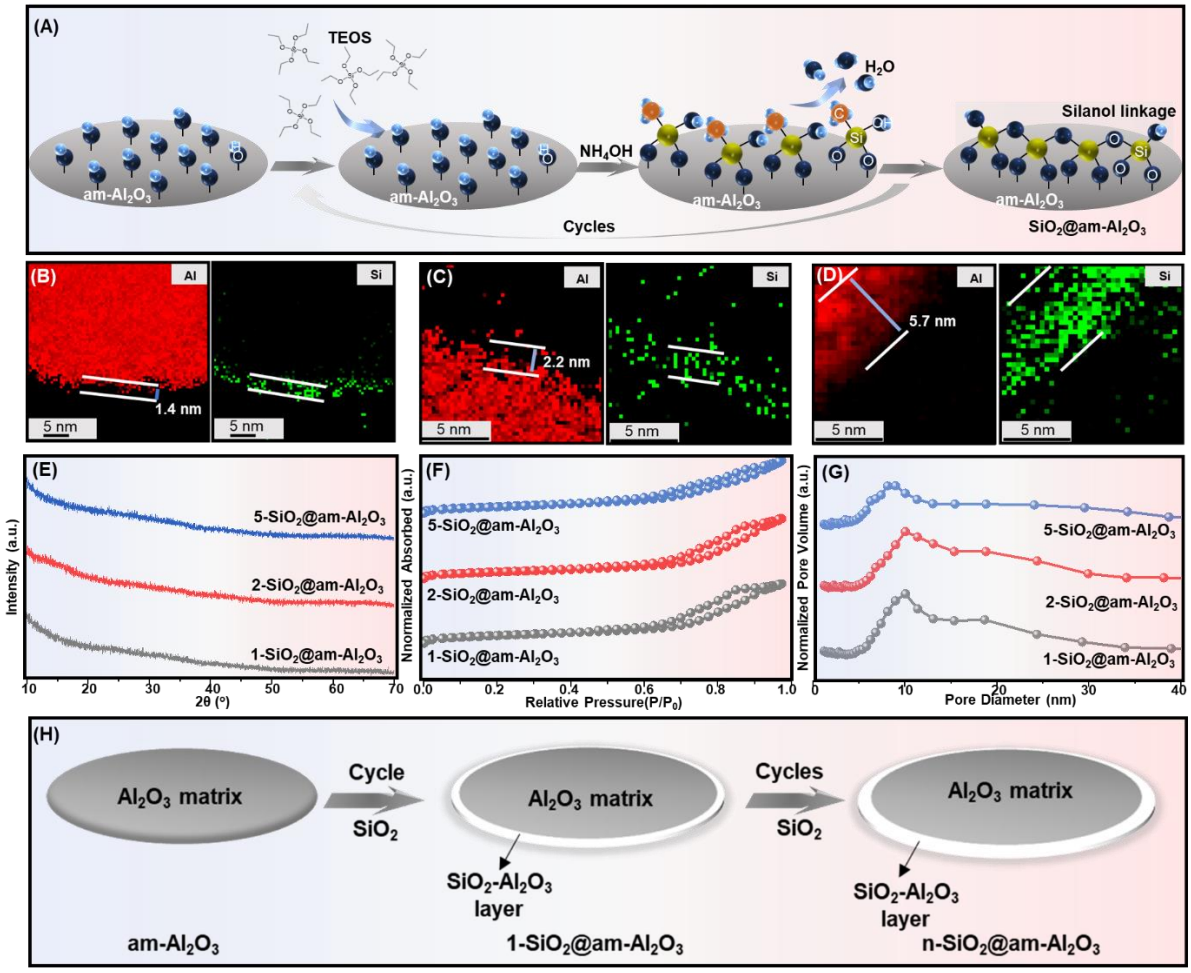

Figure 4-1 (A) Scheme of SiO_2@am-Al_2O_3 synthetic approach, (B-D) electron energy loss spectroscopy mapping, (E) Wide-angle XRD patterns, (F) N_2 adsorption–desorption isotherms, (G) BJH pore size distribution calculations, and (H) the plausible structure modifications of SiO_2@am-Al_2O_3 catalysts.

Table 4-1 Summary of physical characterization for parent amorphous alumina and SiO_2 overcoated amorphous alumina[a]

Catalysts	n(Si)/n(Al)	Surface Area (m^2/g)	Pore Volume (cm^3/g)	Pore Diameter (nm)	Overcoat Thickness (nm)	Penetration Thickness (nm)
am-Al_2O_3	-	122.59	0.29	10.0	-	-
1-SiO_2@am-Al_2O_3	0.05	109.78	0.27	10.1	1.3	-
2-SiO_2@am-Al_2O_3	0.07	91.08	0.26	10.0	1.4	1.0
5-SiO_2@am-Al_2O_3	0.17	89.21	0.23	9.4	1.4	5.2

[a]The surface composition ratio was determined by X-ray photoelectron spectroscopy elemental analysis. [b]The specific surface area (SA), volume of pores (V_{pore}), and pore diameter (d_{BJH}) of Al_{ALD}/nanoreactor catalysts were determined from the adsorption of the N_2 isotherms and corresponding BJH calculation. [c]The thickness of the nanolayer was determined by the EELS mapping.

4.2.2 Silanol linkage for BAS formation on AlV enriched mesoporous alumina

After characterizing the geometry of the SiO_2@am-Al_2O_3 materials, the surface local structure of the catalysts was further studied to understand the contribution of silanol linkage, the corresponding environment of the surface site and the surface acidity on the silica-alumina nanolayer. Due to the severe line broadening of quadrupolar nuclei, the distorted local environments of aluminum species have been distinguished by 2D ^{27}Al Multiple Quantum (MQ) NMR experiments[368]. For the parent mesoporous Al_2O_3 substrate, as presented in **Figure 4-2A**, three different contours can be identified on the spectrum, and which could be assigned to the network four-coordinated (δ_{iso} = 63 ppm, C_{QCC} = 3.6 MHz), five-coordinated (δ_{iso} = 35 ppm, C_{QCC} = 3.8 MHz), and six-coordinated (δ_{iso} = 8 ppm, C_{QCC} = 3.1 MHz) aluminum species. It is worth highlighting that the Al^V-enriched platform of parent am-Al_2O_3 maintains 53.9% of Al^V species, which provides a prerequisite for the formation of Al^V based Brønsted acid site with large quantity.

With the stepwise addition of SiO_2 of only one cycle, except the species have been observed for substrate, the 1SiO_2@am-Al_2O_3 showed one extra Al^{IV}b contour (δ_{iso} = 60 ppm, C_{QCC} = 6.3 MHz, **Figure 4-2B**). The appearance of the Al^{IV}b contour with a much larger C_{QCC} value suggests that the Al^{IV}b species had a much-distorted local structure compared to Al^{IV}a species within the network of mesoporous Al_2O_3[369]. Thus, the Al^{IV}b species have been assigned to surface aluminum species that exist in the SiO_2-Al_2O_3 overlayer which is spatially adjacent to Si species and contributed to the silanol linkage and Brønsted acidity. The absence of zeolitic Si-O-Al bond scattering in FTIR spectra hinted that the spatial interaction between the Si and Al^{IV} species and the silanol linkage over the silica-alumina nanolayer contributed to the surface Si-OH---Al^{IV} group instead of the bridging Si-OH-Al^{IV} group (**Figure S4-1**). As an effect of silanol linkage formation, the Al-O stretching of SiO_2@am-Al_2O_3 was shifted to higher wavenumbers compared to that of am-Al_2O_3 (*ca.* 510 cm^{-1})[370]. The silanol linked Si-OH---Al^{IV} group gives an increase in the local structure asymmetry, which explained the increase in the C_{QCC} value of Al^{IV}b species[371].

With further step-wised cycles of Si species addition, the second Al^V species, Al^Vb appeared on both 2SiO_2@am-Al_2O_3 (δ_{iso} = 31 ppm) and 5SiO_2@am-Al_2O_3 (δ_{iso} = 33 ppm) samples (**Figures 4-2C-D**). With less symmetric local structures (C_{QCC} = 6.5 MHz and 6.8 MHz, respectively), the presence of such species indicates the presence of second silanol linkage, the Si-OH---Al^Vb structure, in the thicker silica-alumina nanolayer which is similar to the Si-OH---Al^{IV}b structure with Brønsted acidity[372-375].

Based on the MQ spectra, corresponding slides, and the summarized quadrupolar parameter tables (**Figure 4-2** and **Table S4-3**), simulations have been performed on the ^{27}Al single-pulse MASNMR spectra (**Figure 4-3**). As evidenced by the observed decrease in the ratio of $Al^{IV}a$ species and appearance of $Al^{IV}b$ species in $1SiO_2$@am-Al_2O_3 ($Al^{IV}a$= 32.3% and 27.3%, $Al^{IV}b$= 0% and 4.5% for am-Al_2O_3 and $1SiO_2$@am-Al_2O_3, respectively, **Table 4-2**), we conclude that the introduced silanol linkage on the mesoporous alumina firstly attract accessible Al^{IV} species for Si-OH---$Al^{IV}b$ Brønsted acid site formation and the creating the SiO_2-Al_2O_3 nanolayer. After consuming all accessible Al^{IV} species, the extra surface silanol originated from adding extra Si species cycles turn to interact with the surface accessible Al^{V} species, and contributes to the increase in the concentration of silanol linkage, the structure of Si-OH---$Al^{V}b$, in $2SiO_2$@am-Al_2O_3 and $5SiO_2$@am-Al_2O_3 catalysts ($Al^{V}b$= 5.1% and 10.3% for $2SiO_2$@am-Al_2O_3 and $5SiO_2$@am-Al_2O_3, respectively, **Table 4-2**) and which led to a thicker mixed oxide nanolayer.

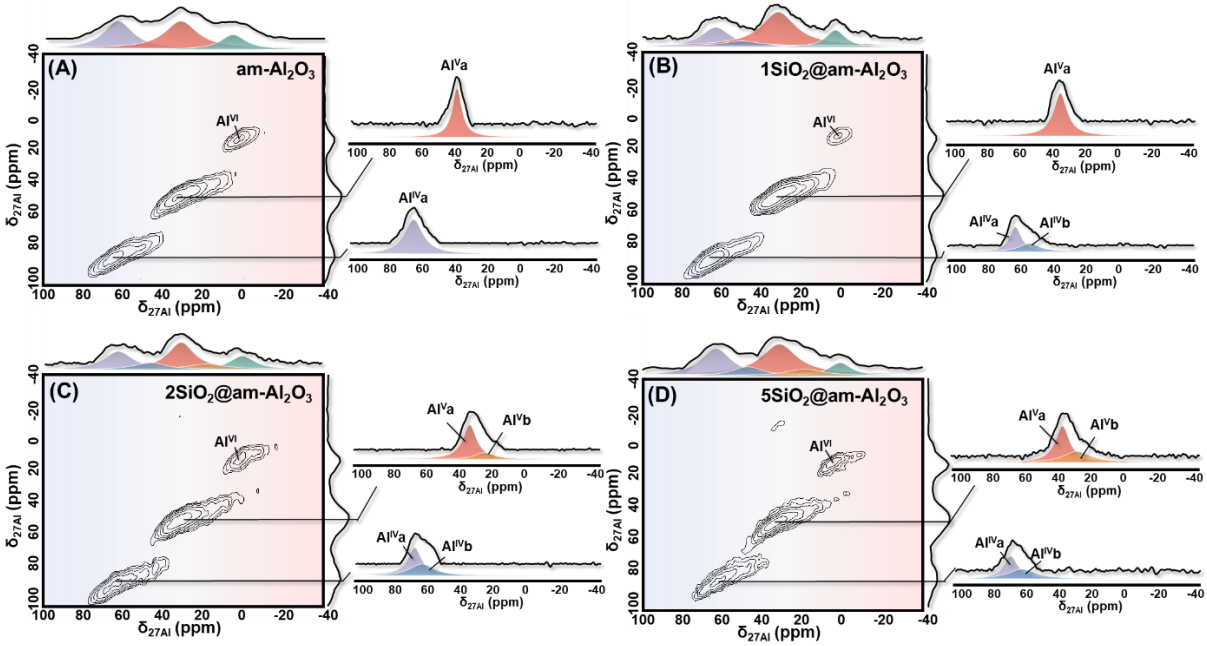

Figure 4-2 2D ^{27}Al multiple quantum MASNMR spectra and corresponding slides for species identification for SiO_2@am-Al_2O_3 and parent am-Al_2O_3 catalysts.

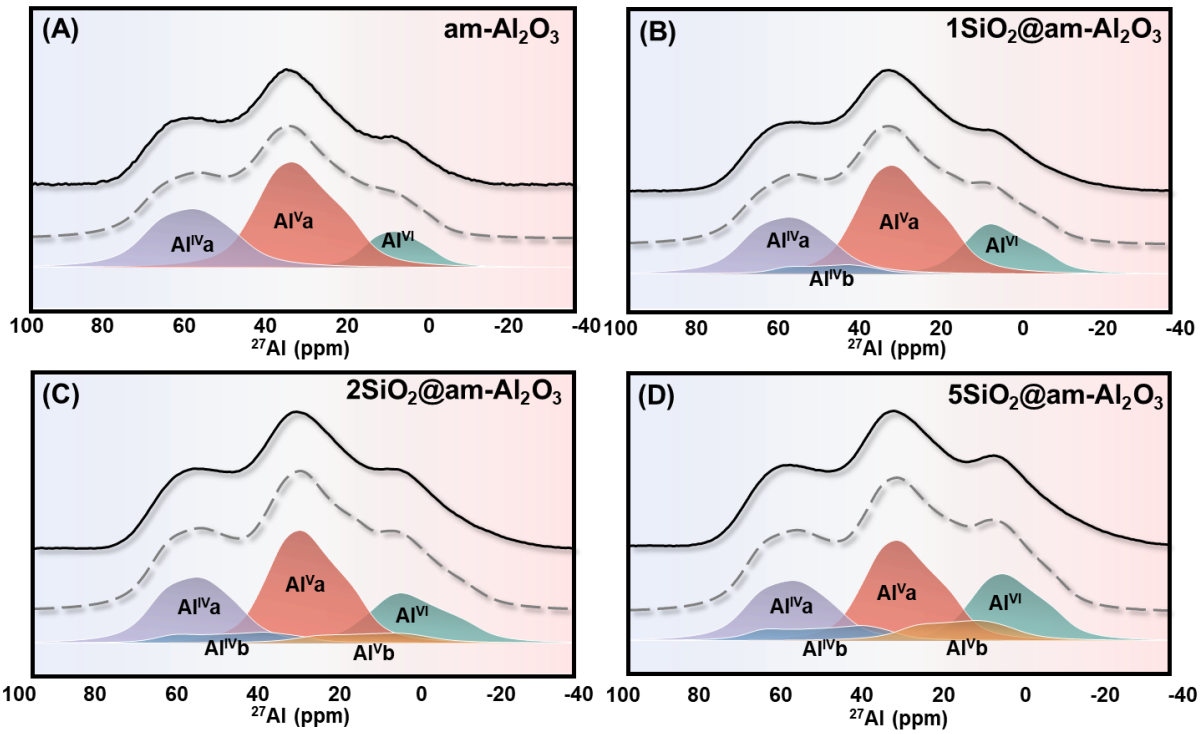

Figure 4-3 ^{27}Al single-pulse MASNMR spectra and corresponding simulations for SiO_2@am-Al_2O_3 and am-Al_2O_3 catalysts.

Table 4-2 Summary of 2D ^{27}Al MQMAS NMR parameters[a]

Catalysts	$Al^{IV}a$ (%)	$Al^{IV}b$ (%)	$Al^{V}a$ (%)	$Al^{V}b$ (%)	Al^{VI} (%)
am-Al_2O_3	32.3	-	53.9	-	13.8
1-SiO_2/am-Al_2O_3	27.3	4.5	51.8	-	16.4
2-SiO_2/am-Al_2O_3	24.5	7.3	44.1	5.1	19.8
5-SiO_2/am-Al_2O_3	21.3	7.1	37.0	10.3	24.3

To reveal the structure-acidity relationship, the surface-accessible acid sites have been probed by trimethylphosphine oxide (TMPO) molecules. Via the utilization of ^{31}P MASNMR experiments, varied acid sites can be quantitatively distinguished[371, 374, 375]. Due to the lack of effect of heteroatoms on the local structure of aluminium sites, Al_2O_3 provides barely any BAS. Compared to the parent mesoporous Al_2O_3 which showed only LAS-related ^{31}P peak at *ca.* δ_{31P} = 46 ppm, the BAS-related ^{31}P peak (δ_{31P} = 61-62 ppm) can be observed for all silanol linked Al^{V} enriched alumina samples (**Figures 4-4A-D**). Because the isolated surface SiOH is non-acidic, the observed BAS could only be generated by silanol linkage on the outermost SiO_2-Al_2O_3 nanolayer. This confirmed that the stepwise addition of SiO_2 resulted silanol linkage contributed to the formation of surface BAS. **Table 4-3** summarized the concentrations and

fractions of different acid sites. The appearance of BAS on the SiO_2-Al_2O_3 overlayer is consistent with the observed second $Al^{IV}b$ and $Al^{V}b$ species in **Figure 4-2** and **Figure 4-3**, indicates that the formed silanol linkage contributed to charge imbalance of the local structure, result in the formation of surface hydroxyl with Brønsted acidity on SiO_2@am-Al_2O_3.

The ^{1}H-^{27}Al CP/MAS HETCOR NMR has provided direct evidence for the formation of BAS on the surface of SiO_2@am-Al_2O_3 (**Figure 4-4E**). Strong interaction contours have been recorded at (δ_{1H} = 1.9 ppm, δ_{27Al} = 61.8 ppm) and (δ_{1H} = 1.9 ppm, δ_{27Al} = 35.7 ppm). According to ^{1}H MASNMR spectra (**Figure S4-4**), the peak at δ_{1H} = 1.9 ppm appeared after the formation of silica-alumina nanolayer, and the intensity increased with the increase in the thickness of the silica-alumina nanolayer. This observation demonstrated that the peak at δ_{1H} = 1.9 ppm originated from the surface silanol linkage (SiOH), which was consistent with the assignments for other amorphous silica-alumina systems such as MCM41 and FSP-ASA[376,377]. Thus, the observed contours in the ^{1}H-^{27}Al CP/MAS HETCOR NMR confirmed the spatial relationship between silanol protons and Al^{IV} and Al^{V} species. These contours give direct spectra evidence on the formation of surface Brønsted acidic Si-OH---$Al^{IV/V}$ structure via silanol linkage in the silica-alumina nanolayer. Most importantly, the contour at (δ_{1H} = 1.9 ppm, δ_{27Al} = 35.7 ppm) with stronger intensity suggests that the surface BAS on 5-SiO_2@am-Al_2O_3 are majorly provided by Al^{V} species. Consistently, the predominance of Al^{V}-BAS on 5-SiO_2@am-Al_2O_3 can also be explained by the relationship between the concentration of silanol linked $Al^{V}b$ species in the silica-alumina nanolayer and surface BAS. Compared to the 2-SiO_2@am-Al_2O_3, the 5-SiO_2@am-Al_2O_3 maintained similar fractions on $Al^{IV}b$ species (7.3% and 7.1% for 2-SiO_2@am-Al_2O_3 and 5-SiO_2@am-Al_2O_3, respectively, **Table 4-2**) but higher fraction on $Al^{V}b$ (5.1% and 10.3% for 2-SiO_2@am-Al_2O_3 and 5-SiO_2@am-Al_2O_3, respectively, **Table 4-2**). This is positively related to the concentration increase in the surface BAS ($1.8x10^{-2}$ mmol/g and $2.9x10^{-2}$ mmol/g for 2-SiO_2@am-Al_2O_3 and 5-SiO_2@am-Al_2O_3, respectively, **Table 4-3**).

Besides, the quench of the AlOH groups and increased intensity of the silanol linkage are in good agreement for the increasement of BAS and the reduction of LAS density (**Figure S4-4, Figure 4-4A-D** and **Table 4-3**). This is because there are fewer surface exposed isolated Al species on the 5-SiO_2@am-Al_2O_3. The surface isolated Al species on am-Al_2O_3 were either entirely covered by the SiO_2-Al_2O_3 nanolayer or contributed to silanol linkage and BAS construction.

Thus, based on abovementioned local structure characterizations, we provide the plausible BAS structures for SiO_2@am-Al_2O_3 (**Figure 4-4F**). Since the silanol linkage contribute to only one new Al^{IV} species after one cycle of SiO_2 deposition on the silica-alumina nanolayer, we reckon that the spatial proximity between the surface active Al^{IV} and silanol linked with the surface BAS (Al^{IV}-BAS) on the outermost surface of 1-SiO_2@am-Al_2O_3. With more cycles of SiO_2 deposition, higher silanol linkage concentrations contributed to the larger surface SiO_2-Al_2O_3 regions. Combining with the observed second Al^V species and its correlation with surface silanol group, we proposed that after consuming all the surface active Al^{IV} species, the Al^V species start to play a dominant role in the formation of BAS within the SiO_2-Al_2O_3 nanolayer (Al^V-BAS).

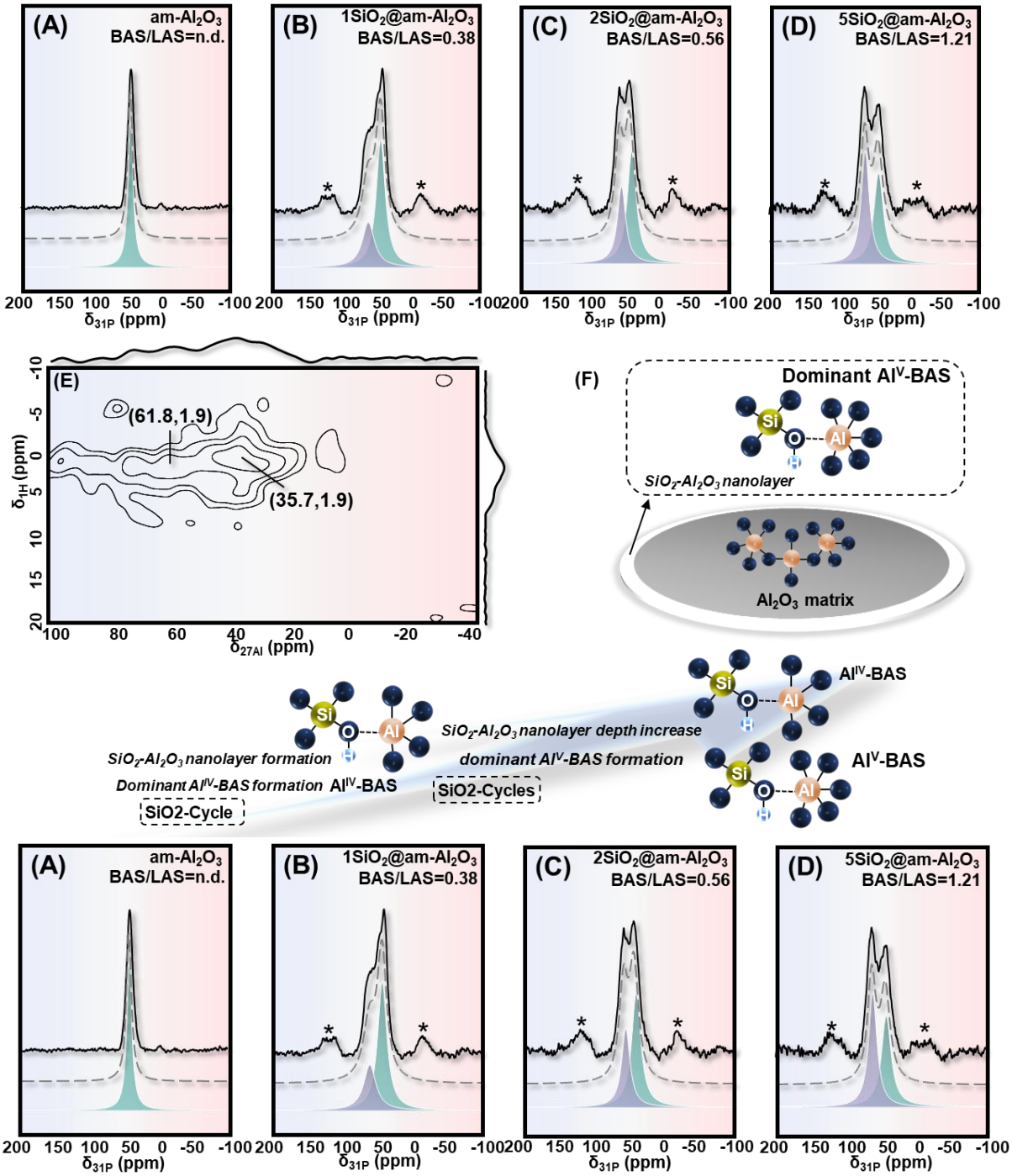

Figure 4-4 (A-D) ^{31}P single-pulse MASNMR spectra and corresponding simulations for SiO_2@am-Al_2O_3 and am-Al_2O_3 catalysts; (E) ^{1}H-^{27}Al HETCOR MASNMR spectra, (F) plausible BAS formation route of 5SiO_2@am-Al_2O_3

Table 4-3 Concentrations and fractions of acid sites of SiO_2@am-Al_2O_3 and parent am-Al_2O_3 materials

Catalysts	Total acidity[a] ($x10^{-2}$mmol/g)	BAS ($x10^{-2}$mmol/g)	LAS ($x10^{-2}$mmol/g)	BAS/LAS (%)
am-Al_2O_3	4.5	-	4.5	-

1-SiO_2/m-Al_2O_3	5.1	1.4	3.7	0.38
2-SiO_2/m-Al_2O_3	5.0	1.8	3.2	0.56
5-SiO_2/m-Al_2O_3	5.3	2.9	2.4	1.21

[a]Total acidity and BAS and LAS were calculated based on the peak integrations and simulations of ^{31}P MAS NMR spectra.

4.2.3 Catalytic performance of 1,2 propanediol conversion to propanal on SiO_2@am-Al_2O_3

The yield of renewable biomass fuels like biodiesel is on the rise. During the manufacture of biodiesel fuel, glycerol is produced as the primary by-product, while 1,2 propanediols are often the primary products in subsequent hydrogenolysis reactions. To fully utilize plant biomass as a carbon resource, it is necessary to produce useful chemicals from propanediols. Herein, the catalytic performance of 1,2 propanediol (1,2PDO) conversion to propanal on the prepared SiO_2@am-Al_2O_3 and conventional zeolite catalysts have been summarized in the **Figure 4-5**.

Compared to Lewis acidic am-Al_2O_3 which showed no catalytic activity to the 1,2 PDO conversion, the observed conversion on all other catalysts proved that the conversion of 1,2 PDO to propanal is driven by BAS. This is also proved by the huge increase in the turnover number (TON) from 12.4 mol_c/g_{cat} for 1SiO_2@am-Al_2O_3 to 62.9 mol_c/g_{cat} for ZSM-5 catalysts with the increase in the total BAS quantity from 1.4 x10^{-2} mmol/g to 28 x10^{-2} mmol/g. However, with respect to turnover frequency (TOF), the efficiency of the BAS on SiO_2@am-Al_2O_3 catalysts were much higher compared to the silica-alumina counterparts of ZSM-5 (>7.0 $mmol_c/(mmol_{BAS}$ g) and 1.9 $mmol_c/(mmol_{BAS}$ g), respectively). The enhanced TOF for SiO_2@am-Al_2O_3 could originate from the relatively homogenous distribution of the BAS on the outermost surface of the catalysts[378]. And the presence of BAS within mesoporous gives no limitation on the diffusion of the large biomass 1,2PDO molecules. Interestingly, although the BAS acidity was identical for SiO_2@am-Al_2O_3 (**Figure 4-5A**), compared to the TOF for 2SiO_2@am-Al_2O_3 and 5SiO_2@am-Al_2O_3 (7.61 and 7.77 $mmol_c/(mmol_{BAS}$ g, respectively), the TOF for 1SiO_2@am-Al_2O_3 was slightly lower (7.08 $mmol_c/(mmol_{BAS}$ g). Because the Al^V-BAS is only present in the 2SiO_2@am-Al_2O_3 and 5SiO_2@am-Al_2O_3, the higher TOF could be explained by the higher catalytic activity of Al^V-BAS to Al^{IV}-BAS with respect to 1,2PDO conversion. With the presence of the highest amount of Al^Vb species and silanol linkage (**Table 4-2**), the 5SiO_2@am-Al_2O_3 gave the highest TOF with predominant Al^V-BAS.

The effect of temperature has also been evaluated on the SiO_2@am-Al_2O_3 catalysts. As can be seen from **Figure 4-5B-D**, the TON of 1,2PDO conversion increased with the increase of temperature, proving the temperature dependence of the reaction. Especially, with the presence

of a large amount of Al^{V}-BAS with higher catalytic activity, the 1,2PDO conversion initiate at a lower temperature (190°C for $5SiO_2$@am-Al_2O_3) compared to other counterparts with predominant Al^{IV}-BAS. (210°C for $1SiO_2$@am-Al_2O_3 and $2SiO_2$@am-Al_2O_3). With the increase in temperature, the TON of the aim product propanal increased at a faster rate compared to the side-product of DXO, which was the predominant product at low reaction temperature results from the acetalization of propanal with 1,2PDO[379]. With the increase in temperature, the increase rate in the TON of DXO is limited with a concurrent quick yield increase in propanal. This can be explained by the hydrolysis of DXO to propanal under elevated temperature[380]. Additionally, compared to the moderate selectivity of side-product of allyl alcohol and other C3 from parallel dehydration on $1SiO_2$@am-Al_2O_3 (**Table 4-4**), the much lower selectivity of such product on $5SiO_2$@am-Al_2O_3 also suggests the enhanced catalytic performance of Al^{V}-BAS.

Because the crude industrial-level biomass 1,2PDO solution contains water in large quantity. The functional industrial catalyst for 1,2PDO conversion should maintain high water tolerance. To evaluate the water tolerance and stability of Al^{V}-BAS, $5SiO_2$@am-Al_2O_3 have been applied for the conversion of 1,2PDO under the presence of cofeed steam (10 and 20 %v/v). By changing the flow rate of the carrier gas (H_2), the feed rate of 1,2PDO was kept constant with varied cofeed steam concentrations. As shown in **Figure 4-5E**, with the co-existence of steam, the propanal selectivity is largely increased. This improvement indicates a positive effect of water vapor in promoting the hydrolysis of DXO to propanal, which is consistent with the study for other catalyst systems[380, 381]. With the presence of water vapor at different concentrations, the reaction rate and selectivity have barely varied (**Figure 4-5E**). This observation supports that the catalyst is highly tolerant to co-existing steam and the active Al^{V}-BAS showed stability. The observed stable catalytic performance can be explained by the unaltered acid sites on the catalyst surface during the contact with vapor and reaction. Because the hydrolyzation of Al-O-Al, Si-O-Si, and/or Al-O-Si bond by cofeed steam contributes to no BAS but only non-acidic SiOH or basic AlOH, the unaffected acid properties of the catalyst lad to no influence on the 1,2PDO conversion. This is unlike the proposed positive effect of high steam concentration on the 1,2PDO conversion as reported for other catalysts due to the altered surface acid properties[380].

The best SiO_2@am-Al_2O_3 catalyst has also been applied for the stability test and have been shown in **Figure 4-5F**. Because the metal-H_2 and steam contribute to the suppression of coke deposition during the 1,2PDO conversion, the stability test has been done with the presence of

carrier gas of H_2 and cofeed steam (20 %v/v)[382]. Unlike microporous zeolite catalysts which deactivate quickly, the $5SiO_2$@am-Al_2O_3 showed relatively stable catalytic performance during the 12 h continuous 1,2PDO conversion reaction, demonstrating that the Al^V-BAS was stabilized as active sites. When compared to microporous ZSM-5, the absence of micropores allows for smoother reaction and product release because coke can block the active surface BAS on the micropores, causing deactivation. The slight reduction in the conversion and selectivity might originate from the deposition of removable organic compounds on the surface of the catalyst.

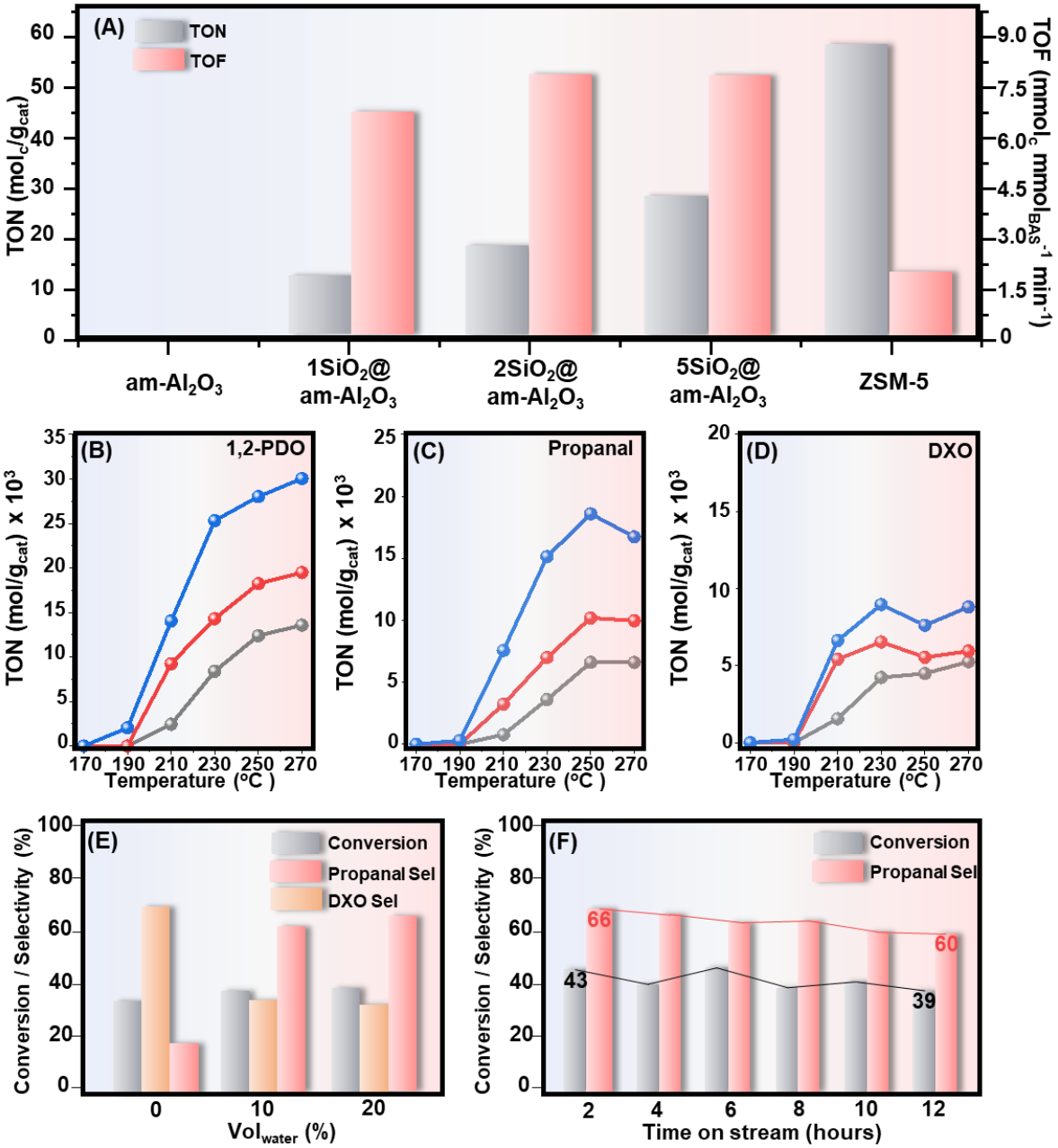

Figure 4-5 Reaction performance of SiO_2@am-Al_2O_3 and counterpart catalysts. (A) Conversion of 1,2 PDO (80% v/v) aqueous solution (0.6 mL/h) at 250 ºC for 2 h in a continuous reactor (TONs = converted reactant (mol_c)/mass of catalysts (g)) (B) 1,2 PDO conversion (C) Propanal yield (D) DXO yield over SiO_2@am-Al_2O_3 catalysts (TON = converted reactant or yield product (mol)/mass of catalyst (g)). (E) Conversion of 1,2 PDO solution (0.6 mL/h) without/with cofeed steam (0, 10, 20 %v/v) over 5SiO_2@am-Al_2O_3, (F) stability test on 5SiO_2@am-Al_2O_3 with 1,2 PDO (80% v/v) aqueous solution (0.6 mL/h).

Table 4-4 Catalytic performance of the tested zeolites in acetalization of furfural with ethanol

Catalysts	1,2 PDO Conversion (%)[a]	Propanal Selectivity (%)	Dioxolane Selectivity (%)	Allyl Alcohol Selectivity (%)	Other C3 Selectivity (%)	TOF (min^{-1})
am-Al_2O_3	-	-	-	-	-	-
1-SiO_2@am-Al_2O_3	18.9	52.3	35.2	2.9	9.6	7.08

2-SiO_2@am-Al_2O_3	27.8	56.9	32.4	3.4	7.3	7.61
5-SiO_2@am-Al_2O_3	42.7	66.4	27.2	1.8	4.6	7.74
ASA/15	61.5	41.5	54.1	2.6	1.8	4.20
ZSM-5	95.8	88.9	10.2	0.5	0.4	1.87

[a]Conversion of 1,2 PDO (80% v/v) aqueous solution (0.6 mL/h) using 50 mg catalyst at 250 °C for 2 h in a continuous reactor with carrier gas of H_2, total flow rate with H_2 balanced of 30 ml/min. [b] Turnover frequency (TOF) was calculated when the 1,2 PDO conversion was lower than 10%. TOF= Total mole of reactant consumed / Total Brønsted acid sites / Reaction time. Total density of acid sites and the density of Brønsted acidity were calculated via ^{31}P MAS NMR spectra.

To further verify how the predominant Al^V-BAS drives the 1,2 PDO conversion to propanal, *in situ DRIFTS* was conducted to monitor the 1,2 PDO evolution on the 5-SiO_2@am-Al_2O_3 under the reaction temperature of 250°C. **Figure 4-6A** gives the plots of the typical DRIFTS spectra on different reaction stages. After the addition of 1,2 PDO vapour with a carrier gas of H_2, -OH bonds of 1,2 PDO molecules can be observed on the spectra at *ca.* 2790 cm^{-1} to 2960 cm^{-1}. Due to the presence of Al^V-BAS with mobile proton, the conversion of 1,2 PDO to propanal involves an initial protonation step. Because the hydroxyl groups at the β position maintain a higher negative charge compared to the primary α hydroxyl groups[383], the mobile proton of Al^V-BAS could selectively protonate the hydroxyl groups at β position of 1,2 PDO. The protonated unstable 1,2 PDO then rapidly dehydrated to a propanol carbenium ion with the observed -OH stretch of H_2O molecule at *ca.*3550-3750 cm^{-1}. After adding the 1,2 PDO vapour, with time evolving, the C=C stretch peak appeared at 1660 cm^{-1}, this hints at the formation of prop-1-en-1-ol or allyl alcohol[384]. Because the selectivity to allyl alcohol was low (<5%, **Table 4-4**), the C=C stretch was assigned from prop-1-en-1-ol. It originated from the deprotonation of the carbenium ion. The generated protons from the deprotonation process can replenish the consumption of the mobile protons of Al^V-BAS and contribute to active Al^V-BAS for the next catalytic cycle. After removing the 1,2 PDO vapour from the system, the -OH bands related to 1,2 PDO molecule gradually disappeared (**Figure 4-6A**). Besides, the peak at 1660 cm^{-1} gradually disappeared with the observation of a new peak at 1710 cm^{-1} with time evolves. This change can be assigned to the disappearance of the C=C stretch followed by the appearance of the C=O stretch, which indicates the formation of the aim product propanal from the tautomerization of prop-1-en-1-ol[385, 386].

The corresponding plausible reaction pathway has been drawn in **Figure 4-6B**. After the introduction of 1,2 PDO vapour on the surface of 5-SiO_2@am-Al_2O_3, the accessible surface BAS selectively protonates the secondary hydroxyl group of the incoming 1,2 PDO molecules. The protonated 1,2 PDO molecule readily converts into the propanol carbenium ion with the

formation of one H_2O molecule. Then, the unstable carbenium ion releases one mobile proton to replenish the consumed proton from BAS for the next catalytic cycle and form prop-1-en-1-ol. And the tautomerization process eventually converts the prop-1-en-1-ol into desired propanal.

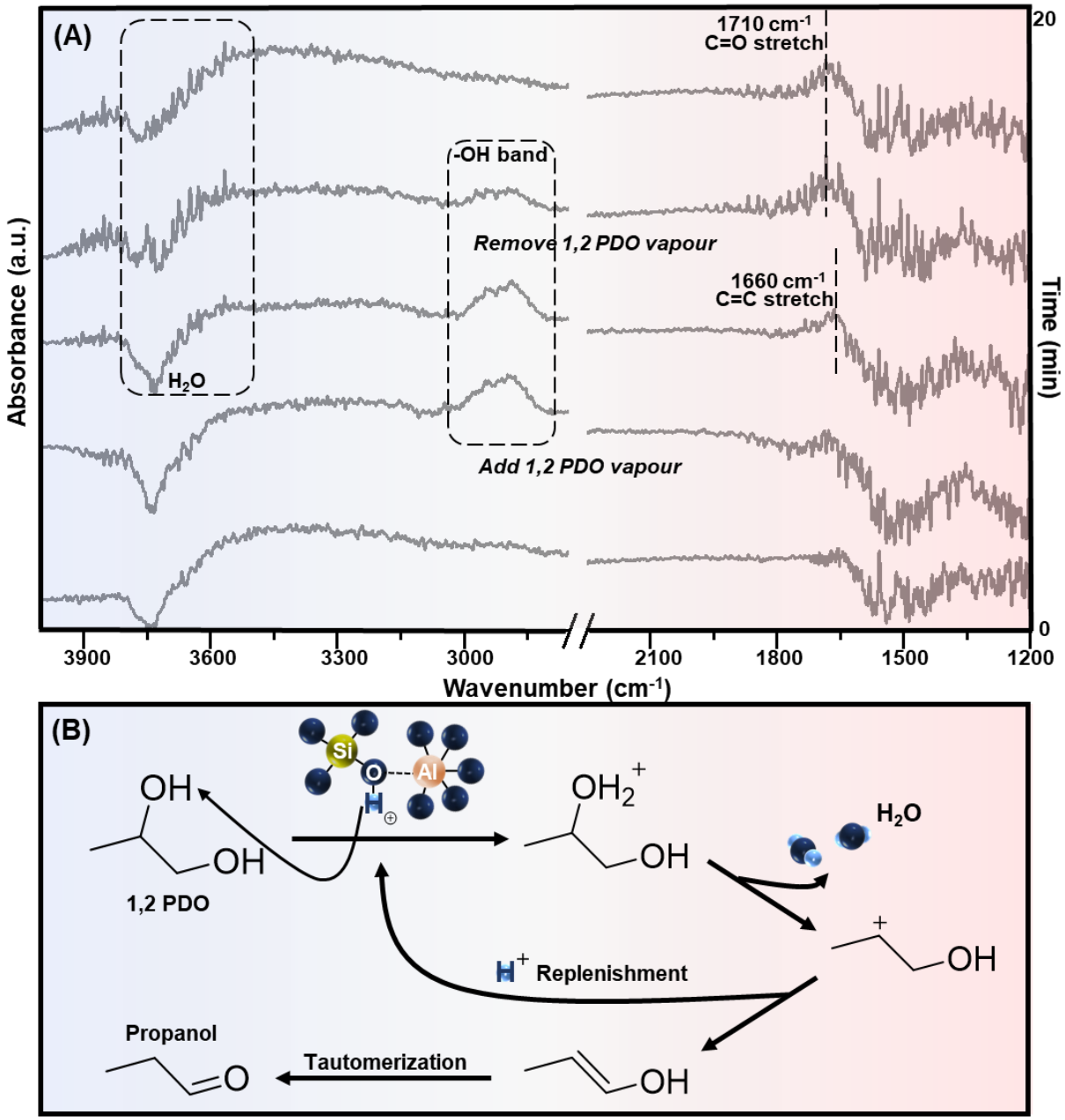

Figure 4-6 (A) Real-time DRIFTS spectra on $5SiO_2$@am-Al_2O_3 were conducted with/without 1,2 PDO vapour flow at 250°C under carrier gas of H_2. The single-beam spectrum recorded on 5-SiO_2@am-Al_2O_3 at 250°C under carrier gas of H_2 was used as the reference spectrum. (B) The corresponding plausible reaction mechanism of the 1,2 PDO conversion on $5SiO_2$@am-Al_2O_3.

4.3 Conclusions

In conclusion, this work demonstrated the cheap and simple preparation of Al^V-based moderate Brønsted acid site on conformal SiO_2-Al_2O_3 overlayer of silanol linked mesoporous

Al_2O_3. The addition of cycles of Si species deposition alters the concentration of silanol linkage and the thickness of the SiO_2-Al_2O_3 overlayer. Based on the EELS and multinuclear ssNMR characterizations, the mechanism for Brønsted acid site formation has been proposed. Initially, the incoming silanol link with neighbouring Al^{IV} to create Al^{IV}-BAS on the oxide-oxide nanolayer. However, once all accessible Al^{IV} species are consumed, any remaining surface silanol groups that are adjacent to Al^{V} take over the responsibility of forming BAS and contribute to the formation of Al^{V}-BAS on the SiO_2-Al_2O_3 nanolayer. And the silanol linked Al^{V}-BAS showed enhanced catalytic efficiency compared to Al^{IV}-BAS for 1,2 PDO conversion. The application of low-cost and straightforward synthesis approach enables the potential large-scale utilization of Al^{V}-BAS catalysts.

4.4 Appendix

Figure S4-1 showed the simulation on the ^{29}Si MASNMR spectra, where four signals of Q^n ($Si(OSi)_n$ species have been recorded with the fraction of 23% (δ_{29Si} = -113 ppm), 26% (δ_{29Si} = -104 ppm), 32% (δ_{29Si} = -94 ppm), and 18% (δ_{29Si} = -85 ppm) (corresponding to n from 4 to 1).

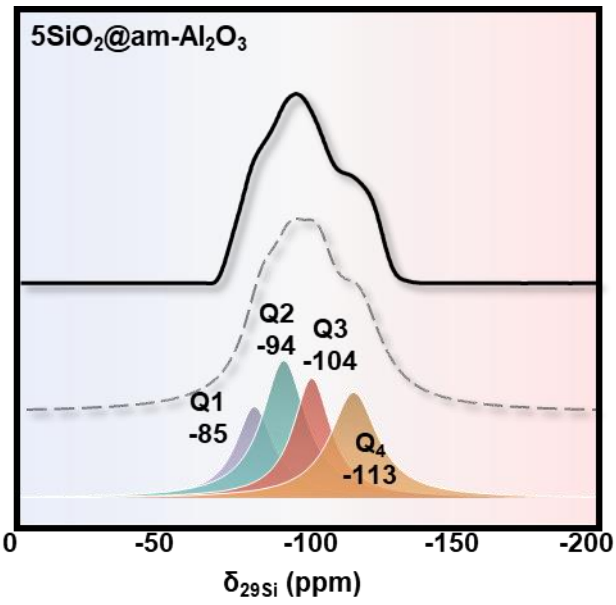

Figure S 4-1 ^{29}Si single-pulse MASNMR spectra and corresponding simulations for $5SiO_2$@am-Al_2O_3

Table S 4-1 Summary of deconvolution of silica species ratio based on the ^{29}Si single-pulse MASNMR spectra

Catalysts	Q^1	Q^2	Q^3	Q^4
5-SiO_2/am-Al_2O_3	18	32	26	23

The ^{29}Si CP MASNMR spectra have only recorded Q^1 and Q^2 species (**Figure S4-2**). The species ratio has varied and are 69% and 31% after CP enhancement for Q^1 and Q^2 species. Thus, the Q^3 species has been assigned to interlayer ($Si(OSi)_3(OAl)$. After CP enhancement, the fraction of Q^1 and Q^2 species varied (18% and 32% before CP enhancement and 69% and 31% after CP enhancement for Q^1 and Q^2 species, respectively). The peaks at δ_{29Si} = -94 and -85 ppm are assigned to the overlaps of $Si(OSi)_2(OAl)_2$ and $Si(OSi)_2(OH)_2$ as well as the mixture of $Si(OSi)_1(OAl)_3$ and $Si(OSi)_1(OH)_3$ groups[387]. These Q^1 and Q^2 species resulted in silanol groups with spatial proximity to aluminium species are the origin of Brønsted acidity.

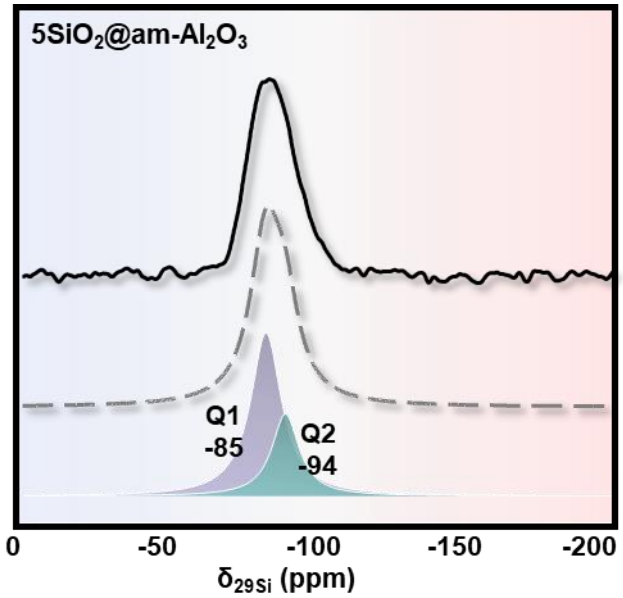

Figure S 4-2 ^{29}Si Cross-Polarization MASNMR spectra and corresponding simulations for 5SiO_2@am-Al_2O_3

Table S 4-2 Summary of deconvolution of silica species ratio based on the ^{29}Si CP MASNMR spectra

Catalysts	Q^1	Q^2	Q^3	Q^4
5-SiO_2/am-Al_2O_3	69	31	-	-

Based on the FTIR spectra (**Figure S4-3**), The positions of the peaks at *ca.* 1100 cm^{-1} and ca. 850 cm^{-1} (T-O-T asymmetry stretching and T-O-T symmetry stretching, respectively) have little variation after the SiO_2 film modification on the am-Al_2O_3 surface, indicating an absence of the large amount of Al-O-Si bonds[388].

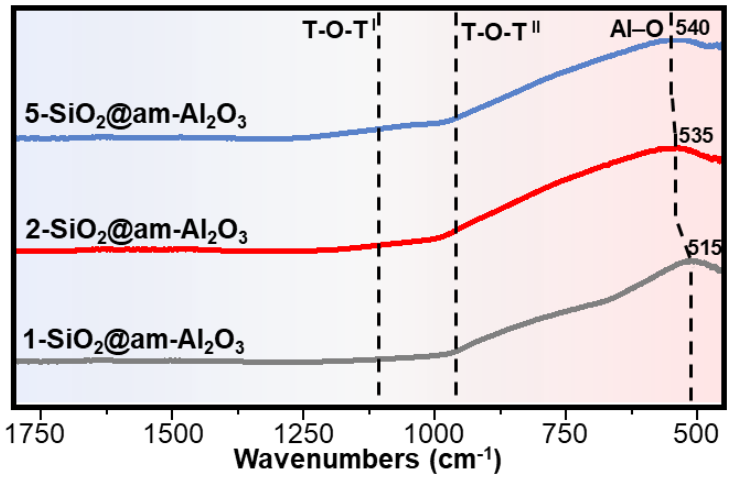

Figure S 4-3 FTIR spectra of the prepared SiO_2@am-Al_2O_3 catalysts

As shown in **Figure S4-4A**, with respect to the Si-O-Si bonds (102.9 eV) in pure silica, a decrease in the Si 2P binding energy for the Si-O bond in SiO_2@am-Al_2O_3 has been observed[389]. The observed decrease indicated an effect of adjacent Al atoms on the Si-O bond, which confirmed the formation of silanol linkage on the surface nanolayer. Consistently, with the presence of neighbouring Si atoms, the Al 2P binding energy of the surface Al-O bond shown in **Figure 4-4B** showed a shift towards higher binding energy with respect to the Al-O-Al bond (73.8 eV) in alumina[390]. These observations suggested the formation of surface Si-O-Al and/or pseudo Si-O---Al bond, which contributes to the electro-negative shift of the Si-O bond and the electro-positive shift of the Al-O bond[391].

Additionally, the oxygen species simulation in **Figure 4-4C** gives the ratio of Si-O^{I} (532.6 eV) and Al-O^{II} (531.0 eV)[390]. Since the ratios of surface O^{I}/O^{II} are much smaller compared to the surface atom% of n(Si)/n(Al) (Shown in **Table 1**), this observation also supports the presence of surface silanol linkage and the corresponding surface Si-O-Al and/or Si-O---Al bond, which also appeared at *ca.* 531.0 eV. With similar binding energy as the Al-O^{II} bond, the silanol linkage contributed to the larger quantity of O^{II} species. Additionally, the increase in SiO_2 deposition cycles contributed to little difference between the ratio of n(Si)/n(Al) and O^{I}/O^{II} (0.04, 0.04, and 0.05 for 1- SiO_2@am-Al_2O_3, 2-SiO_2@am-Al_2O_3, and 5-SiO_2@am-Al_2O_3, respectively). This is consistent with the observed silanol linked SiO_2-Al_2O_3 mixed oxide

overlayer rather than the pure SiO_2 overcoat on the mesoporous alumina substrate. Otherwise, if the step-wised Si species addition cycles lead to the formation of SiO_2 film, the Si-O-Si within pure silica domain should lead to a much higher O^I/O^{II} ratio.

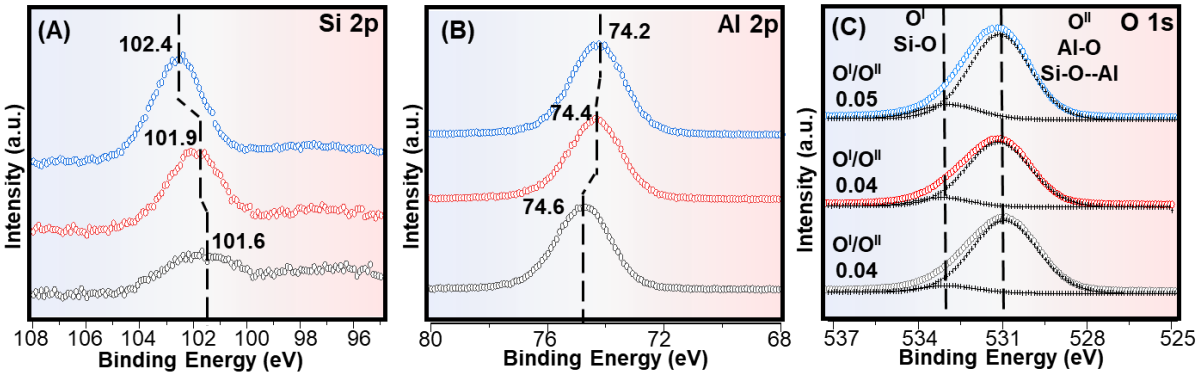

Figure S 4-4 XPS spectra of the prepared SiO_2@am-Al_2O_3 catalysts for (A) the surface Si 2p, (B) the surface Al 2p, and (C) the surface O 1s of the prepared SiO_2@am-Al_2O_3 catalysts.

Table S4-3 was calculated based on Equation 1-4 and the ^{27}Al MQ MASNMR spectra of dehydrated samples.

Table S 4-3 Summary of 2D ^{27}Al MQMAS NMR parameters[a]

	am-Al_2O_3			**1-SiO_2/m-Al_2O_3**			**2-SiO_2/m-Al_2O_3**			**5-SiO_2/m-Al_2O_3**		
	δiso (ppm)	C_{QCC} (MHz)	η	δiso (ppm)	C_{QCC} (MHz)	η	δiso (ppm)	C_{QCC} (MHz)	η	δiso (ppm)	C_{QCC} (MHz)	η
$Al^{IV}a$	63	3.6	0.5	64	3.5	0.5	63	3.6	0.5	65	3.6	0.5
$Al^{IV}b$	-	-	-	60	6.3	0.5	59	6.1	0.5	60	6.4	0.5
$Al^{V}a$	35	3.8	0.5	38	3.8	0.5	38	3.7	0.5	39	3.9	0.5
$Al^{V}b$	-	-	-	-	-	-	31	6.5	0.5	33	6.8	0.5
Al^{IV}	8	3.1	0.7	7	3.1	0.7	8	3.0	0.7	6	3.1	0.7

[a] Isotropic chemical shifts (δ_{iso}), quadrupole coupling constant (C_{QCC}) and asymmetry parameters (η) of each aluminum species were determined by the MQMAS NMR spectra and corresponding calculation of dehydrated SiO_2@am-Al_2O_3 and parent Al_2O_3 samples.

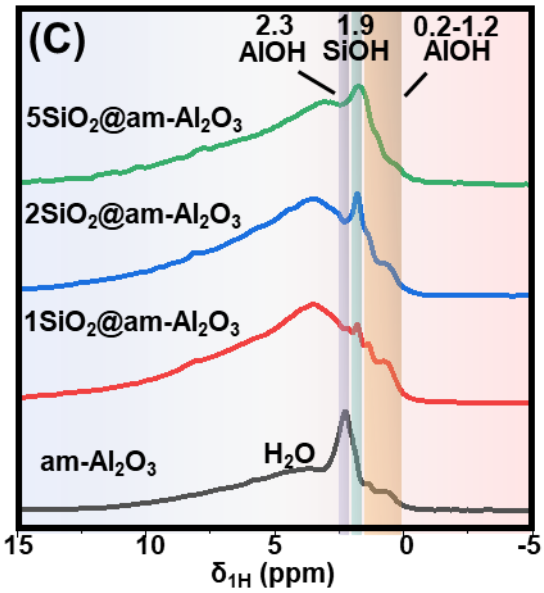

Figure S 4-5 ^{1}H single-pulse MASNMR spectra for am-Al_2O_3 catalysts and SiO_2@am-Al_2O_3

Based on the zoomed EELS mapping image in **Figure S4-6A**, three different sub-nano domains can be observed within the SiO_2-Al_2O_3 nanolayer, which has been assigned accordingly: 1. SiO_2 dominant sub-nano domain, 2. SiO_2-Al_2O_3 mixed oxide sub-nano domain, 3. Al_2O_3 dominant sub-nano domain. The EELS spectra **in Figure S4-6B** were collected on different regions of the SiO_2-Al_2O_3 oxide layer based on **Figure S4-6A**. Compared to SiO_2 dominant sub-nano domain which shows a Si $L_{2,3}$ peak at 108.5 eV, the Si $L_{2,3}$ peak at the SiO_2-Al_2O_3 mixed oxide sub-nano domain showed a negative shift to 108.0 eV[392]. This is consistent with the XPS observation (**Figure 2**) and observed second Al^{IV} and Al^{V} species on ^{27}Al MQ MASNMR spectra (**Figure 3**), confirming the spatial interaction between Si and Al species on the network of SiO_2-Al_2O_3 as the interface. Compared to the Al_2O_3 dominant sub-nano domain, SiO_2-Al_2O_3 mixed oxide sub-nano domain showed a much lower intensity in the octahedral Al species (Al^{VI}, $L_{2,3}$ peak at 84.2 eV). This observation suggests that the majority of the Al species within this sub-nano region are surface active unsaturated Al species.

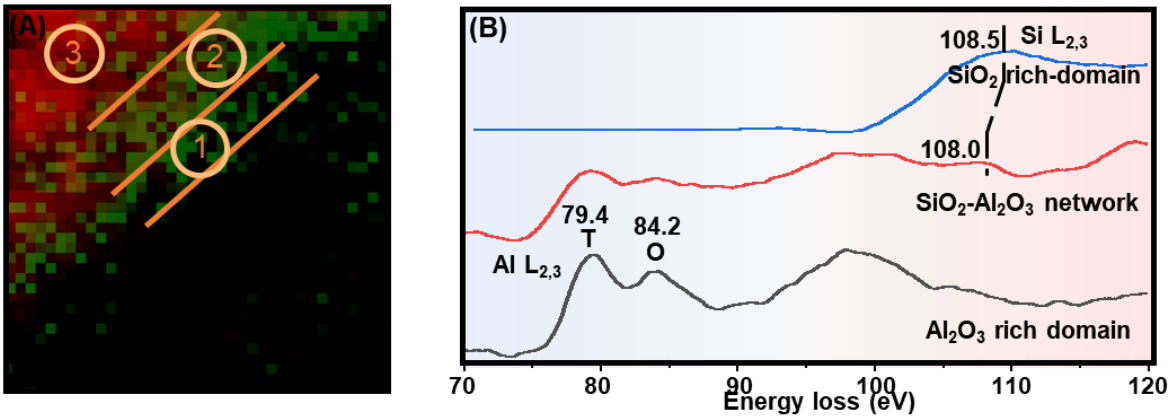

Figure S 4-6 (A) Electron energy loss spectroscopy mapping catalysts with assigned separated regions (1 SiO_2 rich domain, 2 SiO_2-Al_2O_3 network, 3 Al_2O_3 rich domain), (B) Electron energy loss spectra of different regions.

5. Atomic layer deposition of Lewis acidic aluminum species on mesoporous silica-alumina with Brønsted acidity for cascade catalysis

5.1 Introduction

Solid acid, as the most popular heterogeneous catalyst, has received much research and industrial interest in promoting sustainable hydrocarbon transformation and biorefining. Among solid acids, due to the advantages of tunable surface acidity of both Lewis acid site (LAS) and Brønsted acid site (BAS), large specific surface area, adjustable porosity, and cheap synthesis, aluminosilicate materials attracted the most attention[393-395]. Generally, on crystalline aluminosilicates, such as zeolites, the penetration of four-coordinated aluminum species into the tetrahedral silica framework contributes to the establishment of BAS via the formation of bridging hydroxyl structure for compensating local negative charges[396], whereas the dihydroxylation, steaming, or dealumination resulting in extraframework Al species on zeolites are believed to be the origin of surface Lewis acidity[397]. Therefore, both BAS and LAS on zeolites contribute to the bi-acidic catalysts, where a synergistic effect between Brønsted-Lewis pairs has been observed[398, 399]. The synergistic effect gives enhancement of Brønsted acidity for the catalysis[400,401,] , and the cooperation between both acid sites leads to the enhanced performance of multistep catalytic conversion[402, 403].

However, the spatially adjacent BAS-LAS pairs on zeolites generally contribute to the ultra-strong acidity of BAS via LAS withdrawing electron pair from the BAS hydroxyl group. This is beneficial only for catalytic reactions that require strong acidity. For example, with a spatial interaction between a Lewis acidic Zn^{2+} cation and Brønsted acidic SiOHAl, the synergetic effect contributes to an ultra-strong BAS that enhances the activation of the methane C-H bond[404]. The Ga^{3+}-BAS pair results in the enhanced acid strength of Ga-modified ZSM-5, which contributes to an enhanced aromatic selectivity on methanol-to-aromatic conversion[405]. Caused by the polarizing effect of multivalent extraframework Al cations on the SiOHAl group of BAS, the BAS shows a much stronger interaction with the basic probe molecule of acetonitrile (CD_3CN) compared to that of zeolite H, Na-X and H, Na-Y[406]. Nevertheless, the ultra-strong acid site limits the cascade reaction on both sites and results in lower selectivity

for the target products due to side reactions such as over-oxidation[395, 407, 408]. Additionally, the microporous nature of zeolites restricts the entry and diffusion of bulky biomass molecules, limiting their access to the active sites, which further hurdles performance.

In this research, we develop the synthesis strategy to separate BAS and LAS in geometry and promote the cascade reactions on both acid sites via atomic layer deposition (ALD) of the LAS-based domain on BAS-based supports. ALD, as a method to grow thin films, has been considered as a way to coat uniform conformal overlayers and tune the surface properties of catalysts within defined overlayer regions[409]. Currently, ALD has been mainly applied in BAS formation and improvement of silica-alumina catalysts. Stair et al.[410] observed the BAS formation ability of the ALD-deposited non-acidic SiO_2 overlayer on alumina. The formed BAS-based $(AlO)_3Si(OH)$ sites showed enhanced catalytic performance on cyclohexanol dehydration. Ardagh et al.[411] demonstrated the criticalness of the thickness of the overcoat layer to the formation of BAS on the external surface. They found that the catalyst with ~2 nm coatings of SiO_x on Al_2O_3 substrate gives the highest BAS concentration and the prepared BAS on the external surface leads to enhanced performance on 1,3,5-triisopropylbenzene cracking. Similarly, coating alumina on silica also contributes to BAS. Krishna et al.[412] identified the formation of surface BAS between the ALD-formed alumina overlayer and the silica substrate. With 5-10 ALD cycles, the majority of isolated SiOH can be covered, contributing to an enhanced concentration of BAS. Nevertheless, little research focuses on the formation and development of LAS via ALD on silica-alumina catalysts.

Herein, via atomic layer deposited alumina, we develop an LAS-based domain on the external surface of a BAS-based mesoporous silica-alumina substrate and hide the majority of the intrinsic BAS of the substrate inside the nanopores. Thus, BAS and LAS have been separated by the geometry in the catalysts, which is promising for cascade reactions with controlled diffusion. The geometry of the prepared catalysts and the distribution of ALD alumina are characterized by High-Resolution Transmission Electron Microscopy (HRTEM) combined with Electron Energy Loss Spectroscopy (EELS) mapping. Multinuclear ssNMR was used to characterize the BAS and LAS of the samples. Among biomass conversions, converting glucose into platform chemicals 5-hydroxymethylfurfural (HMF) stands as one of the most promising routes for green chemistry[394, 413]. Thus, the typical biorefining cascade glucose conversion is applied as the testing reaction for cascade performance of the prepared catalysts.

5.2 Results and Discussion

5.2.1 Synthesis and geometry of ALD catalysts

To construct the presicely controlled cascade architectural structure, the ALD cycles under elevated temperature were conducted in order to make nano-level architectural modification on the outermost surface. The TMA pulses led to the formation of the Al-C bonds on the outermost surface of the substrate via the replacement of surface silanol hydroxyl protons with Al ions, which provides the prerequisites of the formation of the unique geometry of alumina nanolayer on the silica-based substrates[417]. The following H_2O pulse contributed to the replacement of the outermost surface Al-C bonds with Al-O bonds and led to the formation of alumina nanofilm. With more ALD cycles, the protons of surface AlOH groups can continue to be replaced by Al ions, leading to the increase in the thickness of the alumina nanolayer (**Figures 5-1A-B**).

The geometry of the ALD silica-alumina catalysts has been visualized by high resolution transimission electron microscopy (HRTEM). As shown in **Figures 5-1C-D**, on the outermost surface of the prepared catalysts, a thin nanolayer with similar thickness (d = 3.0 nm and d = 3.3 nm, respectively) can be observed. This finding is in line with the observation of a translucent covering layer in HRTEM images for Al_2O_{3ALD}-SiO_2[419], SiO_{2MLD}-TiO_2[420], and Al_{ALD}-Pt/Al_2O_3[421]. It supports that the ALD process predominantly creates an alumina nanolayer on the outermost surface as an overcoat instead of dispersing aluminium species into the nanopores or network lattice of the support, and which is independent of the substrate composition. Compared to the parent substrates, this is consistent with the observed the small reduction in surface area and pore volume characterized via Nitrogen adsorption/desorption (**Figure S5-1 & S5-3**, **Tables S5-1 & S5-2**), where the ALD-alumina overcoat geometrally partially fill or cap the mesopores. Besides, the absence of crystalline structure in HRTEM images agrees well with the X-ray amorphous structure (**Figure S2**), demonstrating that not only the amorphous nature of the material remained after ALD treatment, but also the alumina overcoat from ALD deposition maintained an amorphous geometry. The EDS elemental mappings in **Figure 5-1E-F** demonstrate the shell-like homogenous coverage of alumina thin overcoat on the support. The absence of an obvious isolated Al domain could contribute to the rapid surface Al-O-Al condensation[422], hinting that no large aggregation of alumina had been formed during the ALD aluminum deposition. Furthermore, to visualize the detailed nano-level local geometry of the prepared cascade architectural silica-alumina, the Electron Energy Loss (EELS) EDS mapping has been applied. In the **Figures 5-1G-H**, the ALD deposited alumina

geometrically contributes to a nano-level shell with *ca.* 3 nm thickness. **Table S5-2** summarizes the physiochemical properties of Al_{ALD}@high silica substrate samples. Based on the surface composition characterization via XPS surface elemental analysis, the surface $n(Si)/n(Al)_{surface}$ of the Al_{ALD}@high silica substrate are much smaller compared to that of the parent substrates (**Tables S5-1 & 5-2**). This finding also supports the visualized observation of the outermost surface distribution of alumina.

Thus, with the characterization evidence mentioned above, regardless of the substrate, we demonstrated that the ALD process can generate shell-like thin alumina nanolayer with *ca.* 3 nm in thickness (0.15 nm/cycle) on the substrate while having minimal effect on the existing global geometry (**Figure 5-1B**).

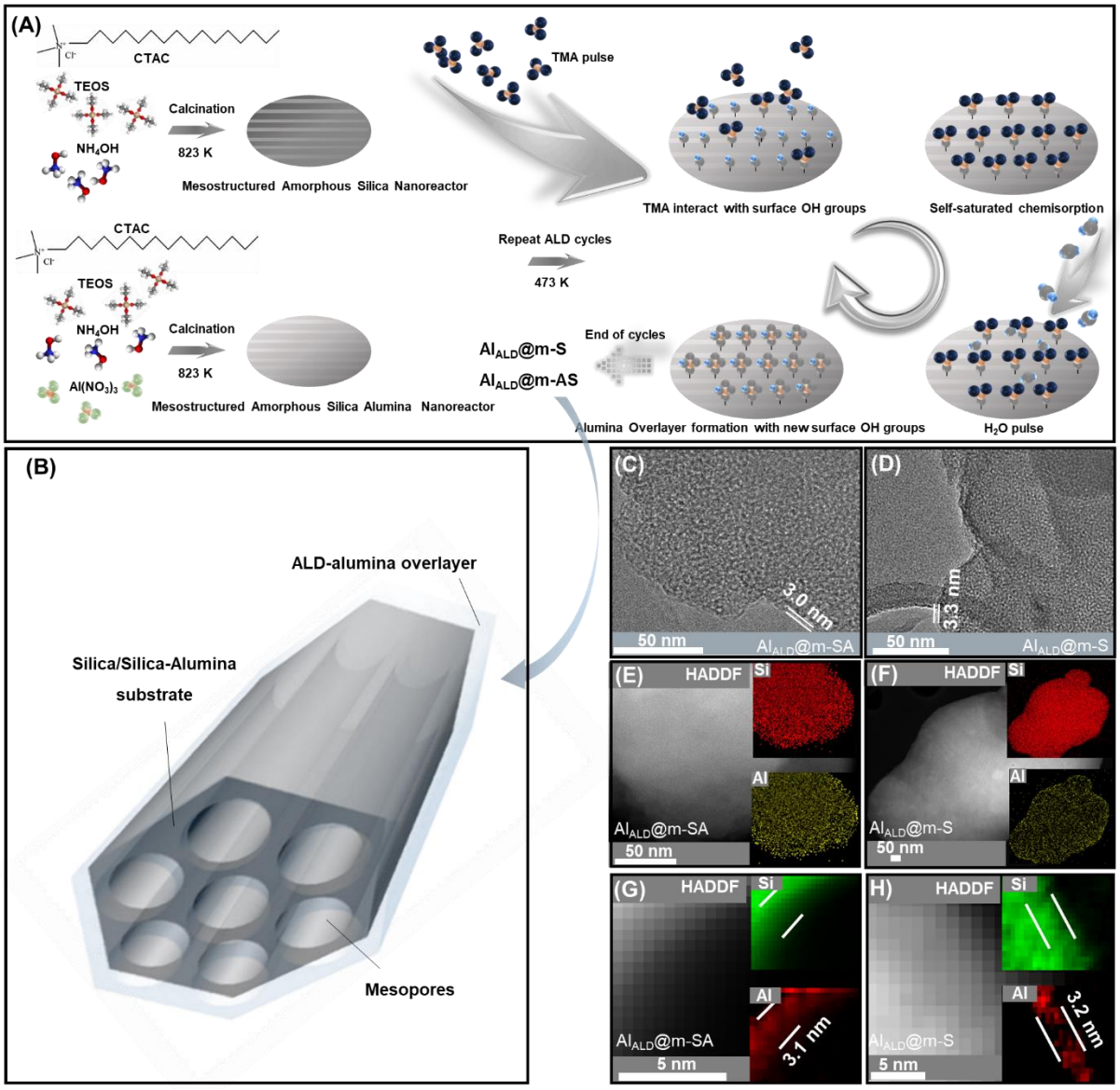

Figure 5-1 (A) Scheme of Al_{ALD}@high silica substrate synthetic approach; (B) Schemitic diagram of Al_{ALD}/high silica substrate; HRTEM images of (C) Al_{ALD}/m-SA and (D) Al_{ALD}/m-S; EDS mapping image of (E) Al_{ALD}/m-SA and (F) Al_{ALD}/m-S; Electron Energy Loss EDS-Mappings of (G) Al_{ALD}/m-SA and (H) Al_{ALD}/m-S

5.2.2 Acidity characterization of ALD catalysts

The characterization of acid sites and their local structure was performed by multinuclear solid-state NMR spectroscopy. With the ability of spin manipulation to avoid second-order quadripolar line broadening, 2D ^{27}Al MQMAS NMR has been conducted (**Figures 5-2A-B**) for resolving Al coordination of ALD catalysts with higher resolution and which can be utilized to predict the surface acidity[423]. The isotropic chemical shift demonstrated the presence of four-coordinated Al (Al^{IV}, δ_{iso} = *ca.* 57 ppm), five-coordinated Al (Al^{V}, δ_{iso} = *ca.* 36 ppm), and six-coordinated Al (Al^{VI}, δ_{iso}= *ca.* 7 ppm) in the samples. With the ALD of alumina on pure silica support (Al_{ALD}@m-S), the 2D ^{27}Al MQMAS NMR spectrum and the corresponding 1D ^{27}Al

MAS NMR spectrum of Al_{ALD}@m-S are similar to that of the pure Al_2O_3[424] (**Figures 5-2B & 5-2D**). With the fitting on 1D ^{27}Al MASNMR spectra for quantitative evaluation of Al species, the Al_{ALD}@m-S showed a dominat Al^{VI} species (70.9%, **Table 5-1**), which was generally the contributor of the surface LAS[425]. Differently, the 2D ^{27}Al MQMAS NMR spectrum recorded both strong Al^{VI} and Al^{IV} signals of ALD-alumina on mesoporous silica-alumina (Al_{ALD}@m-SA)(**Figure 5-2A**) and the corresponding 1D ^{27}Al MAS NMR spectrum showed a relatively balanced Al^{VI} and Al^{IV} ratio (36.2% and 45.5% for Al^{IV} and Al^{VI}, respectively, **Figure 5-2C**). Similar to Al_{ALD}@m-S, the surface exposed Al^{VI} species on the ALD deposited alumina nanolayer can generate LAS on external surface of m-SA, while the Al^{IV} species inside the silica network on nanopores of the m-SA support lead to the presence of BAS[414].

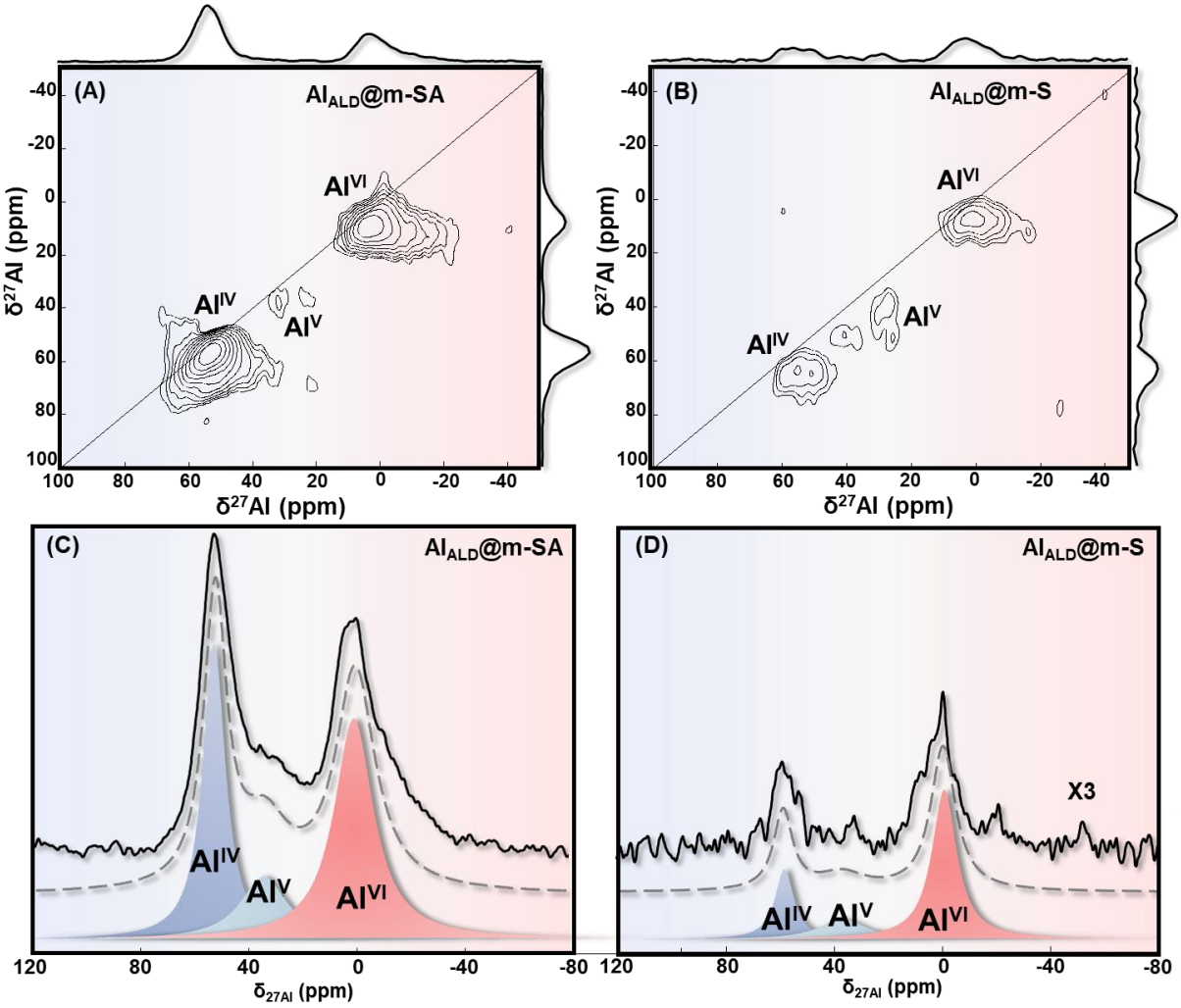

Figure 5-2 Sheared 2D ^{27}Al MQMAS NMR spectra of (A) Al_{ALD}@m-SA and (B) Al_{ALD}@m-S. Contours between F1 and F2 dimensions have been assigned to aluminium species based on the isotropic chemical shift. (C) and (D)

Table 5-1 Summary of deconvolution results and DMFit calculated aluminum species molar ratio.

Catalyst	Al^{IV} (%)	Al^{V} (%)	Al^{VI} (%)
Al_{ALD}@m-SA	36.2	18.3	45.5
Al_{ALD}@m-S	21.3	7.8	70.9
m-SA[22]	94.0	-	6.0

With the help of the TMPO probe molecule, ^{31}P MAS NMR has been utilized to quantitatively test the LAS and BAS acidity on ALD catalysts. Numerous studies demonstrated that TMPO can perform as a functional molecular probe for characterizing the type, strength, and accessibility of surface acid sites[426-427]. With accessible BAS inside nanopores, a hydrogen bond can be formed between the hydroxyl proton of BAS and the oxygen atoms of P═O, giving δ_{31P} = 65 to 67 ppm in ^{31}P MAS NMR spectra (**Figure 5-3**)[428]. The direct adsorption of TMPO on LAS also contributes to δ_{31P} = 43-45 ppm in ^{31}P MAS NMR spectra (**Figure 5-3**). This is attributed to the positive charge compensation of LAS by the electron cloud density around the ^{31}P nucleus. The chemical shifts observed in the 31P MAS NMR spectra of TMPO-loaded samples are indicative of the acidic strength of the acid sites within the catalyst. The chemical shifts observed suggest that this catalyst exhibits moderate acidity.

The one-dimensional ^{31}P MAS NMR spectra provies the quantitative information on the surface accessible acid sites (**Figures 5-3A-C**). With the predominant Al^{IV} species on the m-SA substrate, the m-SA support exhibits predominant Brønsted acidity of 0.17 μmol/g (**Figure 5-3A**, **Table S5-1**). With the identified strong Al^{VI} signal intensity, the Al_{ALD}@m-S had dominant surface LAS of 0.19 μmol/g (**Figure 5-3B, Table S5-2**). Because the network with pure silica (m-S) exhibits almost no acidity, this observation confirmed that the ALD process produces mainly LAS on the outermost surface of mesoporous silica. The generated 0.01 μmol/g BAS could contribute to the BAS at the interface between the silica domain of the m-S substrate and the ALD produced alumina nanolayer domain. In the Al_{ALD}@m-SA, the BAS has ten times higher concentration (0.10 μmol/g) compared to that of Al_{ALD}@m-S. It can be explained by the BAS originally existing on the mesopores of the m-SA support, which was not overlapped by the surface LAS generated by ALD process and was still accessible to the reactant (**Figure 5-3C**). This is in agreement with the predominance of BAS on m-SA (**Figure 5-3A**). Besides, the lower BAS concentration in Al_{ALD}@m-SA compared to that of m-SA confirmed that the ALD generated alumina overlayer covered the majority of the BAS on the

external surface of the m-SA substrate, but leaves BAS on nanopores intact (0.17 μmol/g and 0.10 μmol/g for m-SA and Al_{ALD}@m-SA, respectively, **Table S5-1 & 5-2**). Additionally, the similar LAS concentrations observed on both catalysts (0.19 μmol/g and 0.22 μmol/g for Al_{ALD}/m-S and Al_{ALD}/m-SA, respectively, **Table S5-2**) confirm that the identical ALD deposition contributes to the surface LAS on the outermost alumina nanolayer, and which is spatially and chemically independent with the BAS inside the nanopores. Thus, the spatially separated acid sites distribution has been drawn in **Figure 5-3D,** where BAS is located inside the nanopores and LAS on the external surface.

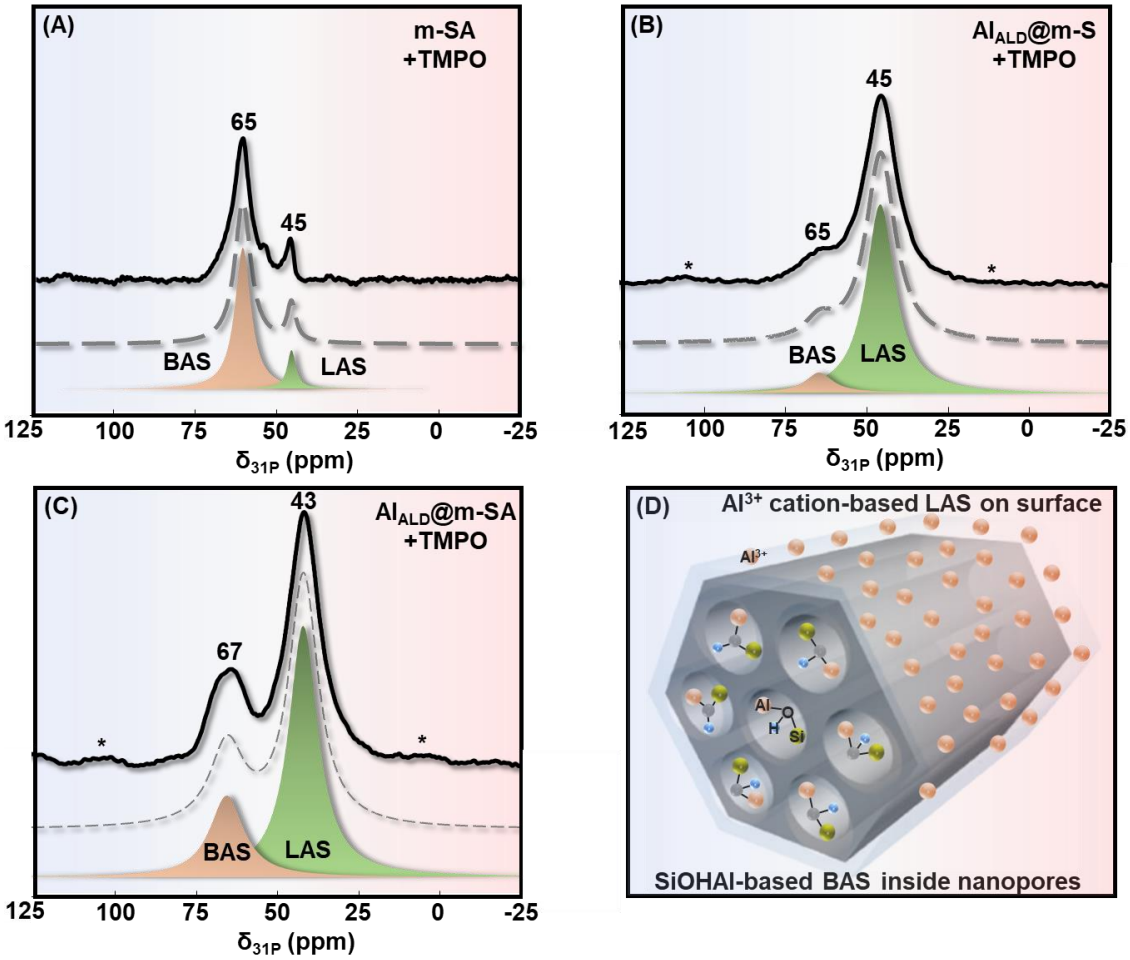

Figure 5-3 ^{31}P MAS NMR spectra of (A)m-SA, (B)Al_{ALD}@m-S, and (C) Al_{ALD}@m-SA catalysts (*represent sidebands) (Black line: spectra, dash line: simulations; coloured blocks: components), (D) the proposed schemetic diagram of the acid site distrubution on Al_{ALD}@m-SA.

5.2.3 Cascade Glucose Conversion on ALD catalysts

The glucose conversion to HMF is a widely studied biomass value-added cascade reaction driven by bi-acidic catalysts and the selectivity of which is largely determined by the acidic properties of the catalyst[430]. It is widely accepted that the LAS promotes the isomerization of glucose to fructose, while BAS is responsible for the secondary dehydration step[431, 432]. For the

applied catalysts, with predominant accessible non-acidic SiOH, accessible surface BAS, and predominant surface LAS on m-S, m-SA, and Al_{ALD}@m-S surface, these catalysts are assigned to be catalysts with non-acidity, predominant Brønsted acidity, and predominant Lewis acidity, respectively. The Al_{ALD}@m-SA catalyst with LAS on the external surface and BAS inside the nanopores is assigned to the cascade structured bi-acidic catalyst, as characterized above.

As shown in **Figure S5-6**, with the absence of acid site (m-S), only low conversion ($C_{Glucose,\ 180min}$ = 21%) can be identified. The reaction rate constants could not be optimized from the non-linear least square regression (not shown). Moderate conversions of glucose can be observed on catalysts with either predominant Lewis acidity (Al_{ALD}@m-S, **Figure 5-4A**) or Brønsted acidity (m-SA, **Figure 5-4B**). With dominant surface Lewis acidity on the ALD deposited alumina overlayer of Al_{ALD}@m-S, the constant rates of glucose decomposition are doubled compared to non-acidic m-S (k_G = 0.00309, and 0.00154 min^{-1}, respectively, **Table S5-4**). This suggests the importance of LAS on glucose activation. And this is also consistent with the observed relationship between chemical hardness and experimental HMF yields in the rate-limiting step of glucose-to-fructose isomerization for six metal chlorides.

With only few accessible BAS on the interface of outermost alumina nanolayer and pure silica substrate, the selectivity of HMF did not increase obviously with the increase in reaction time ($S_{HMF,60min}$ = 13% vs $S_{HMF,180min}$ = 17%, respectively. **Table 5-2**). The accumulation of intermediate fructose with the evolution of time ($S_{fructose,180min}$ = 20%) on the Al_{ALD}@m-S agreed well with the reported claim that the LAS contributes little to the dehydration of fructose but only the glucose isomerization. Consistently, regarding fructose dehydration, the observed low conversion rate and HMF selectivity on Al_{ALD}@m-S ($C_{Fructose,\ 90min}$ = 40% and $S_{HMF,90min}$ = 13%, **Figure 5-4D**) proved that the predominant LAS contribute little to the dehydration of fructose to HMF.

With predominant BAS, the m-SA catalyst showed enhanced glucose conversion and HMF selectivity, where HMF selective achieved a maximum of $S_{HMF,180min}$ = 39% (**Figure 5-4B**). The enhanced glucose conversion on BAS catalyst compared to LAS catalyst could be explained by the easier glucose isomerization compared to fructose dehydration at elevated temperature without acid sites, the former can occur faster with a smaller energy barrier[433]. The important role of BAS in producing HMF via dehydration step is also supported by the observed highest HMF selective on fructose dehydration ($S_{HMF,45min}$ = 76%, **Figure 5-4E**). The

observed catalytic performance of LAS catalyst and BAS catalyst is in good agreement with the importance of acid site identity for cascade glucose conversion.

With a cascade architectural structure and the presence of spatially separated LAS and BAS, the Al_{ALD}@m-SA gave an much enhanced catalytic performance such that, after three hours of reaction, *ca.* 93% of glucose was converted, and high selectivity to HMF of 66% was achieved (**Figure 5-4C**). Additionally, as demonstrated by **Table 5-2**, the Al_{ALD}@m-SA showed the best catalytic activity regarding the calculation of turnover frequency (TOF). In the first 30 minutes of the reaction, the high TOF and relatively low HMF selectivity over Al_{ALD}@m-SA can be explained by the high concentration of only LAS on the outermost alumina nanolayer coated by the ALD process. Because the BAS are only present inside the nanopores of the support, the free surface diffusion of reactant directly to BAS is hindered[408]. The limited contact between glucose and/or glucose isomer at the beginning of the reaction leads to the low initial selectivity of HMF. As the cascade glucose conversion reaction progresses, the HMF selectivity increased significantly while the fructose selectivity reduced on Al_{ALD}@m-SA. This is since the fructose produced further diffuses along the catalyst from outermost surface LAS to BAS inside the nanopores to produce HMF. It is also supported by the relatively high fructose selectivity at only the first hour of the reaction ($S_{fructose,60\ min}$ = 11%, **Figure 5-4C**). Consistently, in fructose dehydration, a relatively slower initial reaction speed on Al_{ALD}@m-SA compared to m-SA with freely accessible Brønsted acidity has been recorded ($C_{fructose,15\ min}$ = 44% and $C_{fructose,15\ min}$ = 57%, respectively. **Figures 5-4E-F**). This is because the BAS on Al_{ALD}@m-SA is not distributed on the outermost surface but only distributed inside the nanopores.

Except for the advantage of the control of diffusion from outermost surface LAS to BAS inside the nanopores, the spatial separation of LAS and BAS limits the synergistic effect, resulting in a more uniform distribution of acidity. It benefits the cascade catalytic performance of the Al_{ALD}@m-SA since side reactions such as over-oxidation and rehydration of HMF are preferred to occur on strong BAS and LAS[434]. Thus, with the control of diffusion and surface acidity, the cascade structured LAS-BAS system contributes to the enhanced cascade reaction performance.

Glucose conversion has also been conducted on a powder mixture of BAS catalyst, m-SA, and LAS catalyst, Al_{ALD}@m-S (**Figure S5-8**), in order to construct a BAS-LAS system without cascade architectural structure resulted diffusion control. Under identical reaction conditions,

the reactant should have access to the active sites of physical mixture of BAS catalyst and LAS catalyst. Without diffusion control, the observed $C_{Glucose,\ 180min}$ = 63% and $S_{HMF,180min}$ = 33% are much lower than that of the cascade architectural structured BAS-LAS system, which well-supports the importance of the spatially well-separated LAS and BAS for cascade reaction catalytic performance improvement. Through the comparison of catalysts with and without a cascade structure, our primary aim was to isolate and analyse the specific influence of the cascade architectural design. Furthermore, the beneficial effect of the BAS-LAS system with a cascade structure was evident from the significant enhancement in HMF selectivity when compared to other amorphous silica-alumina counterparts lacking a spatially-separated BAS-LAS system.

Compared to amorphous silica-alumina prepared by typical co-precipitation and sol-gel synthesis without the precise control of acid site location, with close n(Si)/n(Al) ratio (9.0, 9.0, and 7.5 for $ASA_{co\text{-}precipitation}$, $ASA_{sol\text{-}gel}$ and Al_{ALD}@m-SA, respectively), the prepared Al_{ALD}@m-SA in this study showed more than nine-fold (Al_{ALD}@m-SA 66% vs $ASA_{co\text{-}precipitation}$ 6.3%) and three-fold (Al_{ALD}@m-SA 66% vs $ASA_{sol\text{-}gel}$ 18.8%) enhancement in HMF yield at identical conditions[43]. Besides, under comparable reaction conditions, the AlALD@m-SA with a spatially separated LAS-BAS system showed better performance than the bi-acidic catalysts with disorderly arranged acid sites, such as zeolites of Sn-Beta, MCM41, ZSM-5, SBA15, etc (**Table S5-3**).

Additionally, recyclability, an important performance factor for practical applications has been studied under identical reaction conditions. **Figure 5-4H-J** display the reusability of the catalysts. After recycling, only a slight reduction in glucose conversion has been observed for catalysts. These observations support that the ALD-deposited alumina overlayer can stay stable on the outmost surface of the support, which is independent of the stability of the substrate. The slight reduction might originate from the tiny amount of sample loss during the wash and activation processes among cycles.

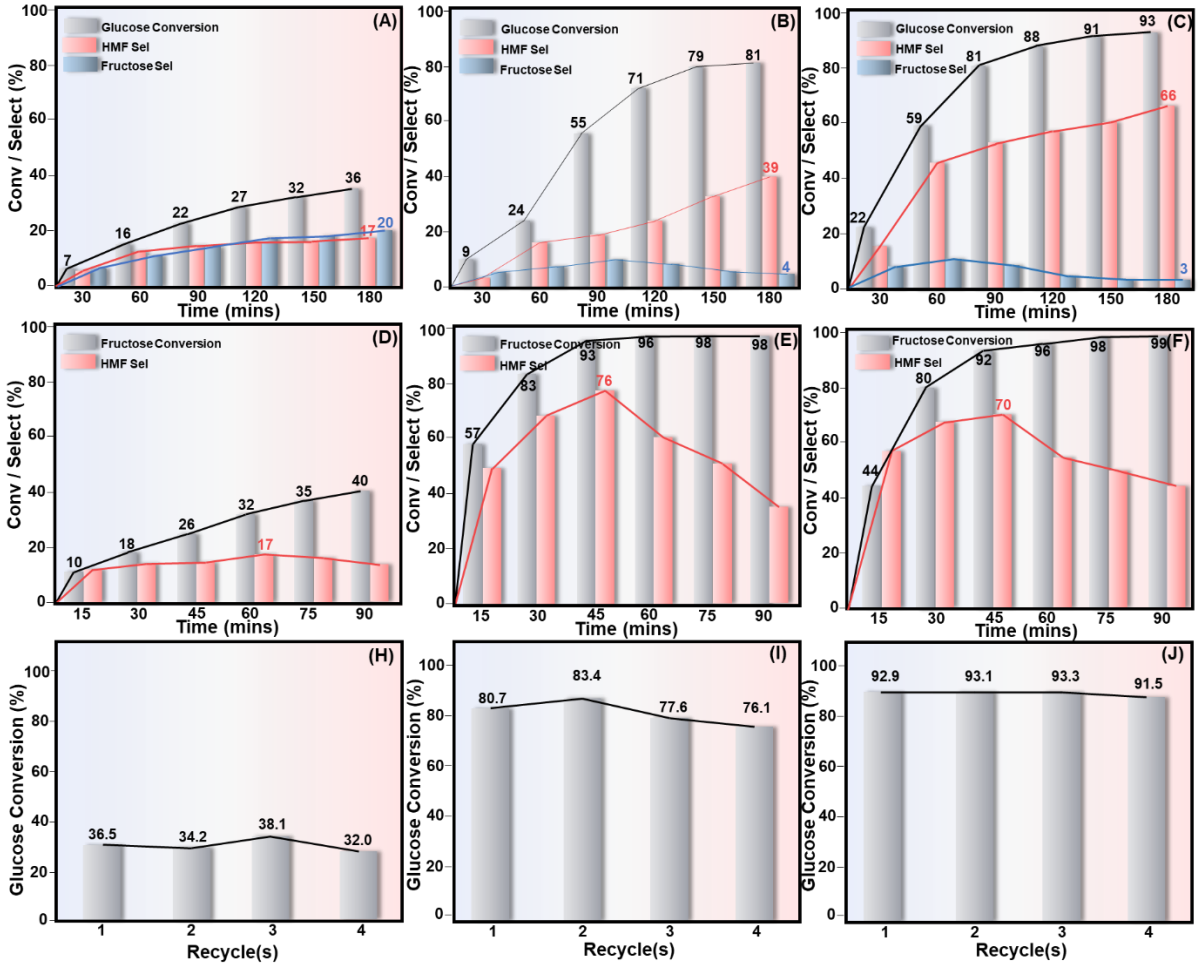

Figure 5-4 Glucose conversion to HMF with (A)Al_{ALD}@m-S, (B)m-SA, and (C) Al_{ALD}@m-SA catalysts; Fructose dehydration to HMF with (D)Al_{ALD}@m-S, (E) m-SA, and (F) Al_{ALD}@m-SA catalysts; Recycling experiments for glucose conversion with (H)Al_{ALD}@m-S, (I) m-SA, and (J) Al_{ALD}@m-SA catalysts. Reaction conditions: 20 mg of Al_{ALD}@high silica substrate catalysts, 2 ml biphasic solution (DMSO/Water = 7/3) containing 60 mg glucose or fructose at 160°C under continuous stirring.

Table 5-2 Summary of catalytic data of glucose conversion to HMF over the catalysts.

Catalysts	$C_{Glucose}$[a] (%)	S_{HMF}[b] (%)	$S_{Fructose}$[b] (%)	TOF[c] (h^{-1})
Al_{ALD}@m-SA	59(93)	43(66)	11(3)	6.00
Al_{ALD}@m-S	16(36)	13(17)	10(20)	1.26
m-SA	24(81)	19(39)	9(4)	3.54
m-S	3(21)	12(14)	18(13)	-

[a]$C_{glucose}$= conversion of glucose. [b]S_{HMF}= selectivity of HMF. They are provided after 60 mins of batch reaction, and the results after 180 mins of reaction are given in parentheses. [c] Turnover frequency (TOF) calculated based on the glucose conversion at 160°C within the kinetic range.

Based on the characterizations and catalytic performance tests, the structure-acidity-catalytic performance relationship has been plotted (**Figure 5-5**). On the ALD-generated overcoat, the alumina nanolayer contains LAS with a high concentration on the outermost surface. The concentrated reactant glucose efficiently isomerizes into intermediate fructose on the outermost

surface. Because the distribution of BAS is predominantly inside the nanopores of the silica-alumina substrate instead of the alumina overlayer, the physical distance between LAS and BAS limits the surface diffusion of the absorbed glucose. This results in the introduced glucose always coming into contact with the surface LAS first, followed by the produced isomer, i.e. fructose, coming into contact with the BAS inside the nanopores. The unique geometric distribution of the LAS on the outermost overlayer and the BAS inside the nanopores effectively promote the stepwise diffusion and occurrence of the cascade reaction of glucose isomerization and fructose dehydration.

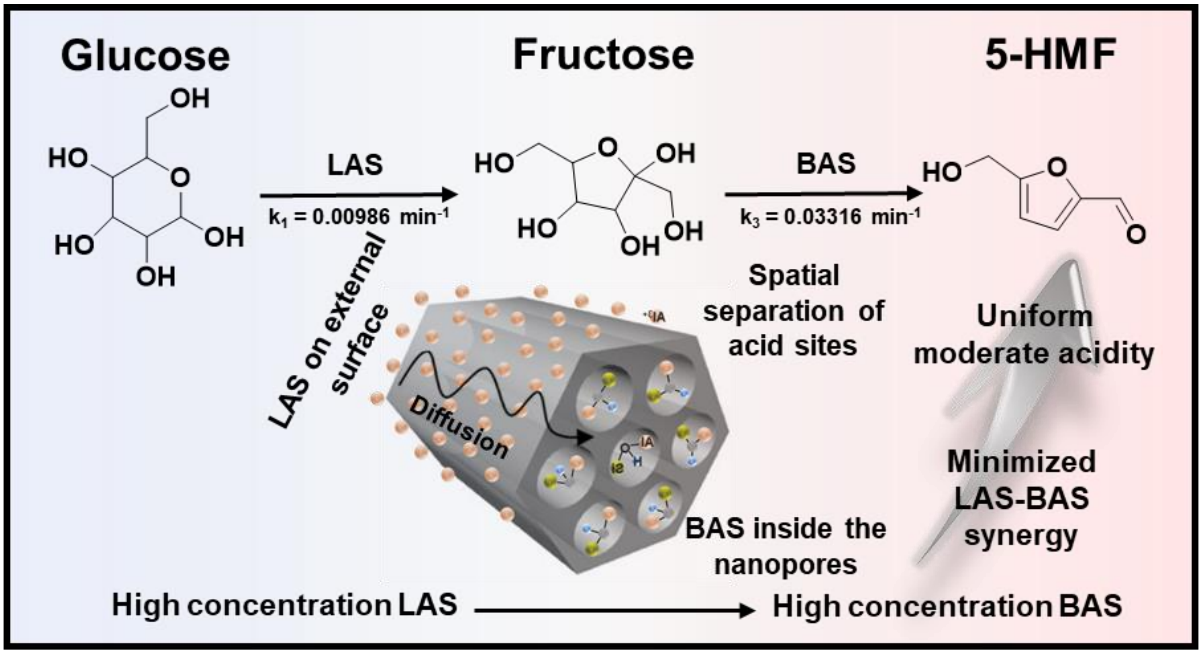

Figure 5-5 Proposed cascade reaction scheme for glucose conversion into HMF on Al_{ALD}@m-SA

5.3 Conclusions

In conclusion, this work demonstrates the design of a bi-acidic solid acid catalyst with cascade architectural structured BAS and LAS. Via the TEM, EELS visualizations and 1D, 2D ssNMR methodologies, we successfully demonstrated that the alumina overcoat produced by the ALD process mainly contributes to the formation of LAS on the external surface. With the BAS inside the nanopores of the silica-alumina substrate, the LAS on the outermost surface and BAS inside the nanopores are geometrically separated, thereby leading to the formation of cascade architecturally structured surface acid sites with moderate and uniform acidity. We also demonstrated that with directional diffusion of glucose reactant from the LAS domain to the BAS domain, excellent catalytic performances on both glucose conversion and HMF selectivity have been observed over the Al_{ALD}@m-SA. The superior catalytic performance of the cascade structured Al_{ALD}@m-SA, compared to its counterparts without the cascade

architectural structure, including $ASA_{sol\text{-}gel}$, $ASA_{nano\text{-}domain}$, and previously published zeolites such as ZSM-5, zeolite H, and SBA-15 (refer to **Table S5-3**), highlights the significance of the cascade architectural structure in enhancing the cascade reaction performance. This observation reinforces the potential of the cascade design for optimizing catalytic processes. Thus, this work paves the way for designing bi-acidic catalyst with unique cascade architectural structure for efficient cascade reactions.

5.4 Appendix

5.4.1 Physiochemical properties characterization

Transmission electron microscopy images have been obtained to characterize the micro-level structure of parent nanoreactor substates. The addition of Al (Si/Al = 35.44, table S1) shows little influence in the mesopores structure.

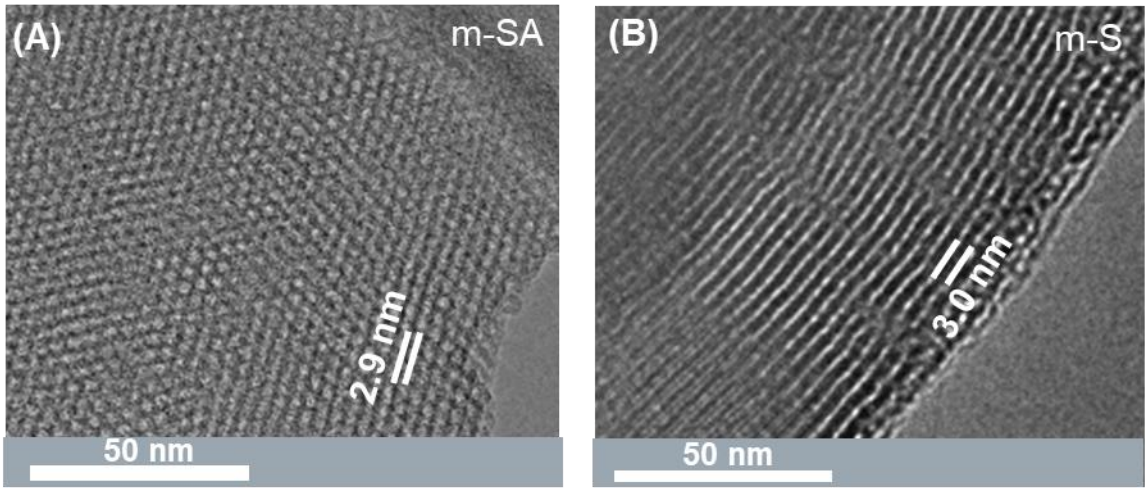

Figure S 5-1 HRTEM image of (A) m-SA and (B) m-S

No crystalline alumina or silica peak can be observed in the wide-angle XRD pattern for substrates (**Figure S5-1**). This suggests that the addition of alumina have no affection on the nanoreactor amorphous global structure. After AlO_x-rich films grafting on the surface, the amorphous nature of substrates has been maintained.

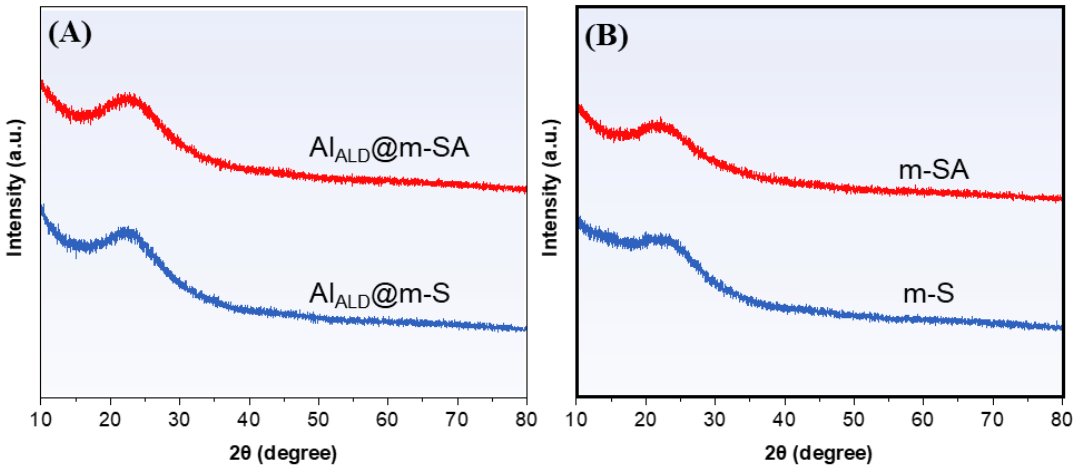

Figure S 5-2 wide-angle XRD patterns of (A) ALD catalysts (B) parent amorphous nanoreactor substates

The doping of alumina into nanoreactor shows no affection on the mesoporous structure of the substates. Both parent substrates show mesopores with diameter ~ 2.5 nm. After the processes of atomic layer deposition, the unmodified type IV isotherms suggest that the samples kept mesoporous structure after TMA grafting, the mesoporous structure has been maintained.

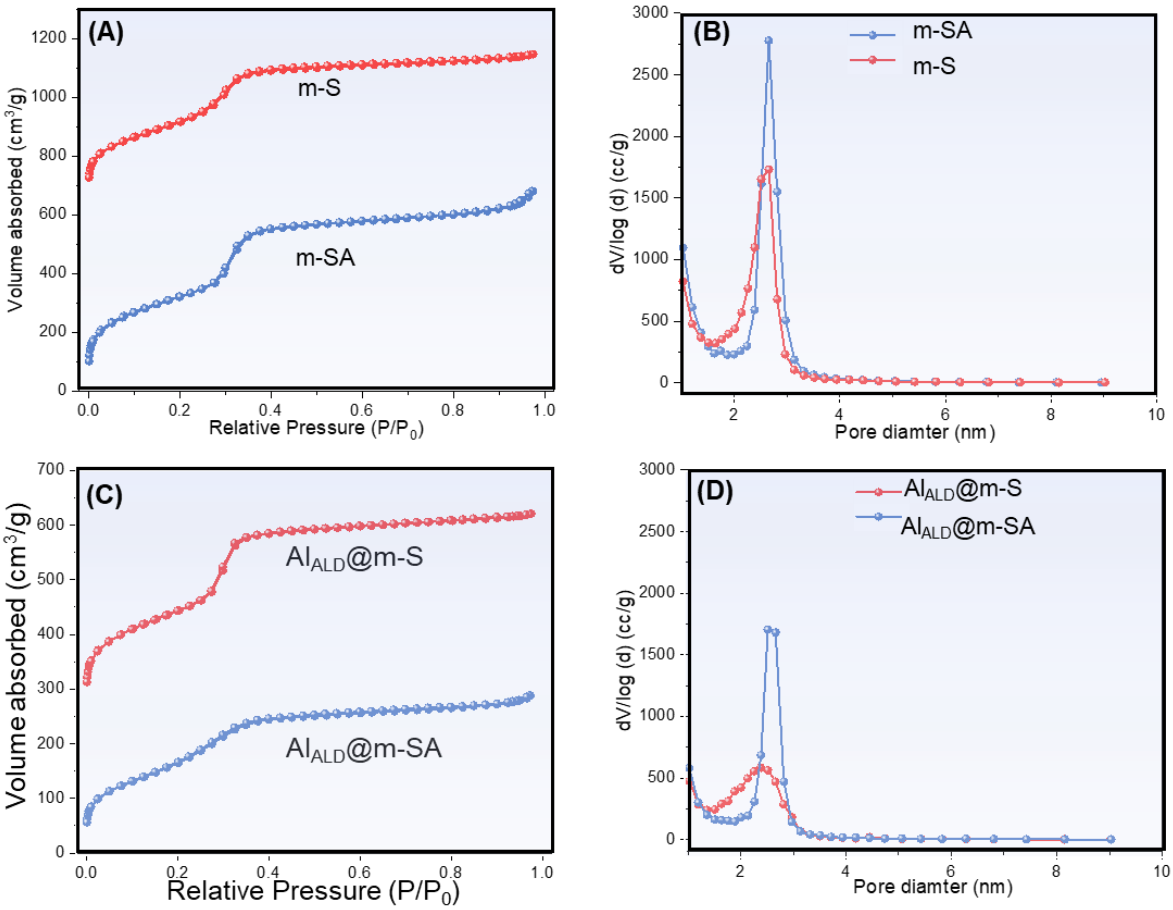

Figure S 5-3 (A) N_2 adsorption/desorption isotherms, and (B) BJH pore size distribution calculation for parent nanoreactor substrates, (C) N_2 adsorption/desorption isotherms, and (D) BJH pore size distribution calculation for ALD catalysts.

Table S 5-1 Summary of surface area, average pore size, pore diameter, and Si to Al molar ratio of parent MCM41 substates.

Sample	SA[a] (m^2/g)	V_{Pore}[a] (cm^3/g)	d_{BJH}[a] (nm)	BAS (μmol/g)	LAS (μmol/g)	Si/Al[b]
m-S	1154.0	0.79	2.65	-	-	NA
m-SA	1222.7	1.05	2.65	0.17	0.01	35.44

[a]The specific surface area (SA), volume of pores (V_{pore}), and pore diameter (d_{BJH}) of Al_{ALD}/nanoreactor catalysts were determined from the adsorption of the N_2 isotherms and corresponding BJH calculation. [b]The surface composition ratio was determined by X-ray photoelectron spectroscopy elemental analysis.

Table S 5-2 Summary of physiochemical properties of Al_{ALD}@high silica substrate catalysts.

Catalysts	SA[a] (m^2/g)	V_{Pore}[a] (cm^3/g)	d_{BJH}[a] (nm)	n(Si)/n(Al)[b]	LAS[c] (μmol/g)	BAS[c] (μmol/g)	L/B
Al_{ALD}/@m-S	789.1	0.57	2.66	9.07	0.19	0.01	19
Al_{ALD}@m-SA	686.0	0.45	2.52	7.51	0.22	0.10	2.2

[a]The specific surface area (SA), volume of pores (V_{pore}), and pore diameter (d_{BJH}) of Al_{ALD}@high silica substrate was determined from the adsorption of the N_2 isotherms and corresponding BJH calculation. [b]The surface composition ratio was determined by X-ray photoelectron spectroscopy elemental analysis. [c] The acidity of Brønsted acid sites (BAS) and density of Lewis acid sites (LAS) were calculated based on the simulation and integration of ^{31}P MASNMR spectra.

5.4.2 Local structure characterization

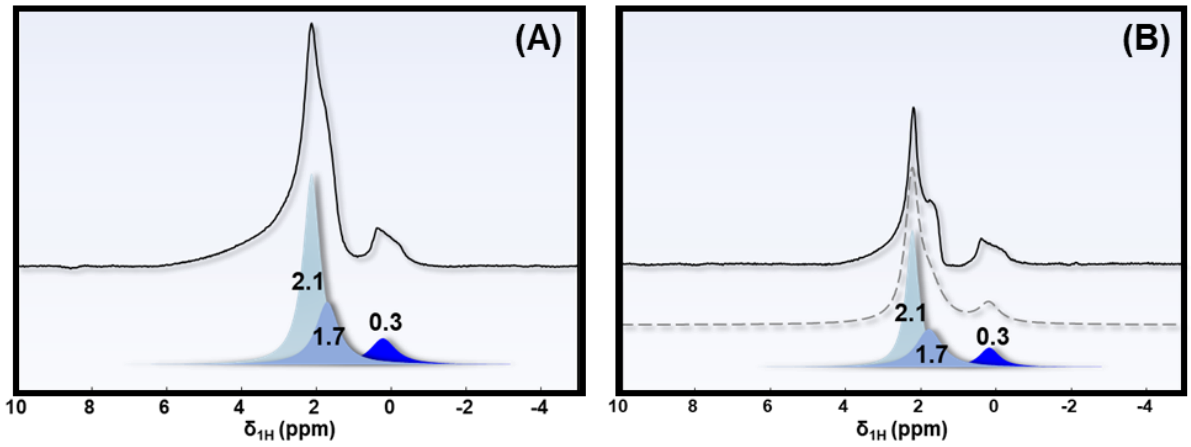

Figure S 5-4 ^1H MASNMR spectra of (A) Dehydrated Al_{ALD}@m-SA and (B) Dehydrated Al_{ALD}@m-S; (Black line: spectra, dash line: simulations; coloured blocks: components).

The nature of surface BAS, the spatial distribution of proton and aluminum species in the Al_{ALD}/nanoreactor can be visioned by $^1H/^{27}Al$ TRAPDOR NMR spectra. As shown in **Figure S5-5,** characteristic peaks at δ_{1H} = 2.1 and 0.3 ppm can be evidenced for both samples. This suggests that these proton species have spatial correlation with aluminum species, identified

by the promoted dipolar couplings and the ^{1}H and ^{27}Al pair dephasing shown in the difference spectra (ΔS).

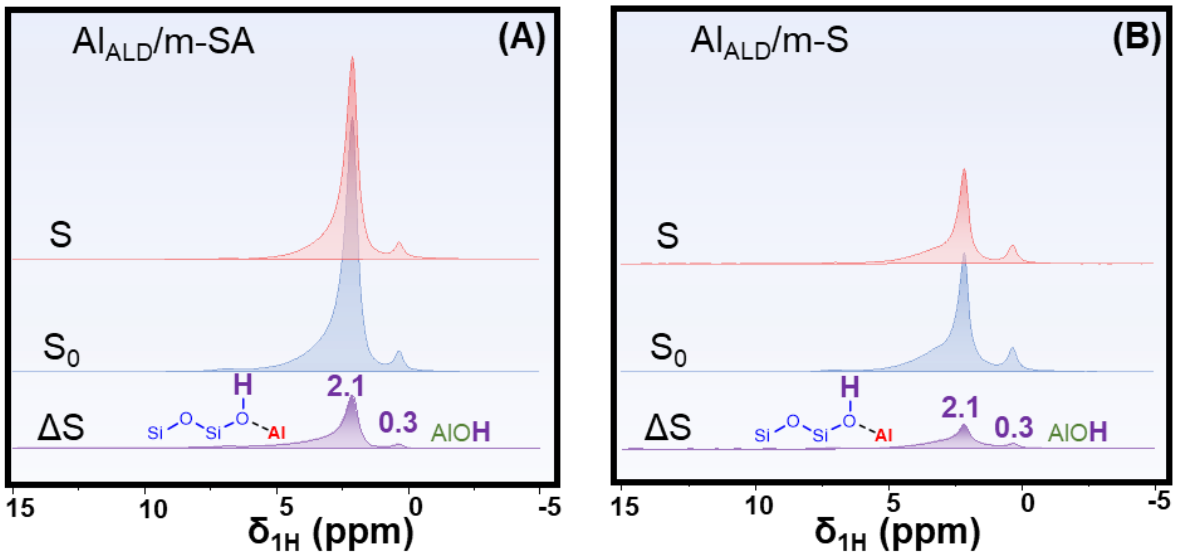

Figure S 5-5 The $^{1}H/^{27}Al$ TRAPDOR NMR spectra of (A)Al$_{ALD}$@m-SA and (B) Al$_{ALD}$@m-S (Si. S_0 (blue regions): spectra obtained without REDOR pulse; S (red regions): spectra obtained with 100W 27Al dephasing pulse. ΔS (Purple regions): difference spectra = S_0-S.

5.4.3 Glucose Conversion and Fructose Conversion to HMF

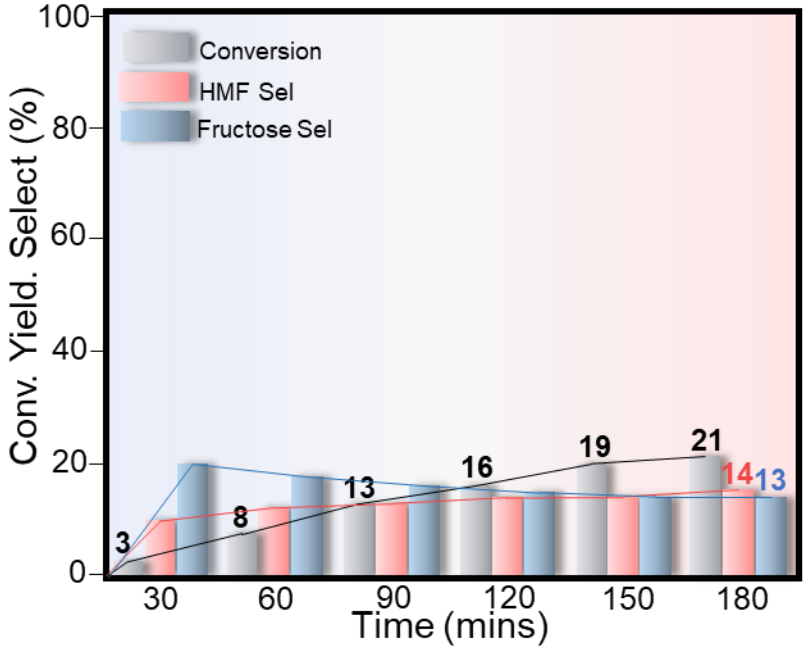

Figure S 5-6 Glucose conversion to HMF on m-S substrate; Reaction conditions: 20 mg catalysts, 2 ml biphasic solution (DMSO/Water = 7/3) containing 60 mg glucose at 160 °C under continuous stirring.

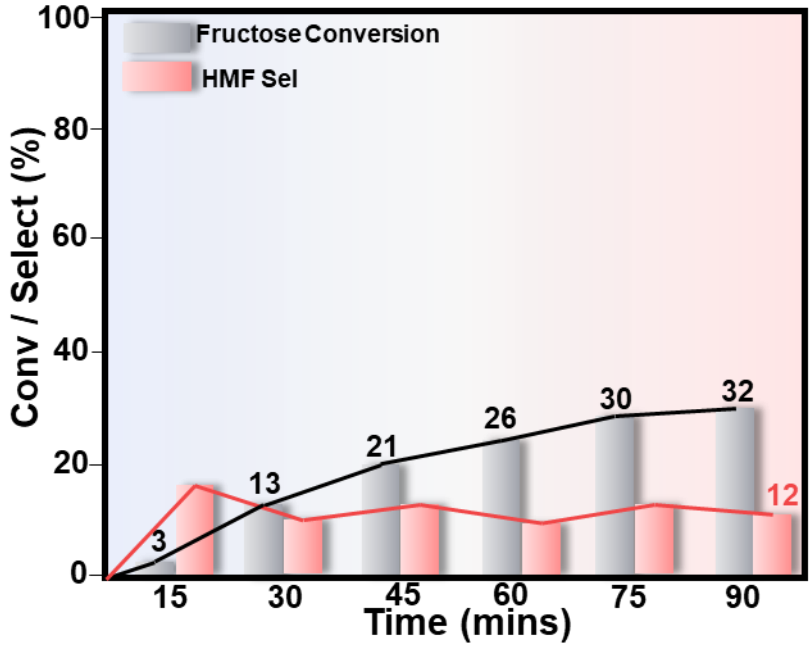

Figure S 5-7 Fructose conversion to HMF on m-S substrate; Reaction conditions: 20 mg catalysts, 2 ml biphasic solution (DMSO/Water = 7/3) containing 60 mg fructose at 160 °C under continuous stirring.

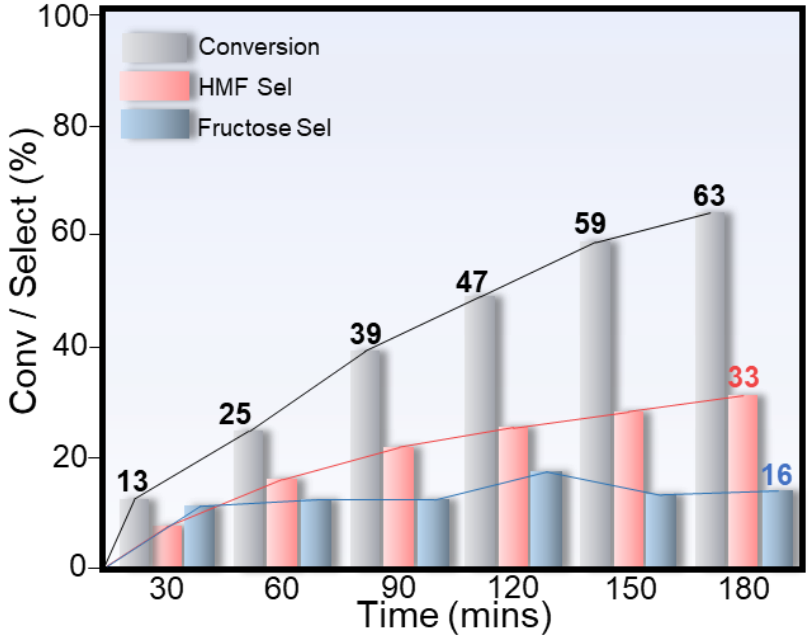

Figure S 5-8 Glucose conversion to HMF on physical mixture of BAS-dominated m-SA and LAS-dominated Al_{ALD}@m-S catalysts; Reaction conditions: mixture of 10 mg of m-SA and 10 mg Al_{ALD}@m-S, 2 ml biphasic solution (DMSO/Water = 7/3) containing 60 mg glucose at 160 °C under continuous stirring.

Table S 5-3 Summarized HMF yield from glucose conversion on difference typical heterogeneous catalysts

Catalysts	Maximum HMF yield (%)	Reference
Al_{ALD}@m-SA	61	This work
Al_{ALD}@m-S	7	This work
m-SA	32	This work
m-S	3	This work
Zr-MCM41	23	436
Cr-USY zeolites	27	437
Hβ-zeolite	49	438
Fe/β zeolite	61	439
d-SA/30 ASA	64	440
Nb(0.05)-Beta 18 zeolite	81	441
CrOx–Y zeolite	53	442
Cu–Cr/ZSM-5 zeolite	52	443
Ga-deAl-HY	35	444
Sn-deAl-HY	22	444
Cu-ZSM5	42	445
Sn20/γ-Al_2O_3	28	446
Nb-SBA-15	51	447
CrCl2-Im-SBA-15	28	448

5.4.4 Kinetic study

To study the influence of varied acid sites on the cascade reaction rate, the chemical kinetic of such reactions on different catalysts have been studied with a pseudo homogeneous first-order kinetic model[449]. **Figure S5-9** shows the reaction pathways for the establishment of the first-order kinetic model, where four steps have been considered with the assumption of all reactions are irreversible. Except considering the reaction rate of initial glucose isomerization which could be accelerated on LAS (k_1) and fructose dehydration on BAS (k_2), respectively, the model also considered the rate of side reactions of degradation of glucose and fructose to humins and other soluble products (k_3 and k_4). The reaction rate equations can be expressed as follows[450,451]:

$$-\frac{dC_G}{dt} = k_G C_G \quad \text{(S1)}$$

$$\frac{dC_F}{dt} = k_1 C_G - k_F C_F \quad \text{(S2)}$$

$$\frac{dC_H}{dt} = k_3 C_F \quad \text{(S3)}$$

$$C_G = C_{G,inital} e^{-k_G t} \quad \text{(S4)}$$

$$C_F = \frac{k_1 C_{G,inital}}{k_F - k_G}\left(e^{-k_G t} - e^{-k_F t}\right) \quad \text{(S5)}$$

$$C_H = \frac{k_1 k_3 C_{G,inital}}{k_F - k_G} \cdot \frac{k_F\left(1-e^{-k_G t}\right) - k_G\left(1-e^{-k_F t}\right)}{k_G k_F} \quad \text{(S6)}$$

Where k_G and k_F equal to the sum of k_1 and k_3, and k_3 and k_4, respectively. G, F, and H represent glucose, fructose, and 5-HMF, respectively.

To verify the validity of the kinetic model, the analytical expression can be displayed as Eq. S8.

$$\ln\left(C_{G/F}\right) = -k_{G/F} t + \ln\left(C_{G/F,inital}\right) \quad \text{(S7)}$$

$$-\ln(1 - X) = k_{G/F} t \quad \text{(S8)}$$

Where X is the glucose/fructose conversion.

As shown in **Figures S5-9B-C**, a linear fit on-ln (1-X) versus time ($R^2 > 0.90$) for glucose and fructose conversion can be observed for all catalysts. This observation confirmed the reaction kinetics were governed by first-order rate equations. Compared with mono-acidic catalysts (Al_{ALD}@m-S and m-SA), with the presence of a separated LAS-BAS system on Al_{ALD}@m-SA, the constant rates of k_1 and k_3 reach maximum.

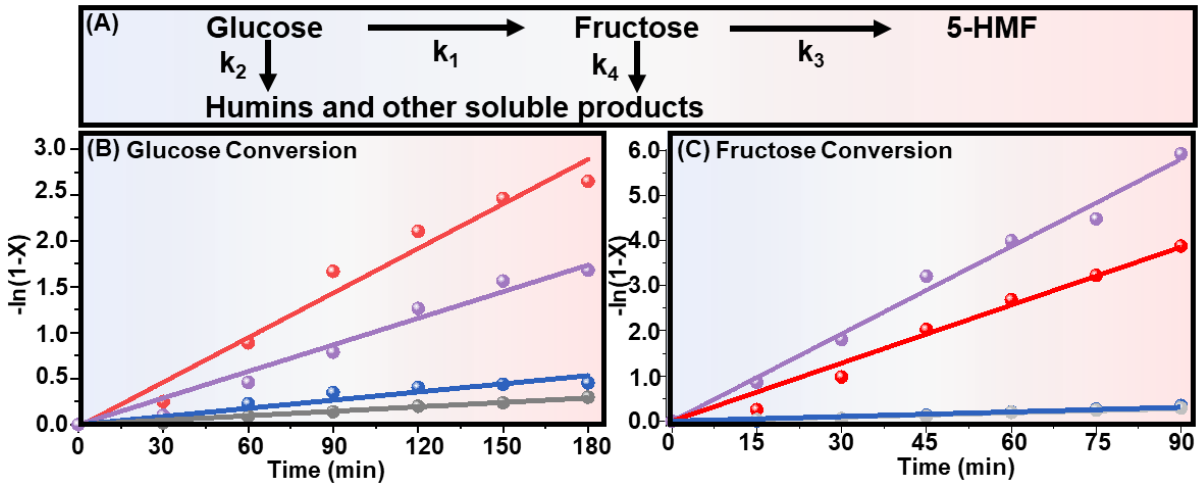

Figure S 5-9 (A) Reaction pathways of cascade glucose conversion to 5-HMF; (B) -ln (1-X) versus time for glucose conversion (C) -ln (1-X) versus time for fructose conversion on Al_{ALD}@m-SA (red), Al_{ALD}@m-S (blue), m-SA (purple), m-S (grey).

Table S 5-4 Kinetic parameters of cascade glucose conversion[a].

Catalysts	k_G (min^{-1})	k_1 (min^{-1})	k_2 (min^{-1})	k_F (min^{-1})	k_3 (min^{-1})	k_4 (min^{-1})
Al_{ALD}@m-SA	0.01632	0.00986	0.00646	0.04284	0.03316	0.00968
Al_{ALD}@m-S	0.00309	0.00256	0.00053	0.00341	0.00074	0.00267
m-SA	0.01166	0.00637	0.00529	0.04471	0.03001	0.01470
m-S[b]	0.00154	-	-	0.00308	-	-

[a]The global error is less than 5×10^{-5}. [b]No acceptable optimization could be obtained for k values.

6.summary and future work

In conclusion, the works summarised in this thesis highlights the potential of amorphous alumina materials to be used as solid catalysts for green and sustainable processes for high-value chemical production from biomass. Amorphous alumina based solid materials showed advanced performance in biomass conversion compared to its crystalline counterparts mainly due to the non-restricted mass transfer and the large amount of active surface-exposed penta-coordinated aluminium species. Specifically, with an oxygen vacancy as defect site, penta-coordinated aluminium species have shown enhanced performance to be utilised as surface sites for both Bronsted acid site and Lewis acid site construction

In summary, this thesis underscores the promising prospects of utilizing amorphous alumina materials as robust catalysts in environmentally friendly and sustainable processes for generating valuable chemicals from biomass. Amorphous alumina-based solid materials have demonstrated enhanced efficacy in biomass conversion when compared to their crystalline counterparts. This can primarily be attributed to their unhindered mass transfer capabilities and the abundant presence of exposed penta-coordinated aluminum species on their surfaces. In particular, penta-coordinated aluminum species, with an oxygen vacancy as a defect site, have exhibited enhanced potential as active sites for constructing both Bronsted acid and Lewis acid sites.

However, when considering the synthesis process, it is more challenging to create materials containing ample surface-active Al^{V} sites within alumina under mild conditions compared to generating Al^{IV} species with surface activity. This difficulty arises because Al^{V} species typically exhibit significantly distorted local structures, while Al^{IV} and Al^{VI} species with more symmetrical local structures have a greater likelihood of forming in crystalline alumina. Consequently, effort will be made to explore methods for increasing the prevalence of Al^{V} species in Al-containing systems, especially those with crystalline structures in the future. This pursuit is crucial for facilitating the development of active Al^{V} sites in diverse systems and expanding their utility in catalytic applications.

Furthermore, owing to the inherent distorted local structure of Al^{V} species, elucidating the geometric and electronic properties of an Al^{V}-enriched system poses a formidable challenge. Conventional analytical methods like X-ray diffraction, transmission electron microscopy, and X-ray absorption spectroscopy are suboptimal for characterizing Al^{V}-enriched systems. Even the most promising technique, solid-state nuclear magnetic resonance, has limitations in

resolution. Consequently, efforts will be dedicated to explore methodologies for using ssNMR to characterize the local structure and acidity of alumina-containing materials. Additionally, efforts will be endeavoured to develop *in-situ* ssNMR techniques that can unveil the relationships between local structure, acidity, and catalytic activity of surface aluminum species.

Moreover, since there are currently no established comprehensive models for Al^{V}-rich amorphous materials, density functional theory (DFT) investigations yield contradictory insights and, to some extent, do not align with experimental findings. Hence, additional efforts should be dedicated to formulating a coherent and generalized DFT model for Al^{V}-enriched systems. This model should be instrumental in deepening our understanding of the role played by Al^{V} species in various catalytic reactions.

Last but not least, it is worth noting that the present technique for producing Al^{V}-based solid catalysts is rather intricate, involving an extremely high-temperature Flame Spray Pyrolysis process. Furthermore, the resulting particles possess a relatively modest surface area and lack a porous structure. In light of this, efforts should be made to design an economical and scalable method to fabricate Al^{V}-based solid catalysts with a nanoporous structure holds significant promise for enhancing the eco-friendly and sustainable production of high-value chemicals from biomass.

7.References

1. Satterfield, C. N., Heterogeneous catalysis in industrial practice. **1991**.
2. Schlögl, R., Heterogeneous catalysis. *Angewandte Chemie International Edition* **2015,** *54* (11), 3465-3520.
3. Schwab, G.-M., About the mechanism of contact catalysis. *Advances in Catalysis*, Elsevier: 1950; Vol. 2, pp 251-267.
4. Ma, Z.; Zaera, F., Heterogeneous catalysis by metals. *Encyclopedia of Inorganic* Chemistry **2006**.
5. Corma, A., Inorganic solid acids and their use in acid-catalyzed hydrocarbon reactions *Chemical Reviews* **1995,** *95* (3), 559-614.
6. Busca, G., Acid catalysts in industrial hydrocarbon chemistry. *Chemical Reviews* **2007,** *107* (11), 5366-5410.
7. Li, Y.; Li, L.; Yu, J., Applications of Zeolites in Sustainable Chemistry. *Chem* **2017,** *3* (6), 928-949.
8. Hattori, H., Solid Acid Catalysts: Roles in Chemical Industries and New Concepts. *Topics in Catalysis* **2010,** *53* (7-10), 432-438.
9. Wang, Z.; Ling, H.; Shi, J.; Stampfl, C.; Yu, A.; Hunger, M.; Huang, J., Acidity enhanced [Al]MCM-41 via ultrasonic irradiation for the Beckmann rearrangement of cyclohexanone oxime to ε-caprolactam. *Journal of Catalysis* **2018,** *358*, 71-79.
10. Wang, Z.; Wang, L.; Zhou, Z.; Zhang, Y.; Li, T.; Stampfl, C.; Liang, C. H.; Huang, J., Benzylation of Arenes with Benzyl Chloride over H-Beta Zeolite: Effects from Acidity and Shape-Selectivity. *Journal of Physical Chemistry C* **2017,** *121* (28), 15248-15255.
11. Kauffman, B., The Bronsted-Lowry acid base concept. *Journal of Chemical Education* **1988,** *65* (1), 28.
12. Peng, Q.; Wang, T.; Wang, C.; Jiang, L.; Wang, D.; Chen, F.; Huang, J., Tuning Hydrocarbon Pool Intermediates by the Acidity of SAPO-34 Catalysts for Improving Methanol-to-Olefins Reaction. *Acs Sustainable Chemistry & Engineering* **2018,** *6* (12), 16867-16875.
13. Zhou, X.; Wang, C.; Chu, Y.; Xu, J.; Wang, Q.; Qi, G.; Zhao, X.; Feng, N.; Deng, F., Observation of an oxonium ion intermediate in ethanol dehydration to ethene on zeolite. *Nature Communications* **2019,** *10* (1), 1961.
14. Dai, W. L.; Wang, M.; Dyballa, M.; Wu, J.; Guan, J.; Li, D.; Xie, K.; Hunger, M., Understanding the Early Stages of the Methanol-to-Olefin Conversion on H-SAPO-34. *Acs Catalysis* **2015,** *5* (1), 317-326.
15. Xu, S.; Zheng, A.; Wei, Y.; Chen, J.; Li, J.; Chu, Y.; Zhang, M.; Wang, Q.; Zhou, Y.; Wang, J.; Deng, F.; Liu, Z., Direct Observation of Cyclic Carbenium Ions and Their Role in the Catalytic Cycle of the Methanol-to-Olefin Reaction over Chabazite Zeolites. *Angewandte Chemie International Edition* **2013,** *52* (44), 11564-11568.
16. Tanabe, K., Solid Acids and Bases: Their Catalytic Properties. *Elsevier* 2012.
17. Wischert, R.; Laurent, P.; Coperet, C.; Delbecq, F.; Sautet, P., gamma-Alumina: The Essential and Unexpected Role of Water for the Structure, Stability, and Reactivity of "Defect" Sites. *Journal of the American Chemical Society* **2012,** *134* (35), 14430-14449.
18. Chupas, P. J.; Chapman, K. W.; Halder, G. J., Elucidating the Structure of Surface Acid Sites on gamma-Al2O3. *Journal of the American Chemical Society* **2011,** *133* (22), 8522-8524.
19. Pescarmona, P.; Janssen, F.; Delaet, C.; Stroobants, C.; Houthoofd, K.; Philippaerts, A.; De Jonghe, C.; Paul, S.; Jacobs, A.; Sels, F., Zeolite-catalysed conversion of C(3) sugars to alkyl lactates. *Green Chemistry* **2010,** *12* (6), 1083-1089.

20. Wang, Z.; Wang, L.; Jiang, Y.; Hunger, M.; Huang, J., Cooperativity of Brønsted and Lewis Acid Sites on Zeolite for Glycerol Dehydration. *Acs Catalysis* **2014,** *4* (4), 1144-1147.
21. Wang, C.; Chu, Y.; Xu, J.; Wang, Q.; Qi, G.; Gao, P.; Zhou, X.; Deng, F., Extra-Framework Aluminum-Assisted Initial C−C Bond Formation in Methanol-to-Olefins Conversion on Zeolite H-ZSM-5. *Angewandte Chemie International Edition* **2018,** *57* (32), 10197-10201.
22. Kim, D.; Wang, Z.; Jiang, Y.; Hunger, M.; Huang, J., The cooperative effect of Lewis and Brønsted acid sites on Sn-MCM-41 catalysts for the conversion of 1,3-dihydroxyacetone to ethyl lactate. *Green Chemistry* **2019,** *21* (12), 3383-3393.
23. Li, S.; Zheng, A.; Su, Y.; Zhang, H.; Chen, L.; Yang, J.; Ye, C.; Deng, F., Bronsted/Lewis acid synergy in dealuminated HY zeolite: A combined solid-state NMR and theoretical calculation study. *Journal of the American Chemical Society* **2007,** *129* (36), 11161-11171.
24. Yi, X.; Liu, K.; Chen, W.; Li, J.; Xu, S.; Li, C.; Xiao, Y.; Liu, H.; Guo, X.; Liu, S.-B.; Zheng, A., Origin and Structural Characteristics of Tri-coordinated Extra-framework Aluminum Species in Dealuminated Zeolites. *Journal of the American Chemical Society* **2018,** *140* (34), 10764-10774.
25. Huang, Z. W. J., Brønsted-Lewis Acids for Effcient Conversion of Renewables. *Production of Biofuels and Chemicals with Bifunctional Catalysts* **2017,** 99-135.
26. Busca, G., Silica-alumina catalytic materials: A critical review. Catalysis Today 2020, 357, 621-629.
27. Wang, Z.; O'Dell, L. A.; Zeng, X.; Liu, C.; Zhao, S.; Zhang, W.; Gaborieau, M.; Jiang, Y.; Huang, J., Insight into Three-Coordinate Aluminum Species on Ethanol-to-Olefin Conversion over ZSM-5 Zeolites. *Angewandte Chemie International Edition* **2019,** *58*, 18061-18068.
28. Zeng, X.; Wang, Z.; Ding, J.; Wang, L.; Jiang, Y.; Stampfl, C.; Hunger, M.; Huang, J., Catalytic arene alkylation over H-Beta zeolite: Influence of zeolite shape selectivity and reactant nucleophilicity. *Journal of Catalysis* **2019,** *380*, 9-20.
29. Wang, Z.; Jiang, Y.; Baiker, A.; Huang, J., Efficient Acid-Catalyzed Conversion of Phenylglyoxal to Mandelates on Flame-Derived Silica/Alumina. *ACS Catalysis* **2013,** *3* (7), 1573-1577.
30. Wang, Z.; Pokhrel, S.; Chen, M.; Hunger, M.; Mädler, L.; Huang, J., Palladium-doped silica–alumina catalysts obtained from double-flame FSP for chemoselective hydrogenation of the model aromatic ketone acetophenone. *Journal of Catalysis* **2013,** *302* (0), 10-19.
31. Wang, Z.; Kim, K.-D.; Zhou, C.; Chen, M.; Maeda, N.; Liu, Z.; Shi, J.; Baiker, A.; Hunger, M.; Huang, J., Influence of support acidity on the performance of size-confined Pt nanoparticles in the chemoselective hydrogenation of acetophenone. *Catalysis Science & Technology* **2015,** *5* (5), 2788-2797.
32. Kwak, J. H.; Hu, J.; Mei, D.; Yi, C.-W.; Kim, D. H.; Peden, C. H. F.; Allard, L. F.; Szanyi, J., Coordinatively Unsaturated Al3+ Centers as Binding Sites for Active Catalyst Phases of Platinum on gamma-Al2O3. *Science* **2009,** *325* (5948), 1670-1673.
33. Shi, L.; Deng, G.-M.; Li, C.; Miao, S.; Wang, N.; Zhang, P.; Lu, H., Al2O3 Nanosheets Rich in Pentacoordinate Al3+ Ions Stabilize Pt-Sn Clusters for Propane Dehydrogenation. *Angewandte Chemie-International Edition* **2015,** *54* (47), 13994-13998.
34. Duan, H.; You, R.; Xu, S.; Li, Z.; Qian, K.; Cao, T.; Huang, W.; Bao, X., Pentacoordinated Al3+-Stabilized Active Pd Structures on Al2O3-Coated Palladium Catalysts for Methane Combustion. *Angewandte Chemie* **2019,** *131*, 12171 –12176.
35. Larmier, K.; Chizallet, C.; Cadran, N.; Maury, S.; Abboud, J.; Lamic-Humblot, A.-F.; Marceau, E.; Lauron-Pernot, H., Mechanistic investigation of isopropanol conversion on

alumina catalysts: location of active sites for alkene/ether production. *ACS Catalysis* **2015,** *5* (7), 4423-4437.
36. Wang, Z.; Jiang, Y.; Lafon, O.; Trébosc, J.; Duk Kim, K.; Stampfl, C.; Baiker, A.; Amoureux, J.-P.; Huang, J., Brønsted acid sites based on penta-coordinated aluminum species. *Nature Communications* **2016,** *7* (1), 1-5.
37. Kwak, H.; Hu, J.; Mei, D.; Yi, W.; Kim, H.; Peden, H.; Allard, F.; Szanyi, J., Coordinatively unsaturated Al3+ centers as binding sites for active catalyst phases of platinum on γ-Al2O3. *Science* **2009,** *325* (5948), 1670-1673.
38. Wang, Z.; Jiang, Y.; Jin, F.; Stampfl, C.; Hunger, M.; Baiker, A.; Huang, J., Strongly enhanced acidity and activity of amorphous silica–alumina by formation of pentacoordinated AlV species. *Journal of Catalysis* **2019,** *372*, 1-7.
39. Wang, Z.; Buechel, R.; Jiang, Y.; Wang, L.; Xu, H.; Castignolles, P.; Gaborieau, M.; Lafon, O.; Amoureux, J.-P.; Hunger, M.Jun. H, Engineering the distinct structure interface of subnano-alumina domains on silica for acidic amorphous silica–alumina toward biorefining. *JACS Au* **2021,** *1* (3), 262-271.
40. Han, W.; Liu, B.; Chen, Y.; Jia, Z.; Wei, X.; Song, W., Coordinatively unsaturated aluminum anchored Ru cluster for catalytic hydrogenation of benzene. *Journal of Catalysis* **2021,** *400*, 255-264.
41. Kaushik, M.; Leroy, C.; Chen, Z.; Gajan, D.; Willinger, E.; Müller, R.; Fayon, F.; Massiot, D.; Fedorov, C., Atomic-scale structure and its impact on chemical properties of aluminum oxide layers prepared by atomic layer deposition on silica. *Chemistry of Materials* **2021,** *33* (9), 3335-3348.
42. Xiu, T.; Wang, J.; Liu, Q., Ordered bimodal mesoporous boria–alumina composite: One-step synthesis, structural characterization, active catalysis for methanol dehydration. *Microporous and mesoporous materials* **2011,** *143* (2-3), 362-367.
43. Zhao, Z.; Xiao, D.; Chen, K.; Wang, R.; Liang, L.; Liu, Z.; Hung, I.; Gan, Z.; Hou, G., Nature of Five-Coordinated Al in γ-Al2O3 Revealed by Ultra-High-Field Solid-State NMR. *ACS Central Science* **2022**.
44. Shi, L.; Deng, G. M.; Li, W. C.; Miao, S.; Wang, Q. N.; Zhang, W. P.; Lu, A. H., Al2O3 nanosheets rich in pentacoordinate Al3+ ions stabilize Pt-Sn clusters for propane dehydrogenation. *Angewandte Chemie International Edition* **2015,** *54* (47), 13994-13998.
45. Hu, J. Z.; Xu, S.; Kwak, J. H.; Hu, M. Y.; Wan, C.; Zhao, Z.; Szanyi, J.; Bao, X.; Han, X.; Wang, Y., High field 27Al MAS NMR and TPD studies of active sites in ethanol dehydration using thermally treated transitional aluminas as catalysts. *Journal of Catalysis* **2016,** *336*, 85-93.
46. Perras, F. A.; Wang, Z.; Kobayashi, T.; Baiker, A.; Huang, J.; Pruski, M., Shedding light on the atomic-scale structure of amorphous silica–alumina and its Brønsted acid sites. *Physical Chemistry Chemical Physics* **2019,** *21* (35), 19529-19537.
47. Wang, Z.; Li, T.; Jiang, Y.; Lafon, O.; Liu, Z.; Trébosc, J.; Baiker, A.; Amoureux, J.-P.; Huang, J., Acidity enhancement through synergy of penta-and tetra-coordinated aluminum species in amorphous silica networks. *Nature Communications* **2020,** *11* (1), 1-9.
48. Chen, F.; Jiang, X.; Zhang, L.; Lang, R.; Qiao, B., Single-atom catalysis: Bridging the homo-and heterogeneous catalysis. *Chinese Journal of Catalysis* **2018,** *39* (5), 893-898.
49. Guo, T.; Tang, N.; Lin, F.; Shang, Q.; Chen, S.; Qi, H.; Pan, X.; Wu, C.; Xu, G.; Zhang, J., High-Loading Single-Atom Copper Catalyst Supported on Coordinatively Unsaturated Al2O3 for Selective Synthesis of Homoallylboronates. *ChemSusChem* **2020,** *13* (12), 3115-3121.
50. Zhao, Y.; Wang, L.; Kochubei, A.; Yang, W.; Xu, H.; Luo, Y.; Baiker, A.; Huang, J.; Wang, Z.; Jiang, Y., Formation and Location of Pt Single Sites Induced by Pentacoordinated

Al Species on Amorphous Silica–Alumina. *The Journal of Physical Chemistry Letters* **2021,** *12* (10), 2536-2546.
51. Christiansen, M. A.; Mpourmpakis, G.; Vlachos, G., Density functional theory-computed mechanisms of ethylene and diethyl ether formation from ethanol on γ-Al2O3 (100) *Acs Catalysis* **2013,** *3* (9), 1965-1975.
52. Wischert, R.; Copéret, C.; Delbecq, F.; Sautet, P., Optimal Water Coverage on Alumina: A Key to Generate Lewis Acid–Base Pairs that are Reactive Towards the C-H Bond Activation of Methane. *Angewandte Chemie* **2011,** *123* (14), 3260-3263.
53. Jiang, Y.; Huang, J.; Dai, W.; Hunger, M., Solid-state nuclear magnetic resonance investigations of the nature, property, and activity of acid sites on solid catalysts. *Solid State Nuclear Magnetic Resonance* **2011,** *39* (3–4), 116-141.
54. Xu, J.; Wang, Q.; Li, S.; Deng, F., Solid-State NMR Characterization of Acid Properties of Zeolites and Solid Acid Catalysts. *Solid-State NMR in Zeolite Catalysis* **2019**, 159-197.
55. Paul, G.; Bisio, C.; Braschi, I.; Cossi, M.; Gatti, G.; Gianotti, E.; Marchese, L., Combined solid-state NMR, FT-IR and computational studies on layered and porous materials. *Chemical Society Reviews* **2018,** *47* (15), 5684-5739.
56. Gorte, R. J.; Crossley, S. P., A perspective on catalysis in solid acids. *Journal of Catalysis* **2019,** *375*, 524-530.
57. Hunger, M., Catalytically Active Sites: Generation and Characterization. *Zeolites and Catalysis: Synthesis, Reactions and Applications* **2010**, 2, 493-546.
58. Schlögl, R., Heterogeneous catalysis. *Angewandte Chemie International Edition* **2015,** 54(11), 3465-3520.
59. Gabrienko, A.; Danilova,G.; Arzumanov, S.; Pirutko, V.; Freude, D.; Stepanov, G., Direct Measurement of Zeolite Brønsted Acidity by FTIR Spectroscopy: Solid-State 1H MAS NMR Approach for Reliable Determination of the Integrated Molar Absorption Coefficients. *The Journal of Physical Chemistry C* **2018,** *122* (44), 25386-25395.
60. Zheng, A.; Liu, S.-B.; Deng, F., 31P NMR Chemical Shifts of Phosphorus Probes as Reliable and Practical Acidity Scales for Solid and Liquid Catalysts. *Chemical Reviews* **2017,** *117* (19), 12475-12531.
61. Yi, X.; Ko, H.; Deng, F.; Liu, B.; Zheng, A., Solid-state 31P NMR mapping of active centers and relevant spatial correlations in solid acid catalysts. *Nature Protocols* **2020,** *15* (10), 3527-3555.
62. Wang, Z.; Jiang, Y.; Baiker, A.; Huang, J., Pentacoordinated Aluminum Species: New Frontier for Tailoring Acidity-Enhanced Silica–Alumina Catalysts. *Accounts of Chemical Research* **2020,** *53* (11), 2648–2658.
63. Li, S.; Lafon, O.; Wang, W.; Wang, Q.; Wang, X.; Li, Y.; Xu, J.; Deng, F., Recent Advances of Solid-State NMR Spectroscopy for Microporous Materials. *Advanced Materials* **2020,** *32* (44), 2002879.
64. Wu, H.; Ramamoorthy, A; Opella, S., High-resolution heteronuclear dipolar solid-state NMR spectroscopy. *Journal of Magnetic Resonance Series A* **1994**, 109, 270-270.
65. Andrew, E. R.; Bradbury, A.; Eades, R. G., Nuclear Magnetic Resonance Spectra from a Crystal rotated at High Speed. *Nature* **1958,** *182* (4650), 1659-1659.
66. Hunger, M., Solid-State NMR Spectroscopy. *Zeolite Characterization and Catalysis: A Tutorial*, **2009**
67. Wang, Q.; Li, W.; Hung, I.; Mentink-Vigier, F.; Wang, X.; Qi, G.; Wang, X.; Gan, Z.; Xu, J.; Deng, F., Mapping the oxygen structure of γ-Al2O3 by high-field solid-state NMR spectroscopy. *Nature Communications* **2020,** *11* (1), 3620.
68. Chen, K.; Horstmeier, S.; Nguyen, V. T.; Wang, B.; Crossley, S. P.; Pham, T.; Gan, Z.; Hung, I.; White, J. L., Structure and Catalytic Characterization of a Second Framework

Al(IV) Site in Zeolite Catalysts Revealed by NMR at 35.2 T. *Journal of the American Chemical Society* **2020,** *142* (16), 7514-7523.
69. Vasa, S. K.; Singh, H.; Grohe, K.; Linser, R., Assessment of a Large Enzyme–Drug Complex by Proton-Detected Solid-State NMR Spectroscopy without Deuteration. *Angewandte Chemie International Edition* **2019,** *58* (17), 5758-5762.
70. Xue, K.; Sarkar, R.; Motz, C.; Asami, S.; Decker, V.; Wegner, S.; Tosner, Z.; Reif, B., Magic-Angle Spinning Frequencies beyond 300 kHz Are Necessary To Yield Maximum Sensitivity in Selectively Methyl Protonated Protein Samples in Solid-State NMR. *The Journal of Physical Chemistry C* **2018,** *122* (28), 16437-16442.
71. Perras, A.; Wang, Z.; Kobayashi, T.; Baiker, A.; Huang, J.; Pruski, M., Shedding Light on the Atomic-Scale Structure of Amorphous Silica-Alumina and its Brønsted Acid Sites. *Physical Chemistry Chemical Physics.* **2019,** *21*, 19529-19537.
72. Valla, M.; Rossini, A. J.; Caillot, M.; Chizallet, C.; Raybaud, P.; Digne, M.; Chaumonnot, A.; Lesage, A.; Emsley, L.; van Bokhoven, J. A.; Coperet, C., Atomic Description of the Interface between Silica and Alumina in Aluminosilicates through Dynamic Nuclear Polarization Surface-Enhanced NMR Spectroscopy and First-Principles Calculations. *Journal of the American Chemical Society* **2015,** *137* (33), 10710-10719.
73. Perras, F. A.; Kobayashi, T.; Pruski, M., Natural Abundance 17O DNP Two-Dimensional and Surface-Enhanced NMR Spectroscopy. *Journal of the American Chemical Society* **2015,** *137* (26), 8336-8339.
74. Lee, D.; Monin, G.; Duong, N. T.; Lopez, I. Z.; Bardet, M.; Mareau, V.; Gonon, L.; De Paëpe, G., Untangling the condensation network of organosiloxanes on nanoparticles using 2D (29)Si-(29)Si solid-state NMR enhanced by dynamic nuclear polarization. *Journal of the American Chemical Society* **2014,** *136* (39), 13781-13788.
75. Lee, D.; Takahashi, H.; Thankamony, A. S. L.; Dacquin, J.-P.; Bardet, M.; Lafon, O.; De Paepe, G., Enhanced Solid-State NMR Correlation Spectroscopy of Quadrupolar Nuclei Using Dynamic Nuclear Polarization. *Journal of the American Chemical Society* **2012,** *134* (45), 18491-18494.
76. Liao, C.; Ghaffari, B.; Gordon, P.; Xu, J.; Copéret, C., Dynamic Nuclear Polarization Surface Enhanced NMR spectroscopy (DNP SENS): Principles, protocols, and practice. *Current Opinion in Colloid & Interface Science* **2018,** *33*, 63-71.
77. Gunther, W. R.; Michaelis, V. K.; Caporini, M. A.; Griffin, R. G.; Román-Leshkov, Y., Dynamic Nuclear Polarization NMR Enables the Analysis of Sn-Beta Zeolite Prepared with Natural Abundance 119Sn Precursors. *Journal of the American Chemical Society* **2014,** *136* (17), 6219-6222.
78. Wang, Z.; Jiang, Y.; Yi, X.; Zhou, C.; Rawal, A.; Hook, J.; Liu, Z.; Deng, F.; Zheng, A.; Hunger, M.; Baiker, A.; Huang, J., High population and dispersion of pentacoordinated AlV species on the surface of flame-made amorphous silica-alumina. *Science Bulletin* **2019,** *64* (8), 516-523.
79. Huo, H.; Peng, L.; Gan, Z.; Grey, C. P., Solid-State MAS NMR Studies of Brønsted Acid Sites in Zeolite H-Mordenite. *Journal of the American Chemical Society* **2012,** *134* (23), 9708-9720.
80. Amoureux, P.; Fernandez, C.; Steuernagel, S., Z filtering in MQMAS NMR. *Journal of Magnetic Resonance Series A* **1996,** *123* (1), 116-118.
81. Jiao, J.; Kanellopoulos, J.; Wang, W.; Ray, S. S.; Foerster, H.; Freude, D.; Hunger, M., Characterization of framework and extra-framework aluminum species in non-hydrated zeolites Y by Al-27 spin-echo, high-speed MAS, and MQMAS NMR spectroscopy at B-0=9.4 to 17.6 T. *Physical Chemistry Chemical Physics.* **2005,** *7* (17), 3221-3226.
82. Alemany, B.; Steuernagel, S.; Amoureux, P.; Callender, L.; Barron, R., Very fast MAS and MQMAS NMR studies of the spectroscopically challenging minerals kyanite and

andalusite on 400, 500, and 800 MHz spectrometers. *Solid State Nuclear Magnetic Resonance* **1999,** *14* (1), 1-18.
83. Gore, U.; Abraham, A.; Hegde, G.; Kumar, R.; Amoureux, P.; Ganapathy, S., Si-29 and Al-27 MAS/3Q-MAS NMR studies of high silica USY zeolites. *The Journal of Physical Chemistry B* **2002,** *106* (23), 6115-6120.
84. Busca, G., Catalytic materials based on silica and alumina: Structural features and generation of surface acidity. *Progress in Materials Science* **2019,** *104*, 215-249.
85. Yu, Z.; Zheng, A.; Wang, Q.; Chen, L.; Xu, J.; Amoureux, J.-P.; Deng, F., Insights into the Dealumination of Zeolite HY Revealed by Sensitivity-Enhanced Al-27 DQ-MAS NMR Spectroscopy at High Field. *Angewandte Chemie-International Edition* **2010,** *49* (46), 8657-8661.
86. Li, S.; Zheng, A.; Su, Y.; Fang, H.; Shen, W.; Yu, Z.; Chen, L.; Deng, F., Extra-framework aluminium species in hydrated faujasite zeolite as investigated by two-dimensional solid-state NMR spectroscopy and theoretical calculations. *Physical Chemistry Chemical Physics.* **2010,** *12* (15), 3895-3903.
87. Wang, Q.; Hu, B.; Lafon, O.; Trébosc, J.; Deng, F.; Amoureux, J. P., Double-quantum homonuclear NMR correlation spectroscopy of quadrupolar nuclei subjected to magic-angle spinning and high magnetic field. *Journal of Magnetic Resonance* **2009,** *200* (2), 251-260.
88. Luo, Q.; Deng, F.; Yuan, Z. Y.; Yang, J.; Zhang, M. J.; Yue, Y.; Ye, C. H., Using trimethylphosphine as a probe molecule to study the acid states in Al-MCM-41 materials by solid-state NMR spectroscopy. *The Journal of Physical Chemistry B* **2003,** *107* (11), 2435-2442.
89. Xu, M.; Wang, W.; Seiler, M.; Buchholz, A.; Hunger, M., Improved Brønsted Acidity of Mesoporous [Al]MCM-41 Material Treated with Ammonium Fluoride†. *The Journal of Physical Chemistry B* **2002,** *106* (12), 3202-3208.
90. Grey, P.; Vega, J., Determination of the Quadrupole Coupling Constant of the Invisible Aluminum Spins in Zeolite HY with 1H/27Al TRAPDOR NMR. *Journal of the American Chemical Society* **1995,** *117* (31), 8232-8242.
91. Wang, C.; Jiang, J.; Lafon, O.; Trebosc, J.; Kim, D.; Stampfl, C.; Baiker, A.; Amoureux, P.; Huang, J., Bronsted acid sites based on penta-coordinated aluminum species. *Nature Communications* **2016,** *7*, 13820.
92. Peng, L.; Huo, H.; Liu, Y.; Grey, C. P., O-17 magic angle spinning NMR studies of Bronsted acid sites in zeolites HY and HZSM-5. *Journal of the American Chemical Society* **2007,** *129* (2), 335-346.
93. Bignami, M.; Dawson, M.; Seymour, R.; Wheatley, S.; Morris, E.; Ashbrook, E., Synthesis, Isotopic Enrichment, and Solid-State NMR Characterization of Zeolites Derived from the Assembly, Disassembly, Organization, Reassembly Process. *Journal of the American Chemical Society* **2017,** *139* (14), 5140-5148.
94. Xu, J.; Wang, Q.; Deng, F., Metal Active Sites and Their Catalytic Functions in Zeolites: Insights from Solid-State NMR Spectroscopy. *Accounts of Chemical Research* **2019,** *52* (8), 2179-2189.
95. Chizallet, C., Toward the Atomic Scale Simulation of Intricate Acidic Aluminosilicate Catalysts. *ACS Catalysis* **2020,** *10* (10), 5579-5601.
96. Hunger, M.; Wang, W., Formation of cyclic compounds and carbenium ions by conversion of methanol on weakly dealuminated zeolite H-ZSM-5 investigated via a novel in situ CF MAS NMR/UV-Vis technique. *Chemical communications* **2004,** (5), 584-585.
97. Blanc, F.; Leskes, M.; Grey, P., In situ solid-state NMR spectroscopy of electrochemical cells: batteries, supercapacitors, and fuel cells. *Accounts of chemical research* **2013,** *46* (9), 1952-1963.

98. Hwang, J.; Petucci, C.; Raftery, D., In situ solid-state NMR studies of trichloroethylene photocatalysis: formation and characterization of surface-bound intermediates. *Journal of the American Chemical Society* **1998,** *120* (18), 4388-4397.
99. Weitkamp, J. a. H., M., Acid and base catalysis on zeolites. *Studies in Surface Science and Catalysis* **2007**, 787-835
100. Peng, L. M.; Liu, Y.; Kim, N. J.; Readman, J. E.; Grey, C. P., Detection of Bronsted acid sites in zeolite HY with high-field O-17-MAS-NMR techniques. *Nature Materials* **2005,** *4* (3), 216-219.
101. Hunger, M.; Freude, D.; Pfeifer, H.; Prager, D.; Reschetilowski, W., Proton MAS NMR studies of hydroxyl groups in alkaline earth cation-exchanged zeolite Y *Chemical physics letters* **1989,** *163* (2-3), 221-224.
102. Hirschler, A. E., The measurement of catalyst acidity using indicators forming stable surface carbonium ions *Journal Of Catalysis* **1963,** *2* (5), 428-439.
103. Yu, Z.; Li, S.; Wang, Q.; Zheng, A.; Jun, X.; Chen, L.; Deng, F., Brønsted/Lewis Acid Synergy in H–ZSM-5 and H–MOR Zeolites Studied by 1H and 27Al DQ-MAS Solid-State NMR Spectroscopy. *The Journal of Physical Chemistry C* **2011,** *115* (45), 22320-22327.
104. Gao, P.; Wang, Q.; Xu, J.; Qi, G.; Wang, C.; Zhou, X.; Zhao, X.; Feng, N.; Liu, X.; Deng, F., Brønsted/Lewis Acid Synergy in Methanol-to-Aromatics Conversion on Ga-Modified ZSM-5 Zeolites, As Studied by Solid-State NMR Spectroscopy. *ACS Catalysis* **2018,** *8* (1), 69-74.
105. Qi, G.; Wang, Q.; Xu, J.; Trébosc, J.; Lafon, O.; Wang, C.; Amoureux, J.-P.; Deng, F., Synergic Effect of Active Sites in Zinc-Modified ZSM-5 Zeolites as Revealed by High-Field Solid-State NMR Spectroscopy. *Angewandte Chemie International Edition* **2016,** *55* (51), 15826-15830.
106. Brown, S. P.; Spiess, H. W., Advanced Solid-State NMR Methods for the Elucidation of Structure and Dynamics of Molecular, Macromolecular, and Supramolecular Systems. *Chemical Reviews* **2001,** *101* (12), 4125-4156.
107. Xin, S.; Wang, Q.; Xu, J.; Chu, Y.; Wang, P.; Feng, N.; Qi, G.; Trébosc, J.; Lafon, O.; Fan, W.; Deng, F., The acidic nature of "NMR-invisible" tri-coordinated framework aluminum species in zeolites. *Chemical Science* **2019,** *10* (43), 10159-10169.
108. Corma, A.; Nemeth, L. T.; Renz, M.; Valencia, S., Sn-zeolite beta as a heterogeneous chemoselective catalyst for Baeyer–Villiger oxidations. *Nature* **2001,** *412* (6845), 423-425.
109. Moliner, M.; Roman-Leshkov, Y.; Davis, M. E., Tin-containing zeolites are highly active catalysts for the isomerization of glucose in water. *Proceedings of the National Academy of Sciences of the United States of America* **2010,** *107* (14), 6164-6168.
110. Qi, G.; Wang, Q.; Xu, J.; Wu, Q.; Wang, C.; Zhao, X.; Meng, X.; Xiao, F.; Deng, F., Direct observation of tin sites and their reversible interconversion in zeolites by solid-state NMR spectroscopy. *Communications Chemistry* **2018,** *1* (1), 22.
111. Wang, Z.; Jiang, Y.; Jin, F.; Stampfl, C.; Hunger, M.; Baiker, A.; Huang, J., Strongly enhanced acidity and activity of amorphous silica–alumina by formation of pentacoordinated AlV species. *Journal of Catalysis* **2019,** *372*, 1-7.
112. Wang, Z.; Jiang, Y.; Rachwalik, R.; Liu, Z.; Shi, J.; Hunger, M.; Huang, J., One-Step Room-Temperature Synthesis of Al MCM-41 Materials for the Catalytic Conversion of Phenylglyoxal to Ethylmandelate. *ChemCatChem* **2013,** *5* (12), 3889-3896.
113. Huang, J.; van Vegten, N.; Jiang, Y.; Hunger, M.; Baiker, A., Increasing the Bronsted Acidity of Flame-Derived Silica/Alumina up to Zeolitic Strength. *Angewandte Chemie-International Edition* **2010,** *49* (42), 7776-7781.
114. Tamele, M. W., Chemistry of the surface and the activity of alumina-silica cracking catalyst. *Discussions of the Faraday Society* **1950,** *8*, 270-279.

115. Thomas, L., Chemistry of Cracking Catalysts. *Industrial & Engineering Chemistry* **1949,** *41* (11), 2564-2573.
116. Eichler, U.; Brandle, M.; Sauer, J., Predicting absolute and site specific acidities for zeolite catalysts by a combined quantum mechanics interatomic potential function approach. *The Journal of Physical Chemistry B* **1997,** *101* (48), 10035-10050.
117. Chizallet, C.; Raybaud, P., Pseudo-Bridging Silanols as Versatile Brønsted Acid Sites of Amorphous Aluminosilicate Surfaces. *Angewandte Chemie International Edition* **2009,** *48* (16), 2891-2893.
118. Omegna, A.; van Bokhoven, A.; Prins, R., Flexible aluminum coordination in alumino-silicates. Structure of zeolite H-USY and amorphous silica-alumina. *The Journal of Physical Chemistry B* **2003,** *107* (34), 8854-8860.
119. Mouat, A. R.; George, C.; Kobayashi, T.; Pruski, M.; van Duyne, R. P.; Marks, T. J.; Stair, P. C., Highly Dispersed SiOx/Al2O3 Catalysts Illuminate the Reactivity of Isolated Silanol Sites. *Angewandte Chemie International Edition* **2015,** *54* (45), 13346-13351.
120. Hunger, M.; Freude, D.; Pfeifer, H.; Bremer, H.; Jank, M.; Wendlandt, K. P., High-resolution proton magnetic resonance and catalytic studies concerning brønsted centers of amorphous Al2O3-SiO2 solids *Chemical physics letters* **1983,** *100* (1), 29-33.
121. Xu, B.; Sievers, C.; Lercher, A.; van Veen, R.; Giltay, P.; Prins, R.; van Bokhoven, J. A., Strong Brønsted Acidity in Amorphous Silica−Aluminas. *The Journal of Physical Chemistry C* **2007,** *111* (32), 12075-12079.
122. Poduval, D. G.; van Veen, J. A. R.; Rigutto, M. S.; Hensen, E. J. M., Bronsted acid sites of zeolitic strength in amorphous silica-alumina. *Chemical Communications* **2010,** *46* (20), 3466-3468.
123. Bevilacqua, M.; Montanari, T.; Finocchio, E.; Busca, G., Are the active sites of protonic zeolites generated by the cavities? *Catalysis Today* **2006,** *116* (2), 132-142.
124. Stebbins, J. F.; Xu, Z., NMR evidence for excess non-bridging oxygen in an aluminosilicate glass. *Nature* **1997,** *390* (6655), 60-62.
125. Caillot, M.; Chaumonnot, A.; Digne, M.; van Bokhoven, J. A., The variety of Brønsted acid sites in amorphous aluminosilicates and zeolites. *Journal of Catalysis* **2014,** *316*, 47-56.
126. Larmier, K.; Chizallet, C.; Maury, S.; Cadran, N.; Abboud, J.; Lamic-Humblot, A. F.; Marceau, E.; Lauron-Pernot, H., Isopropanol Dehydration on Amorphous Silica-Alumina: Synergy of Bronsted and Lewis Acidities at Pseudo-Bridging Silanols. *Angewandte Chemie-International Edition* **2017,** *56* (1), 230-234.
127. Freeman, D. L.; Doll, J. D., The influence of diffusion on surface reaction kinetics *The Journal of Physical Chemistry* **1983,** *78* (10), 6002-6009.
128. Lei, G. D.; Carvill, B. T.; Sachtler, W. M. H., Single file diffusion in mordenite channels: Neopentane conversion and H/D exchange as catalytic probes. *Applied Catalysis A-General* **1996,** *142* (2), 347-359.
129. Ryder, A.; Chakraborty, K.; Bell, T., Density functional theory study of proton mobility in zeolites: Proton migration and hydrogen exchange in ZSM-5. *The Journal of Physical Chemistry B* **2000,** *104* (30), 6998-7011.
130. Hensen, M.; Poduval, G.; Magusin, P. M.; Coumans, A. E.; van Veen, J. A. R., Formation of acid sites in amorphous silica-alumina. *Journal of Catalysis* **2010,** *269* (1), 201-218.
131. MacKenzie, D.; Temuujin, J.; Okada, K., Thermal decomposition of mechanically activated gibbsite. *Thermochimica Acta* **1999,** *327* (1–2), 103-108.
132. Rosenholm, M.; Czuryszkiewicz, T.; Kleitz, F.; Rosenholm, B.; Linden, M., On the nature of the bronsted acidic groups on native and functionalized mesoporous siliceous SBA-15 as studied by benzylamine adsorption from solution. *Langmuir* **2007,** *23* (8), 4315-4323.

133. Shaw, A. M.; Hannon, T. E.; Li, F.; Zare, R. N., Adsorption of Crystal Violet to the Silica−Water Interface Monitored by Evanescent Wave Cavity Ring-Down Spectroscopy. *The Journal of Physical Chemistry B* **2003,** *107* (29), 7070-7075.
134. Dijkstra, T. W.; Duchateau, R.; Van Santen, R. A.; Meetsma, A.; Yap, G. P. A., Silsesquioxane Models for Geminal Silica Surface Silanol Sites. A Spectroscopic Investigation of Different Types of Silanols. *Journal of the American Chemical Society* **2002,** *124* (33), 9856-9864.
135. Chronister, C. W.; Drago, R. S., Determination of hydrogen-bonding acid sites on silica using the Cal-Ad method. *Journal of the American Chemical Society* **1993,** *115* (11), 4793-4798.
136. Wang, C.; Jiang, J.; Zhang, Y.; Shi, J.; Stampfl, C.; Hunger, M.; Huang, J., Identification of Vicinal Silanols and Promotion of Their Formation on MCM-41 via Ultrasonic Assisted One-Step Room-Temperature Synthesis for Beckmann Rearrangement. *Industrial & Engineering Chemistry Research* **2018,** *57* (16), 5550-5557.
137. Mastikhin, V. M.; Nosov, A. V.; Terskikh, V. V.; Zamaraev, K. I.; Wachs, I. E., 1H MAS NMR studies of alumina-supported metal oxide catalysts *The Journal of Physical Chemistry* **1994,** *98* (51), 13621-13624.
138. Crocker, M.; Herold, R. H. M.; Wilson, A. E.; Mackay, M.; Emeis, C. A.; Hoogendoorn, A. M., H-1 NMR spectroscopy of titania - Chemical shift assignments for hydroxy groups in crystalline and amorphous forms of TiO2. *Journal Of the Chemical Society-Faraday Transactions* **1996,** *92* (15), 2791-2798.
139. Turek, M.; Wachs, E.; Decanio, E., Acidic properties of alumina-supported metal oxide catalysts: an infrared spectroscopy study *The Journal of Physical Chemistry* **1992,** *96* (12), 5000-5007.
140. Xu, J.; Zheng, A. M.; Yang, J.; Su, Y. C.; Wang, J. Q.; Zeng, D. L.; Zhang, M. J.; Ye, C. H.; Deng, F., Acidity of mesoporous MoOx/ZrO2 and WOx/ZrO2 materials: A combined solid-state NMR and theoretical calculation study. *The Journal of Physical Chemistry B* **2006,** *110* (22), 10662-10671.
141. Riemer, T.; Spielbauer, D.; Hunger, M.; Mekhemer, G. A. H.; Knozinger, H., Superacid properties of sulfated zirconia as measured by Raman and 1 H MAS NMR spectroscopy *Journal of the Chemical Society-Chemical Communications* **1994,** (10), 1181-1182.
142. Mastikhin, M.; Mudrakovsky, L.; Nosov, V., 1H NMR magic angle spinning (MAS) studies of heterogeneous catalysis. *Progress In Nuclear Magnetic Resonance Spectroscopy* **1991,** *23*, 259-299.
143. Boronat, M.; Corma, A., Factors Controlling the Acidity of Zeolites. *Catalysis Letters* **2015,** *145* (1), 162-172.
144. Hunger, M.; Ernst, S.; Steuernagel, S.; Weitkamp, J., High-field H-1 MAS NMR investigations of acidic and non-acidic hydroxyl groups in zeolites H-Beta, H-ZSM-5, H-ZSM-58 and H-MCM-22. *Microporous Materials* **1996,** *6* (5-6), 349-353.
145. Huang, J.; Jiang, Y. J.; Marthala, V. R. R.; Wang, W.; Sulikowski, B.; Hunger, M., In situ H-1 MAS NMR investigations of the H/D exchange of alkylaromatic hydrocarbons on zeolites H-Y, La,Na-Y, and H-ZSM-5. *Microporous and Mesoporous Materials* **2007,** *99* (1-2), 86-90.
146. Omegna, A.; Vasic, M.; van Bokhoven, J. A.; Pirngruber, G.; Prins, R., Dealumination and realumination of microcrystalline zeolite beta: an XRD, FTIR and quantitative multinuclear (MQ) MAS NMR study. *Physical Chemistry Chemical Physics* **2004,** *6* (2), 447-452.

147. Kennedy, J.; Afeworki, M.; Calabro, C.; Chase, E.; Smiley, J., H MAS NMR (magic-angle spinning nuclear magnetic resonance) techniques for the quantitative determination of hydrogen types in solid catalysts and supports. *Applied Spectroscopy* **2004,** *58* (6), 698-704.
148. Zhang, P.; Ma, D.; Liu, C.; Liu, M.; Bao, H., Perfluorotributylamine as a probe molecule for distinguishing internal and external acidic sites in zeolites by high-resolution H-1 MAS NMR spectroscopy. *Chemical Communications* **1999,** (12), 1091-1092.
149. Ma, D.; Han, W.; Xie, J.; Bao, H.; Hu, B.; Au-Yeung, F., An investigation of the roles of surface aluminum and acid sites in the zeolite MCM-22. *Chemistry–A European Journal* **2002,** *8* (1), 162-170.
150. Pazè, C.; Zecchina, A.; Spera, S.; Cosma, A.; Merlo, E.; Spanò, G.; Girotti, G., Comparative IR and 1H-MAS NMR study of adsorption of CD3CN on zeolite H-β: evidence of the presence of two families of bridged Brnsted sites. *Physical Chemistry Chemical Physics* **1999,** *1* (10), 2627-2629.
151. Gabrienko, A.; Danilova, G.; Arzumanov, S.; Toktarev, V.; Freude, D.; Stepanov, G., Strong acidity of silanol groups of zeolite beta: Evidence from the studies by IR spectroscopy of adsorbed CO and H-1 MAS NMR. *Microporous and Mesoporous Materials* **2010,** *131* (1-3), 210-216.
152. Huang, J.; Jiang, J.; Marthala, V. R.; Ooi, Y. S.; Hunger, M., Regioselective H/D exchange at the side-chain of ethylbenzene on dealuminated zeolite H-Y studied by in situ MAS NMR-UV/Vis spectroscopy. *Chemphyschem* **2008,** *9* (8), 1107-1109.
153. Sanchez Escribano, V.; Garbarino, G.; Finocchio, E.; Busca, G., γ-Alumina and Amorphous Silica–Alumina: Structural Features, Acid Sites and the Role of Adsorbed Water. *Topics in Catalysis* **2017,** *60* (19), 1554-1564.
154. Crepeau, G.; Montouillout, V.; Vimont, A.; Mariey, L.; Cseri, T.; Mauge, F., Nature, structure and strength of the acidic sites of amorphous silica alumina: An IR and NMR study. *The Journal of Physical Chemistry B* **2006,** *110* (31), 15172-15185.
155. Kim, K. D.; Pokhrel, S.; Wang, Z. C.; Ling, H. J.; Zhou, C. F.; Liu, Z. W.; Hunger, M.; Madler, L.; Huangt, J., Tailoring High-Performance Pd Catalysts for Chemoselective Hydrogenation Reactions via Optimizing the Parameters of the Double-Flame Spray Pyrolysis. *ACS Catalysis* **2016,** *6* (4), 2372-2381.
156. Chen, K.; Abdolrhamani, M.; Sheets, E.; Freeman, J.; Ward, G.; White, J. L., Direct Detection of Multiple Acidic Proton Sites in Zeolite HZSM-5. *Journal of the American Chemical Society* **2017,** *139* (51), 18698-18704.
157. Sandoval-Díaz, L.-E.; González-Amaya, J.-A.; Trujillo, C.-A., General aspects of zeolite acidity characterization. *Microporous and Mesoporous Materials* **2015,** *215*, 229-243.
158. Freude, D.; Hunger, M.; Pfeifer, H.; Schwieger, W., H-1 MAS NMR-STUDIES ON THE ACIDITY OF ZEOLITES. *Chemical Physics Letters* **1986,** *128* (1), 62-66.
159. Samoson, A.; Lippmaa, E.; Engelhardt, G.; Lohse, U.; Jerschkewitz, H. G., Quantitative high-resolution 27Al NMR: tetrahedral non-framework aluminium in hydrothermally treated zeolites *Chemical physics letters* **1987,** *134* (6), 589-592.
160. Hunger, M.; Anderson, M. W.; Ojo, A.; Pfeifer, H., Study of the geometry and location of the bridging OH groups in aluminosilicate and silicoaluminophosphate type zeolites using 1H MAS NMR sideband analysis and CP/MAS NMR *Microporous Material* **1993,** *1* (1), 17-32.
161. Deng, F.; Yue, Y.; Ye, H., H-1/Al-27 TRAPDOR NMR studies on aluminum species in dealuminated zeolites. *Solid State Nuclear Magnetic Resonance* **1998,** *10* (3), 151-160.
162. Zhang, W. P.; Bao, X. H.; Guo, X. W.; Wang, X. S., A high-resolution solid-state NMR study on nano-structured HZSM-5 zeolite. *Catalysis Letters* **1999,** *60* (1-2), 89-94.

163. Simon, A.; Gougeon, R. D.; Paillaud, J. L.; Valtchev, V.; Kessler, H., Characterization of the acidity of Mu-14 by solid-state NMR and NH3-STD. *Physical Chemistry Chemical Physics* **2001,** *3* (5), 867-872.
164. Kao, H. M.; Grey, C. P.; Pitchumani, K.; Lakshminarasimhan, P. H.; Ramamurthy, V., Activation conditions play a key role in the activity of zeolite CaY: NMR and product studies of Bronsted acidity. *The Journal of Physical Chemistry A* **1998,** *102* (28), 5627-5638.
165. Staudte, B.; Hunger, M.; Nimz, M., 1H MAS nmr and nir studies of aluminum-exchanged ZSM-5 zeolites *Zeolites* **1991,** *11* (8), 837-841.
166. Weihe, M.; Hunger, M.; Breuninger, M.; Karge, H. G.; Whitkamp, J., Influence of the nature of residual alkali cations on the catalytic activity of zeolites X, Y, and EMT in their Bronsted acid forms. *Journal Of Catalysis* **2001,** *198* (2), 256-265.
167. Zhang, W. P.; Sun, M. Y.; Prins, R., Multinuclear MAS NMR identification of fluorine species on the surface of fluorinated gamma-alumina. *The Journal of Physical Chemistry B* **2002,** *106* (45), 11805-11809.
168. Huang, J.; Jiang, Y.; Marthala, V. R. R.; Thomas, B.; Romanova, E.; Hunger, M., Characterization and acidic properties of aluminum-exchanged zeolites X and Y. *Journal of Physical Chemistry C* **2008,** *112* (10), 3811-3818.
169. Nesterenko, N. S.; Thibault-Starzyk, F.; Montouillout, V.; Yuschenko, V. V.; Fernandez, C.; Gilson, J. P.; Fajula, F.; Ivanova, II, Accessibility of the acid sites in dealuminated small-port mordenites studied by FTIR of co-adsorbed alkylpyridines and CO. *Microporous And Mesoporous Materials* **2004,** *71* (1-3), 157-166.
170. Buchholz, A.; Wang, W.; Xu, M.; Arnold, A.; Hunger, M., Thermal stability and dehydroxylation of Bronsted acid sites in silicoaluminophosphates H-SAPO-11, H-SAPO-81 H-SAPO-31, and H-SAPO-34 investigated by multi-nuclear solid-state NMR spectroscopy. *Microporous And Mesoporous Materials* **2002,** *56* (3), 267-278.
171. Hajjar, R.; Millot, Y.; Man, P. P.; Che, M.; Dzwigaj, S., Two Kinds of Framework Al Sites Studied in BEA Zeolite by X-ray Diffraction, Fourier Transform Infrared Spectroscopy, NMR Techniques, and V Probe. *The Journal of Physical Chemistry C* **2008,** *112* (51), 20167-20175.
172. Zhao, Z.; Li, X.; Li, S.; Xu, S.; Bao, X.; Bilge, Y.; Andrei-Nicolae, P.; Ulrich, M.; Zhang, W., Structural investigation of interlayer-expanded zeolite by hyperpolarized 129Xe and 1H NMR spectroscopy. *Microporous and Mesoporous Materials* **2019,** *288*, 109555.
173. Koller, H.; Lobo, R. F.; Burkett, S. L.; Davis, M. E., SiO---HOSi Hydrogen Bonds in As-Synthesized High-Silica Zeolites *The Journal of Physical Chemistry* **1995,** *99* (33), 12588-12596.
174. Wolf, I.; Gies, H.; Fyfe, C. A., Ordering of silicate layers by hydrogen-bonding networks: Solid state NMR investigation of the perfect three-dimensional registration in the layer silicate RUB-18. *The Journal of Physical Chemistry B* **1999,** *103* (29), 5933-5938.
175. Gun'ko, V. M.; Zarko, V. I.; Turov, V. V.; Leboda, R.; Chibowski, E.; Pakhlov, E. M.; Goncharuk, E. V.; Marciniak, M.; Voronin, F.; Chuiko, A., Characterization of Fumed Alumina/Silica/Titania in the Gas Phase and in Aqueous Suspension. *Journal of Colloid and Interface Science* **1999,** *220* (2), 302-323.
176. Jiang, Y. J.; Huang, J.; Marx, S.; Kleist, W.; Hunger, M.; Baiker, A., Effect of Dehydration on the Local Structure of Framework Aluminum Atoms in Mixed Linker MIL-53(Al) Materials Studied by Solid-State NMR Spectroscopy. *The Journal of Physical Chemistry Letter* **2010,** *1* (19), 2886-2890.
177. Loiseau, T.; Serre, C.; Huguenard, C.; Fink, G.; Taulelle, F.; Henry, M.; Bataille, T.; Ferey, G., A rationale for the large breathing of the porous aluminum terephthalate (MIL-53) upon hydration. *Chemistry – A European Journal* **2004,** *10* (6), 1373-1382.

178. Lieder, C.; Opelt, S.; Dyballa, M.; Henning, H.; Klemm, E.; Hunger, M., Adsorbate Effect on AlO4(OH)(2) Centers in the Metal-Organic Framework MIL-53 Investigated by Solid-State NMR Spectroscopy. *Journal Of Physical Chemistry C* **2010,** *114* (39), 16596-16602.
179. Volkringer, C.; Loiseau, T.; Guillou, N.; Ferey, G.; Haouas, M.; Taulelle, F.; Audebrand, N.; Margiolaki, I.; Popov, D.; Burghammer, M.; Riekel, C., Structural Transitions and Flexibility during Dehydration-Rehydration Process in the MOF-type Aluminum Pyromellitate Al(2)(OH)(2) C(10)O(8)H(2) (MIL-118). *Crystal Growth & Design* **2009,** *9* (6), 2927-2936.
180. Dec, S. F.; Herring, A. M., Solid-State 1H NMR Study of Structures and Dynamics of Proton Sites in Group II Salts of 12-Tungstophosphoric Acid and Related Compounds. *The Journal of Physical Chemistry C* **2018,** *122* (27), 15539-15557.
181. Baba, T.; Nomura, M.; Ono, Y.; Ohno, Y., Solid-state proton MAS NMR study on the highly active protons in partially reduced trisilver dodecatungstophosphate (Ag3PW12O40). *The Journal of Physical Chemistry* **1993,** *97* (49), 12888-12893.
182. Baba, T.; Ono, Y., Dynamic properties of protons in solid acids as studied by variable temperature H-1 MAS NMR. *Applied Catalysis A-General* **1999,** *181* (2), 227-238.
183. Filek, U.; Bressel, A.; Sulikowski, B.; Hunger, M., Structural Stability and Bronsted Acidity of Thermally Treated AlPW(12)O(40) in Comparison with H(3)PW(12)O(40). *Journal Of Physical Chemistry C* **2008,** *112* (49), 19470-19476.
184. Brunner, E.; Beck, K.; Koch, M.; Heeribout, L.; Karge, H. G., Verification and quantitative determination of a new type of Brønsted acid sites in H-ZSM-5 by 1H magic-angle spinning nuclear magnetic resonance spectroscopy. *Microporous Mater.* **1995,** *3* (4-5), 395-399.
185. Nakashima, S.; Takahashi, Y.; Kiguchi, M., Effect of the environment on the electrical conductance of the single benzene-1,4-diamine molecule junction. *Beilstein Journal of Nanotechnology* **2011,** *2*, 755-759.
186. Kao, H.-M.; Grey, C. P., Determination of the 31P−27Al J-Coupling Constant for Trimethylphosphine Bound to the Lewis Acid Site of Zeolite HY. *Journal of the American Chemical Society* **1997,** *119* (3), 627-628.
187. Hunger, M.; Schenk, U.; Breuninger, M.; Glaser, R.; Weitkamp, J., Characterization of the acid sites in MCM-41-type materials by spectroscopic and catalytic techniques. *Microporous and Mesoporous Materials* **1999,** *27* (2-3), 261-271.
188. Lang, S.; Benz, M.; Obenaus, U.; Himmelmann, R.; Hunger, M., Novel Approach for the Characterization of Lewis Acidic Solid Catalysts by Solid-State NMR Spectroscopy. *ChemCatChem* **2016,** *8* (12), 2031-2036.
189. Wang, Z.; Jiang, Y.; Stampfl, C.; Baiker, A.; Hunger, M.; Huang, J., NMR Spectroscopic Characterization of Flame-Made Amorphous Silica-Alumina for Cyclohexanol and Glyceraldehyde Conversion. *ChemCatChem* **2020,** *12*, 287-293.
190. Yin, F.; Blumenfeld, A. L.; Gruver, V.; Fripiat, J. J., NH3 as a Probe Molecule for NMR and IR Study of Zeolite Catalyst Acidity. *The Journal of Physical Chemistry B* **1997,** *101* (10), 1824-1830.
191. Hunger, M., Multinuclear solid-state NMR studies of acidic and non-acidic hydroxyl protons in zeolites. *Solid State Nuclear Magnetic Resonance* **1996,** *6* (1), 1-29.
192. Jacobs, H.; de Haan, W.; van, M.; van, A., Interaction of ammonia with Broensted acid sites in different cages of zeolite Y as studied by proton MAS NMR. *The Journal of Physical Chemistry* **1993,** *97* (40), 10394-10402.
193. Kim, D.; Wang, Z.; Tao, Y.; Ling, H.; Yuan, Y.; Zhou, C.; Liu, Z.; Gaborieau, M.; Huang, J.; Yu, A., The Comparative Effect of Particle Size and Support Acidity on Hydrogenation of Aromatic Ketones. *ChemCatChem* **2019,** *11* (0), 1-9.

194. Wang, Z.; Jiang, Y.; Hunger, M.; Baiker, A.; Huang, J., Catalytic Performance of Bronsted and Lewis Acid Sites in Phenylglyoxal Conversion on Flame-Derived Silica-Zirconia. *ChemCatChem* **2014,** *6* (10), 2970-2975.
195. Engelhardt, G., Solid state NMR spectroscopy applied to zeolites. *Studies in Surface Science and Catalysis*, **2001**, 387-418.
196. Freude, D.; Ernst, H.; Hunger, M.; Pfeifer, H.; Jahn, E., Magic-angle-spinning NMR studies of zeolite SAPO-5. *Chemical Physics Letters* **1988,** *143* (5), 477-481.
197. Hunger, M.; Freude, D.; Pfeifer, H., 1H MAS studies of acid sites in ZSM-5 type zeolites. *Catalysis Today* **1988,** *3* (5), 507-512.
198. Weihe, M.; Hunger, M.; Breuninger, M.; Karge, H. G.; Weitkamp, J., Influence of the Nature of Residual Alkali Cations on the Catalytic Activity of Zeolites X, Y, and EMT in their Brønsted Acid Forms. *Journal of Catalysis* **2001,** *198* (2), 256-265.
199. Huang, J.; Jiang, Y.; Reddy Marthala, V. R.; Ooi, Y. S.; Weitkamp, J.; Hunger, M., Concentration and acid strength of hydroxyl groups in zeolites La,Na-X and La,Na-Y with different lanthanum exchange degrees studied by solid-state NMR spectroscopy. *Microporous and Mesoporous Materials* **2007,** *104* (1-3), 129-136.
200. Zheng, A.; Zhang, H.; Chen, L.; Yue, Y.; Ye, C.; Deng, F., Relationship Between 1H Chemical Shifts of Deuterated Pyridinium Ions and Brønsted Acid Strength of Solid Acids. *The Journal of Physical Chemistry B* **2007,** *111* (12), 3085-3089.
201. Haw, J. F.; Chuang, I. S.; Hawkins, B. L.; Maciel, G. E., Surface titration of silica-alumina monitored by nitrogen-15 NMR with cross polarization and magic-angle spinning. *Journal of the American Chemical Society* **1983,** *105* (24), 7206-7207.
202. Ripmeester, J. A., Surface acid site characterization by means of CP/MAS nitrogen-15 NMR. *Journal of the American Chemical Society* **1983,** *105* (9), 2925-2927.
203. Haw, J. F.; Zhang, J.; Shimizu, K.; Venkatraman, T. N.; Luigi, D.-P.; Song, W.; Barich, D. H.; Nicholas, J. B., NMR and Theoretical Study of Acidity Probes on Sulfated Zirconia Catalysts. *Journal of the American Chemical Society* **2000,** *122* (50), 12561-12570.
204. Gunther, W. R.; Michaelis, V. K.; Griffin, R. G.; Román-Leshkov, Y., Interrogating the Lewis Acidity of Metal Sites in Beta Zeolites with 15N Pyridine Adsorption Coupled with MAS NMR Spectroscopy. *The Journal of Physical Chemistry C* **2016,** *120* (50), 28533-28544.
205. Gurinov, A. A.; Rozhkova, Y. A.; Zukal, A.; Čejka, J.; Shenderovich, I. G., Mutable Lewis and Brønsted Acidity of Aluminated SBA-15 as Revealed by NMR of Adsorbed Pyridine-15N. *Langmuir* **2011,** *27* (19), 12115-12123.
206. Shenderovich, I. G.; Buntkowsky, G.; Schreiber, A.; Gedat, E.; Sharif, S.; Albrecht, J.; Golubev, N. S.; Findenegg, G. H.; Limbach, H.-H., Pyridine-15N A Mobile NMR Sensor for Surface Acidity and Surface Defects of Mesoporous Silica. *The Journal of Physical Chemistry B* **2003,** *107* (43), 11924-11939.
207. Hemmann, F.; Agirrezabal-Telleria, I.; Kemnitz, E.; Jäger, C., Probing Slow Chemical Exchange of Pyridine Molecules at Acid Magnesium Hydroxide Fluoride Surfaces by 15N NMR. *The Journal of Physical Chemistry C* **2013,** *117* (28), 14710-14716.
208. Jänchen, J.; van Wolput, J. H. M. C.; van de Ven, L. J. M.; de Haan, J. W.; van Santen, R. A., FTIR spectroscopic and1 H MAS NMR studies of the influence of lattice chemistry and structure on Brønsted acidity in zeolites. *Catalysis Letters* **1996,** *39* (3), 147-152.
209. Haw, J. F.; Nicholas, J. B.; Xu, T.; Beck, L. W.; Ferguson, D. B., Physical organic chemistry of solid acids: Lessons from in situ NMR and theoretical chemistry. *Accounts of Chemical Research* **1996,** *29* (6), 259-267.
210. Biaglow, A. I.; Gorte, R. J.; Kokotailo, G. T.; White, D., A probe of Brønsted site acidity in zeolites: 13C chemical shift of acetone. *Journal of Catalysis* **1994,** *148* (2), 779-786.
211. Biaglow, A. I.; Gorte, R. J.; White, D., 13C NMR studies of acetone in dealuminated faujasites: a probe for nonframework alumina*Journal of Catalysis* **1994,** *150* (1), 221-224.

212. Biaglow, A. I.; Sepa, J.; Gorte, R. J.; White, D., A 13C NMR study of the condensation chemistry of acetone and acetaldehyde adsorbed at the Brønsted acid sites in H-ZSM-5 *Journal of Catalysis* **1995,** *151* (2), 373-384.
213. Yang, J.; Janik, M. J.; Ma, D.; Zheng, A. M.; Zhang, M. J.; Neurock, M.; Davis, R. J.; Ye, C. H.; Deng, F., Location, acid strength, and mobility of the acidic protons in Keggin 12-H3PW12O40: A combined solid-state NMR spectroscopy and DFT quantum chemical calculation study. *Journal of the American Chemical Society* **2005,** *127* (51), 18274-18280.
214. Fang, H.; Zheng, A.; Chu, Y.; Deng, F., 13C Chemical Shift of Adsorbed Acetone for Measuring the Acid Strength of Solid Acids: A Theoretical Calculation Study. *The Journal of Physical Chemistry C* **2010,** *114* (29), 12711-12718.
215. Chu, Y.; Yu, Z.; Zheng, A.; Fang, H.; Zhang, H.; Huang, S.-J.; Liu, S.-B.; Deng, F., Acidic Strengths of Brønsted and Lewis Acid Sites in Solid Acids Scaled by 31P NMR Chemical Shifts of Adsorbed Trimethylphosphine. *The Journal of Physical Chemistry C* **2011,** *115* (15), 7660-7667.
216. Lunsford, J. H.; Rothwell, W. P.; Shen, W., Acid sites in zeolite Y: a solid-state NMR and infrared study using trimethylphosphine as a probe molecule. *Journal of the American Chemical Society* **1985,** *107* (6), 1540-1547.
217. Lunsford, J. H.; Tutunjian, P. N.; Chu, P. J.; Yeh, E. B.; Zalewski, D. J., Solid-state NMR study using trimethylphosphine as a probe of acid sites in normal and dealuminated zeolite Y. *The Journal of Physical Chemistry* **1989,** *93* (6), 2590-2595.
218. Kao, H.-M.; Yu, C.-Y.; Yeh, M.-C., Detection of the inhomogeneity of Brønsted acidity in H-mordenite and H-β zeolites: a comparative NMR study using trimethylphosphine and trimethylphosphine oxide as 31P NMR probes. *Microporous and Mesoporous Materials* **2002,** *53* (1), 1-12.
219. Zhang, W.; Han, X.; Liu, X.; Bao, X., Characterization of the acid sites in dealuminated nanosized HZSM-5 zeolite with the probe molecule trimethylphosphine. *Journal of Molecular Catalysis A: Chemical* **2003,** *194* (1), 107-113.
220. Baltusis, L.; Frye, J. S.; Maciel, G. E., Phosphorus 31 NMR study of trialkylphosphine probes adsorbed on silica-alumina. *Journal of the American Chemical Society* **1987,** *109* (1), 40-46.
221. Zhao, B.; Pan, H.; Lunsford, J. H., Characterization of [(CH3)3P−H]+ Complexes in Normal H-Y, Dealuminated H-Y, and H-ZSM-5 Zeolites Using 31P Solid-State NMR Spectroscopy. *Langmuir* **1999,** *15* (8), 2761-2765.
222. Yang, G.; Lan, X.; Zhuang, J.; Ma, D.; Zhou, L.; Liu, X.; Han, X.; Bao, X., Acidity and defect sites in titanium silicalite catalyst. *Applied Catalysis A: General* **2008,** *337* (1), 58-65.
223. Deng, F.; Du, Y.; Ye, C.; Wang, J.; Ding, T.; Li, H., Acid Sites and Hydration Behavior of Dealuminated Zeolite HZSM-5: A High-Resolution Solid State NMR Study. *The Journal of Physical Chemistry* **1995,** *99* (41), 15208-15214.
224. Kao, H.-M.; Chang, P.-C.; Liao, Y.-W.; Lee, L.-P.; Chien, C.-H., Solid-state NMR characterization of the acid sites in cubic mesoporous Al-MCM-48 materials using trimethylphosphine oxide as a 31P NMR probe. *Microporous and Mesoporous Materials* **2008,** *114* (1), 352-364.
225. Hu, W.; Luo, Q.; Su, Y.; Chen, L.; Yue, Y.; Ye, C.; Deng, F., Acid sites in mesoporous Al-SBA-15 material as revealed by solid-state NMR spectroscopy. *Microporous and Mesoporous Materials* **2006,** *92* (1), 22-30.
226. Wang, J.; Yu, N.; Zheng, A.; Yang, J.; Wu, D.; Sun, Y.; Ye, C.; Deng, F., Mesoporous MSU materials functionalized with sulfonic group: A multinuclear NMR and theoretical calculation study. *Microporous and Mesoporous Materials* **2006,** *89* (1), 219-226.

227. Yu, H.; Fang, H.; Zhang, H.; Li, B.; Deng, F., Acidity of sulfated tin oxide and sulfated zirconia: A view from solid-state NMR spectroscopy. *Catalysis Communications* **2009,** *10* (6), 920-924.
228. Yang, J.; Zhang, M.; Deng, F.; Luo, Q.; Yi, D.; Ye, C., Solid state NMR study of acid sites formed by adsorption of SO3 onto γ-Al2O3. *Chemical Communications* **2003,** (7), 884-885.
229. Zhang, H.; Yu, H.; Zheng, A.; Li, S.; Shen, W.; Deng, F., Reactivity Enhancement of 2-Propanol Photocatalysis on SO42−/TiO2: Insights from Solid-State NMR Spectroscopy. *Environmental Science & Technology* **2008,** *42* (14), 5316-5321.
230. Xu, H. M.; Wang, Z. C.; Miao, Z. C.; Zhu, Y. X.; Marianov, A.; Wang, L. Z.; Castignolles, P.; Gaborieau, M.; Huang, J.; Jiang, Y. J., Correlation between Acidity and Catalytic Performance of Mesoporous Zirconium Oxophosphate in Phenylglyoxal Conversion. *Acs Sustainable Chemistry & Engineering* **2019,** *7* (9), 8931-8942.
231. Karra, M. D.; Sutovich, K. J.; Mueller, K. T., NMR characterization of Bronsted acid sites in faujasitic zeolites with use of perdeuterated trimethylphosphine oxide. *Journal of the American Chemical Society* **2002,** *124* (6), 902-903.
232. Liu, F.; Zheng, A.; Noshadi, I.; Xiao, F.-S., Design and synthesis of hydrophobic and stable mesoporous polymeric solid acid with ultra strong acid strength and excellent catalytic activities for biomass transformation. *Applied Catalysis B: Environmental* **2013,** *136-137*, 193-201.
233. Rakiewicz, F.; Peters, W.; Wormsbecher, F.; Sutovich, J.; Mueller, T., Characterization of acid sites in zeolitic and other inorganic systems using solid-state P-31 NMR of the probe molecule trimethylphosphine oxide. *The Journal of Physical Chemistry B* **1998,** *102* (16), 2890-2896.
234. Sutovich, K. J.; Peters, A. W.; Rakiewicz, E. F.; Wormsbecher, R. F.; Mattingly, S. M.; Mueller, K. T., Simultaneous Quantification of Brønsted- and Lewis-Acid Sites in a USY Zeolite. *Journal of Catalysis* **1999,** *183* (1), 155-158.
235. Osegovic, P.; Drago, S., Measurement of the Global Acidity of Solid Acids by 31P MAS NMR of Chemisorbed Triethylphosphine Oxide. *The Journal of Physical Chemistry B* **2000,** *104* (1), 147-154.
236. Osegovic, P.; Drago, S., A Solid Acidity Scale Based on the31P MAS-NMR Shift of Chemisorbed Triethylphosphine Oxide. *Journal of Catalysis* **1999,** *182* (1), 1-4.
237. Alonso, B.; Klur, I.; Massiot, D., Studies of surfaces through molecular probe adsorption and solid-state NMR. *Chemical Communications* **2002,** (8), 804-805.
238. Zheng, A.; Chen, L.; Yang, J.; Zhang, M.; Su, Y.; Yue, Y.; Ye, C.; Deng, F., Combined DFT Theoretical Calculation and Solid-State NMR Studies of Al Substitution and Acid Sites in Zeolite MCM-22. *The Journal of Physical Chemistry B* **2005,** *109* (51), 24273-24279.
239. Tagusagawa, C.; Takagaki, A.; Iguchi, A.; Takanabe, K.; Kondo, J. N.; Ebitani, K.; Hayashi, S.; Tatsumi, T.; Domen, K., Highly Active Mesoporous Nb–W Oxide Solid-Acid Catalyst. *Angewandte Chemie International Edition* **2010,** *49* (6), 1128-1132.
240. Zheng, A.; Huang, J.; Chen, H.; Wu, H.; Zhang, H.; Lee, K.; de Ménorval, L.-C.; Deng, F.; Liu, S.-B., 31P Chemical Shift of Adsorbed Trialkylphosphine Oxides for Acidity Characterization of Solid Acids Catalysts. *The Journal of Physical Chemistry A* **2008,** *112* (32), 7349-7356.
241. Tagusagawa, C.; Takagaki, A.; Hayashi, S.; Domen, K., Characterization of HNbWO6 and HTaWO6 Metal Oxide Nanosheet Aggregates As Solid Acid Catalysts. *The Journal of Physical Chemistry C* **2009,** *113* (18), 7831-7837.

242. Zhao, Q.; Chen, W.-H.; Huang, S.-J.; Wu, Y.-C.; Lee, H.-K.; Liu, S.-B., Discernment and Quantification of Internal and External Acid Sites on Zeolites. *The Journal of Physical Chemistry B* **2002,** *106* (17), 4462-4469.
243. Wang, Z. B., Robert; Jiang, Yijiao; Wang, Lizhuo; Xu, Haimei; Castignolles, Patrice; Gaborieau, Marianne; Lafon, Olivier; Amoureux, Jean-paul; Hunger, Michael; Baiker, Alfons; Huang, Jun, Engineering distinct structure-interface of sub-nano alumina domains on silica for acidic amorphous silica-alumina towards bio-refining. *Journal of the American Chemical Society Au* **2021**.
244. Jacobs, P. A.; Mortier, W. J.; Uytterhoeven, J. B., Properties of zeolites in relation to their electronegativity: Acidity, carboniogenic activity and strength of interaction in transition metal complexes *Journal of Inorganic & Nuclear Chemistry* **1978,** *40* (11), 1919-1923.
245. Mortier, W. J., Zeolite electronegativity related to physicochemical properties. *Journal of Catalysis* **1978,** *55* (2), 138-145.
246. Hobza, P.; Sauer, J., Minimal basis set MINI-1—powerful tool for calculating of molecular interactions. I. Neutral complexes. *Theoretica Chimica Acta* **1984,** *65* (4), 279-290.
247. Zheng, A.; Huang, S.-J.; Liu, S.-B.; Deng, F., Acid properties of solid acid catalysts characterized by solid-state 31P NMR of adsorbed phosphorous probe molecules. *Physical Chemistry Chemical Physics.* **2011,** *13* (33), 14889.
248. Hernandez-Tamargo, C. E.; Roldan, A.; De Leeuw, N. H., DFT Modeling of the Adsorption of Trimethylphosphine Oxide at the Internal and External Surfaces of Zeolite MFI. *The Journal of Physical Chemistry C* **2016,** *120* (34), 19097-19106.
249. Zhang, W.; Ma, D.; Liu, X.; Liu, X.; Bao, X., Perfluorotributylamine as a probe molecule for distinguishing internal and external acidic sites in zeolites by high-resolution 1H MAS NMR spectroscopy. *Chemical Communications* **1999,** (12), 1091-1092.
250. Zhang, W.; Bao, X.; Guo, X.; Wang, X., *Catalysis Letters* **1999,** *60* (1/2), 89-94.
251. Valyon, J.; Engelhardt, J.; Kallo, D.; Hegedus, M., The activation of CD4 for H/D exchange over H-zeolites. *Catalysis Letters* **2002,** *82* (1-2), 29-35.
252. Wischert, R.; Coperet, C.; Delbecq, F.; Sautet, P., Optimal Water Coverage on Alumina: A Key to Generate Lewis Acid-Base Pairs that are Reactive Towards the C-H Bond Activation of Methane. *Angewandte Chemie-International Edition* **2011,** *50* (14), 3202-3205.
253. Haw, J. F., Zeolite acid strength and reaction mechanisms in catalysist. *Physical Chemistry Chemical Physics* **2002,** *4* (22), 5431-5441.
254. White, J. L.; Beck, L. W.; Haw, J. F., Characterization of hydrogen bonding in zeolites by proton solid-state NMR spectroscopy *Journal of the American Chemical Society* **1992,** *114* (15), 6182-6189.
255. Beck, W.; Xu, T.; Nicholas, B.; Haw, F., Kinetic NMR and density functional study of benzene H/D exchange in zeolites, the most simple aromatic substitution *Journal of the American Chemical Society* **1995,** *117* (46), 11594-11595.
256. Mildner, T.; Freude, D., Proton transfer between bronsted sites and benzene molecules in zeolites H-Y studies by in situ MAS NMR. *Journal of Catalysis* **1998,** *178* (1), 309-314.
257. Huang, J.; Jiang, Y.; Marthala, V. R. R.; Hunger, M., Insight into the mechanisms of the ethylbenzene disproportionation: Transition state shape selectivity on zeolites. *Journal of the American Chemical Society* **2008,** *130* (38), 12642-12644.
258. Kubota, T.; Osuga, R.; Yokoi, T.; Kondo, J. N., Consideration of Acid Strength of a Single OH Group on Zeolites by Isotope Exchange Reaction with Ethane at High Temperatures. *Topics in Catalysis* **2017,** *60* (19-20), 1496-1505.
259. Umar, M.; Ji, X.; Kirikkaleli, D.; Alola, A., The imperativeness of environmental quality in the United States transportation sector amidst biomass-fossil energy consumption and growth. *Journal of Cleaner Production* **2021,** *285*, 124863.

260. Alakomi, H.-L.; Skytta, E.; Saarela, M.; Mattila-Sandholm, T.; Latva-Kala, K.; Helander, I., Lactic acid permeabilizes gram-negative bacteria by disrupting the outer membrane. *Applied and environmental microbiology* **2000,** *66* (5), 2001-2005.
261. Kim, D.; Wang, Z.; Jiang, Y.; Hunger, M.; Huang, J., The cooperative effect of Lewis and Brønsted acid sites on Sn-MCM-41 catalysts for the conversion of 1, 3-dihydroxyacetone to ethyl lactate. *Green Chemistry* **2019,** *21* (12), 3383-3393.
262. Xu, H.; Wang, Z.; Miao, Z.; Zhu, Y.; Marianov, A.; Wang, L.; Castignolles, P.; Gaborieau, M.; Huang, J.; Jiang, J., Correlation between acidity and catalytic performance of mesoporous zirconium oxophosphate in phenylglyoxal conversion. *ACS Sustainable Chemistry & Engineering* **2019,** *7* (9), 8931-8942.
263. Wang, Z.; Jiang, Y.; Hunger, M.; Baiker, A.; Huang, J., Catalytic Performance of Brønsted and Lewis Acid Sites in Phenylglyoxal Conversion on Flame-Derived Silica–Zirconia. *ChemCatChem* **2014,** *6* (10), 2970-2975.
264. Marianou, A.; Michailof, M.; Pineda, A.; Iliopoulou, E.; Triantafyllidis, K.; Lappas, A., Effect of Lewis and Brønsted acidity on glucose conversion to 5-HMF and lactic acid in aqueous and organic media. *Applied Catalysis A: General* **2018,** *555*, 75-87.
265. Iris, K.; Tsang, C., Conversion of biomass to hydroxymethylfurfural: A review of catalytic systems and underlying mechanisms. *Bioresource technology* **2017,** *238*, 716-732.
266. An, H.; Kweon, S.; Kang, C.; Shin, H.; Kim, F.; Park, B.; Min, K., Cascade conversion of glucose to 5-hydroxymethylfurfural over Brönsted-Lewis bi-acidic SnAl-beta zeolites. *Korean Journal of Chemical Engineering* **2021**, 1-9.
267. Otomo, R.; Yokoi, T.; Kondo, J. N.; Tatsumi, T., Dealuminated Beta zeolite as effective bifunctional catalyst for direct transformation of glucose to 5-hydroxymethylfurfural. *Applied Catalysis A: General* **2014,** *470*, 318-326.
268. Carreon, M. A.; Guliants, V. V., Mesostructuring of metal oxides through EISA: fundamentals and applications. In *Ordered Porous Solids*, Elsevier: 2009; pp 413-439.
269. Wang, Z.; Jiang, Y.; Rachwalik, R.; Liu, Z.; Shi, J.; Hunger, M.; Huang, J. J. C., One-Step Room-Temperature Synthesis of [Al] MCM-41 Materials for the Catalytic Conversion of Phenylglyoxal to Ethylmandelate. **2013,** *5* (12), 3889-3896.
270. Duan, C.-L.; Liu, X.; Shan, B.; Chen, R. J. R. o. S. I., Fluidized bed coupled rotary reactor for nanoparticles coating via atomic layer deposition. **2015,** *86* (7), 075101.
271. Yang, W.; Kim, K. D.; O'Dell, L. A.; Wang, L.; Xu, H.; Ruan, M.; Wang, W.; Ryoo, R.; Jiang, Y.; Huang, J. J. J. o. C., Brønsted acid sites formation through penta-coordinated aluminum species on alumina-boria for phenylglyoxal conversion. **2022,** *416*, 375-386.
272. Ardagh, M. A.; Bo, Z.; Nauert, S. L.; Notestein, J. M. J. A. C., Depositing SiO2 on Al2O3: A route to tunable Brønsted acid catalysts. **2016,** *6* (9), 6156-6164.
273. Epp, J., X-ray diffraction (XRD) techniques for materials characterization. In *Materials characterization using nondestructive evaluation (NDE) methods*, Elsevier: 2016; pp 81-124.
274. Wang, L.; Tang, R.; Kheradmand, A.; Jiang, Y.; Wang, H.; Yang, W.; Chen, Z.; Zhong, X.; Ringer, S. P.; Liao, X. J. A. C. B. E., Enhanced solar-driven benzaldehyde oxidation with simultaneous hydrogen production on Pt single-atom catalyst. **2021,** *284*, 119759.
275. Luo, Z., *A practical guide to transmission electron microscopy: Fundamentals*. Momentum Press: 2015.
276. https://www.phi.com/surface-analysis-techniques/xps-esca.html.
277. Yang, W.; Wang, Z.; Huang, J.; Jiang, Y. J. T. J. o. P. C. C., Qualitative and quantitative analysis of acid properties for solid acids by solid-state nuclear magnetic resonance spectroscopy. **2021,** *125* (19), 10179-10197.

278. Grey, C. P.; Vega, A. J. J. J. o. t. A. C. S., Determination of the quadrupole coupling constant of the invisible aluminum spins in zeolite HY with 1H/27Al TRAPDOR NMR. **1995,** *117* (31), 8232-8242.
279. Kentgens, A. J. G., A practical guide to solid-state NMR of half-integer quadrupolar nuclei with some applications to disordered systems. **1997,** *80* (3-4), 271-306.
280. Massiot, D.; Fayon, F.; Capron, M.; King, I.; Le Calvé, S.; Alonso, B.; Durand, J. O.; Bujoli, B.; Gan, Z.; Hoatson, G. J. M. r. i. c., Modelling one-and two-dimensional solid-state NMR spectra. 2002, 40 (1), 70-76.
281. Wang, Z.; Jiang, Y.; Yi, X.; Zhou, C.; Rawal, A.; Hook, J.; Liu, Z.; Deng, F.; Zheng, A.; Hunger, M. J. S. B., High population and dispersion of pentacoordinated AlV species on the surface of flame-made amorphous silica-alumina. **2019**, *64* (8), 516-523.
282. Feng, R.; Liu, S.; Bai, P.; Qiao, K.; Wang, Y.; Al-Megren, H. A.; Rood, M. J.; Yan, Z., Preparation and characterization of γ-Al2O3 with rich Brönsted acid sites and its application in the fluid catalytic cracking process. *The Journal of Physical Chemistry C* **2014,** *118* (12), 6226-6234.
283. Wilson, K.; Clark, J. H., Solid acids and their use as environmentally friendly catalysts in organic synthesis. *Pure and Applied Chemistry* **2000,** *72* (7), 1313-1319.
284. Hara, M., Biomass conversion by a solid acid catalyst. *Energy & Environmental Science* **2010,** *3* (5), 601-607.
285. Ennaert, T.; Van Aelst, J.; Dijkmans, J.; De Clercq, R.; Schutyser, W.; Dusselier, M.; Verboekend, D.; Sels, B., Potential and challenges of zeolite chemistry in the catalytic conversion of biomass. *Chemical Society Review* **2016,** *45* (3), 584-611.
286. Ji, Y. J.; Yang, H. H.; Yan, W., Strategies to Enhance the Catalytic Performance of ZSM-5 Zeolite in Hydrocarbon Cracking: A Review. *Catalysts* **2017,** *7* (12), 367.
287. Sani, Y. M.; Daud, W. M. A. W.; Aziz, A., Activity of solid acid catalysts for biodiesel production: a critical review. *Applied Catalysis A: General* **2014,** *470*, 140-161.
288. Zhang, W.; Smirniotis, P., Effect of zeolite structure and acidity on the product selectivity and reaction mechanism forn-octane hydroisomerization and hydrocracking. *Journal of Catalysis* **1999,** *182* (2), 400-416.
289. Dai, W.; Wang, X.; Wu, G.; Guan, N.; Hunger, M.; Li, L., Methanol-to-olefin conversion on silicoaluminophosphate catalysts: effect of Brønsted acid sites and framework structures. *ACS catalysis* **2011,** *1* (4), 292-299.
290. Xu, S.; Zhi, Y.; Han, J.; Zhang, W.; Wu, X.; Sun, T.; Wei, Y.; Liu, Z., Advances in catalysis for methanol-to-olefins conversion. *Advances in catalysis* **2017,** *61*, 37-122.
291. Nakabayashi, H., Properties of acid sites on TiO2–SiO2 and TiO2–Al2O3 mixed oxides measured by infrared spectroscopy. *Bulletin of the Chemical Society of Japan* **1992,** *65* (3), 914-916.
292. Liu, Z.; Tabora, J.; Davis, R., Relationships between microstructure and surface acidity of Ti-Si mixed oxide catalysts. *Journal of Catalysis* **1994,** *149* (1), 117-126.
293. Ravi, M.; Sushkevich, V. L.; van Bokhoven, J., Towards a better understanding of Lewis acidic aluminium in zeolites. *Nature Materials* **2020,** *19* (10), 1047-1056.
294. Zhu, Z.; Ma, H.; Liao, W.; Tang, P.; Yang, K.; Su, T.; Ren, W.; Lü, H., Insight into tri-coordinated aluminum dependent catalytic properties of dealuminated Y zeolites in oxidative desulfurization. *Applied Catalysis B: Environmental* **2021,** *288*, 120022.
295. Jenness, G. R.; Christiansen, M. A.; Caratzoulas, S.; Vlachos, D. G.; Gorte, R., Site-dependent Lewis acidity of γ-Al2O3 and its impact on ethanol dehydration and etherification. *The Journal of Physical Chemistry C* **2014,** *118* (24), 12899-12907.
296. Jia, W.; Wu, Q.; Lang, X.; Hu, C.; Zhao, G.; Li, J.; Zhu, Z., Influence of lewis acidity on catalytic activity of the porous alumina for dehydrofluorination of 1, 1, 1, 2-tetrafluoroethane to trifluoroethylene. *Catalysis Letters* **2015,** *145* (2), 654-661.

297. Camposeco, R.; Castillo, S.; Mejía-Centeno, I.; Navarrete, J.; Nava, N., Boosted surface acidity in TiO2 and Al2O3-TiO2 nanotubes as catalytic supports. *Applied Surface Science* **2015,** *356*, 115-123.
298. Izumi, Y.; Shiba, T., Characterization of the Alumina-Boria Catalyst. *Bulletin of the Chemical Society of Japan* **1964,** *37* (12), 1797-1809.
299. Petre, A.; Perdigon-Melon, J.; Gervasini, A.; Auroux, A., Acid-Base Properties of Alumina-Supported M2O3 (M= B, Ga, In) Catalysts. *Topics in catalysis* **2002,** *19* (3-4), 271-281.
300. Mnasri, S.; Frini-Srasra, N., Evolution of Brönsted and Lewis acidity of single and mixed pillared bentonite. *Infrared Physics & Technology* **2013,** *58*, 15-20.
301. Chu, Y.; Yi, X.; Li, C.; Sun, X.; Zheng, A., Brønsted/Lewis acid sites synergistically promote the initial C–C bond formation in the MTO reaction. *Chemical science* **2018,** *9* (31), 6470-6479.
302. Xin, S.; Wang, Q.; Xu, J.; Chu, Y.; Wang, P.; Feng, N.; Qi, G.; Trébosc, J.; Lafon, O.; Fan, W., The acidic nature of "NMR-invisible" tri-coordinated framework aluminum species in zeolites. *Chemical science* **2019,** *10* (43), 10159-10169.
303. Šepelák, V.; Düvel, A.; Wilkening, M.; Becker, K.-D.; Heitjans, P., Mechanochemical reactions and syntheses of oxides. *Chemical Society Reviews* **2013,** *42* (18), 7507-7520.
304. Wang, Z.; Jiang, Y.; Lafon, O.; Trébosc, J.; Kim, K. D.; Stampfl, C.; Baiker, A.; Amoureux, J.-P.; Huang, J., Brønsted acid sites based on penta-coordinated aluminum species. *Nature communications* **2016,** *7* (1), 1-5.
305. Kwak, J. H.; Hu, J.; Mei, D.; Yi, C.-W.; Kim, D. H.; Peden, C. H.; Allard, L. F.; Szanyi, J., Coordinatively unsaturated Al3+ centers as binding sites for active catalyst phases of platinum on γ-Al2O3. *Science* **2009,** *325* (5948), 1670-1673.
306. Duan, H. M.; You, R.; Xu, S. T.; Li, Z. R.; Qian, K.; Cao, T.; Huang, W. X.; Bao, X., Pentacoordinated Al3+-Stabilized Active Pd Structures on Al2O3-Coated Palladium Catalysts for Methane Combustion. *Angewandte Chemie-International Edition* **2019,** *58* (35), 12043-12048.
307. Zhang, Z.; Zhu, Y.; Asakura, H.; Zhang, B.; Zhang, J.; Zhou, M.; Han, Y.; Tanaka, T.; Wang, A.; Zhang, T., Thermally stable single atom Pt/m-Al2O3 for selective hydrogenation and CO oxidation. *Nature communications* **2017,** *8* (1), 1-10.
308. Wang, Z. C.; Li, T.; Jiang, Y. J.; Lafon, O.; Liu, Z. W.; Trebosc, J.; Baiker, A.; Amoureux, J. P.; Huang, J., Acidity enhancement through synergy of penta- and tetra-coordinated aluminum species in amorphous silica networks. *Nature Communications* **2020,** *11* (1), 1-9.
309. Wang, Z.; Jiang, Y.; Baiker, A.; Huang, J., Pentacoordinated Aluminum Species: New Frontier for Tailoring Acidity-Enhanced Silica-Alumina Catalysts. *Accounts of Chemical Research* **2020,** *53* (11), 2648-2658.
310. Xiu, T. P.; Wang, J. C.; Liu, Q., Ordered bimodal mesoporous boria-alumina composite: One-step synthesis, structural characterization, active catalysis for methanol dehydration. *Microporous and Mesoporous Materials* **2011,** *143* (2-3), 362-367.
311. Xu, J.; Wang, Q.; Li, S.; Deng, F., *Solid-state NMR in zeolite catalysis*. Springer: 2019; Vol. 103.
312. Coster, D.; Blumenfeld, A. L.; Fripiat, J., Lewis-Acid Sites and Surface Aluminum in Aluminas and Zeolites - a High-Resolution Nmr-Study. *Journal of Physical Chemistry* **1994,** *98* (24), 6201-6211.
313. Crepeau, G.; Montouillout, V.; Vimont, A.; Mariey, L.; Cseri, T.; Mauge, F., Nature, structure and strength of the acidic sites of amorphous silica alumina: an IR and NMR study. *Journal of Physical Chemistry B* **2006,** *110* (31), 15172-85.

314. Dumeignil, F.; Rigole, M.; Guelton, M.; Grimblot, J., Characterization of boria− alumina mixed oxides prepared by a sol− gel method. 1. NMR characterization of the xerogels. *Chemistry of materials* **2005,** *17* (9), 2361-2368.
315. Hansen, M. R.; Jakobsen, H. J.; Skibsted, J., Structure and Dynamics of Hydrous Surface Species on Alumina− Boria Catalysts and Their Precursors from 1H, 2H, 11B, and 27Al MAS NMR Spectroscopy. *The Journal of Physical Chemistry C* **2009,** *113* (6), 2475-2486.
316. Zheng, A.; Li, S.; Liu, S. B.; Deng, F., Acidic Properties and Structure-Activity Correlations of Solid Acid Catalysts Revealed by Solid-State NMR Spectroscopy. *Accounts of Chemical Research* **2016,** *49* (4), 655-63.
317. Ehresmann, J. O.; Wang, W.; Herreros, B.; Luigi, D.-P.; Venkatraman, T.; Song, W.; Nicholas, J. B.; Haw, J. F., Theoretical and experimental investigation of the effect of proton transfer on the 27Al MAS NMR line shapes of zeolite− adsorbate complexes: an independent measure of solid acid strength. *Journal of the American Chemical Society* **2002,** *124* (36), 10868-10874.
318. Massiot, D.; Fayon, F.; Capron, M.; King, I.; Le Calve, S.; Alonso, B.; Durand, J. O.; Bujoli, B.; Gan, Z. H.; Hoatson, G., Modelling one- and two-dimensional solid-state NMR spectra. *Magnetic Resonance in Chemistry* **2002,** *40* (1), 70-76.
319. Dumeignil, F.; Rigole, M.; Guelton, M.; Grimblot, J., Characterization of boria-alumina mixed oxides prepared by a sol-gel method. 2. Characterization of the calcined xerogels. *Chemistry of Materials* **2005,** *17* (9), 2369-2377.
320. Wang, Z.; Jiang, Y.; Yi, X.; Zhou, C.; Rawal, A.; Hook, J.; Liu, Z.; Deng, F.; Zheng, A.; Hunger, M., High population and dispersion of pentacoordinated AlV species on the surface of flame-made amorphous silica-alumina. *Science Bulletin* **2019,** *64* (8), 516-523.
321. Feng, R.; Yan, X.; Hu, X., Effects of boron and fluorine modified γ-Al2O3 with tailored surface acidity on catalytic ethanol dehydration to ethylene. *Journal of Porous Materials* **2018,** *25* (4), 1105-1114.
322. Carreon, M. A.; Guliants, V. V., Mesostructuring of metal oxides through EISA: fundamentals and applications. In *Ordered Porous Solids*, Elsevier: 2009; pp 413-439.
323. Zhao, D.; Feng, J.; Huo, Q.; Melosh, N.; Fredrickson, G. H.; Chmelka, B. F.; Stucky, G. D., Triblock copolymer syntheses of mesoporous silica with periodic 50 to 300 angstrom pores. *Science* **1998,** *279* (5350), 548-52.
324. Huang, J.; Jiang, Y. J.; Marthala, V. R. R.; Ooi, Y. S.; Hunger, M., Regioselective H/D exchange at the side-chain of ethylbenzene on dealuminated zeolite H-Y studied by in situ MAS NMR-UV/Vis spectroscopy. *Chemphyschem* **2008,** *9* (8), 1107-1109.
325. Massiot, D.; Touzo, B.; Trumeau, D.; Coutures, J.; Virlet, J.; Florian, P.; Grandinetti, P., Two-dimensional magic-angle spinning isotropic reconstruction sequences for quadrupolar nuclei. *Solid state nuclear magnetic resonance* **1996,** *6* (1), 73-83.
326. Jiao, J.; Kanellopoulos, J.; Wang, W.; Ray, S. S.; Foerster, H.; Freude, D.; Hunger, M., Characterization of framework and extra-framework aluminum species in non-hydrated zeolites Y by 27 Al spin-echo, high-speed MAS, and MQMAS NMR spectroscopy at B0= 9.4 to 17.6 T. *Physical Chemistry Chemical Physics* **2005,** *7* (17), 3221-3226.
327. Huang, J.; Jiang, Y.; Marthala, V. R.; Thomas, B.; Romanova, E.; Hunger, M., Characterization and acidic properties of aluminum-exchanged zeolites X and Y. *The Journal of Physical Chemistry C* **2008,** *112* (10), 3811-3818.
328. Hernandez, C.; Pierre, A., Influence of the sol− gel acidic synthesis conditions on the porous texture and acidity of SiO2− Al2O3 catalysts with a low Al proportion. *Langmuir* **2000,** *16* (2), 530-536.
329. Hensen, E.; Poduval, D.; Magusin, P.; Coumans, A.; Van Veen., Formation of acid sites in amorphous silica-alumina. *Journal of Catalysis* **2010,** *269* (1), 201-218.

330. Hansen, M. R.; Jakobsen, H. J.; Skibsted, J., Structural Environments for Boron and Aluminum in Alumina− Boria Catalysts and Their Precursors from 11B and 27Al Single-and Double-Resonance MAS NMR Experiments. *The Journal of Physical Chemistry C* **2008,** *112* (18), 7210-7222.
331. Xu, S.; Jaegers, N. R.; Hu, W.; Kwak, J. H.; Bao, X.; Sun, J.; Wang, Y.; Hu, J. Z., High-Field One-Dimensional and Two-Dimensional 27Al Magic-Angle Spinning Nuclear Magnetic Resonance Study of θ-, δ-, and γ-Al2O3 Dominated Aluminum Oxides: Toward Understanding the Al Sites in γ-Al2O3. *ACS omega* **2021,** *6* (5), 4090-4099.
332. Yang, W.; Wang, Z.; Huang, Jun., Qualitative and Quantitative Analysis of Acid Properties for Solid Acids by Solid-State Nuclear Magnetic Resonance Spectroscopy. *Journal of Physical Chemistry C* **2021,** *125* (19), 10179-10197
333. Sastre, G.; Lewis, D. W., Modelling of Bronsted acidity in AFI and CHA zeotypes. *Journal of the Chemical Society-Faraday Transactions* **1998,** *94* (19), 3049-3058.
334. Perras, F. A.; Wang, Z.; Kobayashi, T.; Baiker, A.; Huang, J.; Pruski, M., Shedding light on the atomic-scale structure of amorphous silica-alumina and its Bronsted acid sites. *Physical Chemistry Chemical Physics* **2019,** *21* (35), 19529-19537.
335. Shah, R.; Gale, J. D.; Payne, M. C., Comparing the acidities of zeolites and SAPOs from firstprinciples. *Chemical Communications* **1997,** (1), 131-132.
336. Zheng, A.; Huang, S. J.; Liu, S. B.; Deng, F., Acid properties of solid acid catalysts characterized by solid-state 31P NMR of adsorbed phosphorous probe molecules. *Physical Chemistry Chemical Physics* **2011,** *13* (33), 14889-901.
337. Zheng, A.; Liu, S.-B.; Deng, F., 31P NMR chemical shifts of phosphorus probes as reliable and practical acidity scales for solid and liquid catalysts. *Chemical reviews* **2017,** *117* (19), 12475-12531.
338. Lewis, J. D.; Ha, M.; Luo, H.; Faucher, A.; Michaelis, V. K.; Román-Leshkov, Y., Distinguishing active site identity in Sn-beta zeolites using 31P MAS NMR of adsorbed trimethylphosphine oxide. *ACS Catalysis* **2018,** *8* (4), 3076-3086.
339. Jiang, Y.; Huang, J.; Dai, W.; Hunger, M., Solid-state nuclear magnetic resonance investigations of the nature, property, and activity of acid sites on solid catalysts. *Solid state nuclear magnetic resonance* **2011,** *39* (3-4), 116-41.
340. Hu, W.; Luo, Q.; Su, Y. C.; Chen, L.; Yue, Y.; Ye, C. H.; Deng, F., Acid sites in mesoporous Al-SBA-15 material as revealed by solid-state NMR spectroscopy. *Microporous and Mesoporous Materials* **2006,** *92* (1-3), 22-30.
341. Feng, N. D.; Zheng, A. M.; Huang, S. J.; Zhang, H. L.; Yu, N. Y.; Yang, C. Y.; Liu, S. B.; Deng, F., Combined Solid-State NMR and Theoretical Calculation Studies of Bronsted Acid Properties in Anhydrous 12-Molybdophosphoric Acid. *Journal of Physical Chemistry C* **2010,** *114* (36), 15464-15472.
342. Yi, X. F.; Ko, H. H.; Deng, F.; Liu, S. B.; Zheng, A. M., Solid-state(31)P NMR mapping of active centers and relevant spatial correlations in solid acid catalysts. *Nature Protocols* **2020,** *15* (10), 3527-3555.
343. Takagaki, A.; Jung, J. C.; Hayashi, S., Solid Lewis acidity of boehmite γ-AlO (OH) and its catalytic activity for transformation of sugars in water. *RSC Advances* **2014,** *4* (82), 43785-43791.
344. Sato, S.; Kuroki, M.; Sodesawa, T.; Nozaki, F.; Maciel, G. E., Surface structure and acidity of alumina-boria catalysts. *Journal of Molecular Catalysis a-Chemical* **1995,** *104* (2), 171-177.
345. Chen, W. B.; Mauge, F.; van Gestel, J.; Nie, H.; Li, D. D.; Long, X. Y., Effect of modification of the alumina acidity on the properties of supported Mo and CoMo sulfide catalysts. *Journal of Catalysis* **2013,** *304*, 47-62.

346. Ishihara, K.; Yano, T.; Fushimi, M., Asymmetric intramolecular Cannizzaro reaction of anhydrous phenylglyoxal. *Journal of Fluorine Chemistry* **2008,** *129* (10), 994-997.
347. Manning, D. T.; Stansbury Jr, H. A., The Reaction of Nitrosyl Chloride with Acetophenone in Ethanol-Pyridine Solution1. *Journal of the American Chemical Society* **1959,** *81* (18), 4885-4890.
348. Doering, W. V.; Taylor, T. I.; Schoenewaldt, E. F., Mechanism of the Conversion of Phenylglyoxal to Mandelic Acid. *Journal of the American Chemical Society* **1948,** *70* (2), 455-457
349. Corma, A., Inorganic solid acids and their use in acid-catalyzed hydrocarbon reactions. *Chemical reviews* **1995,** *95* (3), 559-614.
350. Helwani, Z.; Othman, M.; Aziz, N.; Kim, J.; Fernando, W., Solid heterogeneous catalysts for transesterification of triglycerides with methanol: a review. *Applied Catalysis A: General* **2009,** *363* (1-2), 1-10.
351. Lok, C.; Van Doorn, J.; Almansa, G. A., Promoted ZSM-5 catalysts for the production of bio-aromatics, a review. *Renewable Sustainable Energy Reviews* **2019,** *113*, 109248.
352. Baba, T.; Watanabe, H.; Ono, Y., Generation of acidic sites in metal salts of heteropoly acids. *The Journal of Physical Chemistry* **1983,** *87* (13), 2406-2411.
353. Pal, R.; Sarkar, T.; Khasnobis, S., Amberlyst-15 in organic synthesis. *Arkivoc* **2012,** *2012* (1), 570-609.
354. Sacia, E. R.; Balakrishnan, M.; Bell, A. T., Biomass conversion to diesel via the etherification of furanyl alcohols catalyzed by Amberlyst-15. *Journal of catalysis* **2014,** *313*, 70-79.
355. Komadel, P.; Madejová, J., Acid activation of clay minerals. *Developments in clay science* **2006,** *1*, 263-287.
356. Wang, Z.; Jiang, Y.; Yi, X.; Zhou, C.; Rawal, A.; Hook, J.; Liu, Z.; Deng, F.; Zheng, A.; Hunger, M., High population and dispersion of pentacoordinated AlV species on the surface of flame-made amorphous silica-alumina. *Science Bulletin* **2019,** *64* (8), 516-523.
357. Zhao, Z.; Xiao, D.; Chen, K.; Wang, R.; Liang, L.; Liu, Z.; Hung, I.; Gan, Z.; Hou, G., Nature of Five-Coordinated Al in γ-Al2O3 Revealed by Ultra-High-Field Solid-State NMR. *ACS Central Science* **2022**.
358. Wang, Z.; Jiang, Y.; Baiker, A.; Hunger, M.; Huang, J., Promoting Aromatic C–H Activation through Reactive Brønsted Acid–Base Pairs on Penta-Coordinated Al-Enriched Amorphous Silica–Alumina. *The Journal of Physical Chemistry Letters* **2022,** *13* (2), 486-491.
359. Wang, Z.; Chen, K.; Jiang, Y.; Trébosc, J.; Yang, W.; Amoureux, J.-P.; Hung, I.; Gan, Z.; Baiker, A.; Lafon, O. J. T. j. o. p. c. l., Revealing Brønsted acidic bridging SiOHAl groups on amorphous silica–alumina by ultrahigh field solid-state NMR. **2021,** *12* (47), 11563-11572.
360. Yang, W.; Kim, K. D.; O'Dell, L. A.; Wang, L.; Xu, H.; Ruan, M.; Wang, W.; Ryoo, R.; Jiang, Y.; Huang, J., Brønsted acid sites formation through penta-coordinated aluminum species on alumina-boria for phenylglyoxal conversion. *Journal of Catalysis* **2022,** *416*, 375-386.
361. Bang, Y.; Han, S. J.; Yoo, J.; Choi, J. H.; Lee, J. K.; Song, J. H.; Lee, J.; Song, I. K., Hydrogen production by steam reforming of simulated liquefied natural gas (LNG) over nickel catalyst supported on mesoporous phosphorus-modified alumina xerogel. *Applied Catalysis B: Environmental* **2014,** *148*, 269-280.
362. Kang, Y.; Rao, X.; Yuan, P.; Wang, C.; Wang, T.; Yue, Y., Al-functionalized mesoporous SBA-15 with enhanced acidity for hydroisomerization of n-octane. *Fuel Processing Technology* **2021,** *215*, 106765.
363. Fu, L.; Li, X.; Liu, M.; Yang, H., Insights into the nature of Cu doping in amorphous mesoporous alumina. *Journal of Materials Chemistry A* **2013,** *1* (46), 14592-14605.

364. Yang, W.; Kim, K. D.; O'Dell, L. A.; Wang, L.; Xu, H.; Ruan, M.; Wang, W.; Ryoo, R.; Jiang, Y.; Huang, J., Brønsted acid sites formation through penta-coordinated aluminum species on alumina-boria for phenylglyoxal conversion. *Journal of Catalysis* **2022,** *416*, 375-386.
365. McMillan, M.; Brinen, J.; Carruthers, J.; Haller, G., A 29Si NMR investigation of the structure of amorphous silica—alumina supports. *Colloids surfaces* **1989,** *38* (1), 133-148.
366. Ren, J.; Eckert, H., Superstructural units involving six-coordinated silicon in sodium phosphosilicate glasses detected by solid-state NMR spectroscopy. *The Journal of Physical Chemistry C* **2018,** *122* (48), 27620-27630.
367. Xiao, Z.; Hou, F.; Zhang, J.; Zheng, Q.; Xu, J.; Pan, L.; Wang, L.; Zou, J.; Zhang, X.; Li, G., Methane Dry Reforming by Ni–Cu Nanoalloys Anchored on Periclase-Phase MgAlO x Nanosheets for Enhanced Syngas Production. *ACS Applied Materials & Interfaces* **2021,** *13* (41), 48838-48854.
368. van Bokhoven, J. A.; Roest, A.; Koningsberger, D.; Miller, J.; Nachtegaal, G.; Kentgens, A., Changes in structural and electronic properties of the zeolite framework induced by extraframework Al and La in H-USY and La (x) NaY: A 29Si and 27Al MAS NMR and 27Al MQ MAS NMR study. *The Journal of Physical Chemistry B* **2000,** *104* (29), 6743-6754.
369. Chen, T.-H.; Houthoofd, K.; Grobet, P., Toward the aluminum coordination in dealuminated mordenite and amorphous silica–alumina: a high resolution 27Al MAS and MQ MAS NMR study. *Microporous mesoporous materials* **2005,** *86* (1-3), 31-37.
370. Senthilkumar, S.; Zhong, W.; Natarajan, M.; Lu, C.; Xu, B.; Liu, X., A green approach for aerobic oxidation of benzylic alcohols catalysed by Cu I–Y zeolite/TEMPO in ethanol without additional additives. *New Journal of Chemistry* **2021,** *45* (2), 705-713.
371. Wang, Z.; Jiang, Y.; Lafon, O.; Trébosc, J.; Duk Kim, K.; Stampfl, C.; Baiker, A.; Amoureux, J.-P.; Huang, J., Brønsted acid sites based on penta-coordinated aluminum species. *Nature Communications* **2016,** *7* (1), 13820.
372. Wang, Z.; Li, T.; Jiang, Y.; Lafon, O.; Liu, Z.; Trébosc, J.; Baiker, A.; Amoureux, J.-P.; Huang, J., Acidity enhancement through synergy of penta-and tetra-coordinated aluminum species in amorphous silica networks. *Nature communications* **2020,** *11* (1), 1-9.
373. Wang, Z.; Jiang, Y.; Lafon, O.; Trébosc, J.; Duk Kim, K.; Stampfl, C.; Baiker, A.; Amoureux, J.-P.; Huang, J. J. N. c., Brønsted acid sites based on penta-coordinated aluminum species. **2016,** *7* (1), 1-5.
374. Zheng, A.; Huang, S.-J.; Liu, S.-B.; Deng, F., Acid properties of solid acid catalysts characterized by solid-state 31P NMR of adsorbed phosphorous probe molecules. *Physical Chemistry Chemical Physics* **2011,** *13* (33), 14889-14901.
375. Yang, W.; Wang, Z.; Huang, J.; Jiang, Y., Qualitative and quantitative analysis of acid properties for solid acids by solid-state nuclear magnetic resonance spectroscopy. *The Journal of Physical Chemistry C* **2021,** *125* (19), 10179-10197.
376. Wang, Z.; Ling, H.; Shi, J.; Stampfl, C.; Yu, A.; Hunger, M.; Huang, J., Acidity enhanced [Al] MCM-41 via ultrasonic irradiation for the Beckmann rearrangement of cyclohexanone oxime to ε-caprolactam. *Journal of catalysis* **2018,** *358*, 71-79.
377. Valla, M.; Rossini, A. J.; Caillot, M.; Chizallet, C. l.; Raybaud, P.; Digne, M.; Chaumonnot, A.; Lesage, A.; Emsley, L.; Van Bokhoven, J. A., Atomic description of the interface between silica and alumina in aluminosilicates through dynamic nuclear polarization surface-enhanced NMR spectroscopy and first-principles calculations. *Journal of the American Chemical Society* **2015,** *137* (33), 10710-10719.
378. Wang, F.; Xiao, W. Y.; Xiao, G. M., Atomic layer deposition of zinc oxide on HZSM-5 template and its methanol aromatization performance. *Catalysis Letters* **2015,** *145* (3), 860-867.

379. Mori, K.; Yamada, Y.; Sato, S., Catalytic dehydration of 1, 2-propanediol into propanal. *Applied Catalysis A: General* **2009,** *366* (2), 304-308.
380. Otomo, R.; Yamaguchi, C.; Iwaisako, D.; Oyamada, S.; Kamiya, Y., Selective dehydration of 1, 2-propanediol to propanal over boron phosphate catalyst in the presence of steam. *ACS Sustainable Chemistry Engineering* **2019,** *7* (3), 3027-3033.
381. Sun, D.; Yamada, Y.; Sato, S., Production of propanal from 1, 2-propanediol over silica-supported WO3 catalyst. *Applied Catalysis A: General* **2014,** *487*, 234-241.
382. Zhang, D.; Barri, S. A.; Chadwick, D., Dehydration of 1, 2-propanediol to propionaldehyde over zeolite catalysts. *Applied Catalysis A: General* **2011,** *400* (1-2), 148-155.
383. Wang, Z.; Wang, L.; Jiang, Y.; Hunger, M.; Huang, J., Cooperativity of Brønsted and Lewis acid sites on zeolite for glycerol dehydration. *ACS Catalysis* **2014,** *4* (4), 1144-1147.
384. Gauthier, M. A.; Stangel, I.; Ellis, T. H.; Zhu, X., A new method for quantifying the intensity of the C= C band of dimethacrylate dental monomers in their FTIR and Raman spectra. *Biomaterials* **2005,** *26* (33), 6440-6448.
385. Razali, N.; Conte, M.; McGregor, J., The role of impurities in the La2O3 catalysed carboxylation of crude glycerol. *Catalysis Letters* **2019,** *149* (5), 1403-1414.
386. Ardagh, A.; Bo, Z.; Nauert, L.; Notestein, M., Depositing SiO2 on Al2O3: A route to tunable Brønsted acid catalysts. *ACS Catalysis* **2016,** *6* (9), 6156-6164.
387. Dorémieux-Morin, C.; Martin, C.; Brégeault, J.-M.; Fraissard, J., Multinuclear high-resolution solid-state nuclear magnetic resonance studies of amorphous silica-aluminas. *Applied catalysis* **1991,** *77* (1), 149-161.
388. Raja, J.; Nguyen, C. P. T.; Lee, C.; Balaji, N.; Chatterjee, S.; Jang, K.; Kim, H.; Yi, J., Improved data retention of InSnZnO nonvolatile memory by H 2 O 2 treated Al 2 O 3 tunneling layer: A cost-effective method. *IEEE Electron Device Letters* **2016,** *37* (10), 1272-1275.
389. Chappex, T.; Scrivener, K. L., The effect of aluminum in solution on the dissolution of amorphous silica and its relation to cementitious systems. *Journal of the American Ceramic Society* **2013,** *96* (2), 592-597.
390. Barr, T. L., The nature of the relative bonding chemistry in zeolites: an XPS study. *Zeolites* **1990,** *10* (8), 760-765.
391. López, J.; López, J. C.; Valerdi, D.; Salgado, G. G.; Díaz-Becerril, T.; Pedraza, A. P.; Gracia, F., Morphological, compositional, structural, and optical properties of Si-nc embedded in SiO x films. *Nanoscale research letters* **2012,** *7* (1), 1-10.
392. Garvie, L. A.; Buseck, P. R., Bonding in silicates: Investigation of the Si L2, 3 edge by parallel electron energy-loss spectroscopy. *American Mineralogist* **1999,** *84* (5-6), 946-964.
393. Busca, G., Silica-alumina catalytic materials: A critical review. *Catalysis Today* **2020,** *357*, 621-629.
394. Marianou, A. A.; Michailof, C. M.; Pineda, A.; Iliopoulou, E.; Triantafyllidis, K.; Lappas, A., Effect of Lewis and Brønsted acidity on glucose conversion to 5-HMF and lactic acid in aqueous and organic media. *Applied Catalysis A: General* **2018,** *555*, 75-87.
395. Otomo, R.; Yokoi, T.; Kondo, J. N.; Tatsumi, T., Dealuminated Beta zeolite as effective bifunctional catalyst for direct transformation of glucose to 5-hydroxymethylfurfural. *Applied Catalysis A: General* **2014,** *470*, 318-326.
396. Sandoval-Díaz, L.-E.; González-Amaya, J.-A.; Trujillo, C.-A., General aspects of zeolite acidity characterization. *Microporous and mesoporous materials* **2015,** *215*, 229-243.
397. Coster, D.; Blumenfeld, A.; Fripiat, J., Lewis acid sites and surface aluminum in aluminas and zeolites: a high-resolution NMR study. *The Journal of Physical Chemistry* **1994,** *98* (24), 6201-6211.

398. Chu, Y.; Yi, X.; Li, C.; Sun, X.; Zheng, A., Brønsted/Lewis acid sites synergistically promote the initial C–C bond formation in the MTO reaction. *Chemical science* **2018,** *9* (31), 6470-6479.
399. Xin, S.; Wang, Q.; Xu, J.; Chu, Y.; Wang, P.; Feng, N.; Qi, G.; Trébosc, J.; Lafon, O.; Fan, W., The acidic nature of "NMR-invisible" tri-coordinated framework aluminum species in zeolites. *Chemical science* **2019,** *10* (43), 10159-10169.
400. Wang, Z.; O'Dell, L. A.; Zeng, X.; Liu, C.; Zhao, S.; Zhang, W.; Gaborieau, M.; Jiang, Y.; Huang, J., Insight into Three-Coordinate Aluminum Species on Ethanol-to-Olefin Conversion over ZSM-5 Zeolites. *Angewandte Chemie International Edition* **2019,** *58* (50), 18061-18068.
401. Zhao, S.; Yang, W.; Kim, K. D.; Wang, L.; Wang, Z.; Ryoo, R.; Huang, J., Synergy of Extraframework Al3+ Cations and Brønsted Acid Sites on Hierarchical ZSM-5 Zeolites for Butanol-to-Olefin Conversion. *The Journal of Physical Chemistry C* **2021,** *125* (21), 11665-11676.
402. Dijkmans, J.; Dusselier, M.; Gabriëls, D.; Houthoofd, K.; Magusin, P. C.; Huang, S.; Pontikes, Y.; Trekels, M.; Vantomme, A.; Giebeler, L., Cooperative catalysis for multistep biomass conversion with Sn/Al Beta zeolite. *Acs Catalysis* **2015,** *5* (2), 928-940.
403. Li, G.; Gao, L.; Sheng, Z.; Zhan, Y.; Zhang, C.; Ju, J.; Zhang, Y.; Tang, Y., A Zr-Al-Beta zeolite with open Zr (iv) sites: an efficient bifunctional Lewis–Brønsted acid catalyst for a cascade reaction. *Catalysis Science & Technology* **2019,** *9* (15), 4055-4065.
404. Qi, G.; Wang, Q.; Xu, J.; Trébosc, J.; Lafon, O.; Wang, C.; Amoureux, J. P.; Deng, F., Synergic Effect of Active Sites in Zinc-Modified ZSM-5 Zeolites as Revealed by High-Field Solid-State NMR Spectroscopy. *Angewandte Chemie International Edition* **2016,** *128* (51), 16058-16062.
405. Gao, P.; Wang, Q.; Xu, J.; Qi, G.; Wang, C.; Zhou, X.; Zhao, X.; Feng, N.; Liu, X.; Deng, F., Brønsted/Lewis acid synergy in methanol-to-aromatics conversion on Ga-modified ZSM-5 zeolites, as studied by solid-state NMR spectroscopy. *ACS Catalysis* **2018,** *8* (1), 69-74.
406. Huang, J.; Jiang, Y.; Marthala, V. R.; Thomas, B.; Romanova, E.; Hunger, M., Characterization and acidic properties of aluminum-exchanged zeolites X and Y. *The Journal of Physical Chemistry C* **2008,** *112* (10), 3811-3818.
407. An, H.; Kweon, S.; Kang, D.-C.; Shin, C.-H.; Kim, J. F.; Park, M. B.; Min, H.-K., Cascade conversion of glucose to 5-hydroxymethylfurfural over Brönsted-Lewis bi-acidic SnAl-beta zeolites. *Korean Journal of Chemical Engineering* **2021,** *38* (6), 1161-1169.
408. Wang, Z.; Buechel, R.; Jiang, Y.; Wang, L.; Xu, H.; Castignolles, P.; Gaborieau, M.; Lafon, O.; Amoureux, J.-P.; Hunger, M., Engineering the distinct structure interface of subnano-alumina domains on silica for acidic amorphous silica–alumina toward biorefining. *JACS Au* **2021,** *1* (3), 262-271.
409. Cao, K.; Cai, J.; Liu, X.; Chen, R., Catalysts design and synthesis via selective atomic layer deposition. *Journal of Vacuum Science Technology A: Vacuum, Surfaces, Films* **2018,** *36* (1), 010801.
410. Mouat, A. R.; George, C.; Kobayashi, T.; Pruski, M.; Van Duyne, R. P.; Marks, T. J.; Stair, P. C., Highly dispersed SiOx/Al2O3 catalysts illuminate the reactivity of isolated silanol sites. *Angewandte Chemie International Edition* **2015,** *127* (45), 13544-13549.
411. Ardagh, M. A.; Bo, Z.; Nauert, S. L.; Notestein, J. M., Depositing SiO2 on Al2O3: A route to tunable Brønsted acid catalysts. *ACS Catalysis* **2016,** *6* (9), 6156-6164.
412. Krishna, S. H.; Zhang, L.; Hermans, I.; Huber, G. W.; Kuech, T. F.; Dumesic, J. A., Rates of levoglucosanol hydrogenolysis over Brønsted and Lewis acid sites on platinum silica-alumina catalysts synthesized by atomic layer deposition. *Journal of catalysis* **2020,** *389*, 111-120.

413. Zhang, W.; Zhu, Y.; Xu, H.; Gaborieau, M.; Huang, J.; Jiang, Y., Glucose conversion to 5-hydroxymethylfurfural on zirconia: tuning surface sites by calcination temperatures. *Catalysis Today* **2020,** *351*, 133-140.
414. Wang, Z.; Jiang, Y.; Rachwalik, R.; Liu, Z.; Shi, J.; Hunger, M.; Huang, J., One-Step Room-Temperature Synthesis of [Al] MCM-41 Materials for the Catalytic Conversion of Phenylglyoxal to Ethylmandelate. *ChemCatChem* **2013,** *5* (12), 3889-3896.
415. Duan, C.-L.; Liu, X.; Shan, B.; Chen, R., Fluidized bed coupled rotary reactor for nanoparticles coating via atomic layer deposition. *Review of Scientific Instruments* **2015,** *86* (7), 075101.
416. Amoureux, J.-P.; Fernandez, C.; Steuernagel, S., ZFiltering in MQMAS NMR. *Journal of Magnetic Resonance* **1996,** *123* (1), 116-118.
417. Massiot, D.; Fayon, F.; Capron, M.; King, I.; Le Calvé, S.; Alonso, B.; Durand, J. O.; Bujoli, B.; Gan, Z.; Hoatson, G., Modelling one-and two-dimensional solid-state NMR spectra. *Magnetic resonance in chemistry* **2002,** *40* (1), 70-76.
418. Kaushik, M.; Leroy, C.; Chen, Z.; Gajan, D.; Willinger, E.; Müller, C. R.; Fayon, F.; Massiot, D.; Fedorov, A.; Copéret, C., Atomic-scale structure and its impact on chemical properties of aluminum oxide layers prepared by atomic layer deposition on silica. *Chemistry of Materials* **2021,** *33* (9), 3335-3348.
419. Hakim, L.; Blackson, J.; Weimer, A., Modification of interparticle forces for nanoparticles using atomic layer deposition. *Chemical Engineering Science* **2007,** *62* (22), 6199-6211.
420. Liang, X.; Weimer, A. W., Photoactivity passivation of TiO 2 nanoparticles using molecular layer deposited (MLD) polymer films. *Journal of Nanoparticle Research* **2010,** *12*, 135-142.
421. Du, H.; Chen, S.; Wang, H.; Lu, J., Acidic alumina overcoating on platinum nanoparticles: Close metal–acid proximity enhances bifunctionality for glycerol hydrogenolysis. *Chinese Journal of Catalysis* **2017,** *38* (7), 1237-1244.
422. Kriesel, J. W.; Sander, M. S.; Tilley, T. D., General route to homogeneous, mesoporous, multicomponent oxides based on the thermolytic transformation of molecular precursors in non-polar media. *Advanced Materials* **2001,** *13* (5), 331-335.
423. Yang, W.; Kim, K. D.; O'Dell, L. A.; Wang, L.; Xu, H.; Ruan, M.; Wang, W.; Ryoo, R.; Jiang, Y.; Huang, J., Brønsted acid sites formation through penta-coordinated aluminum species on alumina-boria for phenylglyoxal conversion. *Journal of Catalysis* **2022,** *416*, 375-386.
424. Xu, S.; Jaegers, N. R.; Hu, W.; Kwak, J. H.; Bao, X.; Sun, J.; Wang, Y.; Hu, J. Z., High-field one-dimensional and two-dimensional 27Al magic-angle spinning nuclear magnetic resonance study of θ-, δ-, and γ-Al2O3 dominated aluminum oxides: toward understanding the Al sites in γ-Al2O3. *ACS omega* **2021,** *6* (5), 4090-4099.
425. Khivantsev, K.; Jaegers, N. R.; Kwak, J. H.; Szanyi, J.; Kovarik, L., Precise Identification and Characterization of Catalytically Active Sites on the Surface of γ-Alumina. *Angewandte Chemie International Edition* **2021,** *133* (32), 17663-17671.
426. Zheng, A.; Liu, S.-B.; Deng, F., Acidity characterization of heterogeneous catalysts by solid-state NMR spectroscopy using probe molecules. *Solid State Nuclear Magnetic Resonance* **2013,** *55*, 12-27.
427. Rakiewicz, E. F.; Peters, A. W.; Wormsbecher, R. F.; Sutovich, K. J.; Mueller, K. T., Characterization of acid sites in zeolitic and other inorganic systems using solid-state 31P NMR of the probe molecule trimethylphosphine oxide. *The Journal of Physical Chemistry B* **1998,** *102* (16), 2890-2896.
428. Obenaus, U.; Dyballa, M.; Lang, S.; Scheibe, M.; Hunger, M., Generation and properties of Brønsted acid sites in bifunctional Rh-, Ir-, Pd-, and Pt-containing zeolites Y

investigated by solid-state NMR spectroscopy. *The Journal of Physical Chemistry C* **2015,** *119* (27), 15254-15262.
429. Yang, W.; Wang, Z.; Huang, J.; Jiang, Y., Qualitative and quantitative analysis of acid properties for solid acids by solid-state nuclear magnetic resonance spectroscopy. *The Journal of Physical Chemistry C* **2021,** *125* (19), 10179-10197.
430. Iris, K.; Tsang, D. C., Conversion of biomass to hydroxymethylfurfural: A review of catalytic systems and underlying mechanisms. *Bioresource technology* **2017,** *238*, 716-732.
431. Ordomsky, V.; Sushkevich, V.; Schouten, J.; Van Der Schaaf, J.; Nijhuis, T., Glucose dehydration to 5-hydroxymethylfurfural over phosphate catalysts. *Journal of catalysis* **2013,** *300*, 37-46.
432. Moreno-Recio, M.; Santamaría-González, J.; Maireles-Torres, P., Brönsted and Lewis acid ZSM-5 zeolites for the catalytic dehydration of glucose into 5-hydroxymethylfurfural. *Chemical Engineering Journal* **2016,** *303*, 22-30.
433. Jimenez-Morales, I.; Moreno-Recio, M.; Santamaria-Gonzalez, J.; Maireles-Torres, P.; Jimenez-Lopez, A., Production of 5-hydroxymethylfurfural from glucose using aluminium doped MCM-41 silica as acid catalyst. *Applied Catalysis B: Environmental* **2015,** *164*, 70-76.
434. Ordomsky, V.; Sushkevich, V.; Schouten, J.; Van Der Schaaf, J.; Nijhuis, T., Glucose dehydration to 5-hydroxymethylfurfural over phosphate catalysts. *Journal of catalysis* **2013,** *300*, 37-46.
435. Wang, Z.; Li, T.; Jiang, Y.; Lafon, O.; Liu, Z.; Trébosc, J.; Baiker, A.; Amoureux, J.-P.; Huang, J., Acidity enhancement through synergy of penta-and tetra-coordinated aluminum species in amorphous silica networks. *Nature Communications* **2020,** *11* (1), 225.
436. Jiménez-Morales, I.; Santamaría-González, J.; Jiménez-López, A.; Maireles-Torres, P., Glucose dehydration to 5-hydroxymethylfurfural on zirconium containing mesoporous MCM-41 silica catalysts. *Fuel* **2014,** *118*, 265-271.
437. Sezgin, E.; Keçeci, M. E.; Akmaz, S.; Koc, S., Heterogeneous Cr-zeolites (USY and Beta) for the conversion of glucose and cellulose to 5-hydroxymethylfurfural (HMF). *Cellulose* **2019,** *26* (17), 9035-9043.
438. Hu, L.; Wu, Z.; Xu, J.; Sun, Y.; Lin, L.; Liu, S., Zeolite-promoted transformation of glucose into 5-hydroxymethylfurfural in ionic liquid. *Chemical Engineering Journal* **2014,** *244*, 137-144.
439. Xia, H.; Hu, H.; Xu, S.; Xiao, K.; Zuo, S., Catalytic conversion of glucose to 5-hydroxymethyfural over Fe/β zeolites with extra-framework isolated Fe species in a biphasic reaction system. *Biomass and bioenergy* **2018,** *108*, 426-432.
440. Wang, Z.; Buechel, R.; Jiang, Y.; Wang, L.; Xu, H.; Castignolles, P.; Gaborieau, M.; Lafon, O.; Amoureux, J.-P.; Hunger, M. J. J. A., Engineering the Distinct Structure Interface of Subnano-alumina Domains on Silica for Acidic Amorphous Silica–Alumina toward Biorefining. *JACS Au* **2021,** *1* (3), 262-271.
441. Candu, N.; El Fergani, M.; Verziu, M.; Cojocaru, B.; Jurca, B.; Apostol, N.; Teodorescu, C.; Parvulescu, V. I.; Coman, S., Efficient glucose dehydration to HMF onto Nb-BEA catalysts. *Catalysis Today* **2019,** *325*, 109-116.
442. Aylak, A. R.; Akmaz, S.; Koc, S. N. J. P. S.; An efficient heterogeneous CrOx–Y zeolite catalyst for glucose to HMF conversion in ionic liquids. *Particulate Science and Technology* **2017,** *35* (4), 490-493.
443. Chung, N. H.; Oanh, V. T.; Thoa, L. K.; Hoang, P, Catalytic conversion of glucose into 5-hydroxymethyl furfural over Cu–Cr/ZSM-5 zeolite. *Waste and biomass valorization* **2020,** *150* (1), 170-177.
444. Oozeerally, R.; Pillier, J.; Kilic, E.; Thompson, P. B.; Walker, M.; Griffith, B. E.; Hanna, J. V.; Degirmenci, V. J., Gallium and tin exchanged Y zeolites for glucose

isomerisation and 5-hydroxymethyl furfural production. *Applied Catalysis A: General* **2020,** *605*, 117798.
445. Moreno-Recio, M.; Santamaría-González, J.; Maireles-Torres, P., Brönsted and Lewis acid ZSM-5 zeolites for the catalytic dehydration of glucose into 5-hydroxymethylfurfural. *Chemical Engineering Journal* **2016,** *303*, 22-30.
446. Marianou, A. A.; Michailof, C. M.; Pineda, A.; Iliopoulou, E.; Triantafyllidis, K.; Lappas, A., Effect of Lewis and Brønsted acidity on glucose conversion to 5-HMF and lactic acid in aqueous and organic media. *Applied Catalysis A: General* **2018,** *555*, 75-87.
447. Peng, K.; Li, X.; Liu, X.; Wang, Y. J. M. C., Hydrothermally stable Nb-SBA-15 catalysts applied in carbohydrate conversion to 5-hydroxymethyl furfural. *Molecular Catalysis* **2017,** *441*, 72-80.
448. Degirmenci, V.; Hensen, Development of a heterogeneous catalyst for lignocellulosic biomass conversion: Glucose dehydration by metal chlorides in a silica-supported ionic liquid layer. *Environmental Progress & Sustainable Energy* **2014,** *33* (2), 657-662.
449. Lei, H.; Wu, Z.; Xu, J.; Sun, Y.; Lin, L.; Liu, S., Zeolite-promoted transformation of glucose into 5-hydroxymethylfurfural in ionic liquid. *Chemical Engineering Journal* **2014**, *244*, 137-144.
450. Ramli, N; Amin, N., Kinetic study of glucose conversion to levulinic acid over Fe/HY zeolite catalyst. *Chemical Engineering Journal* **2016**, *283*, 150-159.
451. Kim, K.; Kim, J.; Teoh, W.; Kim, J.; Huang, J.; Ryoo, R., Cascade reaction engineering on zirconia-supported mesoporous MFI zeolites with tunable Lewis–Brønsted acid sites: A case of the one-pot conversion of furfural to γ-valerolactone. *RSC advances* 2020 *10* (58), 35318-35328.